Epitaxial growth of silicon by PECVD from SiF4/H2/Ar gas mixtures for photovoltaics

Ronan Leal

▶ **To cite this version:**

Ronan Leal. Epitaxial growth of silicon by PECVD from SiF4/H2/Ar gas mixtures for photovoltaics. Materials Science [cond-mat.mtrl-sci]. Université Paris Saclay (COmUE), 2017. English. NNT : 2017SACLX038 . tel-02969502

HAL Id: tel-02969502

https://theses.hal.science/tel-02969502

Submitted on 16 Oct 2020

HAL is a multi-disciplinary open access archive for the deposit and dissemination of scientific research documents, whether they are published or not. The documents may come from teaching and research institutions in France or abroad, or from public or private research centers.

L'archive ouverte pluridisciplinaire **HAL**, est destinée au dépôt et à la diffusion de documents scientifiques de niveau recherche, publiés ou non, émanant des établissements d'enseignement et de recherche français ou étrangers, des laboratoires publics ou privés.

NNT : 2017SACLX038

THESE DE DOCTORAT
DE
L'UNIVERSITE PARIS-SACLAY
PREPAREE A
L'ECOLE POLYTECHNIQUE

ECOLE DOCTORALE N°573
Interfaces : approches interdisciplinaires, fondements, applications et innovation

Spécialité de doctorat : Physique

Par

M. Ronan Léal

Low-temperature formation of epitaxial emitter in crystalline solar cells by plasma-enhanced chemical vapor deposition using $SiF_4/H_2/Ar$ gas mixtures

Thèse présentée et soutenue à Palaiseau, le 11 juillet 2017 :

Composition du Jury :

Prof.	Lecoeur, Philippe	CNRS - IEF	Président du jury
Prof.	Lemiti, Mustapha	INSA-LYON, INL	Rapporteur
Dr.	Slaoui, Abdelilah	CNRS, ICube	Rapporteur
Dr.	De Wolf, Stefaan	KAUST	Examinateur
Dr.	Recamán Payo, María	IMEC	Examinatrice
Dr.	Oberbeck, Lars	TOTAL	Examinateur
Dr.	Poulain, Gilles	TOTAL	Encadrant
Prof.	Roca i Cabarrocas, Pere	LPICM	Directeur de thèse

« Je ne crois pas non plus que dans notre monde l'esprit d'aventure risque de disparaître. Si je vois autour de moi quelque chose de vital, c'est précisément cet esprit d'aventure qui me paraît indéracinable et s'apparente à la curiosité. »

Marie Skłodowska-Curie

Abstract

nPERT (n-type passivated emitter, rear totally diffused) solar cells are gaining more in more interest as a possible next step for the photovoltaic industry. However, boron diffusion from BBr_3, commonly used for the formation of the p-type layer, is known to be not as simple and beneficial as phosphorus diffusion, the latter allowing an efficient impurities gettering. This doctoral work aims to assess the possibility of replacing diffusion by low-temperature (200-300°C) epitaxy using plasma enhanced-chemical vapor deposition (PECVD) to form the boron emitter in nPERT solar cells. This process, using widespread equipment in the PV industry, would allow to simplify and shorten the process flow by suppressing several process steps: BSG (borosilicate glass) formation and removal, drive-in and BRL (boron-rich layer) removal. Also, it limits the risks of oxygen precipitates formation in the wafer and the risk of diffusion-induced dislocations by reducing the thermal budget applied to wafers. Moreover, a precise control of the doping profile is therefore possible due to the low- temperature process. The use of a $SiF_4/H_2/Ar$ gas mixtures combined to the good control of plasma parameters allows to obtain excellent structural properties of intrinsic and doped epitaxial layers and a very smooth interface between the substrate and the epitaxial layers.

The first part of this manuscript concerns the optimization of the process conditions to achieve high quality epitaxy and the identification of epitaxy breakdown causes. The quality of the epitaxy has been assessed via the structural properties measured by ellipsometry, Raman spectroscopy, X-ray diffraction and transmission electron microscopy. The full H_2 depletion, measured by mass spectrometry, and a $[H_2]/[SiF_4]$ gas flow ratio under 1/3 have been identified to be a decisive parameter to perform epitaxy. As a result, intrinsic epi-layers with a 100 % crystalline fraction deduced from ellipsometry measurements and Raman spectroscopy have been achieved. Raman spectroscopy measurements remarkably indicate that the FWHM and peak positions of transverse optical mode for intrinsic epi-layers are identical to those of a c-Si wafer. In the second part of the chapter, the epitaxy breakdown mechanisms have been investigated. Interestingly, TEM analyses and pole figures have shown that twinning was responsible of epitaxy breakdown in case of excessive RF power or incomplete H_2 depletion. However, the epitaxy breakdown caused by an excessive RF power can be distinguished by the presence of <111> oriented grains in the direction of growth.

Then we focused on the growth mechanisms involved in low-temperature epitaxy by PECVD. A good correlation between in situ ellipsometry measurements and TEM characterization in the early stages of growth has been demonstrated, highlighting a Volmer-Weber growth mode on the initial stages of growth. Energy-filtered transmission electron microscopy has been used on carbon covered TEM grids previously exposed to the plasma to investigate the role of nanoparticles, radicals and ions precursors involved in epitaxial growth. A comparative study highlighting differences in morphology, crystallinity and size distribution of nanoparticles depending on the stages of growth has been shown. Although it is difficult as yet to draw general conclusions about the role of each precursor, given the complex environment, this study provides a first step for their identification.

The third part of the manuscript deals with the transfer and scale-up of process conditions from an academic research PECVD reactor to a pre-pilot line tool allowing the deposition on 6 inches wafers. Above all, this allowed to confirm the good parameterization of the process window through the H_2 depletion measurements. Inhomogeneity and growth rate issues have been tackled by fluid dynamics

simulations resulting in the design of a new shower head. Then the results for boron-doped low temperature epitaxy are described. By adding diborane to the gas mixture and optimizing the process conditions we have been able to manufacture boron- doped epi-layers with high quality structural properties. As a result, boron doped epi-layers grown at 300°C with an as-deposited hole concentration of 4.10^{19} cm^{-3} and a doping efficiency up to 70 % have been achieved. The growth rate in these conditions reached 1.1 Å/s, keeping a low mosaicity and a low variation of the lattice parameter. Finally, the passivation of intrinsic and doped epitaxial layers has been investigated with both hydrogenated amorphous silicon (a-Si:H) and aluminum oxide (AlO_x), respectively deposited by PECVD and atomic layer deposition (ALD). In spite of excellent structural properties, we encountered a lot of difficulties to achieve decent minority carriers lifetime. We finally succeeded to reach lifetimes up to 160 µs for a 200 nm thick intrinsic layer passivated with 10 nm of AlO_x. With respect to passivated boron-doped layers, the lifetime dropped to 50 µs. Additional local electric characterizations need to be done to identify the recombination causes but the excellent structural properties achievable below 300°C are already promising results for the low- temperature formation of epitaxial emitter in nPERT solar cells.

Résumé

Les cellules en silicium cristallin, en particulier celles intégrant la structure Al-BSF (*Aluminum back surface field*), dominent le marché des technologies photovoltaïques depuis de nombreuses années. S'il est clair que la structure PERC (*passivated emitter rear contact*) deviendra le nouveau standard dans les prochaines années, beaucoup d'incertitude persiste quant à la technologie qui prendra le relais afin de poursuivre la course au rendement et à la baisse des coûts de production. La structure PERT (*passivated emitter rear totaly diffused*) est un candidat sérieux puisqu'elle permet d'améliorer le rendement tout en restant compatible avec les approches bifaciales, et ce en intégrant seulement une couche dopée de type *p* dans une architecture PERC. Alors que la formation de la couche fortement dopée de type *n* par diffusion $POCl_3$ est très bien maitrisée dans l'industrie et bénéfique pour la cellule du fait de l'effet *gettering*, la formation de la couche de type *p* par diffusion à partir de BBr_3 quant à elle présente quelques difficultés de fabrication. Le manque de reproductibilité, la formation d'une couche excessivement riche en bore (*BRL*) et une optimisation difficile du profil de dopage constituent plusieurs freins qui limitent son développement industriel. Ainsi d'autres approches de fabrication de cette couche de type *p* commencent à émerger.

Cette thèse de doctorat porte sur l'étude de la croissance épitaxiale à basse température (< 300°C) par dépôt chimique en phase vapeur assisté par plasma pour la formation des couches dopées dans les cellules solaires en silicium cristallin. En particulier, elle évalue le potentiel de cette technique pour la formation de la couche de type *p* à partir d'une chimie $SiF_4/H_2/Ar$ dans une cellule *n*-PERT. Cette approche permet de bénéficier du large déploiement des équipements de PECVD déjà présents dans l'industrie pour le dépôt de nitrure de silicium, utilisé comme couche de passivation et antireflet.

La première partie de ce manuscrit concerne l'identification et l'optimisation des conditions de dépôt pour réaliser des couches épitaxiées non relaxées avec une interface epi/wafer de bonne qualité. Pour cela, les couches ont été caractérisées par ellipsométrie, spectroscopie Raman, diffraction de rayons X et microscopie électronique en transmission (MET). Ainsi, des couches épitaxiées avec une cristallinité de 100%, mesurée par ellipsométrie et spectroscopie Raman, ont pu être réalisées. Une attention particulière a été portée à l'absence de dislocations et de platelettes d'hydrogène. Des conditions nécessaires sur les conditions de croissance ont été identifiées, comme la déplétion complète de l'hydrogène moléculaire (H_2), un ratio de débit de gaz $[H_2]/[SiF_4]$ inférieur à 1/3 et une dépendance entre la puissance RF et la pression de travail. Comme en ont déduit les résultats de diffraction de rayons X, une pression de travail plus élevée permet une augmentation de la puissance RF en conservant une qualité structurale similaire. Ensuite, une étude sur les mécanismes de perte d'épitaxie (*epitaxy breakdown*) est présentée. La caractérisation des films par MET et figures de pôles a montré que la formation de macles au cours de la croissance était responsable de la perte d'épitaxie lorsque la puissance RF dépassait un certain seuil (à une pression donnée) ou que la condition de déplétion complète d'H_2 n'était pas respectée. Cependant, les deux conditions de perte d'épitaxie se distinguent par l'observation de grains orientés <111> dans la direction de croissance dans le premier cas, alors qu'ils n'apparaissent pas dans la condition de déplétion incomplète d'H_2.

La seconde partie concerne les mécanismes de croissance par l'étude comparative des phases initiales de croissance par MET et ellipsométrie. L'analyse a permis d'identifier un mode de croissance de type Volmer-Weber en observant une croissance systématique d'ilots de silicium cristallin dans les phases

initiales de croissance. Même si la question reste ouverte, nous avons tenté d'identifier les précurseurs impliqués dans cette croissance. A l'aide de grilles de cuivre recouverte de carbone amorphe analysées par MET filtrée en énergie, la variation de la distribution et de la morphologie des nanoparticules de silicium présentes dans le plasma en fonction des étapes de croissance a été étudiée. Bien qu'il soit encore difficile de tirer des conclusions directes quant au rôle des nanoparticules, radicaux et ions dans leur contribution au dépôt et que d'autres recherches plus approfondies doivent être menées, cette étude fournit une première étape dans l'identification des principaux précurseurs.

Le manuscrit développe dans un troisième temps les étapes de transfert et de *scale-up* du procédé à partir d'un réacteur de recherche vers un réacteur PECVD de ligne pré-pilote permettant la croissance sur des wafers 6 pouces. Les problèmes d'homogénéité et de vitesse de croissance ont été abordés par le design d'une nouvelle injection de gaz basé sur des simulations d'écoulement. S'en suit le détail du développement des couches dopées. Ainsi, des couches épitaxiées dopées bore avec un dopage de type *p* de 4.10^{19} cm^{-3} et une efficacité de dopage jusqu'à 70% ont ainsi été fabriquées à seulement 300°C. La vitesse de croissance dans ces conditions atteint 1.1 Å/s, soit 15 fois plus rapide que les premiers résultats obtenus, et ce en maintenant une faible mosaicité et variation du paramètre de maille dans les couches. Enfin, la passivation des couches épitaxiées a été étudiée et malgré d'excellentes propriétés structurales, les propriétés électriques du matériau ne sont pas encore adaptées à une utilisation dans une cellule à haut rendement. Néanmoins, un temps de vie de 160 µs a été mesuré sur des couches intrinsèques de 200 nm d'épaisseur passivées avec 10 nm d'oxyde d'aluminium déposé par ALD alors que le temps de vie reste en dessous des 50 µs dans le cas des couches dopées bore. Ainsi à l'avenir, un effort particulier doit être porté sur l'identification des causes de recombinaisons dans les couches épitaxiées à basse température par PECVD.

Remerciements

Cette thèse est issue de la collaboration entre Total et le Laboratoire de Physique des Interfaces et des Couches Minces (LPICM), ayant pour tutelle le CNRS et l'Ecole polytechnique, et s'inscrit dans le cadre des projets menés par l'Institut Photovoltaïque d'Île-de-France (IPVF). A ce titre, je souhaiterais remercier ces institutions ainsi que l'ANRT pour le financement des travaux présentés dans ce manuscrit.

Je voudrais avant tout témoigner ma gratitude aux membres de mon jury de thèse, composé de Mustapha Lemiti, Abdelilah Slaoui, Stefaan De Wolf, María Recamán-Payo, Philippe Lecoeur et Lars Oberbeck, qui m'ont fait l'honneur d'accepter mon invitation. Je les remercie sincèrement pour toutes leurs questions et remarques pertinentes qui contribuent à l'amélioration et aux perspectives de ce projet.

Je souhaite exprimer ici toute ma reconnaissance à l'ensemble des personnes qui m'ont accompagné dans la réalisation de ce doctorat. Il en va de soi que le travail présenté dans ce manuscrit est le fruit de nombreuses collaborations qui m'ont amené à rencontrer des scientifiques passionnés et inspirants. Et c'est sincèrement ce que je retiendrai comme fondamental dans cette expérience, côtoyer des personnes qui vous tirent constamment vers le haut. Ce qui fait qu'un doctorat est certes exigeant mais avant tout formidablement enrichissant d'un point de vue intellectuel et professionnel.

Le bon déroulement d'un doctorat est intimement lié à la relation que l'on entretient avec ses encadrants. Je voudrais donc en premier lieu remercier mon directeur de thèse Pere Roca i Cabarrocas. Plus qu'un directeur de thèse, Pere est un mentor, qui vous transmet avec une grande générosité son énergie. Toujours disponible, toujours accessible, toujours optimiste, il vous communique sa passion et son enthousiasme pour la recherche et a une capacité sans égal à motiver ses étudiants, à les faire se relever face à l'échec. J'ai tellement pris plaisir aux discussions scientifiques, souvent animées, qui m'ont permis d'affiner mon argumentation et ma rigueur scientifique. Je souhaiterais également dire un grand merci à Gilles Poulain, mon encadrant de Total, pour la pertinence constante de ses remarques et conseils, pour son pragmatisme, pour m'inciter à me poser les bonnes questions. Gilles m'a permis de me confronter aux réalités industrielles d'un projet, et de constamment remettre en question mes idées et mes certitudes. Merci à vous deux pour m'avoir permis de réaliser ce doctorat et d'avoir tant appris.

Ces trois années auraient été bien plus difficiles sans la compagnie et le soutien des nombreux doctorants, postdocs et stagiaires qui se sont succédé au sein du LPICM et de l'équipe Total. Merci donc à Paul Narchi, formidable co-bureau à la bonne humeur infaillible, qui n'a d'égal que le niveau de ses jeux de mot, mais sachant garder rigueur et efficacité en toutes circonstances. Je garderai un excellent souvenir de nos nombreuses et longues discussions aussi passionnantes que diversifiées, avec parfois un accent marseillais plus ou moins bien maitrisé… Merci à Gwenaëlle Hamon du groupe des co-bureaux et de l'équipe du soir, pour avoir contribué avec dynamisme à la vie du LPICM en menant l'équipe de foot comme personne, en organisant les évènements du labo, en faisant des algecos un endroit agréable dans lequel travailler et en y apportant une touche musicale (certes pas au niveau de mes performances de karaoké…). Je n'oublierai pas tous ces moments partagés au laboratoire et en dehors. Je souhaite ensuite remercier Jean-Christophe Dornstetter d'avoir pris le temps (en 3ème année de thèse) de me former, de m'expliquer, de me guider, tout en gérant deux dépôts et trois « carac » en

même temps… Sans ce passage de témoin, cette thèse aurait été beaucoup plus compliquée et bien moins fournie. J'ai une immense reconnaissance pour le travail que tu as accompli aussi bien d'un point de vue purement scientifique que pour le fonctionnement du labo en intervenant notamment sur les problèmes d'équipements avant tout le monde. Mention spéciale pour rendre mes lundis matin plus agréables en préparant des gaufres ! Je poursuis dans ma lancée des doctorants de la génération d'au-dessus. Merci à Romain Cariou, qui a grandement contribué au domaine de l'épitaxie basse température et pour m'avoir montré la voie dans ce domaine. Merci à Bastien Bruneau, *serial publisher*, qui a beaucoup apporté au compteur des publications du labo, et pour m'avoir éclairé sur la physique des plasmas (mais pas après 17h). Merci à Igor Sobkowicz, recordman du rendement de cellule au LPICM, pour son accueil sur le campus, ses conseils avisés et ses recettes de dépôt sur le Cluster. Enfin merci à Soumyadeep Misra, pour ses conseils (atypiques) sur la rédaction.

Concernant mes contemporains et successeurs je tiens à remercier Guillaume Fischer, collègue de plasma et de karaoké. Au fait, t'as pas ma tasse de café ? Merci à Fabien Lebreton, partenaire de 3x8, pour les discussions de *thermal drift* et de *drift diving* du samedi matin. Merci à Rafaël Peyronnet, qui allie silicium et guitare acoustique mieux que personne, à Linda Hassam pour les discussions passionnantes (cette fois-ci je t'ai pas oublié !) et à Amadéo Michaud, excellent coéquipier de foot comme d'épitaxie. Merci à Marta Chrostowski, de prendre le relais de l'épitaxie basse température, et surtout bonne chance pour la suite. Merci à Wang Junkang, pour avoir partagé mes déboires techniques et réussites sur Philix. Merci à Tang Jian, éternel romantique de la science, et à Mengkoing Sreng, pour son sourire et sa bonne humeur inaltérables. Et merci aussi à Mutaz Al-Ghzaiwat, Rasha Khoury, Jean-Maxime Orlac'h, Arthur Marronnier, Salomé Forel, Alice Defresne, qui ont contribué à rendre le LPICM un formidable laboratoire pour y effectuer son doctorat par la qualité humaine et scientifique de ses doctorants.

Merci à Farah Haddad, pour les innombrables images TEM qu'elle a pu réaliser. J'en profite pour continuer avec l'équipe microscopie, sans qui nous serions bien aveugles. Un immense merci à Jean-Luc Maurice donc, pour son expertise en microscopie et son savoir en science des matériaux, pour toutes ses analyses pertinentes, qui sont complémentaires de celle des « gens du process » et donc indispensables. Et merci bien sûr à Ileana Flora, pour les discussions et les coupes FIB. Je souhaite remercier les quelques postdocs que j'ai pu rencontrer au laboratoire. Merci à Wanghua Chen (C'est parti mon kiki !), pour les innombrables HF que tu m'as dépannés et pour tes enseignements sur l'épitaxie basse température. Merci à Ahmed Ben Slimane pour ses qualités en épitaxie III-V et de 6 sur le terrain… Excellent ! Merci à Nicolas Vaissière pour nos discussions autour de l'épitaxie et du diamant. Promis un jour je ferai le parkrun. Enfin merci à Céline Richard de Total pour avoir partagé sa bonne humeur aux algécos. Merci aux deux stagiaires que j'ai eu la chance d'encadrer au cours de ma thèse, Wonjong Kim et Adrien Rivalland, qui ont beaucoup contribué aux résultats présentés dans ce manuscrit. Vous ferez de très bonnes thèses j'en suis certain.

J'ai une reconnaissance particulière pour l'ensemble de l'équipe Total avec laquelle j'ai pu interagir régulièrement. Donc tout d'abord merci à Fabrice Devaux, Lars Oberbeck, Vincent Schächter pour m'avoir permis d'effectuer cette thèse dans cette belle équipe et cet environnement stimulant. C'est un privilège de pouvoir faire de la recherche dans un contexte industriel et dans ces conditions. Au même titre, merci également à Dominique Neerinck et Benoît Lombardet. Un grand merci à Etienne Drahi (Clé à molette !) pour les discussions politico-scientifiques qu'on a pu partager, autour d'un chorizo/cannette ou non. J'ai un immense respect pour le travail que tu as mené avec l'IPVF, et ce quelles que soient les conditions. Merci à Ludovic Hudanski pour les discussions tardives autour des voyages et du sport. Merci à Sergej Filonovich pour son humour et sa bonne humeur en toutes circonstances ! Merci à Nacib Benmammar pour sa bienveillance, les discussions musicales et pour

son aide sur le Cluster en gérant les innombrables problèmes rencontrés. Et merci à Nada Habka, Martin Sanders, Jara Fernandez, Jean-François Besnier, Amjad Deyine, Patricia Prod'homme, Vincent Maillard qui complètent une équipe dans laquelle j'ai pris beaucoup de plaisir à travailler. Merci aussi à Nils-Peter Harder, pour sa curiosité, son expertise, son recul technologique et les discussions scientifiques que j'ai eu la chance d'avoir avec lui. Merci à Christoph Sachs pour ses précieuses connaissances sur le silicium cristallin. Je tiens également à remercier l'ensemble de l'équipe Total Imec avec qui j'ai pu interagir, dont Patricia De Coux, Guillaume Courtois, Michel Ngamo, Amada Montesdeoca-Santana, Jens Jens-Dirk Moschner. Merci à Julien Penaud, la Total Cup restera un des meilleurs souvenirs de ma thèse. Merci à Laurent Fourage, hey pas mal ce ciseau hein et Vamos Torpedos ! Toujours dans la team Torpedos, merci à Jérôme Damon-Lacoste, pour avoir supporté un malencontreux choix radiophonique. Enfin un grand merci à Isabelle Le Bihan pour la gestion des achats, l'organisation des évènements Total et tout le reste qui nous permet de travailler dans les meilleures conditions.

Du côté du LPICM, je ne manquerai pas de remercier toutes les équipes, et en particulier le BEER, sans qui il serait impossible de mener nos recherches. Ainsi un grand merci va à Cyril Jadaud pour sa disponibilité et sa réactivité pour intervenir sur les équipements, et pour les discussions passionnées sur le badminton et la pêche. Merci à François Silva, pour nos discussions sur les plasmas et la XRD, pour les simulations qu'il a réalisées et qui m'ont été d'une grande aide. Je voudrais également remercier Jérôme Charliac et Frédéric Farci pour leur contribution et leur aide sur les problèmes techniques que j'ai pu rencontrer. Je souhaite exprimer ma plus profonde gratitude à Pavel Bulkin pour son aide inconditionnelle. Cette thèse aurait été beaucoup (beaucoup) plus compliquée sans sa présence. Merci pour les réponses franches et précises sur les plasmas et l'éllipsométrie. Toujours disponible pour dépanner, Pavel a eu réponse à toutes les questions techniques que je lui ai posées. Une connaissance aussi inestimable des semiconducteurs que du vignoble français. Merci pour les toutes les discussions et les dégustations auxquelles tu m'as invité. Merci aussi à l'ensemble de l'équipe Nanosil, en premier lieu, Erik Johnson pour mener cette équipe non sans humour (canadien certes), sa créativité pour trouver des acronymes et de nouvelles idées de recherche mais aussi pour ses capacités à négocier des présentations en sachant trouver les bons mots… J'ai une reconnaissance toute particulière pour l'équipe administrative qui fournit un effort considérable pour que les chercheurs puissent travailler dans de bonnes conditions. Merci donc à Laurence Gérot, Gabriela Medina et Fabienne Pandolf, sans qui le laboratoire ne fonctionnerait tout simplement pas. Je souhaite aussi remercier l'équipe G2I. Merci à Jean-Charles Vanel, pour ses mots d'encouragement et sa compassion pendant mes longues soirées de rédaction. Merci à Frédéric Liège, en particulier pour la restauration de mes données après un crash de disque dur en 3ème année de thèse... Et merci à Eric Paillassa pour le dépannage des PC et l'entretien du parc informatique, sans qui nous perdrions un temps considérable. Merci à Enric Caurel Garcia et Martin Foldyna pour les rafraichissements en optique. Merci à Dmitri Daineka pour les conseils en fabrication de dispositifs et métallisation. Merci à Denis Tondelier, pour son inflexible bonne humeur. Merci à Jean-Eric Bourrée pour les discussions scientifiques et les anecdotes de labo. Merci à Yvan Bonnassieux qui m'a permis de donner des cours durant cette thèse et ainsi avoir eu la chance d'enseigner. Enfin merci à Rym Boukhicha, Tatiana Novikova, Bernard Geoffrey, Jacqueline Tran, Jean-Luc Moncel et Garry Rose dont j'ai pu bénéficier de l'aide au cours ces années. Je souhaite également remercier l'ensemble des stagiaires qui contribuent fortement à l'avancement des projets, je pense particulièrement à Chloé Dindault, future experte pérovskite et professeure de natation pour ancres et enclumes. Je souhaite enfin remercier l'ensemble des équipes AOP, OLAE et Nanomade, avec qui j'aurais moins interagis, certes, mais avec qui j'ai toujours eu plaisir de discuter. Il est pour moi primordial dans un but de créativité, d'innovation et tout simplement d'ouverture d'esprit de faire preuve de curiosité pour des thématiques

qui sortent de son propre domaine d'expertise. Une des richesses du LPICM est justement d'offrir cette interaction pluridisciplinaire grâce à l'étendue et la variété de ses thématiques de recherche.

Je n'aurais pas interagi avec des laboratoires extérieurs autant que je l'aurais souhaité, ayant consacré déjà beaucoup de temps aux études menées au sein du LPICM. Mais je voudrais dire un grand merci à Ludovic Largeau du C2N, qui a presque fait naitre chez moi une passion pour la XRD. Merci vraiment pour ta pédagogie, ta disponibilité, ta sympathie. Pour continuer avec la XRD, merci à Sandrine Tusseau-Nenez, Robert Cortes et Fouad Maroun du PMC pour votre patience et votre aide précieuse sur la théorie et la pratique ainsi que les nombreux dépannages sur l'équipement. Je souhaite également témoigner ma sympathie à l'ensemble des personnes impliquées dans le projet A de l'IPVF, pour beaucoup déjà cités précédemment. Merci donc à Sylvain Pouliquen pour les discussions sur les réacteurs PECVD, et Andy Zauner d'Air Liquide pour les discussions sur l'ALD. Merci à vous deux pour les multiples échanges que l'on a pu avoir et qui permettent d'avoir un regard extérieur sur nos recherches.

Plus que de simples relations professionnelles donc, j'ai tissé des liens privilégiés et me suis lié d'amitié avec beaucoup de personnes que j'ai pu rencontrer durant ces trois années. Des relations qui vont au-delà des frontières du laboratoire et des sciences, c'est pour moi là que réside l'essentiel et ce qui a fortement contribué au succès de cette thèse.

Je voudrais enfin remercier chaleureusement ma famille et mes amis pour leur soutien infaillible.

Merci à tous.

Ronan

Contents

List of figures

List of tables

List of acronyms and symbols

µc-Si:H *: hydrogenated microcrystalline silicon*
µ-PCD *: microwave photoconductance decay*
AC *: alternative current*
AES *: Auger electron spectroscopy*
AFM *: atomic force microscopy*
Al *: aluminum*
ALD *: atomic layer deposition*
AlO_x *: aluminum oxide*
APCVD *: atmospheric pressure chemical vapor deposition*
Ar *: argon*
ARC *: anti-reflective coating*
a-Si:H *: hydrogenated amorphous silicon*
B_2H_6 *: diborane*
BBr_3 *: boron tribromide*
BEMA *: Bruggeman effective medium approximation*
BRL *: boron-rich layer*
BSF *: back surface field*
BSG *: borosilicate glass*
CAGR *: compound annual growth rate*
CAPEX *: capital expenditures*
CCS *: carbon capture and storage*
CIGS *: copper indium gallium selenide*
CoO *: cost of ownership*
COP *: conference of the parties*
c-Si *: crystalline silicon*
CVD *: chemical vapor deposition*
Cz *: Czochralski*
DC *: direct current*
DLTS *: deep level transient spectroscopy*
DSMP *: double-side mirror polished*
ECR-PECVD *: electron cyclotron resonance plasma-enhanced chemical vapor deposition*
ECV *: electrochemical capacitance-voltage*
EEDF *: electron energy distribution function*
EFTEM *: energy filtered transmission electron microscopy*
EPBT *: energy payback time*
EPR *: electron paramagnetic resonance*
f_{H_2} *: hydrogen flow rate*
FF *: fill factor*
FSF *: front surface field*
FWHM *: full width at half maximum*
FZ *: floating zone*
GI-XRD *: grazing incidence X-ray diffraction*
H_2 *: hydrogen*
HCl *: hydrochloric acid*
HF *: hydrofluoric acid*
HIT *: heterojunction with intrinsic thin layer*
HNO_3 *: nitric acid*
HR-XRD *: high-resolution X-ray diffraction*
IBC *: interdigitated back contacts*
IBR *: ion beam ratio*
IEA *: international energy agency*
IPCC *: intergovernmental panel on climate change*
ITO *: indium tin oxide*
ITRPV *: international technology roadmap for photovoltaic*
ITZ *: internal transfer zone*
J_{0e} *: emitter saturation current density*
J_{SC} *: short-circuit current density*
KPFM *: Kelvin probe force microscopy*
LCD *: liquid-crystal displays*
LCGGE *: life cycle greenhouse gas emissions*
LCOE *: levelized cost of energy*
LEED *: low-energy electron diffraction*
LID *: light-induced degradation*
LLS *: laser light scattering*
LPCVD *: low pressure chemical vapor deposition*
LTE *: low-temperature epitaxy*
MBE *: molecular beam epitaxy*
ML *: monolayer*
N_A *: acceptor concentration*
N_D *: donor concentration*
O_2 *: dioxygen*
O_3 *: ozone*
OECD *: organisation for economic co-operation and development*
OES *: optical emission spectroscopy*
PAS *: positron annihilation spectroscopy*
PC-calibrated PL *: photoconductance calibrated photoluminescence*
PDA *: post-deposition annealing*
PECVD *: plasma-enhanced chemical vapor deposition*
PERC *: passivated emitter and rear contact*
PERL *: passivated emitter with rear locally diffused*
PERT *: passivated emitter, rear totally diffused*
PH_3 *: phosphine*
photo-CVD *: photochemical vapor deposition*
pm-Si:H *: hydrogenated polymorphous silicon*
$POCl_3$ *: phosphoryl chloride*
poly-Si *: polycrystalline silicon*
PP-TOFMS *: plasma profiling time of flight mass spectrometry*
p_{RF} *: RF power density*

P_{RF} *: RF power*
PSG *: phosphosilicate glass*
PV *: photovoltaic*
PVD *: physical vapor deposition*
QMS *: quadrupole mass spectrometry*
QSS-PC *: quasi-steady-state photoconductance*
RBS *: Rutherford backscattering spectrometry*
RC *: rocking curve*
RCA *: radio corporation of America*
RF *: radio-frequency*
RGA *: residual gas analyzer*
RHEED *: reflection high-energy electron diffraction*
RIE *: reactive ion etching*
RMS *: root mean square*
R_{sheet} *: sheet resistance*
RSM *: reciprocal space mapping*
sccm *: standard cubic centimeters per minute*
SDR *: saw damage removal*
SE *: spectroscopic ellipsometry*
SEM *: scanning-electron microscopy*
SHJ *: silicon heterojunction*
SiF_4 *: silicon tetrafluoride*
SiH_2Cl_2 *: dichlorosilane*
SiH_4 *: silane*
SIMS *: secondary ion mass spectrometry*
SiN_x : *silicon nitride*
SiO_x *: silicon oxide*
SOI *: silicon on insulator*
SOM *: sulfuric acid and ozone mixtures*
SPM *: sulfuric acid and peroxide mixtures*
STM *: scanning tunneling microscopy*
TCO *: transparent conductive oxide*
TCS *: trichlorosilane*
TEM *: transmission electron microscopy*
TFT *: thin film transistors*
TO *: transverse optical*
TRMC *: time resolved microwave conductivity*
UHV-VPE *: ultra-high vacuum vapor phase epitaxy*
UV *: ultraviolet*
V_{DC} *: self-bias voltage*
VHF *: very high frequency*
V_{OC} *: open-circuit voltage*
V_{pl} *: plasma potential*
V_{RF} *: potential at the RF electrode*
WHO *: world health organization*
XRD *: X-ray diffraction*
$\alpha \mid_{Si}$ *: absorption coefficient of silicon*
$\Gamma_{e,i}$ *: electron, ion flux*
Δn *: injection level*
ε_i *: imaginary part of the pseudo-dielectric function*
ω_p *: plasma pulsation*

1. Introduction and context

1.1. The photovoltaic energy in the global energy mix

In December 2015 was held the twenty-first session of the Conference of the Parties (COP) where 195 countries agreed to keep "the increase in the global average temperature to well below 2°C above preindustrial levels". According to a recent publication in *Nature* [1], this ambitious objective would require to keep one third of reserves of oil, the half of the reserves of gas and 80% of the reserves of coal unexploited from 2010 to 2050. This represents the most important challenge of the 21th century knowing that today almost 80% of the energy sources consumed in the world are fossil fuels, as shown in Fig. 1.1, while the part of modern renewables, including hydropower, represents only 10.3% [2]. In the meantime, global population should reach 9.7 billion by 2050 according to the medium-variant projection of the world population prospects published by the United Nations [3]. To support the development of this population, one of the primary course of action is through support to the access to energy. Thus, according to the International Energy Agency (IEA), if the energy mix is not deeply changed, this should lead to a growth of about 60% of the world primary energy demand and CO_2 emissions by 2050, causing an average global temperature increase of 4-6°C by 2100. This demographic context dramatically amplifies the urgent need for new alternatives satisfying this unquenchable demand of energy and limiting the emission of greenhouse-gases.

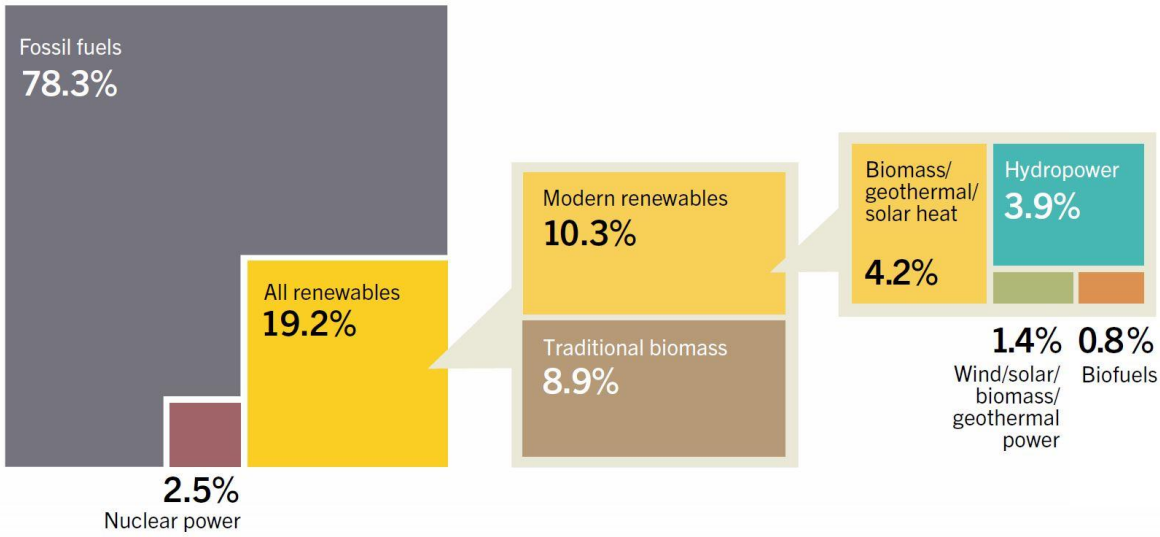

Fig. 1.1 – Global final energy mix and the estimated share of renewables in 2014 [2].

In 2013, the total global CO_2 emissions from the combustion of fossil fuels reached 32.2 giga tons of CO_2 ($GtCO_2$) and half of global emissions came from three countries: China (9 $GtCO_2$), the United States (5 $GtCO_2$) and India (2 $GtCO_2$) [4]. For all of them, coal is the main source of electricity and heat generation, with a part reaching two-thirds of the energy mix for China and India, while it is the most CO_2 emitting developed energy source. The global energy-related CO_2 emissions by sector are shown in Fig. 1.2. As it can be seen, these emissions grew by more than 50% over the last 25 years

[5], particularly due to the doubling of emissions from electricity and heat generation in emerging and developing countries. Today's power generation represents about 40% of the total emissions and is now mostly driven by the non-OECD regions, especially China and its intensive generation from coal. If the struggle against a full carbon energy world is often focused on the electricity production sector, transport and industry sector together also represent another 40% of the current world CO_2 emissions. The challenge in these figures lies on the electrification of these sectors to limit the emissions.

In addition besides greenhouse effect, the burning of fossil fuels induces other pollutant emissions like fine-particles, causing severe health problems. Thus, in urban areas, more than 80% of people live with air quality above pollution thresholds preconized by the World Health Organization (WHO). Not surprisingly, developing countries are more affected, 98% of cities in low and medium-income countries present pollution levels above recommendations of the WHO. Consequently, up to 6.5 million deaths in the world are attributed each year to air pollution [6]. This is a dramatic consequence mostly due to fossil fuels combustion and in particular the use of coal.

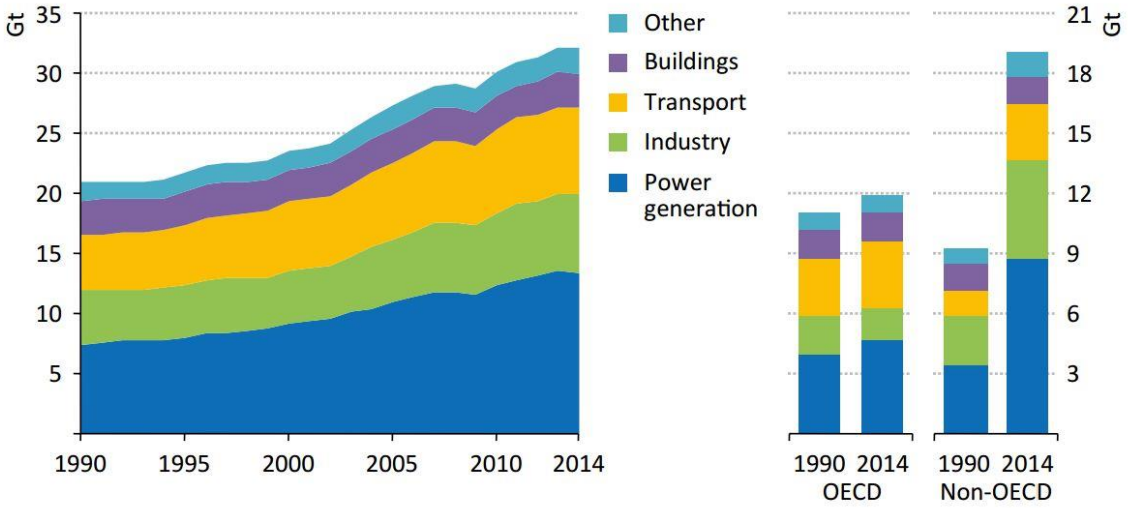

Fig. 1.2 – Global energy-related CO_2 emissions by sector and regions expressed in giga tons (Gt), IEA, 2015 [5].

Since carbon capture and storage (CCS) is struggling to provide viable technical solutions – the CCS only allowed the capture of 26 Mt CO_2 in 2014 [7] – the development of competitive solutions for "carbon-free" energy generation is mandatory to tackle climate changes and air quality issues in a world's growing population context.

Based on this observation, any carbon-free energy would need to play a significant role in the energy transition. As shown in Fig. 1.3, if we look at the comparison of life cycle greenhouse gas emissions (LCGGE) [8], the solution could arise from nuclear energy and hydropower. Indeed, according to the intergovernmental panel on climate change (IPCC), the nuclear energy and hydropower have median LCGGE of 12 and 24 g CO_2eq/kWh [9], respectively, therefore among the lowest LCGGE of the different electricity supply technologies. These two energies also benefit from the best energy production density.

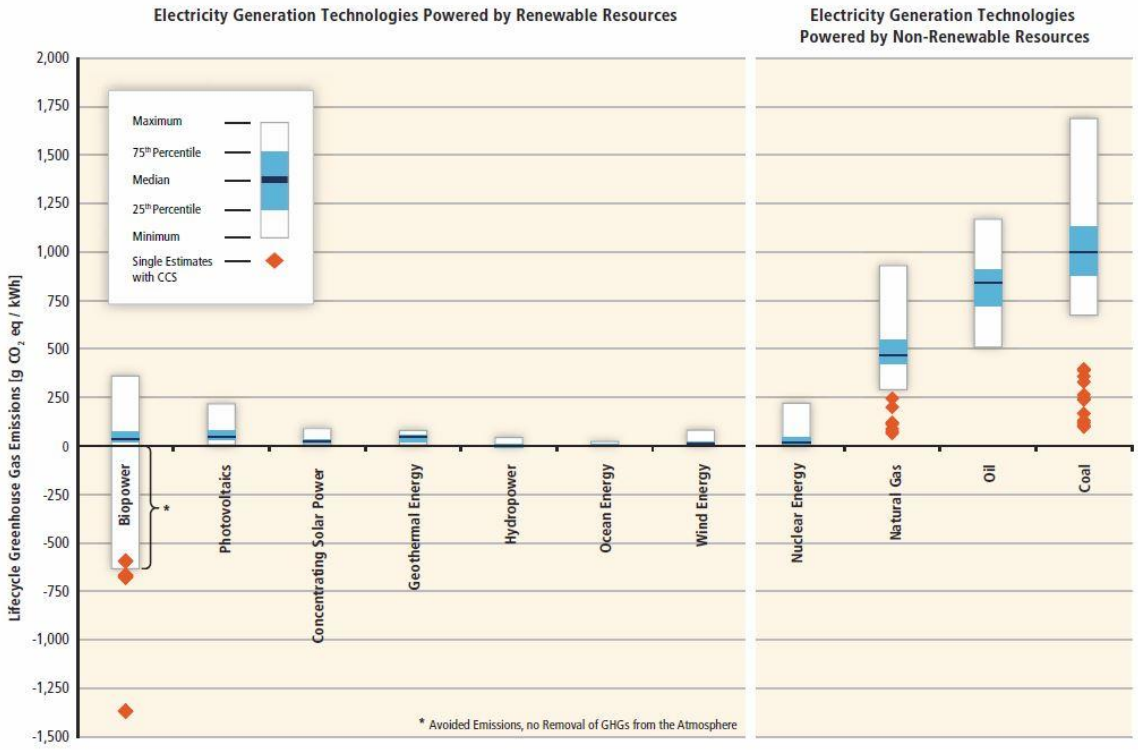

Fig. 1.3 – Estimates of life cycle greenhouse gas emissions for different electricity generation technologies (in g CO_2eq/kWh) [8].

Nuclear energy was considered as the energy of the future since it could ensure low LCGGE, a tremendous energy density and a low Watt-hour (Wh) price. But recent events in Fukushima, Japan, and the requirement to satisfy new norms applied to this industry to ensure the reactors safety, make the future of this energy unclear. If it was considered as low cost before, the new generation of reactors provide an energy at 110$/MWh [10]. Moreover the problem of nuclear waste produced by current reactors generation induces hidden costs for the reprocessing and storage of the nuclear waste. Even if it still represents a non-negligible part (2.5%) of the global final energy mix (Fig. 1.1), the nuclear electricity production started to stagnate in 2006 and dropped in 2011 due to Fukushima. For environmental and economic reasons, the Fukushima accident forced governments to reconsider their energy policy and for some countries to – or to confirm their intention to – withdraw their nuclear program, as Germany, Belgium and Italy for example. Above economical aspects, the question of safety related to energy production sources has become a priority.

The only solution ensuring the best energy independency, a significant drop of greenhouse and other polluting gas emissions, and safety, is to develop an energy mix implementing different renewable energy sources. Beyond finding the best energy for the future, it is also a question of diversification of energy sources. The dependency on one form of energy, whatever it is, inevitably leads to risks of geopolitical tensions. The idea of an energy mix supported by an electrification of the different sectors (industry, transport,…) offers solutions against global warming and avoids the risks of some conflicts linked to the dependence on an unique energy resource. From an economic point of view, the development of carbon- and other pollutants-free energies is also viable and provides opportunities for growth and job creation.

In that context, hydropower benefits from a lot of assets including those cited above, a low levelized cost of electricity with LCCGE between 4 and 14g CO_2eq/kWh, and provides a good energy

independency. In 2014, hydropower represented 3.9% of the global final energy consumption, namely 50% more than nuclear energy [2]. Today, 75% of the total generation from renewables [7] comes from hydropower and this share is projected to decrease by 2040. The hydroelectric power generation capacity has almost reached saturation in the developed countries and the implementation of this technology obviously requires the access to large streamflow which is not adapted to every region on earth.

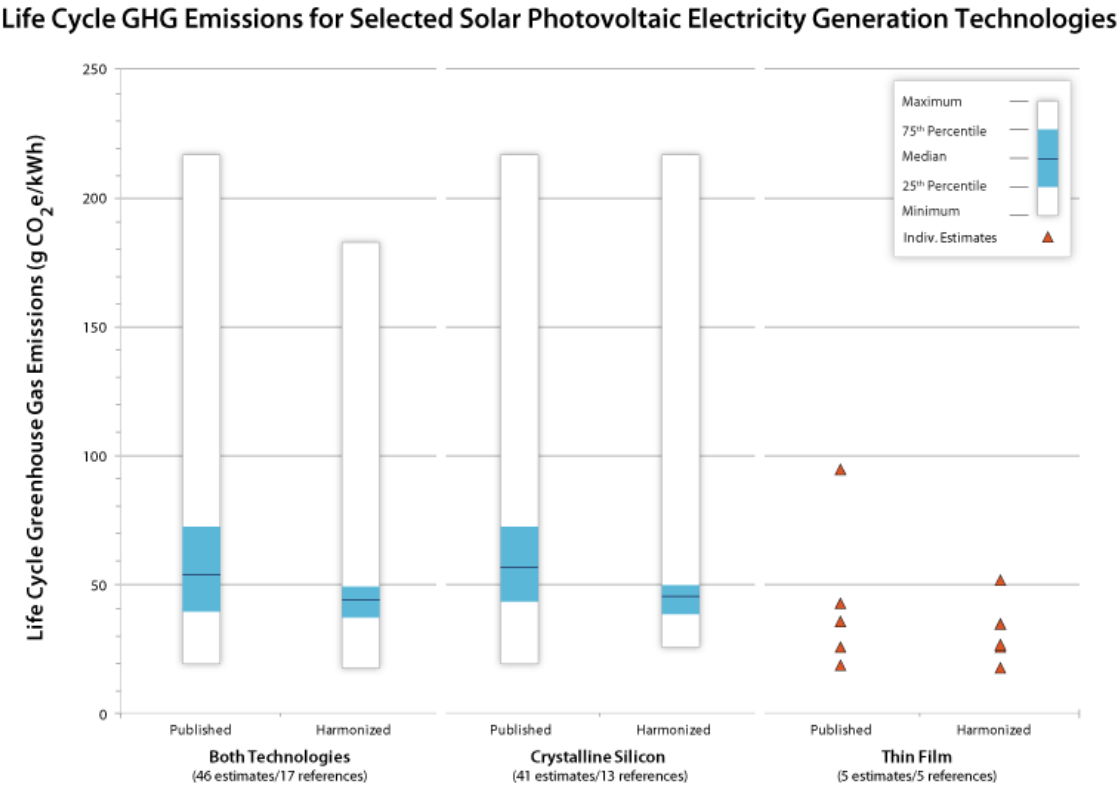

Fig. 1.4 – LCGGE for crystalline silicon and thin film based solar energy [15].

To ensure the complementarity of hydropower other forms of renewables have to be developed. The task will be tough since only 1.4% of the final energy consumption comes from wind, solar, biomass and geothermal power (see Fig. 1.1). The expectations of growth in green energies are mainly led by wind and solar energy according to most of energy roadmaps. Thus in 2015, 118 GW of wind and solar generation capacity have been added. This represents 53.6% of the global new capacities installed in 2015 according to the Bloomberg New Energy Finance (BNEF) [11]. For the first time, without taking into account the difference in capacity charge, more renewables were installed than fossil. The global investment in renewable power capacity, excluding large hydro-electric projects, reached $265.8 billion, meaning more than twice the amount allocated to new coal and gas generation ($130 billion) [11]. In particular in the U.S., wind, solar and natural gas represented 97% of the electric generation capacity additions in 2014 and 2015 [12] and should further represent 90% in 2016. The development of a new electricity generation model based on renewables and natural gas (to manage intermittency) is more and more likely.

Solar in particular shows the most impressive cost decrease for a few years, given that wind energy has almost reached its maturity. The global average levelized cost of energy (LCOE) was 122 $/MWh in the second half of 2015 while it was $20 higher one year before [11]. Solar energy in some countries already reached the grid parity. Thus, the lowest power purchase agreements reach

48$/MWh in Peru [13], 35.4$/MWh in Mexico and even 29.9$/MWh in the United Arab Emirates [14], becoming even cheaper than coal in some regions, considered like the most competitive energy resource. Solar energy benefits from other advantages. First, as shown in Fig. 1.4, it is among the energy sources inducing the lowest LCGGE with a harmonized median result of 45 gCO_2eq/kWh for c-Si technologies [15] (the harmonization considers an irradiation of 1700 $kWh/m^2/yr$, a system lifetime of 30 years, a module efficiency of 13.2% or 14.0%, depending on module type, and a performance ratio[1] of 75% or 80% depending on installation) [16]. The evolution of the energy payback time (EPBT), the time after which the solar panel produces more energy that what has been necessary to its manufacturing, is also impressive. Today, as shown in Fig. 1.5, with a 14% efficient mc-Si solar panel, the EPBT is about two years in Germany (annual irradiation of 1000 $kWh/m^2/yr$) and around one year in southern Europe (annual irradiation of 1700 $kWh/m^2/yr$) [17]. It should be mentioned that this study has been led in 2012 so the values have been determined from the published results in literature prior to 2012. Since then, considerable progress has been done in process optimization and material consumption, in 10 years material usage drop from 16 g/Wp to 6 g/Wp today [18]. The performance ratio has also advanced significantly, it is now in the range of 80% to 90% [18] compared to 70% 10 years ago. In addition, today, the average commercial silicon module efficiency is 17% [18]. Based on these observations, these LCGGE and EPBT values should be considered as overestimated. Moreover, efficiency records continue to increase with 26.33% reached by Kaneka for a c-Si solar cell [19] and 24.1% obtained by SunPower for a c-Si module [20].

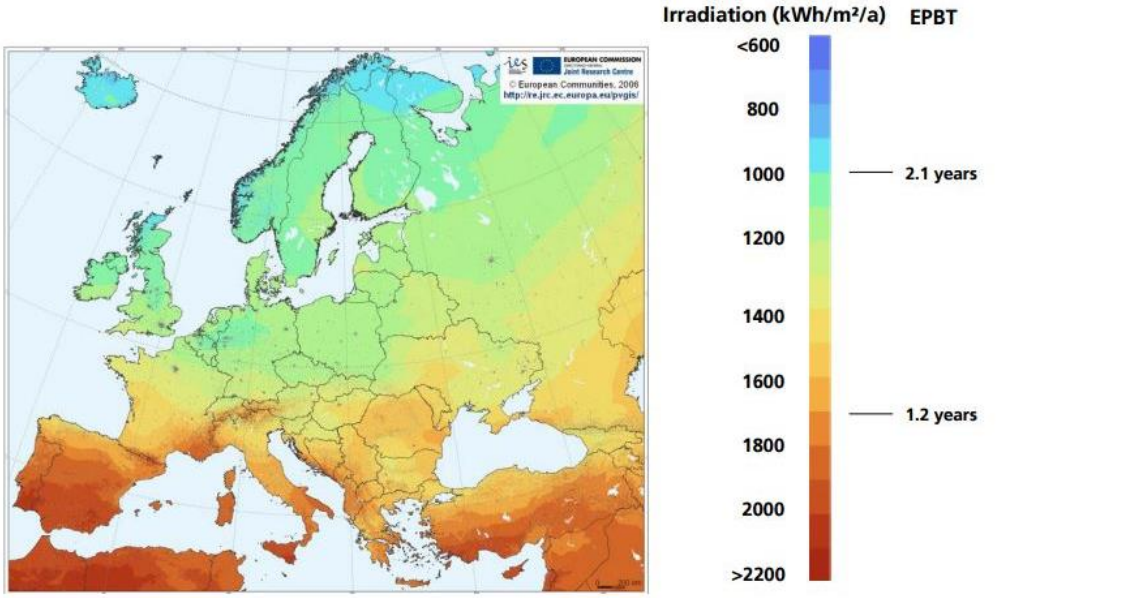

Data: M.J. de Wild-Scholten 2013. Image: JRC European Commision. Graph: PSE AG 2014 (Modified scale with updated data from PSE AG and FraunhoferISE)

Fig. 1.5 – EPBT in Europe for a 14% efficient mc-Si solar panel [18]. Data from [17].

In the meantime, fast deploying solar panels look like an adapted solution for the new challenges of the world where flexibility and reactivity are key words. In two years the Solar Star power plant with a generation capacity of 580 MW_{AC} has been completed. Considering fast growing emerging countries, the response to energy needs with a fast reaction time and the possibility to consume the energy where

[1] The performance ratio is the ratio of net energy production on total energy production of a system. It deducts from energy production, the losses (line resistance, conversion losses from the inverter, dirt, etc) and the consumption for the operation of a system (e.g. solar farm).

it is produced is a tremendous asset, which also favors the momentum of the new model for power generation as a distributed network.

In terms of material scarcity, silicon (which represents 90% of installed PV capacity in 2015 [18]) is the second most abundant element after oxygen in the earth crust. Hence, solar energy does not present risks of material shortage for its active material. Silver reserves, used as metallic contacts in solar cells are a more concerning issue. The global silver mine production reached more than 25.10^3 tons in 2015 while the ultimately recoverable reserves are estimated to be in the range 2.7 - 3.1 million tons, this would lead to a most likely peak silver production in 2034 [21]. However more and more PV cell manufacturers use alternative contact formations solutions using more abundant metals like nickel, copper and aluminum. Solar power offers the possibility to recycle the majority of the whole end-of-life PV installations. The PV cycle organism developed a good expertise on the recycling of solar panels and recently, they accomplished a new record of 96% recycling rate for silicon based PV modules [22]. The rest can easily be stored in open air storage sites with low environmental risks.

1.2. Current status and roadmap for the photovoltaic energy

The installation of PV capacity is a fast growing market with a Compound Annual Growth Rate (CAGR) of 41% between 2000 and 2015. There was an additional installation of 57 GW of PV systems in 2015, which, taking into account an average capacity factor of 15% for PV, represents the energy production of more than 8 nuclear plants of 1 GW. Today, solar energy is no longer a marginal energy production source and analysts forecast the installation of 64 GW of new PV systems in 2016.

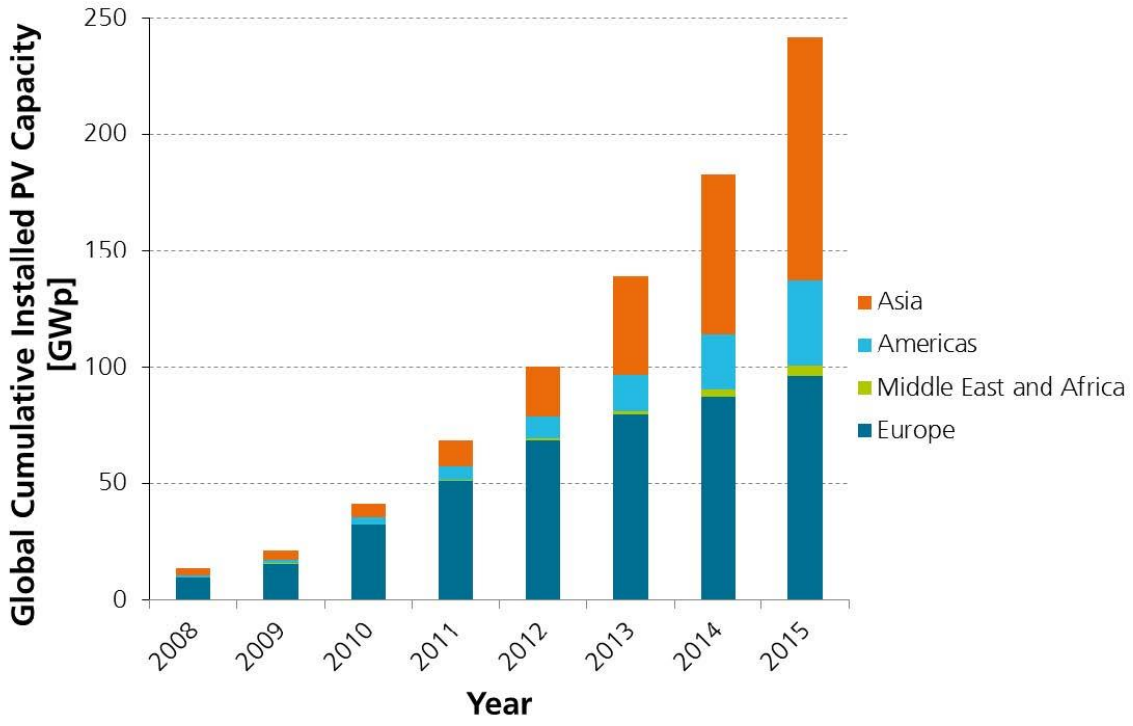

Fig. 1.6 – Evolution of the global cumulative installed PV capacity [18].

Even if the cost of solar installations strongly decreased during the last years to reach grid parity in some countries (Chile, Germany,…) there is a continuous need for research in this area where companies are in a very competitive market. Moreover, additional cost reductions are required to make solar energy a cost competitive solution in any region in the world and to compensate additional costs induced by energy management to tackle intermittency issues, e.g. storage, smart grids, etc.

Two main strategies of research can be identified, the implementation of new materials with better performances but at higher prices or the cost reduction of existing technologies. Both could allow a reduction of the "$/kWh". Increasing efficiency requires the formation of tandem solar cells, i.e. the stacking on the same cell of different materials with different energy bandgaps in order to harvest the maximum of energy. Finding a suitable top cell for c-Si (bottom cell) is not an easy task as it leads to expensive materials such as III-V or (so far) unstable materials such as perovskites. Therefore, a further decrease of production costs in current technologies is also necessary to compensate potential additional costs induced by the use of other materials for the top cell.

Silicon-based technologies have always been and remain the most important player of the PV industry. In 1995, a 24% efficient solar cell was already reported by the UNSW [23]. The efficiency record for c-Si solar cells has not substantially evolved since the 90s but the revolution lied in the drastic cost decreases which happened since then, especially thanks to benefits of mass production, economies of scale and technological improvements (laser processes, number of process steps reduced,…). The evolution of module price as function of cumulative production is shown in Fig. 1.7. The production cost of solar cells experienced a rapid learning curve, called the Swanson law, which shows that the doubling of shipped modules induces a decrease of 20% of the PV modules costs, which is comparable with that of other industrial fields such as automotive for example.

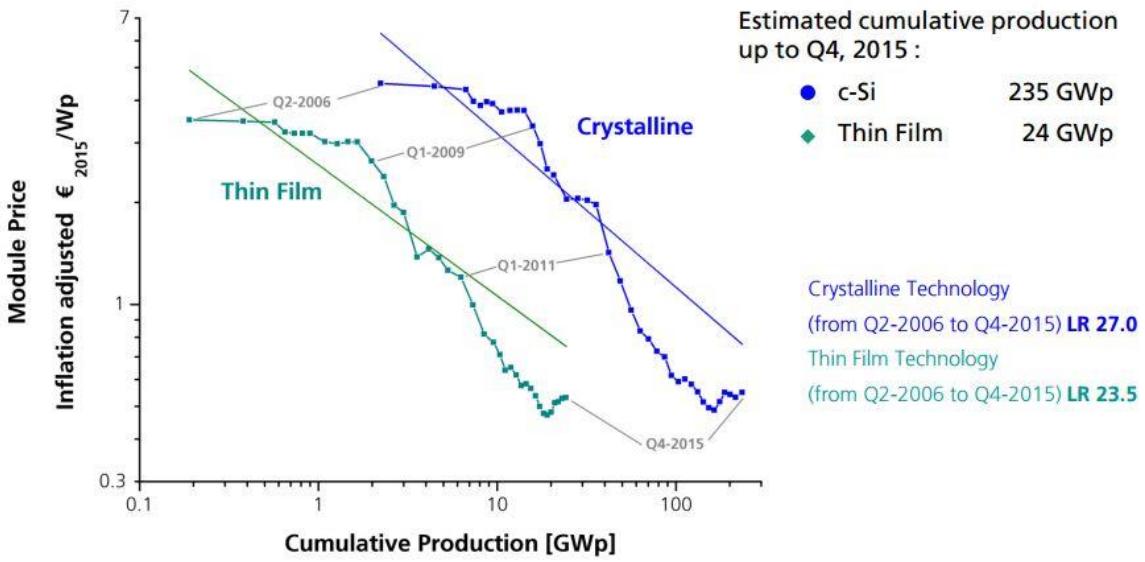

Fig. 1.7 – Learning curve of c-Si and thin film solar cells since 2006 [18].

1.3. Technologies overview in photovoltaics

With more than 90% of the PV production in 2015, crystalline silicon (c-Si) based technologies largely dominate the market as shown in Fig. 1.8. The abundance, good stability and moderate price of silicon PV make it, still today, the best option for large production capacity. Silicon PV also took benefit from the innovations and experience developed in the microelectronics industry and the transfer of process linked to well-known equipment has also been easier for that reason.

The remaining 10% are mostly shared by thin film technologies such as CdTe, CIGS and silicon thin films. If CdTe technology provides among the lowest cost production on the market, it suffers from toxicity of cadmium and scarcity of tellurium. CIGS solar cells reached a new record of 22.6% [24], meaning that the difference with respect to c-Si solar cells is shrinking due to a rapid improvement of cell efficiency over the recent years. Indeed while efficiency record of CIGS solar cells increased by absolute 0.1% per year between 1998 and 2013, the efficiency record gained absolute 0.7% per year over the last 3 years. However this technology exhibits homogeneity problems on large areas, the referenced record has been obtained for a 0.5 cm^2 cell. In addition to implying highly toxic precursors, CIGS technology suffers from the scarcity of indium and high capital expenditures (CAPEX).

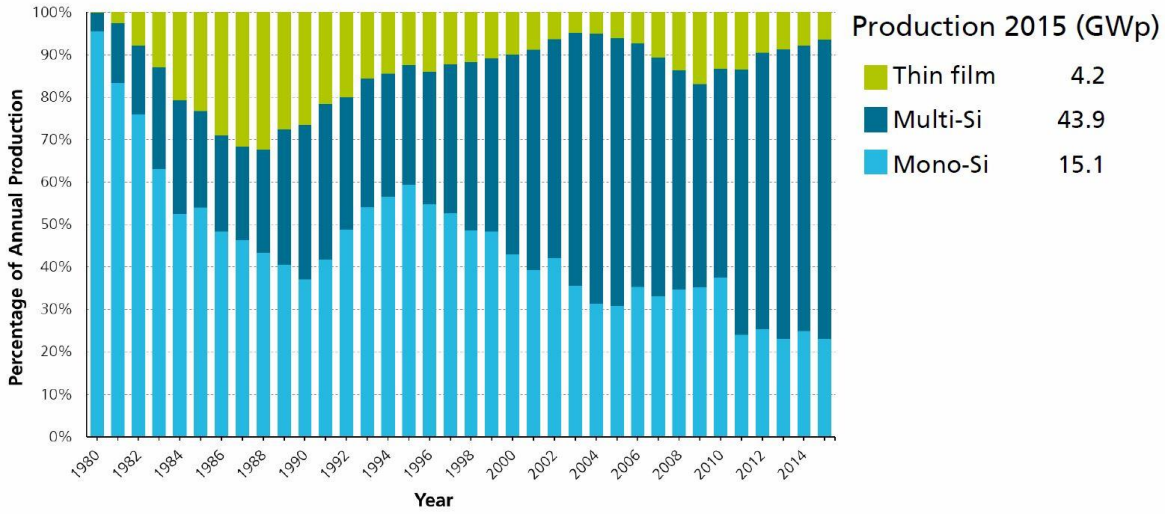

Fig. 1.8 – Share of different technologies on the total PV production over the past 25 years [18].

After a rise in the 2000s, thanks to the development in parallel of facilities for thin film transistors manufacturing used in liquid-crystal displays (LCD), silicon thin films experienced a setback in the 2010s due to the strong cost decrease of silicon wafers. In spite of a full integrated approach – by suppressing wafer feedstock constraints, purification and crystallization phases and loss in wafers cutting – high CAPEX and low efficiencies have not allowed them to reach the hoped success. Even if a stabilized efficiency of 13.6% has recently been reached [25], "high" efficiency approaches, conducted by c-Si solar cells, have conquered the market.

The combination of thin film technologies with c-Si led to the development of silicon heterojunction (SHJ) solar cells, only manufactured at large scale by Panasonic with the HIT™ technology. It uses hydrogenated amorphous silicon (a-Si:H) as passivation layer of the c-Si substrate and as doped layer for the charge carriers collection. This structure demonstrates very high performances and has the record of c-Si solar cells when used with back contacts. With such architecture, Kaneka has recently reached the record of 26.33% for a practical solar cell [19]. According to Louwen *et al.* [26] significant cost cuttings for SHJ modules should happen for the next years. Considering production costs in 2015 of 0.48-0.56 $/Wp [26] (against 0.50 $/Wp for standard mono-Si modules at that time

[27]) they prospect them to drop to 0.29-0.35 $/Wp in the next ten years [26]. However current spot prices for multi-Si and mono-Si modules are already at respectively 0.40 $/Wp and 0.42 $/Wp, and significant production costs for these technologies should arise from economies of scale and technological enhancement. In addition, heterojunction solar cells suffer from high CAPEX and metallization issues due to the low temperature needed in order to not damage the passivating a-Si:H layer processed around 200°C [26]. This implies to use more expensive metallization pastes and the necessity to deposit more silver to create a good conductive contact which means that a doubling of the silver price would induce, in case of bifacial SHJ structure, a raise of cost production for SHJ of 20%. In a volatile silver market this is a big factor of incertitude.

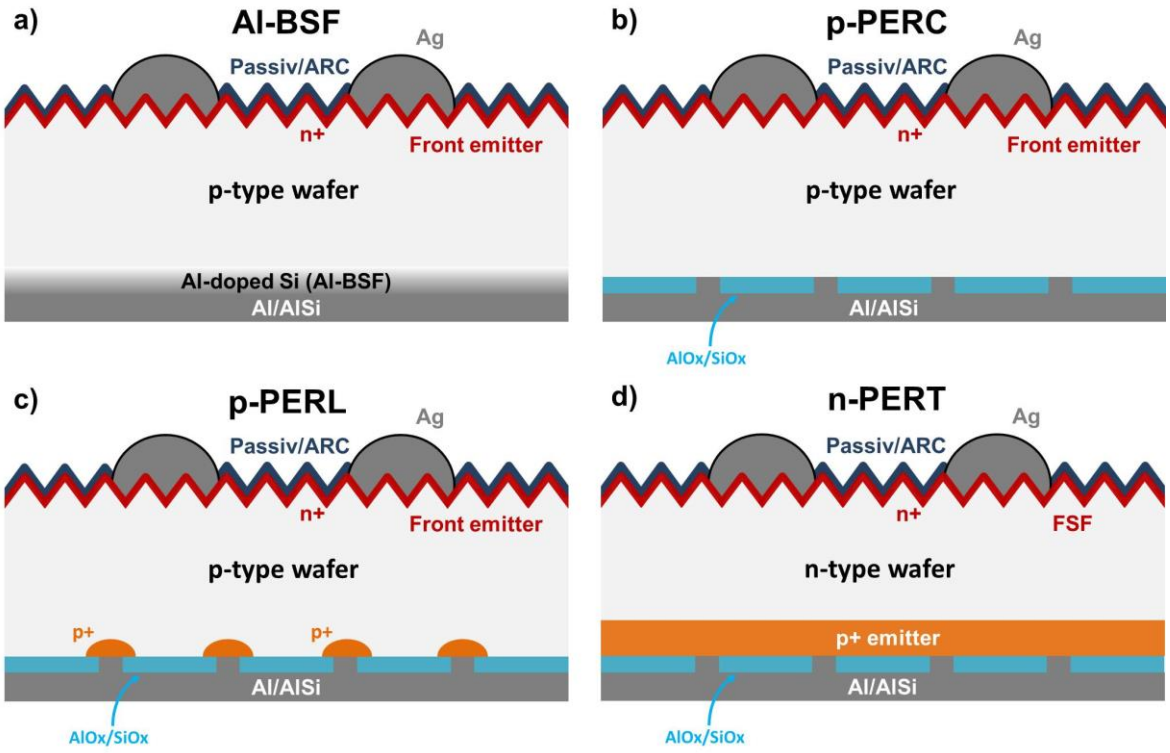

Fig. 1.9 – Main architectures potentially implemented in industry. a) Aluminum back surface field structure b) p-type passivated emitter and rear contact c) p-type passivated emitter with rear locally diffused d) n-type passivated emitter, rear totally diffused.

Among the 93% of c-Si solar cells shipped in 2015, most of them are homojunction based architectures. The schematics of structures to be the most likely implemented in industry are given in Fig. 1.9 and their main characteristics are detailed below:

- The **Al-BSF** structure (Aluminum back surface field) mostly used on mc-Si (multicrystalline silicon) wafers is the most largely produced technology due to its simple and low cost process flow. It is composed of a multicrystalline p-type substrate on which a n^+ doped layer (electron collector or more commonly called emitter) is formed on the front side by phosphorus diffusion to form the PN junction, using phosphoryl chloride ($POCl_3$). It should be clarified that the term “emitter” refers to the minority carriers collector, and the back/front surface field (B/FSF) to the majority carriers collector. In the rear side, an aluminum layer is deposited by screen printing to make a metallic contact and the BSF. Its principle and process are simple, after annealing, the aluminum diffuses in the silicon and form an Al-Si alloy. The aluminum,

having three valence electrons, is an electron acceptor for silicon which allows to create a p^+ doped layer playing the role of field effect passivation at the back by repelling the electrons.

- The **PERC** (passivated emitter and rear contact) solar cell is usually composed of a p-type monocrystalline substrate. The architecture is similar to that of Al-BSF but in the rear side, instead of a direct contact between the substrate and the metallic contact (a strongly recombination source), a dielectric layer is deposited on the full surface of the wafer acting as a chemical passivation layer of dangling bonds by saturating the electrically active interface states. Afterwards, this layer is usually opened by laser to create local metallic contacts with the substrate to be able to collect charge carriers.

- The **PERL** (passivated emitter with rear locally diffused) solar cell has the same architecture as the PERC solar cell but has local p^{++} doped areas at the opened areas. This is now mainly done by laser doping. This allows to have local BSF and improves the metallic contact.

- Finally, the **PERT** (passivated emitter, rear totally diffused) has a p^+ layer on the full surface instead of only at the contacts. This allows holes to laterally move at the rear side of the cell with reduced resistance losses [28],[29]. As a result the solar cell conversion efficiency should be improved due to a higher fill factor (FF). The schematic in Fig. 1.9-d) applies to n-PERT solar cell with rear side emitter. It should be mentioned that this is a popular but not exclusive case, this PhD work refers to this architecture explaining the choice for this type of n-PERT solar cell in the schematic.

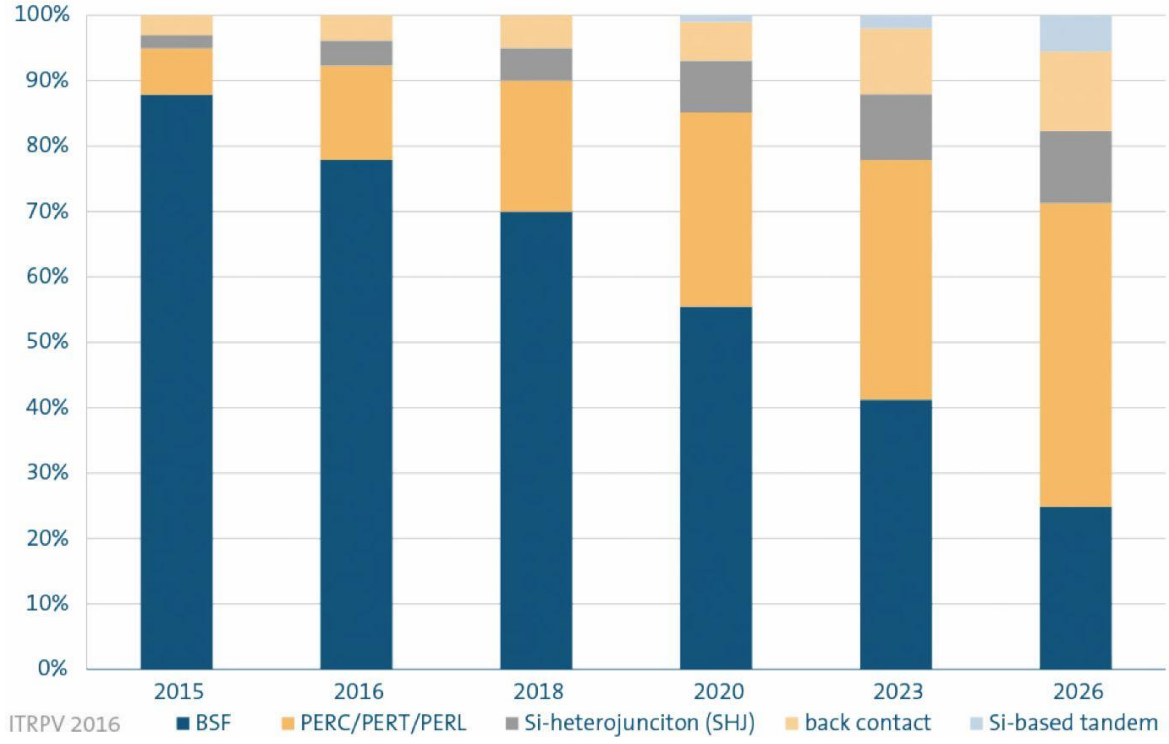

Fig. 1.10 – Roadmap for the evolution of market shares for different c-Si technologies [33].

As shown in Fig. 1.10, a chart from the last international technology roadmap for photovoltaic (ITRPV), despite today's production is dominated by the Al-BSF structure (used with mc-Si wafers),

there is a trend to move towards more efficient, but more complex, technologies like PERC (Passivated Emitter and Rear Cell), PERL (Passivated Emitter, Rear Locally diffused) and PERT (Passivated Emitter, Rear Totally diffused). Moreover, one objective of the PV industry is to reduce wafer thickness in order to reduce production costs; the Al-BSF is not compatible with this trend because of the bowing of the cell. Indeed, the difference of thermal expansion coefficient for silicon and aluminum is significant enough to create a compressive stress at the back of the solar cell resulting in its deformation and potential breakage.

The PV industry is very conservative, meaning that the purchase of new equipment is a real brake to the development of new technologies. This is why p-PERC solar cells are considered as a good potential for industrial applications because they do not require a lot of change in the current fabs process chain. Today the solar cell production is massively dominated by p-type wafers but there is a trend to move towards n-type wafers due to the improved performances achieved with n-type material. The significant difference between these two types of materials has been known for a long time but historical reasons led to the choice of p-type wafers in the industry. Indeed, the improved resistance to irradiation of p-type wafers made them more suitable for space applications [30], the first sector to really use solar cells. Also, the mobility of electrons, the minority carriers in case of p-type material, is three times higher than that of holes. As a result, the choice of p-type wafers was obvious at that time [30]. Afterwards, the PV industry aligned itself with the known processes from CMOS microelectronics industry to develop them at larger scale and for a long time used their waste as wafers material source. But now the limiting issues for the industry are completely different. There is no evidence about which solar cell architecture will be dominant in the future but the move towards n-type solar cell is completely rational and does not involve fundamental hurdle to that. Cotter *et al.* [30] have shown that n-type material is more likely to accept chemical and crystallographic defects. In addition, the Czochralski (Cz) growing method for ingot manufacturing, used for all commercial mono c-Si solar cells, introduces large amounts of oxygen into the silicon wafers. This leads in p-type wafers to the formation of boron-oxygen complexes (B-O complexes) which under illumination are transformed in highly active recombination centers, responsible for a drastic decrease of minority charge carrier lifetime. This phenomenon, discovered in 1973 [31] is known as light-induced degradation (LID). Its mechanism is not completely understood yet, but is related to excess carrier injection by above-bandgap illumination or forward biasing [32]. Considering the LCOE measured in \$/Wh rather than the usual \$/Wp, the development of n-type high efficiency solar cells is therefore a big advantage on the long-term due to a higher efficiency and a better stability over the long term.

The process for n-type wafers manufacturing is a bit more complex due to the segregation of phosphorus but should not be a limiting factor. Also, the formation of the p^+ layer in n-type wafers is more difficult to carry out than the formation of the n^+ layer in p-type wafers. In the standard process flow for n-PERT solar cells manufacturing, the p^+ layer at the rear side is formed by BBr_3 diffusion, a process which can present some complexities, as discussed later. The aim of this PhD work is to address this issue by investigating the possibility to replace the diffusion for the p^+ doped layer manufacturing by low temperature epitaxy using $SiF_4/H_2/Ar$ gas mixtures in a plasma-enhanced chemical vapor deposition (PECVD) reactor.

1.4. Application of silicon epitaxy in solar cells

1.4.1. High temperature epitaxy

Epitaxy is the growth of a crystalline material on a crystalline substrate imposing the orientation of the grown material. The substrate and the grown material are either from the same chemical species, referred as homoepitaxy, or different, referred as heteroepitaxy. In the solar applications, epitaxy can be either used for the manufacturing of the absorber of the solar cell or for the formation of doped layers to create the PN junction and the charge carriers selective contacts.

Several techniques are used for epitaxy, we briefly detail below their principle:

- MBE (Molecular Beam Epitaxy) is a deposition technique based on the evaporation or sublimation of precursors interacting with the sample surface to grow thin films. This technique is used for the growth of high purity materials implemented in high technology devices. Most of MBE reactors are used for growth of III-V or II-VI materials for optoelectronics devices used in defense and nanophotonic area. In spite of excellent material properties, it requires ultra-high vacuum (10^{-8}-10^{-12} Torr) and is not suitable for PV industry due to a very high CAPEX and low throughputs.

- PVD (Physical Vapor Deposition), or sputtering, consists in igniting a plasma, usually from argon, between the substrate and a target composed of the material we want to deposit. The ions from the plasma bombard and sputter the target, the pulled off atoms from the target condense on the grounded substrate through an isotropic deposition.

- CVD (Chemical Vapor Deposition) relies on chemical reactions from the gas precursors and the sample surface, it is subdivided in several techniques whose more suitable for PV industry are:
    - APCVD (Atmospheric Pressure CVD)
    - PECVD (Plasma-Enhanced CVD)

In PV industry, PECVD is already widely used for SiN_x layer deposition to form the anti-reflective coating (ARC) and the passivation layers (SiO_x, a-Si:H in case of HIT™, …). APCVD is not commonly used in today's PV industry but a few applications with excellent recent results could make it a game changer.

1.4.2. Epi-foil and epi-wafer as absorbers in c-Si solar cells

Companies and laboratories such as Crystal solar, previously Solexel and IMEC develop semi-industrial solutions for making monocrystalline silicon substrates via a direct gas-to-wafer method instead of pulling ingots by the standard Czochralski technique. This approach provides several advantages (comparable to thin films industry) because it eliminates any dependency on the ingot and wafer supply chain. It also prevents from kerf loss, the loss of materials due to wafer sawing. For instance, with 160 µm thick wafers the kerf loss for slurry-based and diamond wire-based wiring is respectively around 150 µm and 125 µm [33], it means that on a single ingot, the half is lost due to sawing.

The process flow for Si foils manufacturing performed by IMEC is given in Fig. 1.11-a). The process steps can slightly change between manufacturers but are roughly the same as these detailed in Fig.

1.11. A porous layer is formed at the top of a parent crystalline silicon substrate, then a thermal treatment is performed to reorganize the porous silicon and to prepare the surface for epitaxy as shown in Fig. 1.11-b). The wafer is heated between 900°C and 1100°C and exposed to a silicon based gas, usually trichlorosilane (TCS). Crystalline growth occurs on the full surface and the epitaxial layer, on which the solar cell will be processed, is detached afterwards by etching the fragile porous silicon layer. One big advantage of this approach is the possibility to tune the absorber thickness. Thus, compared to current 160 µm thick wafers used in industry, the thickness can be lowered to 35 µm in case of former Solexel's process and 50 µm for IMEC Si foils.

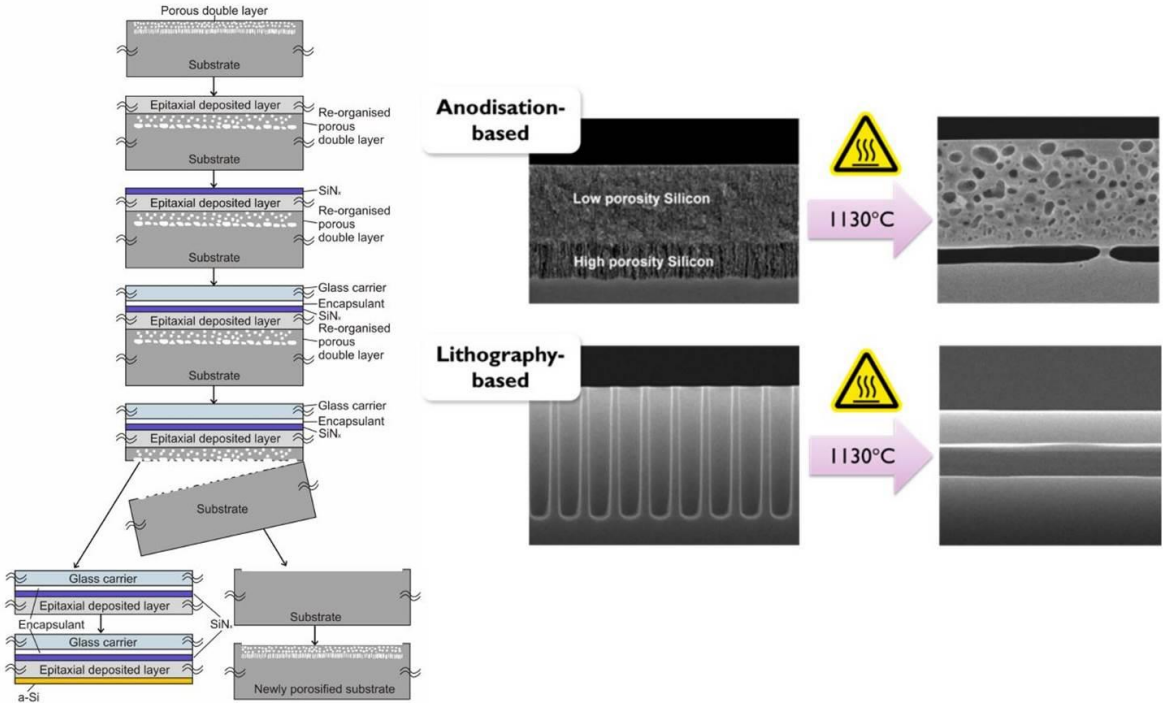

Fig. 1.11 – a) Process flow of the Si foil growth and detachment [63]. b) Thermal treatment applied to porous silicon for the surface preparation prior to epitaxy by APCVD [64].

Regarding the quality of the material, the lifetime in such Si foils and epi-wafer is now sufficiently high to manufacture high efficiency solar cells. The Table 1 lists lifetimes reached by different laboratories and companies reported in the literature. Note that a strong difference is observed between p-type and n-type epi-layers. The maximum lifetime measured in p-type epitaxial silicon is 300 µs and this result is obtained after phosphorus gettering [34]. For n-type silicon, Fraunhofer reached a mean effective charge carrier lifetime, measured by QSS-PC, of 1580 µs on a 5x5 cm^2 epi-wafer at an injection level of 10^{15} cm^{-3}, close to its local maximum of 1720 µs [35]. Nevertheless, the record is held by Crystal Solar which reached 3.5 ms [36].

Solexel reached an efficiency record of 21.2% for a 240 cm^2 submodule with a 35 µm thick back-contacts reported cell [37] and Crystal Solar with Choshu Industry manufactured a 22.5% efficient heterojunction solar cell with an epi-bulk of 130 µm on a 243.4 cm^2 area [36]. More recently, IMEC and Crystal Solar collaborated to make a n-PERT solar cell with a 180 µm thick epi-bulk reaching an efficiency of 22.5% on a 238.9 cm^2 area [38], attaining the same efficiency as their reference cell obtained with standard BBr_3 diffusion on a Cz wafer.

However, this approach suffers so far from insufficient yield, due to several reasons. First in case of thin wafers manufacturing, the probability of breakage during manipulation is higher than for standard "thick" wafers of 150-180 µm. The results can also be not reproducible due to bumps at the surface of wafers caused by the difficulties to achieve a flat surface after the reconstruction of porous silicon.

Team	Process	Lifetime
IMEC	APCVD PSI [39]	195 µs
	APCVD lithography [39]	350 µs
MIT – Crystal Solar [34]	APCVD – before gettering p-type epitaxial	< 20µs
	APCVD – after gettering p-type epitaxial	> 300 µs
Crystal Solar [36]	APCVD – n-type	3.5 ms
Fraunhofer ISE [40]	APCVD – p-type 40 µm (doping 5.10^{16} cm^{-3}) Si foil	80 µs
Fraunhofer ISE [35]	APCVD – n-type 150 µm (doping 5.10^{16} cm^{-3}) Epi wafer	1.5 ms
IBM [41]	PECVD – n+ epi-layer (doping 5.10^{19} cm^{-3}) $SiH_4/H_2/PH_3$	100 ps
LPICM [42]	PECVD – SiH_4/H_2	10 µs

Table 1 – State of the art for lifetime in Si foils, epi-wafers and low temperature epitaxy.

Thus, throughput can be an issue for the current and future development of this technology from an industrial point of view. Moreover the epitaxy for PV not being a sufficiently important market for semiconductor equipment manufacturers, the development of industrially viable APCVD reactors meeting industrial constraints (throughput, reliability, yield,…) to compete with wafer manufacturers is not a priority. A new momentum for this technology coming from an industrial support is necessary to bring this technology to the industry.

Thus, the future of epi-foils and epi-wafers is unclear. Solexel, which was one of the most promising companies in kerfless technology, recently stopped its development of epi-foils because they didn't reach their objective to ship solar modules at 0.42 $/W by 2014 [43]. Even if the current kerfless wafers industry (Crystal Solar, 1366 Technologies,…) is doing good progress, the decrease of ordinary wafers cost in the meantime and overcapacity phases make difficult the perspectives for this new approach. Nevertheless epitaxy can find another promising application for its implementation in industry by the formation of the doped layers in c-Si solar cells.

1.4.3. Epitaxy for the formation of doped layers in c-Si solar cells

In the standard c-Si solar cells, whose architectures (Al-BSF, PERC, PERT, PERL) have been previously detailed, the doped layers are commonly made by diffusion. For Al-BSF and PERC, on p-type material, the PN junction is formed by a phosphorus diffused layer. In a tube furnace, wafers are heated at around 850°C, a phosphosilicate glass (PSG) is formed on the surface of the wafer by introducing $POCl_3$, a subsequent annealling called the drive-in allows to adjust the doping profile. For the n-PERT solar cell, the same diffusion is performed to form the front surface field (FSF) in order to repel minority carriers, so holes in that case. The phosphorus diffusion allows to improve the performances of the cell by the so-called gettering effect.

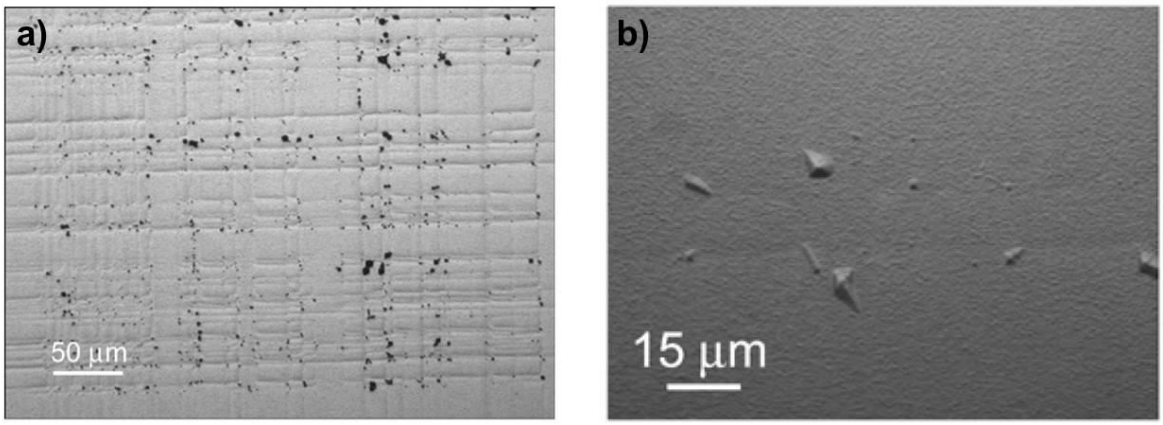

Fig. 1.12 – a) Optical microscope images of a wafer surface after an intentionally heavy planar boron diffusion (10 Ω/sq) after a Yang etch [65] showing misfit dislocations [44]. The BBr_3 diffusion has been performed at 900°C for 45 min, and the drive-in at 1060°C for 900°C. b) Etch pits formed during movement of the misfit dislocation network [44].

For the p^+ doped layer, used as a hole collector, the common process is the boron diffusion. The principle is the same, a borosilicate glass (BSG) is formed from boron tribromide (BBr_3) and dioxygen (O_2) at the surface of the wafer heated around 900°C. Subsequently, the drive-in phase is performed for the diffusion of the elemental boron from the BSG into the wafer. This BBr_3 diffusion is currently the standard way to form the p^+ doped layer, but this process is not as simple as phosphorus diffusion and not as beneficial.

On the one hand, the boron diffusion can cause misfit dislocations due to the high concentration of boron in the top layers. The atomic radius mismatch between boron and silicon induces a stress gradient in the silicon crystal, the covalent radius of boron is 0.88 Å while that of silicon is 1.18 Å. In case of moderate concentration the strain is elastic but above a critical threshold, diffusion-induced misfit dislocations appear [30],[44],[45]. The defects induced by the heavy doping at the surface of the wafer are shown in Fig. 1.12. First, dislocation lines perpendicular to the {100} planes form a dislocations network. Second, the movement of this misfit dislocation network induces the formation of etch pits at the intersection of the dislocation lines. It is worth noticing that even though a dislocation network may be observed in the case of phosphorus diffusion (but no etch pits [44]), the mismatch is lower due to the covalent radius of phosphorus being closer than that of silicon (1.08 Å), compared to boron with respect to silicon.

On the other hand, during the diffusion, boron precipitates on the silicon surface and induces the formation of a boron-rich layer (BRL) beneath the BSG at the surface of the silicon wafer [46]. A scanning-electron microscopy (SEM) image of a BRL between the BSG and the silicon substrate is shown in Fig. 1.13-a). This process suffers from uniformity problems for the BSG deposition, and this is more likely to produce a BRL in the case of thicker BSG layers. The reduction of process temperature to 850°C is beneficial to limit the BRL formation but the process window is narrow, sensitive to temperature variation, which is a problem for large scale industrial applications. The BRL is highly recombinant and requires additional oxidation and removal steps [47] to recover a high minority carrier lifetime. Secondary ion mass spectrometry (SIMS) profiles of BRL before and after oxidation are shown in Fig. 1.13-b). It should be mentioned that this SIMS profile does not correspond with the SEM image from Fig. 1.13-a). It can be seen that before removal, the boron concentration on the first tens of nanometers is up to 10^{22} cm^{-3}. The subsequent oxidation/removal step necessarily affects the sheet resistance. Boron gettering to recover the electrical properties is also reported [46].

The use of alternative dopant sources such as boron spin-on dopant (BSoD) leads to the same observations [48].

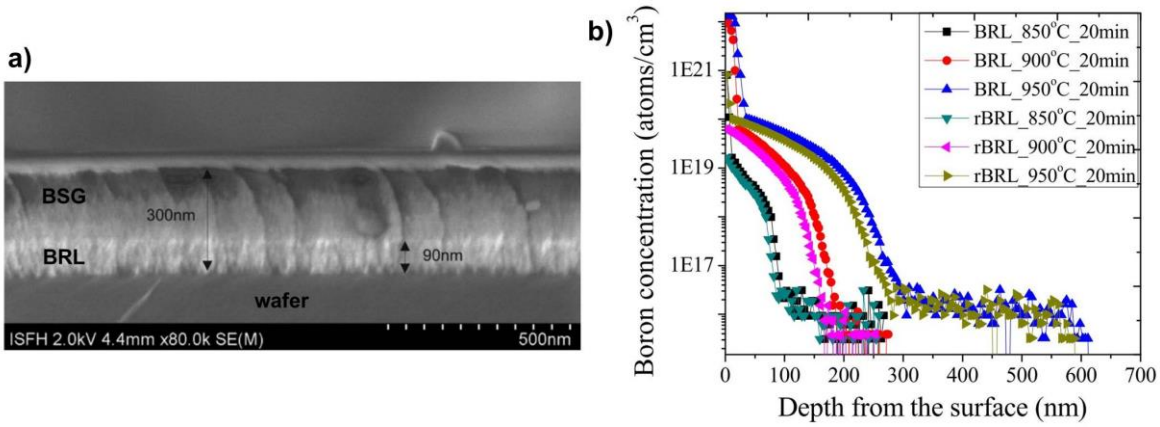

Fig. 1.13 – a) SEM image of the two-phase layers, the BSG at the top is 200 nm thick and the BRL is the beneath 90 nm thick layer [46]. b) SIMS profile of boron emitters with BRL and reduced BRL (rBRL) obtained by *in situ* post oxidation from hot HNO_3 followed by a HF dip [48].

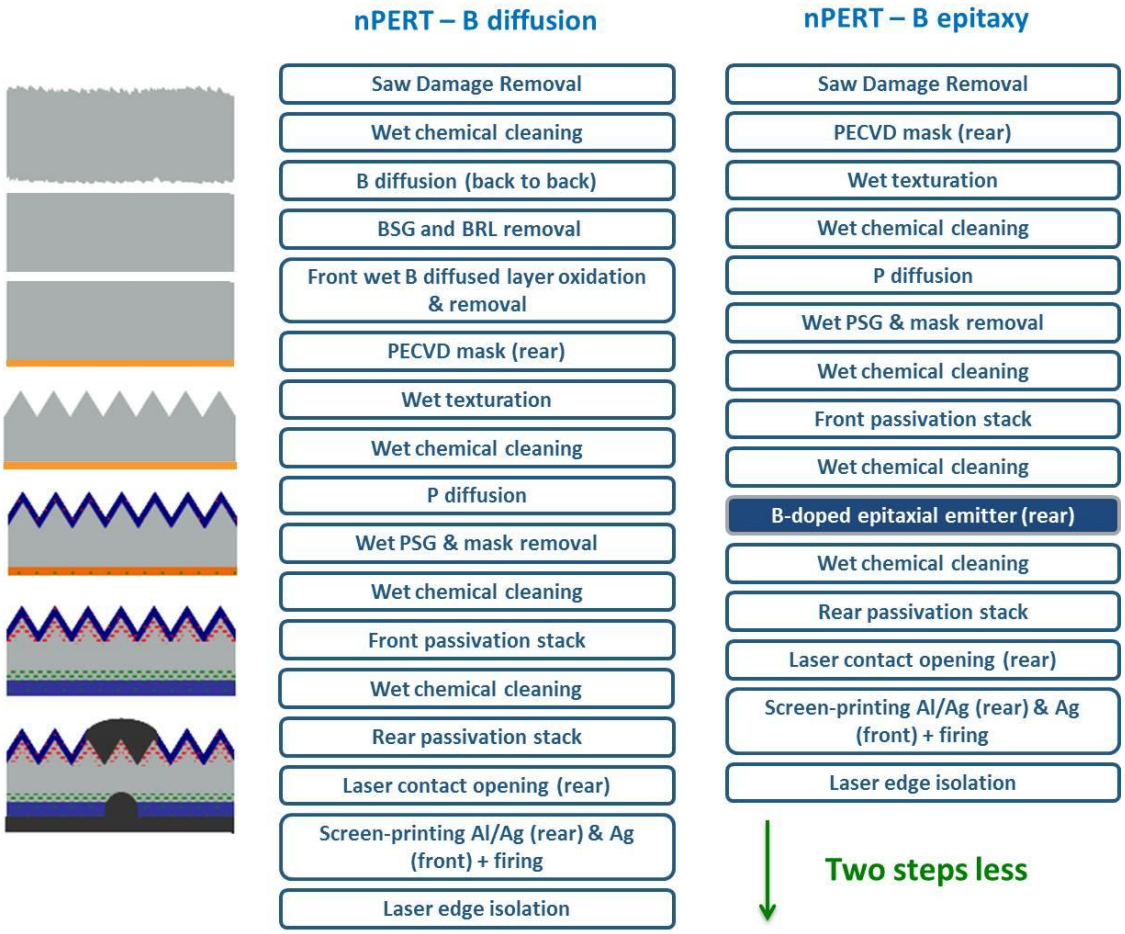

Fig. 1.14 – Process flow for n-PERT solar cell manufacturing with standard BBr_3 diffusion (left) and boron-doped epitaxy (right).

The use of epitaxy to grow the doped layer instead of diffusion allows to avoid the formation of the BRL and the additional process steps to remove it. By doing so, it simplifies the process flow of n-PERT solar cells manufacturing. The comparison of standard and epi boron emitter process flows for n-PERT solar cells is shown in Fig. 1.14.

This innovative process flow requires two steps less than the reference one with boron diffusion and drastically reduces the process time to a few minutes in case of APCVD [49] instead of 45-60 minutes for diffusion, which could allow significant cost reductions. Also the epitaxy can be tuned to be a single side process either due to the equipment configuration [50] or by developing a selective epitaxy [49]. In selective epitaxy, the growth occurs on apparent crystalline surfaces but not on amorphous surfaces (dielectric layer used as passivation layer on the other side) so no mask or additional etching is required.

Besides, according to the last ITRPV, a strong reduction of recombination losses is expected by 2025, with a drop from 30 fA/cm^2 to 10 fA/cm^2 for n-type monocrystalline wafers and a reduction of 50% of J_0 front and rear for p-type materials [51]. This involves a good management of recombination in the doped layers by optimizing the doping profile. Indeed, the dopant concentration should be high enough to create an efficient PN junction and to make a good electrical contact with the metal but it also induces Auger recombination and free carriers absorption.

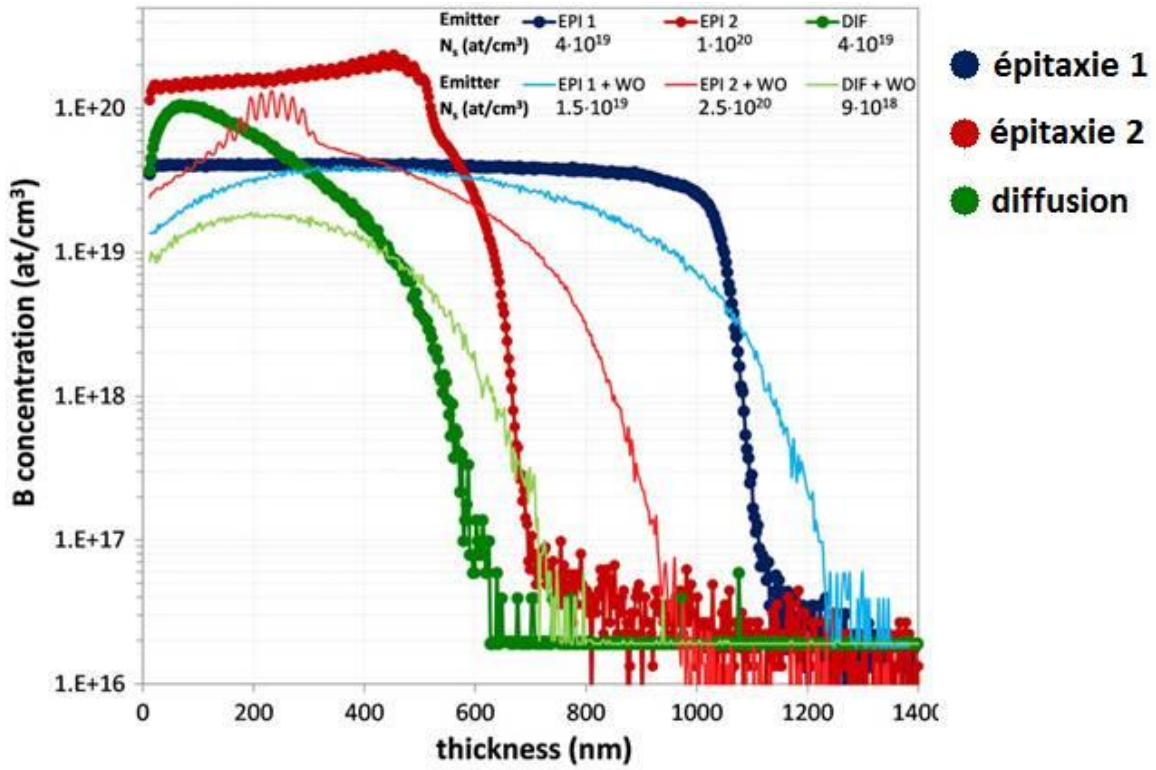

Fig. 1.15 – SIMS profiles of shallow (green) and deep (sky blue) diffused emitters and shallow (red) and deep (blue) epitaxial emitters [50].

Thus a good control of doping profile is mandatory to move towards high efficiency concepts. Contrary to diffusion, for which the doping profile is analytically described by a *Gaussian* or *erfc* function, epitaxy allows any kind of doping profile thanks to the easy control of dopant concentration through the layer by simply varying the dopant gas flow rate (B_2H_6, $(CH_3)_3B$). Therefore the optimization of the doping profile is much easier by epitaxy and also makes possible the formation of

very shallow junctions. Doping profiles can be boxes (constant doping concentration through the layer) or multi-steps. Typically, it is possible with epitaxy to manufacture an emitter with a low boron concentration in its bulk, to limit Auger recombination and free carriers absorption, and a high boron concentration at its surface to reduce the series resistance thanks to a good electrical contact. Something much more difficult with diffusion as shown in the comparison of doping profiles obtained by diffused and epitaxial emitters, in Fig. 1.15. To achieve a deep and lowly doped diffused emitter (in sky blue), the boron concentration at the surface is necessarily reduced with respect to that of the shallow one. Even though the doping profiles for epitaxial emitters shown in Fig. 1.15 are uniform (boxes), epitaxy does not suffer from this constraint of trade-off between thickness of the emitter and the boron concentration within it. Thus, according to Rachow *et al.* [52] the replacement of a front surface diffused emitter by a front surface epitaxial emitter, could lead to a 30% reduction in J_0, an improved blue response, and low contact resistance. However, until recently, the efficiency of solar cells using epitaxial emitters has always been lower than with diffused ones.

This approach of growing doped layers by epitaxy on silicon wafer-based solar cells has first been reported in 2006 by Schmich *et al.* [53] at the Fraunhofer ISE. At that time, they reached a 12.6% efficient solar cell with a phosphorus doped epitaxial emitter and a 12.3% efficient solar cell with a boron doped epitaxial emitter. In 2009, at IMEC, Gong *et al.* [54] also suggested this new approach to form the p^+ emitter by CVD rather than diffusion. They reached an efficiency of 17% with LPCVD and 16.7% by APCVD while their reference cell with diffused emitter was attaining 17.7%. The most critical reasons of efficiency losses were the optical management at the rear side and the cleaning prior to epitaxy, the latter is extremely important to limit recombination at this interface in order to reach high V_{OC}. Rachow, Milenkovic *et al.* [52],[55],[56] used phosphorus doped epitaxial emitters and achieved a 18.4% efficient solar cell. Nevertheless, their reference cell (with phosphorus diffusion) was still giving significantly higher performances with an efficiency at 20.1%, so a nearly 2% absolute difference. But they were focusing on the n^+ layer formation, so without using the gettering effect of the phosphorus diffusion, in a p-PERL structure. By moving towards n-PERL, they achieved a 21% efficient solar cell [49] with epitaxial p^+ emitter by APCVD with a gas mixture composed of TCS and B_2H_6. But compared to their reference cell with diffused emitter using BBr_3, with an efficiency of 22.8%, the results for epitaxial emitters have shown so far lower experimental efficiency values in spite of a better theoretical potential.

That's only very recently that IMEC reported the same efficiency with epitaxial and diffused emitters. They reported a 22.5% efficient solar cell [57] with a boron-doped epi-emitter in a n-PERT structure. As mentioned before, the preparation of the surface prior to epitaxy is a paramount concern. This record has been obtained with sulfuric acid and ozone mixtures (SOM) cleaning. However for economic and environmental perspectives, the use of a sulfur-free mixture based on deionized water and ozone has been investigated and showed a promising 21% efficient solar cell.

A way to get rid of this critical step is to grow the whole cell in the APCVD reactor in the same process flow [58], combining the absorbers and doped layers deposition capability of the APCVD. This led to the same efficiency of 22.5%. This approach allows to considerably reduce the number of process steps because: i) there is no need for a cleaning prior to the doped epitaxy without risk of contaminations ii) no additional pumping step is required and iii) it gives the possibility to produce a very deep and lowly doped emitter to limit Auger recombination and free carriers absorption. The emitter thickness for the best cell efficiency is greater than 10 µm with a carrier concentration of 1.10^{18} cm^{-3} (which is very low for an emitter) and leads to a very low sheet resistance below 30 Ω/sq. They also assure no degradation of cell performances related to the substrate reuse and reach efficiencies of 21.8% after 18 substrate reuses. Nevertheless this approach still relies on APCVD

reactors with low throughputs, compared to industrial diffusion furnaces, and little information regarding the yields is provided. Thus, according to the ITRPV, alternative technologies to standard wafers should enter the market from 2020 but should stay below 5% of market shares in the next decade [33].

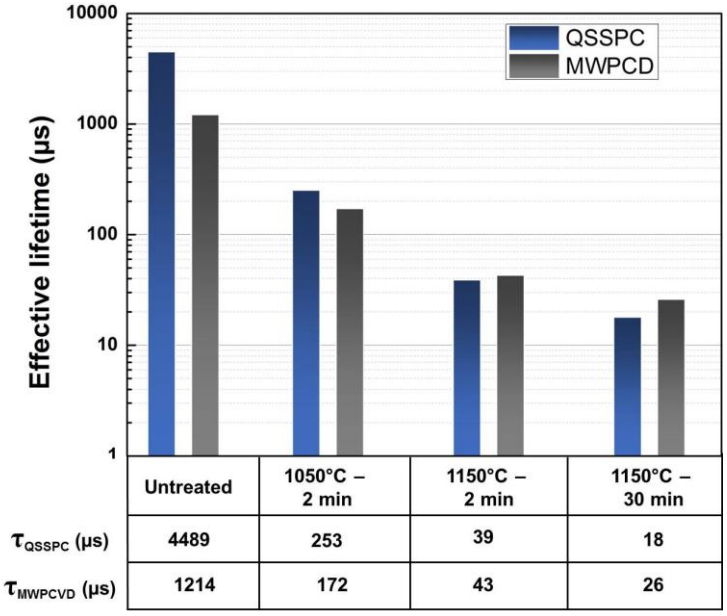

	Untreated	1050°C – 2 min	1150°C – 2 min	1150°C – 30 min
τ_{QSSPC} (µs)	4489	253	39	18
τ_{MWPCVD} (µs)	1214	172	43	26

Fig. 1.16 – Effect of thermal budget for doped layers formation by APCVD processes on the bulk lifetime of a c-Si substrate. Data from [55].

Diffusion and APCVD present another problem due to the high process temperature: 850°C-900°C for diffusion and 850°C-1000°C for epitaxy by APCVD. This represents a high thermal budget and can induce damages in the wafers. Rachow, Milenkovich *et al.* [55] have shown that the thermal budget of their process had a huge effect on the bulk lifetime. Fig. 1.16 relates the influence of the process temperature and time on the bulk lifetime. The wafers annealed at 1050°C for 2min have lifetimes one order of magnitude lower than the non-annealed wafers. The effect is even more critical by increasing the temperature and/or the annealing time. A lower process temperature is thus mandatory to limit the bulk lifetime degradation, but in the meantime, it results in a decrease of the crystalline quality of the grown layer. The use of HCl in the gas mixture which can prevent this negative effect is therefore required [55]. However by decreasing the growth temperature, the growth rate is also lowered.

In diffusion processes, analogue problems of bulk lifetime reduction are encountered. These phenomena are related to oxygen precipitation and/or impurities diffusion [59],[60]. Two distinct phases are identified. The first one is the nucleation phase which occurs around 700-800°C and produces small size oxygen precipitates (around 10 nm). These clusters are not sources of lifetime degradation except if they trap metallic impurities. If they do, this combination increases the cross section of the metallic impurity and makes it a dramatic active recombination center. In case of a subsequent process step at around 1000°C, these oxygen precipitates can diffuse and merge into larger aggregates of about 100 nm in diameter. In that case they become potential sources of dislocations once all vacancies have diffused and the lattice is no longer able to elastically accept the stress induced by the aggregates. A 1000°C process by itself does not necessarily induce this kind of dislocation but the ramp to reach this temperature can be enough to make the nucleation phase possible. Therefore, APCVD is not always associated with oxygen precipitation problems but the metallic impurities

diffusion is inevitable. Moreover, the trapping of iron by oxygen precipitates makes less efficient the gettering effect during phosphorus diffusion. Thus, the gettering in oxygen-rich wafers is less efficient due to these trapping phenomena. This case is critical because the iron concentration is not reduced and the association of trapped iron and oxygen precipitates (iron-decorated oxygen precipitates) becomes extremely recombinant due to an increase of the recombination cross-section. The use of low cost oxygen-rich silicon wafers is therefore critical for high temperature processes. Moreover the loading and unloading of wafer batches in reactors heated to high temperature produces thermal gradients in the wafers and thus causes a thermal stress which can multiply dislocations into the wafer [61].

1.5. Low temperature epitaxy

1.5.1. Advantages of low temperature epitaxy by PECVD

Conventional epitaxy (LPCVD, APCVD) is performed at high temperature to allow the thermal dissociation of gas precursors in the gas phase, the formed species are afterwards chemisorbed at the surface of the substrate. The growth of epitaxial thin films at temperatures below 400°C is possible in the case of plasma-enhanced CVD, which allows the formation of reactive species from the dissociation of gas precursors by their collision with electrons. In this range of temperature, gas precursors cannot react with the substrate. All the problems associated to high temperature processes related previously, can thus be avoided in the case of low-temperature processes. The use of PECVD to grow crystalline silicon is a way to limit the thermal budget and to introduce an alternative to the p^+ emitter formation with already widely spread equipment in the PV industry, therefore compatible with high throughputs.

Our approach is to combine the advantages of heterojunction solar cells, namely the use of low temperature processes, with the advantages of homojunction solar cells, for which no advanced metallization paste and transparent conductive oxide (TCO) are required [26]. Moreover it allows the formation of a sharp junction due to the reduced diffusion of dopants thanks to the low process temperature (200-400°C). It does not induce oxygen precipitation in the wafer due to a low thermal budget and the doping concentration is easily tuned to limit effects of high boron concentration in the layers, as detailed previously. Also, the reduced deposition rate, with respect to APCVD, is a way to genuinely optimize the doping profile. Moreover, epitaxy by PECVD does not require an additional mask to avoid wrap around, simplifying again the process flow. Besides, PECVD has been widely used in thin film transistors (TFT) industry for the manufacturing of LCD and a strong know-how has been developed. It is also well known and implemented in the PV industry: it is already used for the manufacturing of the absorbers in silicon thin film solar cells, the passivation (a-Si-H, SiO_x, SiN_x, …), the doped layers in SHJ solar cells and the silicon nitride (SiN_x) for the antireflective coating. The reactive ion etching (RIE), used for the dry texturation of silicon wafers, is also done via plasma processes whose reactors used for this purpose have similar architectures than deposition ones. Thus from an industrial point of view, PECVD benefits from a strong know-how, the availability of equipment with throughput adapted to industrial standards (a few thousands of wafers per hour) and a large versatility, which allows to perform in the same type of reactors different process steps of solar cell manufacturing. Finally, as mentioned previously the PV industry is very conservative and the implementation of new processes is scarce. The move towards p-PERC solar cell architecture is a

good example as it requires slight changes in the manufacturing process flow with most of production tools already in the industry. The replacement of diffusion by epitaxy using PECVD is therefore conceivable given that PECVD reactors are already implemented in the industry which is a strong asset compared to APCVD reactors. A potential industrial transfer should therefore be easier.

Although the PECVD has been widely used for a lot of different applications, its potential for the silicon epitaxial growth, so far, has not been exploited in the industry, mostly due to lower performances and deposition rate. The recent results obtained at LPICM by Labrune *et al.* [62] have shown that solar cell with low temperature epitaxial emitter grown with a $SiH_4/H_2/B_2H_6$ gas mixture could reach energy conversion efficiencies above 14%. This is encouraging but not sufficient to suggest n-PERT solar cell with low temperature epitaxial emitter as a viable solution for industry. In this PhD work we investigate the potential for low temperature epitaxy by PECVD using an alternative gas mixture composed of silicon tetrafluoride (SiF_4), hydrogen (H_2) and argon (Ar).

1.5.2. Cost of ownership calculations

In order to give some insights on the minimum deposition rate required to lead to a potential transfer to industry, cost of ownership (CoO) calculations for the formation of doped layers in c-Si solar cells by PECVD, BBr_3 diffusion and APCVD processes have been carried out. APCVD and diffusion steps CoO were calculated for a 22% cell efficiency.

Fig. 1.17 compares relative epitaxial PECVD CoO for different solar cell efficiencies, revealing the minimal deposition rate required to compete with both diffusion and APCVD for a given efficiency. It shows that for a cell efficiency of 24%, a deposition rate of 3 Å/s is enough, but if the cell efficiency is only 18% then a deposition rate of 5 Å/s is required. The break even with APCVD is even tougher to reach. For a 24% efficient solar cell, a 10 Å/s deposition rate is required, while it needs to be more than 15 Å/s for a 18% solar cell. The deposition rate required to be cost competitive as a function of cell efficiency is shown in Fig. 1.18. It shows that for a 20% efficient solar cell, PECVD can be cost competitive with diffusion for deposition rates above 4 Å/s, but it needs to reach 15 Å/s to meet APCVD CoO. It must be mentioned that in order to replace diffusion processes in industry, the deposition rate should be faster than the above mentioned break even to justify a change in the production equipment.

Today, the best deposition rate at LPICM for epitaxy by PECVD is 8 Å/s when using SiH_4/H_2 gas mixtures at 300°C. In case of $SiF_4/H_2/Ar$ gas mixtures, it was 3 Å/s at the beginning of this PhD, but the process conditions were not as developed as for the SiH_4/H_2 chemistry.

Nevertheless, for both cases, if these values do not meet industrial requirements, they are clearly not far from consistent economic perspectives, since required deposition rates are not several orders of magnitude higher. Therefore, in order to increase the deposition rate, keeping device-grade quality, and thus favoring a potential transfer in industry, a comprehensive study of process conditions also needs to be led. This PhD work aims to bring new insights on the low temperature epitaxy growth mechanisms and to develop doped epitaxial layers to assess the feasibility of epitaxial emitter manufacturing by PECVD.

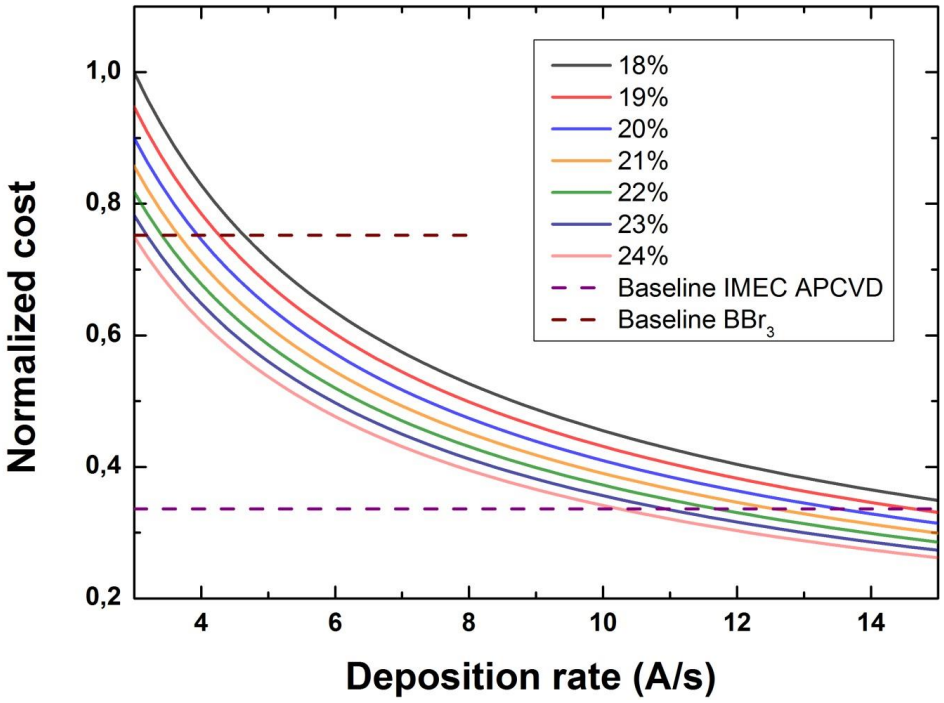

Fig. 1.17 – Relative cost of ownership for emitter formation step based on BBr_3 diffusion, APCVD and low temperature epitaxy by PECVD, as a function of the deposition rate for different n-PERT solar cell efficiencies.

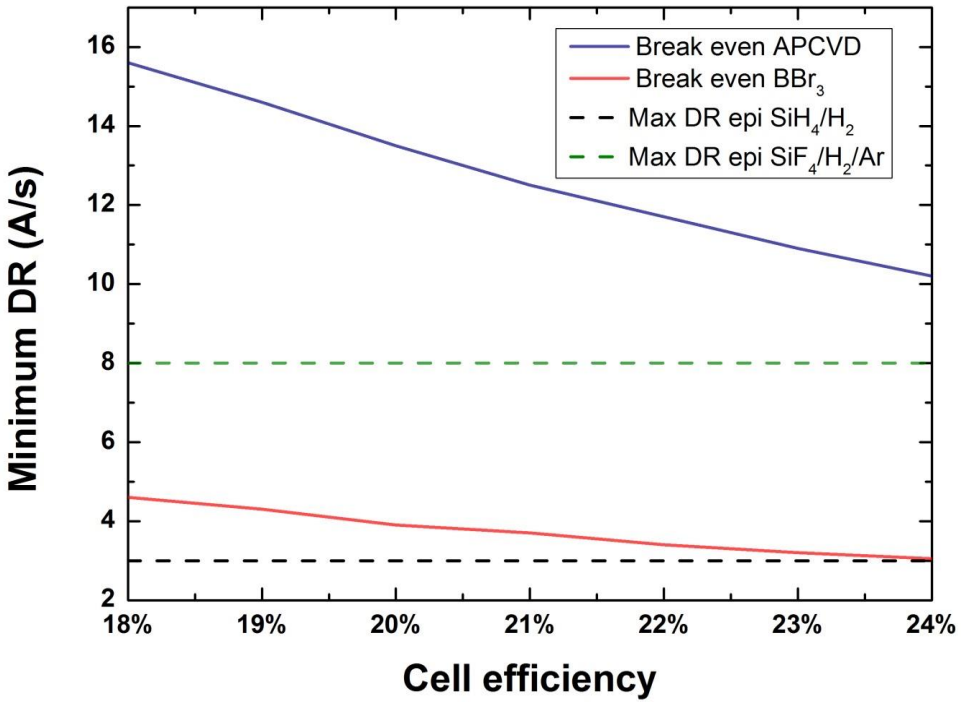

Fig. 1.18 – Comparison of the minimum deposition rate required for the formation of emitter by PECVD to be cost competitive with diffusion (in red) and APCVD (in blue) as a function of solar cell efficiency. The black and green dashed lines represent the maximum deposition rate obtained so far by $SiF_4/H_2/Ar$ and SiH_4/H_2 chemistry respectively.

1.5.3. Outline

While this introduction presented the context of this PhD topic, and the advantages of the PECVD as a way to replace diffusion by a cost competitive solution, we detail below the outline of this manuscript.

Chapter 2 is focused on the definition of the process conditions to perform epitaxy by studying the influence of chemical and physical properties of the plasma on the material properties. The objective is to introduce key process parameters (power, flow rates, pressure,…) in order to determine necessary conditions required to perform epitaxy for the purpose of an easier transfer. It also aims at providing insights on the understanding of the growth mechanisms and epitaxy breakdown. In particular we focus on the influence of H_2 depletion (related to gas-phase reactions) and the plasma potential (related to surface and bulk modifications) on the material properties. Besides, comparative studies of the material properties determined from several characterization techniques (ellipsometry, Raman spectroscopy and X-ray diffraction) for different process conditions, inside and outside the process window, have been led to find out a signature of the cause of epitaxy breakdown.

Chapter 3 is devoted to the understanding of growth mechanisms for the process conditions leading to epitaxy. By studying the early stages of the epitaxial growth, this chapter aims to identify the growth mode of LTE and which plasma species (radicals, ions, nanoparticles, …) are involved in it. A Volmer-Weber growth mode has been highlighted in these early stages and a model for low temperature epitaxy is discussed.

Chapter 4 deals with the transfer of process conditions for epitaxy to a 6-inch semi-industrial PECVD reactor and the development of doped epitaxial silicon layers. Structural and electrical properties of boron- and phosphorus-doped silicon layers are analyzed. Optical and structural properties have been assessed by ellipsometry and X-ray diffraction on the doped epitaxial layers. The boron concentration has been assessed by plasma profiling time of flight mass spectrometry (PP-TOFMS) and SIMS, the carrier concentration by Hall effect and electrochemical capacitance-voltage (ECV) technique. In addition, the homogeneity of doping is assessed by 4-point probe mappings. In this chapter we also tackle homogeneity problems encountered with the gas injection and we suggest the design of an optimum shower head based on fluid dynamic simulations. Properties of epitaxial layers resulting from this new design are compared to those obtained with the former one. Besides, a comprehensive study about the influence of the pressure and the RF power has highlighted the significant influence of these plasma parameters on the structural and electrical properties. Finally the results of passivation of the doped and undoped epitaxial layers by aluminum oxide (AlO_x) deposited by atomic layer deposition (ALD).

Finally, **Chapter 5** concludes this manuscript and perspectives to carry on the work on LTE from $SiF_4/H_2/Ar$ gas mixtures are suggested.

References

[1] C. McGlade and P. Ekins, “The geographical distribution of fossil fuels unused when limiting global warming to 2 °C,” *Nature*, vol. 517, no. 7533, pp. 187–190, Jan. 2015.

[2] “Renewables 2016 Global Status Report,” 2016.

[3] “United Nations, Department of Economic and Social Affairs, Population Division (2015). World Population Prospects: The 2015 Revision, Key Findings and Advance Tables. ESA/P/WP.241.”

[4] International Energy Agency, “CO2 Emissions From Fuel Combustion Highlights 2015.”

[5] International Energy Agency, “Energy Climate and Change World Energy Outlook Special Report,” 2015.

[6] International Energy Agency, “Energy and Air Pollution - World Energy Outlook 2016 Special Report,” 2016.

[7] International Energy Agency, “World Energy Outlook,” 2015.

[8] Intergovernmental Panel on Climate Change, “Renewable Energy Sources and Climate Change Mitigation,” 2012.

[9] T. Bruckner *et al.*, “III ANNEX Technology-specific Cost and Performance Parameters Lead Authors: Technology-specific Cost and Performance Parameters Annex III,” 1330.

[10] A. Topping, “Your guide to Hinkley Point C – the UK’s first new nuclear plant for 20 years | UK news | The Guardian,” *The Guardian*, 2016. [Online]. Available: https://www.theguardian.com/uk-news/2016/sep/15/hinkley-point-c-guide-uk-first-new-nuclear-plant-for-20-years.

[11] “Global trends in renewable energy investment 2016, BNEF,” 2016.

[12] “U.S. Energy Information Administration, Preliminary Monthly Electric Generator Inventory,” 2016. [Online]. Available: http://www.eia.gov/todayinenergy/detail.cfm?id=25492.

[13] Mohit Anand, “Solar Stuns in Mexico’s First Clean Energy Auction: 1,860MW Won at $50.7 per MWh | Greentech Media,” *GTM research*, 2016. [Online]. Available: http://www.greentechmedia.com/articles/read/Solar-Stuns-in-Mexicos-First-Clean-Energy-Auction-1860-MW-Won-at-50.7-P.

[14] A. Hirtenstein, “New Record Set for World’s Cheapest Solar, Now Undercutting Coal - Bloomberg,” *Bloomberg*, 2016. [Online]. Available: http://www.bloomberg.com/news/articles/2016-05-03/solar-developers-undercut-coal-with-another-record-set-in-dubai.

[15] G. Heath and D. Sandor, “Life Cycle Greenhouse Gas Emissions from Solar Photovoltaics (Fact Sheet), NREL (National Renewable Energy Laboratory).”

[16] D. D. Hsu *et al.*, “Life Cycle Greenhouse Gas Emissions of Crystalline Silicon Photovoltaic Electricity Generation,” *J. Ind. Ecol.*, vol. 16, no. s1, pp. S122–S135, Apr. 2012.

[17] M. J. (Mariska) de Wild-Scholten, “Energy payback time and carbon footprint of commercial photovoltaic systems,” 2013.

[18] S. Philipps and W. Warmuth, "©Fraunhofer ISE: Photovoltaics Report, updated: 6 June 2016," 2016.

[19] S. Pothecary, "Kaneka achieves new efficiency record for a practical size crystalline silicon PV cell," *PV Magazine*, 2016. [Online]. Available: http://www.pv-magazine.com/news/details/beitrag/kaneka-achieves-new-efficiency-record-for-a-practical-size-crystalline-silicon-pv-cell_100026182/#axzz4O8WGAFe5.

[20] M. Osborne, "SunPower lab produced solar cells used in 24.1% module efficiency record | PV-Tech," *PV-Tech*, 2016. [Online]. Available: http://www.pv-tech.org/news/sunpower-lab-produced-solar-cells-used-in-24.1-module-efficiency-record.

[21] H. Sverdrup, D. Koca, and K. V. Ragnarsdottir, "Investigating the sustainability of the global silver supply, reserves, stocks in society and market price using different approaches," *Resour. Conserv. Recycl.*, vol. 83, pp. 121–140, 2014.

[22] T. Kenning, "PV Cycle achieves record 96% recycle rate for silicon-based PV modules. | PV-Tech," *PV-Tech*, 2016. [Online]. Available: http://www.pv-tech.org/news/pv-cycle-achieves-record-96-recycle-rate-for-silicon-based-pv-modules.

[23] J. Zhao, A. Wang, P. Altermatt, and M. A. Green, "Twenty-four percent efficient silicon solar cells with double layer antireflection coatings and reduced resistance loss," *Appl. Phys. Lett.*, vol. 66, no. 26, p. 3636, 1995.

[24] ZSW, "ZSW Sets New World Record for Thin-film Solar Cells CIGS PV's efficiency ratings rising fast," 2016.

[25] H. Sai *et al.*, "Triple-junction thin-film silicon solar cell fabricated on periodically textured substrate with a stabilized efficiency of 13.6%," *Cit. Appl. Phys. Lett. Appl. Phys. Lett. Appl. Phys. Lett. Appl. Phys. Lett*, vol. 106, no. 96, pp. 213902–213504, 2015.

[26] A. Louwen, W. van Sark, R. Schropp, and A. Faaij, "A cost roadmap for silicon heterojunction solar cells," *Sol. Energy Mater. Sol. Cells*, vol. 147, pp. 295–314, Apr. 2016.

[27] "EnergyTrend PV."

[28] J. Zhao, A. Wang, and M. A. Green, "High-efficiency PERL and PERT silicon solar cells on FZ and MCZ substrates," *Sol. Energy Mater. Sol. Cells*, vol. 65, no. 1, pp. 429–435, 2001.

[29] C.-W. Chen, R. Hao, V. D. Upadhyaya, T. S. Ravi, and A. Rohatgi, "Development of high-efficiency large-area screen-printed solar cells on direct kerfless epitaxially grown monocrystalline Si wafer and structure," *Prog. Photovoltaics Res. Appl.*, vol. 24, no. 8, pp. 1133–1141, Aug. 2016.

[30] J. E. Cotter, J. H. Guo, P. J. Cousins, M. D. Abbott, F. W. Chen, and K. C. Fisher, "P-type versus n-type silicon wafers: Prospects for high-efficiency commercial silicon solar cells," *IEEE Trans. Electron Devices*, vol. 53, no. 8, pp. 1893–1901, 2006.

[31] H. Fischer and W. Pschunder, "Investigation of photon and thermal induced changes in silicon solar cells," in *10th IEEE Photovoltaic Specialists Conference*, 1973.

[32] J. Lindroos and H. Savin, "Review of light-induced degradation in crystalline silicon solar cells," *Sol. Energy Mater. Sol. Cells*, vol. 147, pp. 115–126, 2016.

[33] "International Technology Roadmap for Photovoltaic (ITRPV)," 2016.

[34] D. M. Powell, J. Hofstetter, D. P. Fenning, R. Hao, T. S. Ravi, and T. Buonassisi, "Effective lifetimes exceeding 300 μs in gettered p-type epitaxial kerfless silicon for photovoltaics," *Appl.*

Phys. Lett., vol. 103, no. 26, p. 263902, Dec. 2013.

[35] M. Drießen *et al.*, "Solar Cells with 20% Efficiency and Lifetime Evaluation of Epitaxial Wafers," *Energy Procedia*, vol. 92, pp. 785–790, 2016.

[36] E. Kobayashi, Y. Watabe, R. Hao, and T. S. Ravi, "High efficiency heterojunction solar cells on n-type kerfless mono crystalline silicon wafers by epitaxial growth," *Appl. Phys. Lett.*, vol. 106, no. 22, p. 223504, Jun. 2015.

[37] M. A. Green, K. Emery, Y. Hishikawa, W. Warta, and E. D. Dunlop, "Solar cell efficiency tables (Version 45)," *Prog. Photovoltaics Res. Appl.*, vol. 23, no. 1, pp. 1–9, Jan. 2015.

[38] R. H. I. Kuzma-Filipek, M. Recamán, F. Duerinckx, TS. Ravi1, M. E. Cornagliotti, P. Choulat, A. Sharma, J. John, and J. S. & J. P. Aleman, L. Tous, R. Russell, A. Uruena, "22.5% n-PERT Solar Cells on Epitaxially Grown Silicon Wafers," in *EUPVSEC Proceedings*, 2016.

[39] H. S. Radhakrishnan *et al.*, "Improving the Quality of Epitaxial Foils Produced Using a Porous Silicon-based Layer Transfer Process for High-Efficiency Thin-Film Crystalline Silicon Solar Cells," *IEEE J. Photovoltaics*, vol. 4, no. 1, pp. 70–77, Jan. 2014.

[40] S. R. S. Janz, N. Milenković, M. Drießen, "N-Type and P-Type Silicon Foils Fabricated in a Quasi-Inline Epi Reactor with Bulk Lifetimes Exceeding 500 Mμs," in *EUPVSEC Proceedings*, 2015.

[41] B. Hekmatshoar, D. Shahrjerdi, M. Hopstaken, J. A. Ott, and D. K. Sadana, "Characterization of thin epitaxial emitters for high-efficiency silicon heterojunction solar cells," *Appl. Phys. Lett.*, vol. 101, no. 10, p. 103906, 2012.

[42] R. Cariou, "Epitaxial growth of Si(Ge) materials on Si and GaAs by low temperature PECVD: towards tandem devices," PhD thesis, Ecole Polytechnique, 2015.

[43] E. Wesoff, "Beamreach Unstealths (Again) With Lightweight PV Module for Commercial Roofs | Greentech Media," *Greentech Media*, 2016. [Online]. Available: http://www.greentechmedia.com/articles/read/Beamreach-Unstealths-Again-With-Light-Weight-PV-Module-For-Commercial-Roo.

[44] P. J. Cousins and J. E. Cotter, "The influence of diffusion-induced dislocations on high efficiency silicon solar cells," *IEEE Trans. Electron Devices*, vol. 53, no. 3, pp. 457–464, Mar. 2006.

[45] F. Gaiseanu, J. Esteve, G. Kissinger, and D. Kruger, "Diffusion-induced dislocations in highly boron-doped silicon layers used for bulk micromachining applications," in *Proc. SPIE 3511, Micromachining and Microfabrication Process Technology IV, (31 August 1998)*, 1998, pp. 88–96.

[46] M. A. Kessler, T. Ohrdes, B. Wolpensinger, and N.-P. Harder, "Charge carrier lifetime degradation in Cz silicon through the formation of a boron-rich layer during BBr3 diffusion processes," *Semicond. Sci. Technol.*, vol. 25, no. 5, p. 55001, May 2010.

[47] S. Werner *et al.*, "Optimization of BBr3 diffusion processes for n-type silicon solar cells," *31st Eur. PV Sol. Energy Conf. Exhib.*, vol. 1, no. September, pp. 14–18, 2015.

[48] B. Singha and C. S. Solanki, "Impact of a boron rich layer on minority carrier lifetime degradation in boron spin-on dopant diffused n -type crystalline silicon solar cells," *Semicond. Sci. Technol.*, vol. 31, no. 3, p. 35009, Mar. 2016.

[49] T. Rachow *et al.*, "Solar Cells with Epitaxial or Gas Phase Diffused Emitters Above 21% Efficiency," *Energy Procedia*, vol. 77, pp. 540–545, Aug. 2015.

[50] M. Recamán Payo, N. Posthuma, A. de Castro, M. Debucquoy, and J. Poortmans, “Boron-doped selective silicon epitaxy: high efficiency and process simplification in interdigitated back contact cells,” *Prog. Photovoltaics Res. Appl.*, vol. 22, no. 7, pp. 711–725, 2014.

[51] “International Technology Roadmap for Photovoltaic - 2015 Edition.” .

[52] T. Rachow *et al.*, “Potential and limitations of epitaxial emitters,” *28th Eur. Photovolt. Sol. Energy Conf. Exhib.*, no. October, pp. 28–31, 2013.

[53] J. Symons, J. Nijs, and R. P. Mertens, “The emitter-base interface current in silicon bipolar transistors with emitters deposited by plasma-enhanced {CVD},” *{IEEE} Trans. Electron Devices*, vol. 36, no. 12, pp. 2889–2894, 1989.

[54] C. Gong, K. Van Nieuwenhuysen, N. E. Posthuma, E. Van Kerschaver, and J. Poortmans, “Another approach to form p+ emitter for rear junction n-type solar cells: Above 17.0% efficiency cells with CVD boron-doped epitaxial emitter,” *Sol. Energy Mater. Sol. Cells*, vol. 95, no. 1, pp. 11–13, 2011.

[55] T. Rachow, N. Milenkovic, S. Janz, and S. Reber, “Formation of High Efficiency Epitaxial Emitters by APCVD,” *Energy Procedia*, 2012.

[56] N. Milenkovic, “Simulation and Characterization of Epitaxial n- and p-Type Emitters on Silicon Wafer Solar Cells,” *Energy Procedia*, 2012.

[57] I. Kuzma-Filipek *et al.*, “Simplified cleaning for 22.5% nPERT solar cells with rear epitaxial emitters,” *Sol. Energy Mater. Sol. Cells*, pp. 1–5, 2016.

[58] R. Hao *et al.*, “Kerfless Epitaxial Mono Crystalline Si Wafers With Built-In Junction and From Reused Substrates for High-Efficiency PERx Cells,” *IEEE J. Photovoltaics*, pp. 1–5, 2016.

[59] L. Chen *et al.*, “Effect of oxygen precipitation on the performance of Czochralski silicon solar cells,” *Sol. Energy Mater. Sol. Cells*, vol. 95, no. 11, pp. 3148–3151, Nov. 2011.

[60] J. D. Murphy, M. Al-Amin, K. Bothe, M. Olmo, V. V. Voronkov, and R. J. Falster, “The effect of oxide precipitates on minority carrier lifetime in n-type silicon,” *J. Appl. Phys.*, vol. 118, no. 21, p. 215706, Dec. 2015.

[61] D. Franke, “Rise of dislocation density in crystalline silicon wafers during diffusion processing.”

[62] M. Labrune, M. Moreno, and P. Roca i Cabarrocas, “Ultra-shallow junctions formed by quasi-epitaxial growth of boron and phosphorous-doped silicon films at 175°C by RF-PECVD,” *Thin Solid Films*, 2010.

[63] V. Steckenreiter, J. Hensen, A. Knorr, S. Kajari-Schroder, and R. Brendel, “Reuse of Substrate Wafers for the Porous Silicon Layer Transfer,” *IEEE J. Photovoltaics*, vol. 6, no. 3, pp. 783–790, May 2016.

[64] J. Govaerts *et al.*, “Solar Cells from Epitaxial Foils: An Epifoil Epiphany,” *Energy Procedia*, vol. 77, pp. 871–880, 2015.

[65] K. H. Yang, “An Etch for Delineation of Defects in Silicon,” *J. Electrochem. Soc.*, vol. 131, no. 5, p. 1140, 1984.

2. Definition of process conditions for low-temperature epitaxy by PECVD using $SiF_4/H_2/Ar$ gas mixtures

2.1. State of the art of low-temperature epitaxy

The first use of PECVD for growth of epitaxial films was reported in the early 1980s by Itoh's and Reif's research groups. At that time, the aim was to reduce the diffusion of impurities by reducing the process temperature and to increase the deposition rate of conventional CVD. By doing so, they reached growth rates of tens of Å/s at substrate temperatures from 750°C to 800°C [1]–[3]. It should be mentioned that the term "low temperature" is completely subjective. In some publications "low-temperature epitaxy" (LTE) can refer to process temperatures higher than 700°C. In our case we will use this naming for processes below 400°C.

2.1.1. Overview of techniques used for LTE

A lot of techniques have been applied to grow monocrystalline silicon thin films at low temperature. Some studies have reported that low temperature epitaxy by molecular beam epitaxy (MBE) faces a systematic thickness limit before epitaxy breaks down when the substrate temperature is kept in the range from room temperature to 200°C [4],[5]. While some publications report the same problem associated to critical thickness with PECVD, other groups have shown that the use of plasma allows to grow thick epitaxial layers (> 5 µm) at 200°C [6]. It should be noted that this is more a practical limit, due to the impossibility to make deposition over more than one day, rather than a scientific threshold above which an epitaxy breakdown is observed.

The use of low temperature epitaxy (< 400°C) in a PECVD reactor was reported for the first time in 1987 by Shibata *et al.* [7]. They were investigating new ways to grow crystalline materials for the manufacturing of very large scale integrated circuits with very abrupt junctions. They showed that epitaxial growth could occur at 300°C using a non-conventional deposition method: the hydrogen radical enhanced chemical vapor deposition (HR-CVD). Interestingly, they were already using a $SiF_4/H_2/Ar$ gas mixture and more generally the use of fluorinated gases in the 80's is often reported in the literature. Using remote microwave plasma with a gas mixture composed of H_2 and Ar reacting with SiF_4 injected near the surface of the substrate, they showed that a highly ordered material with a low density of defects can be obtained at 300°C with interesting deposition rates of 10 to 20 Å/s. The hydrogen was considered as the growth control parameter influencing both the gas-phase reactions and the surface growth mechanisms. Thus, they demonstrated the role of hydrogen to be responsible for the amorphous to microcrystalline transition while epitaxial growth occurs in between [8]. From these studies they concluded that the competing reactions between deposition from SiH_nF_m ($n+m \leq 3$) gas precursors, induced by the reaction of SiF_4 with atomic hydrogen [8], and the etching by fluorine (F) led to the growth of a well ordered Si-Si network. They also investigated doped layers by

incorporating PH_3 and BF_3, and shown that conductivity of, respectively, 10^{-2} Ω.cm (mobility around 10 $cm^2/V.s$) and 1 Ω.cm could be achieved. It should be mentioned that in the case of boron doping, a minimum substrate temperature of 400°C was required, so their technique, in addition to being difficult to scale up, is not adapted for the growth of boron-doped epi-layers at low temperature.

Besides, in the same period, Shibata and Ohmi [9]–[11] also investigated the feasibility of silicon epitaxy by sputtering. They used a 100 MHz plasma under an argon atmosphere at low pressure (10^{-4} mTorr), associated to a DC bias on the silicon target (to tune the deposition rate) and a DC bias on the substrate holder (to vary the ion bombardment energy) heated at 250°C. They found an optimum for the ion bombardment energy to be 25 eV. They demonstrated a n-type defect-free epitaxy at a deposition rate around 1 Å/s, with a very smooth surface and "device grade performances" (reverse bias currents of a few nA/cm^2). They claimed a 100% doping efficiency with a carrier concentration of $1.9.10^{18}$ cm^{-3} (concentration of the doped target) for a mobility of 160 $cm^2/V.s$. However they did not assess the homogeneity and the measurement for the reverse current is done on a 1x1 mm^2 area. This technique is also said to require the use of ultra clean processing environment and ultra clean wafer surface [11], which is hardly suitable for PV industry.

Electron cyclotron resonance PECVD (ECR-PECVD) has also been used to produce mono c-Si thin films but it encountered systematic epitaxy breakdown after a low thickness limit. The limit has been found to be 500 nm at 360°C by Varhue *et al*. [12]. Platen *et al.* obtained similar results at 325°C by observing a slow crystalline to amorphous transition beyond critical thickness of approximately 500 nm [13]. They also observed a critical limit thickness on <111> oriented substrates to be 35 nm at this temperature. By increasing the temperature to 525°C, epitaxial films with thicknesses beyond 1.5 µm (on Si(100)) have been reported [14]. In that case a mobility value of 600 $cm^2/V.s$ for non-intentionally doped n-type silicon epi-layers at 2.10^{17} cm^{-3} was reached. Alike sputtering, they also found that a plasma potential above 25 V deteriorates the film structural properties. Rau *et al.* similarly obtained above 2 µm thick epi-layers from 510°C with a growth rate around 3 Å/s [15],[16].

In addition, Rosenblad *et al.* [17] investigated the low-energy DC PECVD applied to Si homoepitaxy. In a low pressure plasma (around 10 mTorr) composed of SiH_4/H_2 gas mixtures they showed that the bombardment of ions with energies higher than 15 eV leads to the formation of stacking faults in epitaxial films grown between 400°C and 600°C. They also claimed the hydrogen adsorption as a cause for stacking faults formation by limiting the surface mobility of Si atoms. The consequence of these two effects is the accumulation of surface roughness which favors the nucleation of stacking faults after a critical level.

Finally, it is worth noticing that the use of plasma is not necessary to grow crystalline thin films at such low temperature. In the same period, also Japanese research teams [18],[19] reported epitaxial growth using photochemical vapor deposition (photo-CVD). The energy is provided by a UV source (λ=253.7 nm) radiating the substrate in presence of gas precursors allowing their dissociation. Even though at the beginning of the development of this technique the growth rate was low (< 0.3 Å/s) [20], they demonstrated the growth around 200°C of 500 nm thick layers at a rate of 2 Å/s. With a gas mixture composed of SiH_4, H_2, SiH_2Cl_2 and B_2H_6 they achieved doping concentration up to 10^{20} cm^{-3}. However to enhance the dissociation of SiH_4, the addition of a small amount of mercury vapor is required. Other publications report photo-CVD epitaxial growth without mercury sensitivation but to our knowledge it requires a growth temperature above 600°C [21], [22].

2.1.2. RF-PECVD for LTE

In 1987 Nagamine *et al.* [20] demonstrated for the first time LTE using conventional radio frequency-PECVD (RF-PECVD) reactors, using a power supply with a frequency of 13.56 MHz which is the standard in the industry. By using a <100> oriented boron-doped silicon substrate heated at 250°C they achieved the growth of a 120 nm thick epitaxial layer from a gas mixture of SiH_4, SiH_2F_2 and H_2. They were working at pressure of 1 and 3 Torr and achieved growth rates around 0.7 Å/s and 1.2 Å/s respectively. The low temperature of the process made possible a very abrupt transition between the highly boron doped substrate and the epi-layers. SIMS (secondary ion mass spectrometry) measurement showed that at the epi-substrate interface a variation of boron is only visible along 15 nm. It either means that the diffusion occurs on these 15 nm or that the SIMS resolution is within this range, not clear explanation was provided. One year later, Uematsu *et al.* [23] extended the use of RF-PECVD to phosphorus doped (n^+) epitaxial growth. Besides, they used more standard $SiH_4/H_2/PH_3$ gas mixtures for their epitaxial growth, instead of full or partial fluorinated gas chemistries, and reached a minimum resistivity of 4.10^{-4} Ω.cm, corresponding to a doping concentration of 2.10^{20} cm^{-3}, with a mobility of 10 $cm^2/V.s$. The pressure used was 0.6 Torr and the power density 0.25 W/cm^2 which is relatively high and close to what used in this PhD work. However the deposition rate was lower than 0.4 Å/s and they limited the epitaxial layers thickness to 200 nm. In the same period, in the US, similar studies were led at Xerox [24]. They used pure SiH_4/H_2 gas mixtures and showed that fully crystalline growth could occur at temperature below 300°C, also in a conventional PECVD reactor and achieved up to 1 µm thick epitaxial layers. They suggested that instead of a slow deposition rate, etching promoted by H radicals was the main requirement for crystalline growth. They also showed that the defect density was clearly dependent on the temperature and that epitaxial films free of H platelets (accumulation of hydrogen in the {111} planes) were obtained only for films with growth temperature above 350°C [25]. In addition, they showed, by substituting H_2 by deuterium (D_2) in the gas mixtures, that the origin of H platelets was due to the hydrogen incorporated via SiH_x radicals rather than H_2.

In the early 90's, IMEC started to study low temperature epitaxy. Baert *et al.* [26], obtained interesting results on the low temperature epitaxy by RF-PECVD in the 200-400°C range. They first reached phosphorus concentrations up to 10^{21} cm^{-3} in epitaxial silicon [26], claiming a full activation of dopants leading to a mobility of 9 (+/- 3) $cm^2/V.s$. However no significant mobility improvement was observed when doping concentration was lowered to 6.10^{19} cm^{-3}. They already claimed a deposition rate of 1.5 Å/s at a pressure of 3 Torr, i.e. similar at what we used in this PhD work. One year later [27], they succeeded a selective epitaxy by the use of a mixture of SiH_4 and SiF_4, the SiH_4 flow rate controlling the deposition rate and the SiF_4 one controlling the process selectivity. Thus on a patterned dielectric layer deposited on a c-Si substrate, they can selectively grow epitaxial silicon on open areas (crystalline) while on the dielectric (amorphous) material no deposition occurs, not even amorphous. They assumed the selectivity of the process was possible due to the etching by fluorinated species of the less stable amorphous phase (which is deposited on the oxide, an amorphous material) than the epitaxial silicon on the crystalline area (open areas). To achieve this, they had to work at low pressure (50 mTorr, i.e. 2 orders of magnitude lower than what we worked with) and the deposition rate is only 0.6 Å/s.

Later, LTE by PECVD has been extended to boron doped layers on Si(100) and investigated on Si(111) with $SiH_4/H_2/B_2H_6$ gas mixtures. Schwarzopf *et al.* [28] demonstrated excellent quality boron-doped epi-layers grown at 400°C on Si(100) but with a low deposition rate of 0.1 Å/s while the RF power density was high (0.31 W/cm^2). They also showed that fully crystalline growth on Si(111) was

possible at this temperature but with a high level of defects, a disorder level of 1 was deducted from Rutherford backscattering spectrometry (RBS). The feasibility of epitaxy on Si(111) was attributed to the boron doping since intrinsic growth does not work in the same conditions. They also demonstrated a strong correlation between disorder level and H concentration. They assumed that defects acts as "sinks" for H, resulting in higher H concentrations in bad quality epi-layers.

While publications referring to LTE for microelectronics slowed down in the 2000's, it started to gain interest for solar cells since then. Thus, in 2002 Pla *et al.* [29] demonstrated a 13.1% efficient solar cell using VHF-PECVD for the formation of p^+ emitter and intermediate intrinsic epi-layer around 200°C. While the J_{SC} was 4 mA/cm^2 higher than the reference (standard (i) a-Si:H and (p^+) µc-Si:H)) the V_{OC} was 80 mV lower. It is worth noticing that they directly deposited indium-tin-oxide (ITO) at the top of the p^+ epi-layer. Therefore we can expect better results by using a proper passivation layer. Then Farrokh-Baroughi and Sivoththaman [30] used PECVD with $SiH_4/H_2/PH_3$ gas mixtures at 250°C for the formation of (n^+) emitter in a c-Si solar cell without using TCO but a SiN_x anti-reflective coating and reached an efficiency exceeding 10% with a V_{OC} near 600 mV. Later, with the same chemistry, above 13.5% efficient solar cells with a simple ITO / (n^+) c-Si / (p) c-Si / rear contact structure was achieved with growth at both room temperature and 200°C [31]. They reached V_{OC} above 600 mV in both cases with a carrier concentration of 3.10^{18} cm^{-3} and an emitter thickness of 160 nm. Interestingly, although cross-sectional TEM images and diffraction patterns of the bulk region of epitaxial layers show a high density of twins and stacking faults at 200°C and a low doping efficiency of 4%, they achieved relatively high performances for cells with low temperature epitaxial emitters. Surprisingly, for their conditions, by lowering the process temperature to room temperature, twins and stacking faults disappeared. It should be mentioned though that the area of the cell was not exceeding 4x4 mm^2. If all these solar cells have been done on flat <100> oriented silicon (Si(100)) solar cell, it has been shown that efficiency of 13.8% can be achieved with a 50 nm (n^+) quasi epi-emitter grown on a textured p-type wafer [32], meaning on <111> oriented surfaces. The emitter was grown at 300°C by $SiH_4/H_2/PH_3$ chemistry and incorporated in a simple architecture: Al (front grid) / SiN_x:H / 50 nm (n^+) Quasi-epitaxial Si / textured p-type Cz / Al (back contact). However, the layer looks highly defective in TEM images and due to epitaxy breakdown into an amorphous phase, the architecture is more similar to a heterojunction cell with 5 to 10 nm of (defective) epitaxy.

The use of epitaxial layers as intermediate layer between bulk and amorphous layer in silicon heterojunction (SHJ) solar cells has also been investigated. In 2002, Pla *et al.* firstly showed that a 12.8% efficient solar cell could be achieved by introducing an intrinsic epi-layer between the wafer and the (p^+) a-Si:H layer. More recently, Hekmatshoar *et al.* [33] investigated the benefits from introducing doped epitaxial layers in SHJ solar cells. They showed that by growing a 5 nm thin phosphorus doped epitaxial layer between the wafer and the (n^+) doped amorphous silicon layer ((n^+) a-Si:H), it results in a rise of open circuit voltage (V_{OC}) from 620 mV to 650 mV, reaching an efficiency of 21.4%. The improvement of electrical properties is attributed to an enhanced field effect and an increased incorporation of hydrogen at the interface with the wafer. The optimum thickness of 5 nm is considered as a trade-off between advantages mentioned above, which tends to adopt a thick epi-layer, and the limitations due to Auger recombination, which favors the use of a thin epi-layer. The hole lifetime in this n^+ epitaxial layer with a majority carrier concentration $N_D=5.10^{19}$ cm^{-3} has been assessed to be around 100 ps, corresponding to a hole diffusion length of 200 nm, therefore only three times shorter than for n^+ c-Si with the same doping level [34]. The difference is explained by the higher defect density in the low temperature grown epitaxial layers. By moving to n-type wafers, the optimum thickness moves to 7.5 nm but the efficiency is maintained at 21.4% [35]. More recently, Carrere *et al.* [36] studied via numerical simulations the effect of the addition of a thin and highly

doped (p^+) or (n^+) c-Si layer at the (i) a-Si:H/substrate interface on the performances of HIT™ solar cells. While the (n^+) c-Si layer does not show significant enhancement on the cell efficiency, the (p^+) c-Si layer could improve it by almost 1% absolute (simulated). This is attributed to a better field effect passivation [36] and a reduction of contact resistance [37] resulting in a higher V_{OC} and FF. The improvement of performances on manufactured solar cells via this approach has been confirmed [37] but the process flow relies on high temperature processes (950°C) for the activation of the boron implanted by plasma immersion. This can lead to a decrease of the bulk lifetime due to the damage of the substrate because of the high thermal budget [38].

The first work on LTE at LPICM resulted from observations of the interface between c-Si bulk and a-Si:H layer for the formation of heterojunction solar cells [39],[40]. In some conditions, instead of a perfectly abrupt junction, a local epitaxial growth can occur along a few nm at this interface leading to a significant drop of V_{OC}. Other research groups [41],[42] also mentioned this negative effect of local epitaxial growth during the deposition of the passivation layer and try to find solutions to avoid this phenomenon. The LPICM has developed a strong expertise in the optimization of this interface and has brought new elements of understanding allowing to either obtain abrupt interface (without epitaxy) or, at the complete opposite, to grow several microns of epitaxial silicon.

Subsequently, a lot of research has been led to perform silicon epitaxy on various substrates such as Si, Ge and GaAs [43]–[45] paving the way to the manufacturing of multi-junction solar cells. So far, low temperature silicon epitaxy was mainly used at LPICM for manufacturing crystalline silicon absorbers. This application requires several µm thick epitaxial films to favor light absorption. It has been demonstrated that solar cells with good electrical properties could be obtained with several microns thick absorbers grown by RF-PECVD at 200°C [46]. In particular Cariou *et al.* widely studied and optimized silicon epitaxy by PECVD using SiH_4/H_2 chemistry. They achieved a 8.5% efficient solar cell using ~5 µm thick epitaxial layers as absorber, thus showing the good quality of the material [46] and a 7.3% efficient solar cell with a reported (lift-off) epi-Si bulk on glass [6]. The minority carrier lifetime reached in these layers is not easy to evaluate, it has been assessed by time resolved microwave conductivity (TRMC) that the bulk lifetime was around 10 µs. Recent results obtained by Kelvin probe force microscopy on the cross section of an epitaxial silicon solar cell under modulated frequency electrical bias have provided similar results [47]. While microwave detected photoconductance decay technique (µ-PCD) showed this lifetime to be in the range of 50-150 µs [43]. The use of LTE with SiH_4/H_2 gas mixtures has been extended to the formation of doped layers in c-Si solar cells. Thus Labrune *et al.* reported on a 14.2% efficient solar cell with a p-type low temperature emitter using a $SiH_4/H_2/B_2H_6$ gas mixture [48], incorporated in homo-heterojunction solar cell: a front contact (Ag) / ITO/ (p^+) epi-Si / (n) c-Si/(i) pm-Si:H / (n) a-Si:H / ITO / rear contact (Al).

In parallel, several studies on microcrystalline silicon (µc-Si:H) at LPICM have revealed the strong potential of the $SiF_4/H_2/Ar$ chemistry. A higher crystallinity and lower defect density have been obtained by using silicon tetrafluoride (SiF_4) precursors instead of silane [49],[50]. Dornstetter demonstrated a record V_{OC} of 553 mV in a µc-Si:H solar cell [51]. Besides, SiF_4 chemistry allows to reduce the amount of oxygen incorporated into the layers [52], which should enhance the quality of epitaxy. Moreno *et al.* [53] have already demonstrated the strong potential of SiF_4 for epitaxial growth by RF-PECVD, in particular due to the very smooth interface which is possible to achieve. Dornstetter *et al.* [50],[54],[55] also provided a better understanding on the plasma reactions showing the influence of the H_2 depletion on the amorphous to microcrystalline transition with this chemistry [56]. This PhD work addresses the use of SiF_4 instead of SiH_4 to investigate the potential for low temperature epitaxial emitter based on the better understanding of gas-phase reactions in $SiF_4/H_2/Ar$ plasmas.

2.2. Experimental setup

This chapter is devoted to the definition of the conditions required to perform intrinsic epitaxy. Firstly, it allows to define a process window which makes a process transfer and scale-up much easier. Secondly, to separate the effect of gas dopant on the epitaxial growth, required to manufacture doped epi-layers, it is first necessary to understand the conditions of epitaxy breakdown for intrinsic material. This part brings insights on the understanding on low temperature epitaxy and epitaxy breakdown, putting apart the influence of dopant gas on the crystalline growth, which will be studied in **Chapter 4**.

2.2.1. Basics of PECVD

In this section we detail the principle of a capacitively coupled PECVD reactor, which is the most common PECVD reactor found in the industry. As previously said, the use of plasma allows to dissociate gases which are stable at the PECVD working temperature.

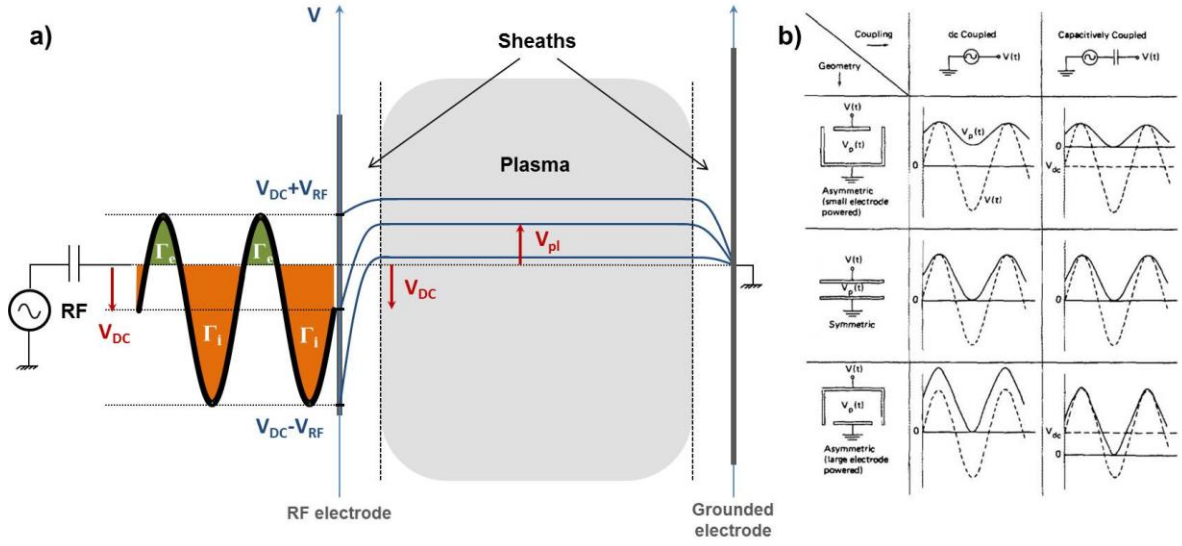

Fig. 2.1 – a) Illustration of the principle of DC self-bias voltage for asymmetric discharge. b) Illustration of plasma potential (V_{pl}), excitation electrode voltage and DC self-bias voltage for three designs with DC and capacitive coupling [79].

The gas dissociation, due to the collision of electrons with gas molecules, induces the formation of reactive species which will contribute to the deposition. For that, gases are injected in a chamber and the pressure is regulated to be typically in the range 20 mTorr to a few Torr. In this chamber two parallel electrodes face each other and are separated by a few centimeters (typically from 10 mm to 50 mm). A sinusoidal radio-frequency (RF) voltage, with a frequency of 13.56 MHz is applied to one electrode (RF electrode) while the other (where the substrate is lying) is grounded. The 13.56 MHz frequency (and its harmonics) is a worldwide standard frequency established by the International

Telecommunications Union in 1947, chosen to avoid disruption with radio communications. The RF excitation induces the ionization of gas between the two electrodes where the glow discharge occurs.

The plasma ignition is induced by the electrical excitation applied to the RF electrode. Given that electrons are much lighter than ions, the electron flux is larger than that of ions. The electron and ion fluxes, Γ_e and Γ_i respectively, are given by:

$$\Gamma_e = \frac{n_0}{4}\sqrt{\frac{8kT_e}{\pi m_e}}$$

and

$$\Gamma_i = \frac{n_0}{4}\sqrt{\frac{8kT_i}{\pi m_i}}$$

where $n_0=n_i=n_e$, k is the Boltzmann constant, T_e and T_i the electron and ion temperature, m_e and m_i electron and ion mass.

As an example, the ratio of mass between ions and electrons (m_i/m_e) in a hydrogen plasma is 1836. This induces that at the ignition of the plasma, electrons are lost to the walls which hence induces a potential drop. To have a stable discharge, the condition $\Gamma_e=\Gamma_i$ needs to be satisfied. As a result, a positive charge space region between the plasma and the walls is created, called the sheath, in such a way that the electrons are confined in the plasma and the ions are accelerated towards the surfaces. This allows to equalize the electron and ions fluxes ($\Gamma_e= \Gamma_i$) on a RF cycle.

At the frequency of RF discharges (13.56 MHz), the electrons are much more mobile than ions. The plasma pulsation ω_p, which corresponds to the maximum pulsation to which a species respond to the plasma, is defined by:

$$\omega_p = \sqrt{\frac{n_0 e^2}{m\varepsilon_0}}$$

where n_0 is the density of the species (electron or ion), m its mass, e the charge of an electron, and ε_0 the vacuum permittivity.

In most of cases, the plasma pulsation of ions is lower than the RF pulsation while it is higher for electrons. As a consequence, electrons instantaneously follow the RF oscillations while ions only respond to the average RF electric field.

It means that for the (positive) first half period of the RF cycle a lot of electrons are attracted to the RF electrode while only a few of ions are attracted to the RF electrodes during the (negative) second half period due to their lower mobility. This situation would lead to the plasma stop because there would be no longer equilibrium between electron and ion density in the plasma, its neutrality would not be respected. Thus a self-bias voltage (V_{DC}) is developed on the RF electrode to "rectify" the RF voltage with a DC voltage for which ions can respond, to satisfy the condition $\langle\Gamma_e\rangle_t=\langle\Gamma_i\rangle_t$ on a full RF cycle (at every moment $\Gamma_e(t)$ and $\Gamma_i(t)$ are different but their integral over a RF period are equal). As shown in Fig. 2.1-a), the V_{DC} allows to compensate the lower mobility of ions by the longer time during which they are attracted to the RF electrode, while the electron flux towards the RF electrode occurs for a short time, when the potential barrier between the RF electrode and the plasma is low.

The formation of this self-bias voltage is possible due to the presence of a blocking capacitor between the RF electrode and the generator. Different architectures of reactors are shown in Fig. 2.1-b), leading to the formation (or not) of negative or positive self-bias. To roughly assess the values of this self-bias, the reactor can be simplified by an equivalent system as shown in Fig. 2.2. The relation between the potential at the RF electrode (V_E) and the plasma potential (V_{pl}) can be described by a voltage divider given that the sheath can be considered as a capacitance. Hence the relation between V_{RF} and V_E depends on the area of the capacitance and therefore on the area of the RF and grounded electrodes.

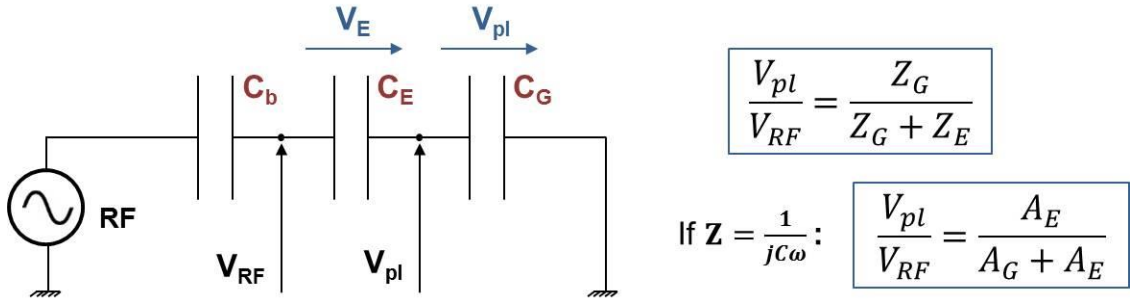

$$\frac{V_{pl}}{V_{RF}} = \frac{Z_G}{Z_G + Z_E}$$

$$\frac{V_{pl}}{V_{RF}} = \frac{A_E}{A_G + A_E}$$

Fig. 2.2 – Equivalent system of a CCP reactor with C_B the blocking capacitor, A_E the area of the RF electrode, A_G the area of the grounded electrode, V_{RF} the RF potential, V_{pl} the plasma potential, V_E the potential between the RF electrode and the plasma (V_E=V_{RF}-V_{pl}). Z_G and Z_E are respectively the impedance of the sheath at the grounded and RF electrode, and A_G and A_E the area of the grounded and RF electrode.

Thus in asymmetric reactors a strong difference between the V_{pl} and the V_{RF} is observed, controlled by the difference of V_{DC}. This also means that in symmetric reactors the amplitude of the V_{pl} is much higher than in asymmetric ones, which means that symmetric reactors are more likely to generate high energy ions impinging on the substrate (placed on the grounded electrode); this is a critical feature for the material properties of our films. It should be noted that even if RF and grounded electrodes have the same area, the walls of the reactor are also grounded, so even in symmetric reactors a DC self-bias voltage can be observed. Finally, it is worth noticing that in typical capacitive discharges the fractional ionization is about 10^{-6}-10^{-4}, meaning that most of gas is not ionized but only dissociated.

2.2.2. PECVD reactors

During this PhD, we worked on two different reactors: “Philix” and “Cluster”. Pictures of Philix are shown in Fig. 2.3. This is a research reactor with a 4-inch substrate holder diameter which operates from room temperature up to 300°C for the substrate holder (grounded electrode) and from room temperature to 200°C for the RF electrode. The pressure can be varied from 40 mTorr to 10 Torr. The surface of the RF electrode is 75 cm^2 and its power supply can deliver up to 100 W ($p_{RF,max}$=1.33 W/cm^2) at a frequency of 13.56 MHz (RF). A plasma box (Fig. 2.3-c)) is fixed to the reactor in order to contain the plasma and to avoid it to spread all over the chamber. Two holes have been drilled in the plasma box for the incident and the reflected light beam of ellipsometry and another one for the optical emission spectroscopy (OES) measurement. It is important to mention that in that case, the reactor is asymmetric, the grounded area is larger than the RF electrode, due to the presence of the plasma box. Thus, for Philix a significant DC self-bias voltage is expected.

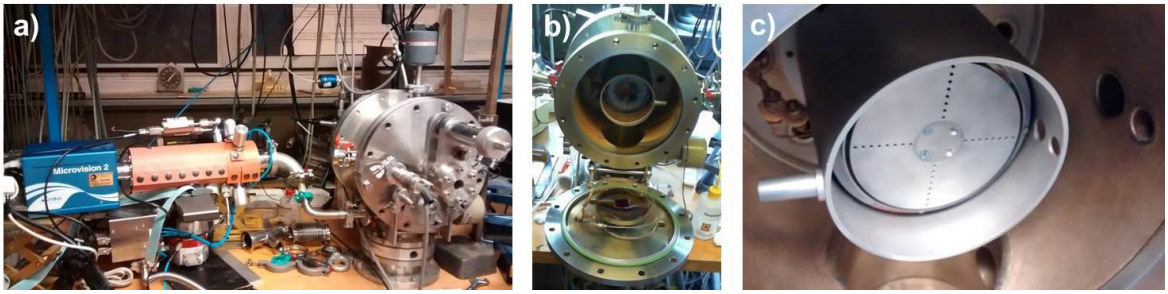

Fig. 2.3 – a) Picture of Philix PECVD reactor with the residual gas analyzer (RGA) connected on the left b) Picture of opened Philix with the substrate holder at the bottom c) Picture of the RF electrode and the plasma box with openings for ellipsometry and OES.

Philix has been used to define the process conditions for intrinsic epitaxy, subsequently transferred to the Cluster in which doped epitaxial layers were developed.

The Cluster (Fig. 2.4) is a semi-industrial tool connecting 6 PECVD chambers, one sputtering chamber with 3 targets (Ag, ITO, Al,…), one characterization chamber under vacuum, one load-lock and one internal transfer zone (ITZ) to transfer substrates from one chamber to another for depositing different materials without breaking the vacuum. It is worth noticing that in this case, samples are loaded in the PECVD chamber via a load-lock, contrary to Philix, reducing contamination and also increasing the reactor throughput. The process chamber operates from room temperature to 300°C for the substrate holder and from room temperature to 200°C for the RF electrode. The pressure can be varied from tens of mTorr to 10 Torr. The base vacuum before process is below 3.10^{-6} Torr. Contrary to Philix, there is no plasma box in the PECVD reactor and the chamber is symmetric, so no self-bias voltage should be expected as shown in Fig. 2.1. This has an impact on the transfer from one reactor to the other and in particular for the maximum power suitable for epitaxy. Given that surface of walls is not negligible with respect to that of electrodes a self-bias is nevertheless observed but is much lower (basically one order of magnitude lower) than in Philix.

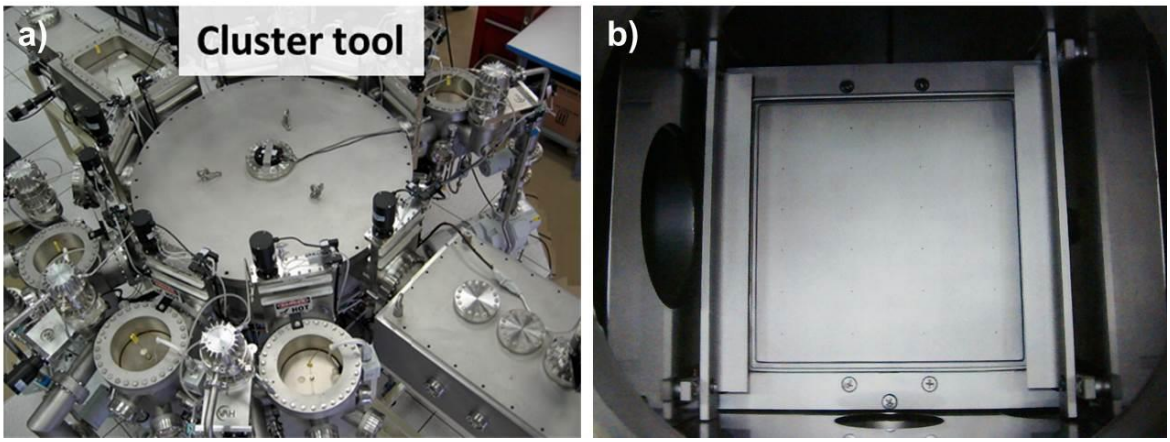

Fig. 2.4 – a) Picture of the cluster tool with 6 PECVD chambers, the characterization chamber on the right, the sputtering chamber at the top left corner and the ITZ in the center. b) Inside of a PECVD chamber, the bottom electrode is the RF electrode (on this picture) and the top electrode (not shown here) is the substrate holder lying on the racks (on the left and right).

2.2.2.1. *In situ* characterization

In addition to RF voltage (V_{RF}) and self-bias voltage (V_{DC}) measurements, *in situ* characterization tools are used to monitor the evolution over time of both plasma and material properties. The standard diagnosis tools used in plasma physics (Langmuir probe,…) are tricky to use in case of PECVD due to the deposition on the probe, thus affecting the quality of the measurement. This reduces the possible choice of characterization tools. We detail below the characterization techniques usually employed on the PECVD reactor.

Optical emission spectroscopy (OES) is a non-intrusive tool for the diagnosis of reactive plasma providing information about chemical species in the plasma. It measures the emission intensity which originates from electronically excited states of the species in the plasma. Given that the proportion of electronically excited species depends on the electron energy distribution function (EEDF), the intensity of emission is a function of both the density of the chemical species in the plasma and the EEDF [57]. This is a significant issue to study the influence of one parameter on the density of species since this parameter can change the density of plasma species and the EEDF as well. To tackle this, in most of experiments involving OES, the emission intensity of the species is compared to that of a noble gas, slightly added to the gas mixture and used as a reference. In most of cases it is argon (Ar). In our case Ar is the diluting gas so a variation of one parameter is hardly detectable on the Ar^+ signal. The equipment we used is a Maya2000 Pro spectrometer from Ocean Optics.

In addition to OES for the plasma characterization, a residual gas analyzer (RGA) has been connected to the reactor. It is used to detect the gas species at the outlet of the PECVD reactor. While driving quantitative conclusions from OES are not straightforward due to the interdependence of the parameters, this tool based on differentially-pumped mass spectrometry allows to easily estimate the species which are consumed (H_2, SiF_4,…) and formed (HF, SiF_x,…) in the reactive plasma. The principle is to compare the partial pressure of the gas species before and after plasma ignition. This approach considers the plasma as a "black box" and does not study in detail all the species (stable and unstable) present in the plasma but provides appropriate information on the plasma behavior for a process development and transfer. The RGA used is a Microvision 2 from MKS and is connected downstream the chamber, in the pumping gas line before the process pump (See Fig. 2.7). During this PhD it was mostly used to measure the H_2 depletion resulting from the reactions in the plasma, which has been correlated to material properties.

2.2.2.2. Spectroscopic ellipsometry

Spectroscopic ellipsometry (SE) is a very convenient tool for the optimization of process conditions for epitaxy. It allows a fast characterization of dielectric properties of the materials by comparing them to reference materials (c-Si, µc-Si:H, a-Si:H,…) or mathematical models (Tauc-Lorentz, Cauchy,…). It is based on the change of light polarization induced by the beam reflection on the sample. By comparing the spectra of the imaginary part of the pseudo-dielectric function ε_i from the grown materials to reference materials we can determine the thickness, the roughness and approximate the structural composition of the sample by using the Bruggeman effective medium approximation (BEMA). The spectra for c-Si, large and small grain poly-Si and a-Si [58] are shown in Fig. 2.5-a).

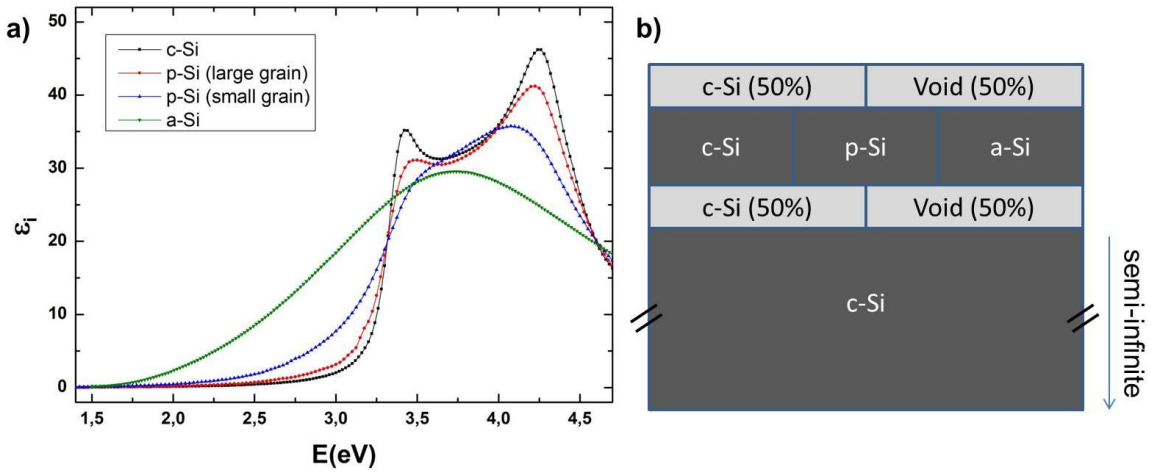

Fig. 2.5 – a) Imaginary part of the pseudo-dielectric function of c-Si, large and small grain poly-Si and a-Si. b) Model of the epitaxial layer grown on a c-Si substrate (semi-infinite medium) composed of an interface represented by a porous layer (50% of c-Si and 50% of void), a bulk composed of a mix of c-Si, poly-Si (large grain) and a-Si and a roughness also represented by a mix of 50% of c-Si and 50% of void.

It can be seen that the presence of grain boundaries in the film affects the absorption and so the pseudo-dielectric function, especially the height of the peaks at 3.4 eV and 4.2 eV which correspond to the Van Hove singularities of silicon. Fitting ellipsometry results with a model composed of different materials (c-Si, poly-Si, a-Si,…) provides information on the quality of the sample by extracting the fraction of each material. The model used for the characterization is shown in Fig. 2.5-b).

This model allows to take into account the potential interface between the epitaxial film and the substrate by representing it by a porous layer composed of a 50%/50% mix of c-Si and void. The 50%/50% mix is arbitrarily fixed, only the thickness of this interface layer is calculated in the model to avoid fitting on too many parameters. The deposited layer is modeled by a mix of c-Si, large grain poly-Si and a-Si. Practically, the amorphous fraction (F_a) often is equal to 0 and only the crystalline (F_c) and polycrystalline fractions (F_p) are needed to fit with the experimental data.

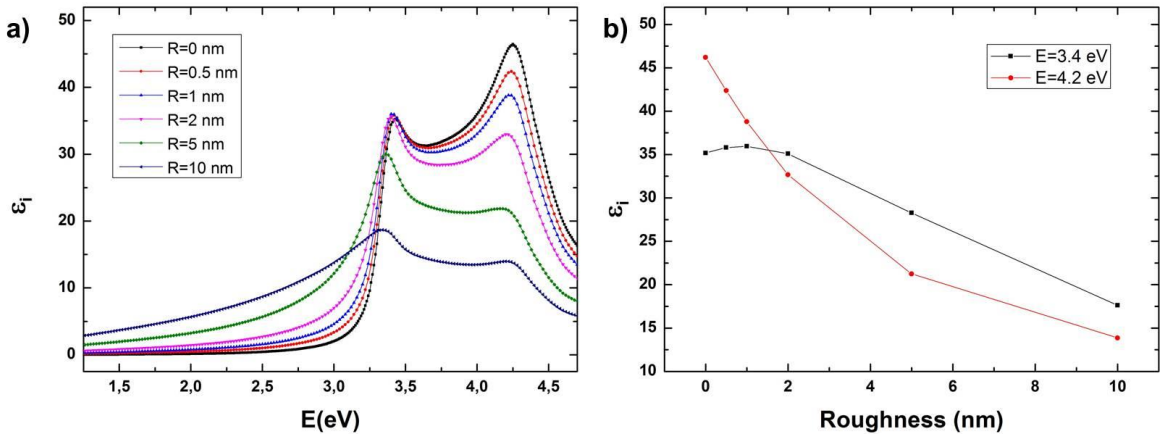

Fig. 2.6 – a) Simulated imaginary part of the pseudo-dielectric function of c-Si for different roughness values. The roughness has been modeled as a mix of c-Si and void (50%/50%), the value R corresponds to the thickness of this layer b) Evolution of the imaginary part of the pseudo-dielectric function at 3.4 eV (black) and 4.2 eV (red) as a function of roughness.

The presence of an interface can negatively affect the structural and electrical properties of the epitaxial film but it also allows to easily measure the thickness of the film and hence to deduce its deposition rate. In case of $SiF_4/H_2/Ar$, the interface is often undetectable by ellipsometry and the only solution is to use transmission electron microscopy (TEM). However, by purposely contaminating the surface of the c-Si on which the epitaxy takes place, for example thanks to a H_2 plasma or by exposing it to the air for a long time after hydrofluoric acid (HF) dip and prior to epitaxy, a deteriorated surface can be achieved and oscillations at low energy (0.7 – 2.5 eV) can be observed allowing to determine the thickness using the optical model and SE measurements.

The pseudo-dielectric function is affected by the crystallinity of the material but is also very sensitive to the roughness. As an example, the effect of roughness on a perfect c-Si substrate is shown in Fig. 2.6. This graph shows that by introducing a roughness of only 1 nm, ε_i(4.2eV) drops from 46 to 39 and down to 14 for a 10 nm roughness. However the first singularity at 3.4 eV is less affected by the roughness, and the latter needs to be above 2 nm to observe a significant difference in ε_i. These differences and the strong effect of roughness on ε_i(4.2eV) are related to the energy dependence of the absorption coefficient (α) and therefore to the penetration depth: ($1/\alpha\,|_{Si}$ (3.4eV) = 10 nm and $1/\alpha\,|_{Si}$ (4.2eV) = 5 nm).

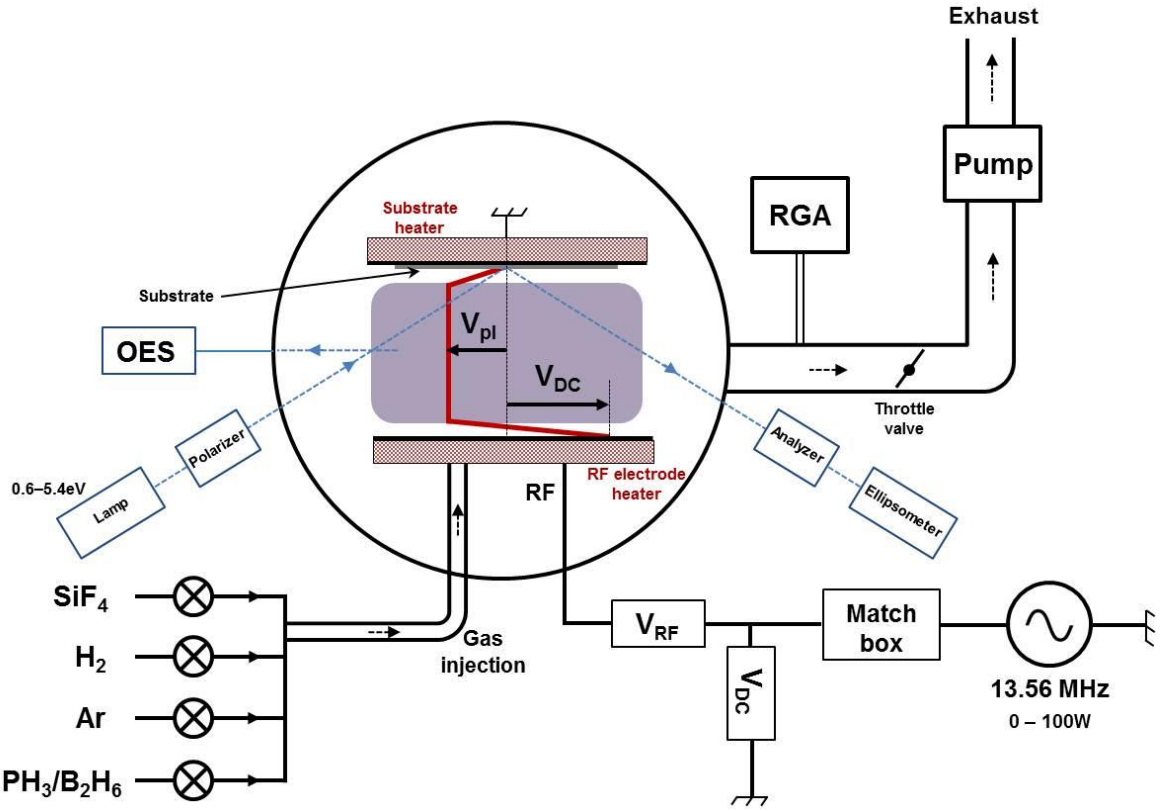

Fig. 2.7 – Schematic of a PECVD reactor with associated characterization techniques: probes for self-bias voltage (V_{DC}) and RF peak-to-peak voltage (V_{RF}), an *in situ* ellipsometer, an optical emission spectroscopy (OES) system and a residual gas analyzer (RGA).

Besides, ellipsometry can also be used *in situ*. This allows to monitor the evolution of the material optical properties during a process. Depending on the technology, the monitoring can be done at one single wavelength (ellipsometer with gratings) or for the full spectrum (CCD sensor). The first technology is used on Philix, an Uvisel 1 from Horiba Jobin Yvon is set up on the reactor, this

ellipsometer can only measure one wavelength at the same time. Most of the time, the energy of the light beam is chosen to be 4.2 eV, due to the high sensitivity of ε_i to surface properties at this energy. This allows to assess in real time the crystalline quality/roughness of the growing material. It will be shown in Chapter 3 that the temperature also has an effect on ε_i and in particular for both silicon singularities. A M-2000 Woollam ellipsometer is used on the Cluster. This ellipsometer uses a CCD camera to acquire the signal, thus the full spectrum (0.75-6.45 eV) can be obtained as a function of time. A summarizing schematic of the PECVD reactor with its associated *in situ* characterization tools is shown in Fig. 2.7.

2.2.2.3. Ex situ characterization techniques

In addition to *in situ* monitoring of the evolution of epi-layers optical properties, ellipsometry is also used *ex situ* to measure the imaginary part of the pseudo-dielectric function after deposition, at ambient air and room temperature. Other characterization techniques used *ex situ* are detailed below.

2.2.2.3.1. Raman spectroscopy

Raman spectroscopy allows to detect vibrational modes in materials by using a laser light interacting with molecules. From these interactions, Rayleigh scattering (same energy as excitation), Stokes Raman scattering (lower energy than excitation) and anti-Stokes Raman scattering (higher energy than excitation) can be observed. In our case, only Stokes Raman scattering will be considered from which we can extract the properties of a sample by deconvoluting the Raman signal by the transverse optical (TO) modes of a-Si:H at 480 cm^{-1} [59], [60] and c-Si at 520 cm^{-1} [61] (See Fig. 2.8-a)) and comparing their full width at half maximum (FWHM). The properties of the films are further analyzed by studying the incorporation of hydrogen through the vibrational modes (stretch) of Si-H and $Si-H_2$ at respectively 2000 and 2100 cm^{-1} [59],[62]. An example of fit for the Raman spectrum of the stretching mode of Si-H and $Si-H_2$ bonds in a µc-Si:H layer after epitaxy breakdown is shown in Fig. 2.8-b).

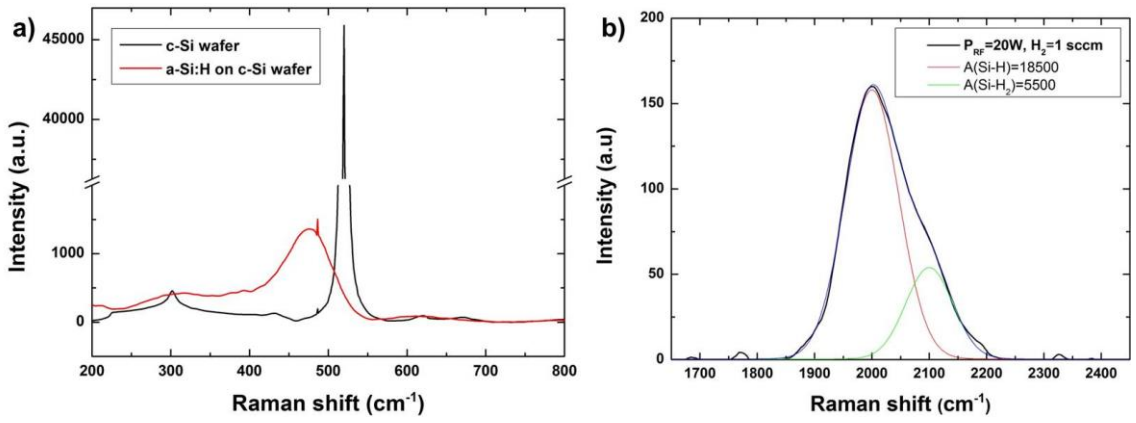

Fig. 2.8 – a) Raman spectra for the TO mode of a bare c-Si wafer and a a-Si:H layer deposited on a c-Si wafer. Raman signals at 480 and 520 cm^{-1} correspond, respectively, to transverse optical (TO) modes of amorphous and crystalline silicon. Note that the acquisition time is three times higher for the a-Si:H layer than for the c-Si wafer. b) Raman spectra around the stretching mode of Si-H (2000 cm^{-1}) and $Si-H_2$ (2100 cm^{-1}) groups for a Si layer after epitaxy breakdown.

2.2.2.3.2. X-ray diffraction

Transmission electron microscopy has been used to give insight on the quality of the interface between the epi-layer and the c-Si substrate, the type of defects, and the presence of H platelets at a local level. To extract macroscopic structural information from samples, X-ray diffraction (XRD) has been performed. This technique is based on elastic scattering of X-rays by atoms electrons [63]. In a crystal, these atoms constitute a regular array of scatterers which induce a regular array of spherical waves. Some constructive interference arises from the crystal which depends on the X-ray wavelength and the incident angle in accordance to the Bragg's law. The principle of Bragg's law is shown in Fig. 2.9.

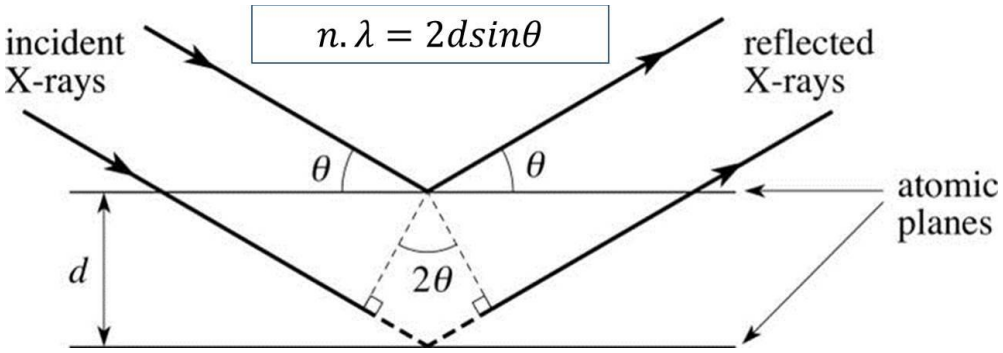

Fig. 2.9 – Schematic of crystallographic planes and the Bragg's law.

In our case the incident X-rays wavelength is the $CuK_{\alpha 1}$ (λ = 1.54056 Å), θ is the incident angle (known) and *d* the interatomic distance, which can vary depending on the material. In the case of low temperature silicon epitaxy, the gas mixtures and the process conditions used can lead to differences in the lattice parameters. In case of low-temperature epitaxy from SiH_4/H_2 gas mixtures for example, the as-grown lattice parameter of the epi-films is larger than that of the substrate. Thus, we will compare the results obtained from $SiF_4/H_2/Ar$ to those obtained from SiH_4/H_2 as regards with the lattice parameter of epitaxial layers. To provide a good understanding of the experiments performed with the Bruker D8 diffractometer we used, basics of high resolution XRD (HR-XRD) are briefly detailed below.

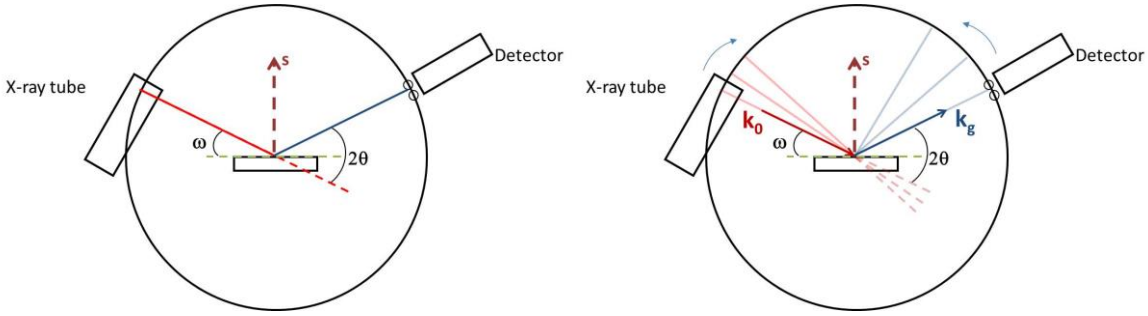

Fig. 2.10 – Schematic of XRD setup with illustration of ω and θ angles and the k_0 and k_g wave vectors.

Three types of scan will be detailed in this chapter, the ω/2θ scan, the ω scan (sometimes called "rocking curve" but depending on the authors the "rocking curve" can also refer to the ω/2θ scan) and the reciprocal space mapping (RSM) which consists of a series of ω/2θ scans for different relative ω at

the start. Thus, two angles are used in these scans: ω and θ. As shown in Fig. 2.10, the first one corresponds to the angle between the surface of the sample and the incident X-ray beam and the second one corresponds to the half of the angle between the incident X-ray beam and the detector direction. For the ω/2θ scan, ω = θ but not for the ω scan.

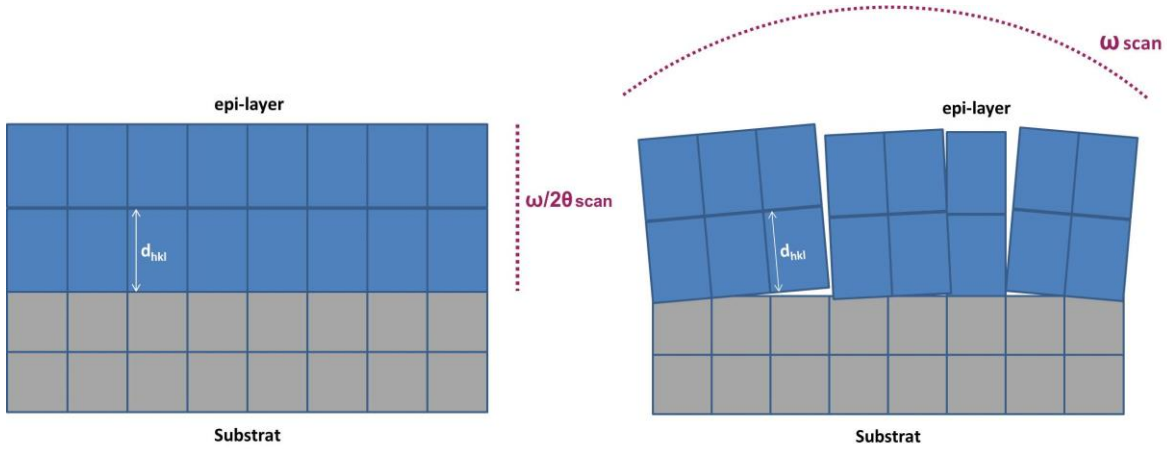

Fig. 2.11 – Objectives of the ω/2θ scan (on the left) and ω scan (on the right). The ω/2θ aims to evaluate the difference of lattice parameter of the epitaxial layer with respect to that of the substrate. The ω scan assesses the mosaicity of the grown material and can be used to determine the dislocation density.

As shown in Fig. 2.11, the objective of the ω/2θ scan is to evaluate the difference of lattice parameter of the epitaxial layer with respect to that of the substrate. The ω scan assesses the mosaicity, i.e. the existence of tilted monocrystalline domains of the grown material and can be used to determine the dislocation density. For a better representation of the scans, their definition in the reciprocal space, i.e. the Fourier transform of the Bravais lattice, is required. The wave vectors (k_0 and k_g), the angles (ω and 2θ) and the crystallographic planes in the reciprocal space, represented as points, are shown in Fig. 2.12.

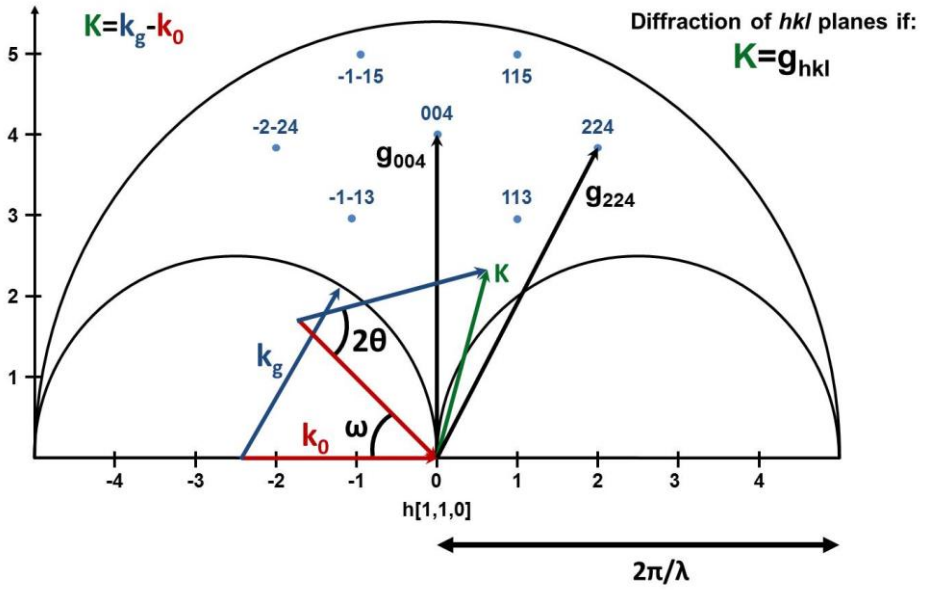

Fig. 2.12 – Representation of characteristic angles and vectors in the reciprocal space.

The orientations which can diffract depend on the X-ray wavelength. The large half-circle with a radius of $2\pi/\lambda$ in Fig. 2.12 defines the orientation which can be observed with $CuK_{\alpha 1}$ (λ = 1.54056 Å). By varying ω and θ, if the angle $K=k_g-k_0$ corresponds to the vector g_{hkl}, which reaches the orientation point (hkl), the diffraction of the (hkl) planes occurs. The (004) planes are the only parallel planes to (001) which induce a reflection with constructive interferences and detectable with the $CuK_{\alpha 1}$. This is due to the structure factor of silicon which has systematic extinctions for (hkl) planes if h, k and l are from different parities.

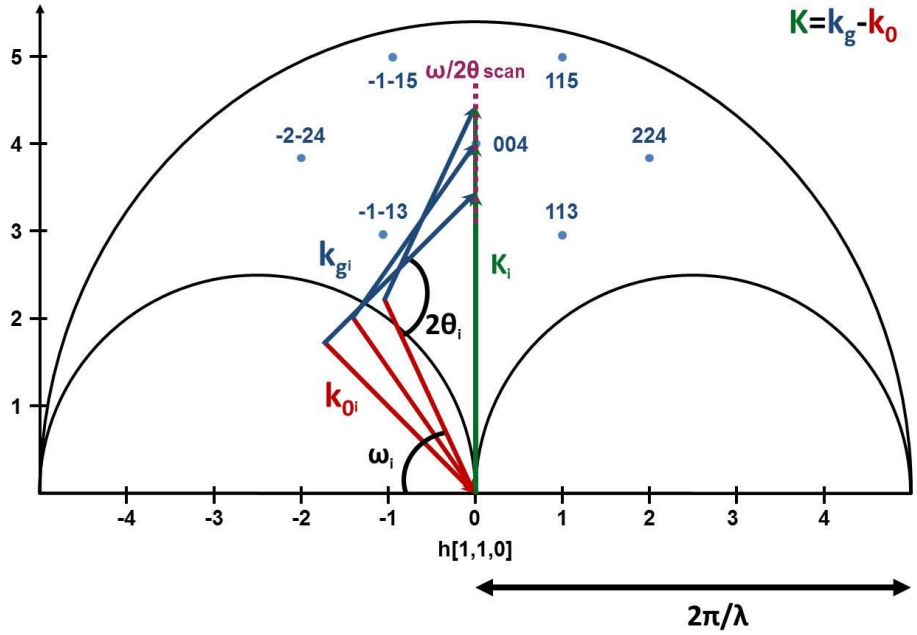

Fig. 2.13 – Principle of ω/2θ scan on the (004) planes shown in the reciprocal space. In that scan, θ varies in such a way that ∀ i, $2\omega_i=2\theta_i$, i.e $\omega_i=\theta_i$.

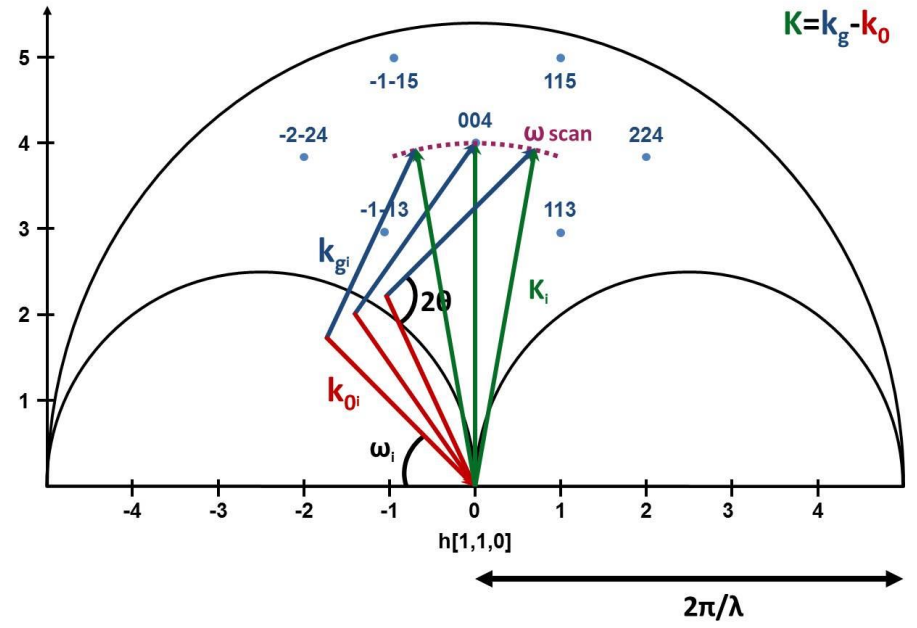

Fig. 2.14 – Principle of ω scan (or rocking curve) on the (004) planes showed in the reciprocal space. In that type of scan, 2θ is kept constant and is set at two times the Bragg angle.

ω/2θ scans and ω scans differentiate themselves through the angles swept by K around the investigated point ((hkl) plane) of the reciprocal space. Fig. 2.13 shows the principle of the ω/2θ scan on (hkl) planes for which K_i is parallel to g_{hkl} ∀ i which means that $\omega_i = \theta_i$ ∀ i. This scan allows to measure the difference of lattice parameter between the substrate and the epitaxial layers. If the lattice parameter of the epitaxial layer is larger than that of the substrate its diffraction peak appears at smaller angles, as expected from Bragg's law.

The quality of the epitaxial layer is assessed by comparing the FWHM of the diffraction peak with respect to the substrate one. In case of perfect monocrystals, if the lattice parameter of the epi-layer is the same as the substrate, then the two diffraction peaks overlap and the FWHM is defined by the instrumental broadening.

The principle of the ω scan is given in Fig. 2.14. In that case ω_i is varied but 2θ is fixed in that way that it respects Bragg's law. As shown in Fig. 2.11, films can be composed of different crystalline domains with the same crystallographic orientation but tilted between each other, which is called mosaicity. Consequently, the diffraction happens for different ω angles (while 2θ is fixed to correspond to the angle for the investigated crystallographic orientation) and induces a broadening of the diffraction peak.

The results of XRD on LTE layers are rather scarce. We detail in Fig. 2.15 the state of the art of LTE layers characterized by XRD.

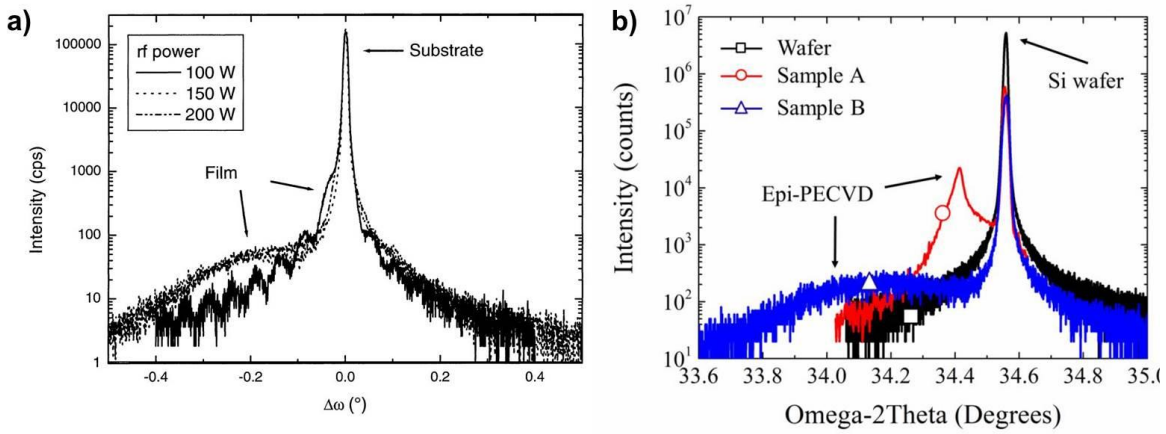

Fig. 2.15 – a) ω/2θ scan for the (004) reflection on epitaxial layers grown at 400°C from SiH_4/H_2 chemistry for power density of 310, 465 and 620 mW/cm² [28] b) ω/2θ scan for the (004) reflection on epitaxial layers grown at LPICM at 200°C from SiH_4/H_2 chemistry [80].

Fig. 2.15-a) and -b) show ω/2θ scans for LTE grown by RF-PECVD from SiH_4/H_2 gas mixtures. For Fig. 2.15-a), Schwarzkopf et *al.* [28] have grown the layers at 400°C and for RF power of 100, 150 and 200 W, corresponding to RF power density of 310, 465 and 620 mW/cm² respectively. The values are relatively high compared to what we use (our power density is commonly around 200 mW/cm²). In the case of low RF power (310 mW/cm²) they achieve epi-layers with excellent structural properties. Indeed the peak of the layer and that of the substrate partially overlap, meaning that the lattice parameter of the epi-layer is very close to that of the substrate. The layer peak is only shifted by 0.05° with respect to that of the substrate. It also means that the in plane compressive strain is low in that case. To our knowledge this is the best result for an epitaxial layer in terms of structural properties reported in the literature.

However when the power is increased the FWHM of the diffraction peak strongly broadens, meaning that a variation of lattice parameter is observed along the layer due to the presence of defects. Moreover the diffraction peak of the layer is shifted to low angles and no longer overlaps with that of the substrate, meaning that in average the lattice parameter of the epi-layer is significantly larger than that of the substrate. They assume the difference of structural properties between low and high power to be associated to the different growth rate. In case of low power, the growth rate is only 0.1 Å/s while it is 0.25 and 0.22 for high power. However, we do not think that a too high growth rate is the actual cause of these differences since we reached growth rates of 3 Å/s for epi-layers with similar properties as those obtained in their low power case condition.

As a comparison for our work, Fig. 2.15-b) shows the results for the layers grown at LPICM with SiH_4/H_2 gas mixtures at 200°C. The growth rate for the Sample A (in red) is 3 Å/s while it is 8 Å/s for the Sample B (in blue) which is grown at higher power. The respective power densities these layers have been grown at are 90 mW/cm^2 and 240 mW/cm^2. The properties of the Sample B are similar to what is obtained by Schwarzkopf et *al.* in case of high power. In case of Sample A, we can see that the diffraction peak of the layer is shifted by around 0.15° towards low angle but is sharp. This means that the lattice parameter is significantly higher ($\Delta a \approx 3.10^{-3}$ Å, [43]) but it is homogeneous along the layer. The scan of Sample A can be used as a reference for our epitaxial layer given that it has been measured on the same equipment with the same configuration as our epitaxial layers.

When the lattice parameter of the epitaxial layer is different from that of the substrate, the epitaxial layer can be strained, relaxed or a combination of both. The RSM allows to identify in which situation the system is. The Fig. 2.16 illustrates the representation in the reciprocal space of fully relaxed (in green) and fully strained (in red) epitaxial layers.

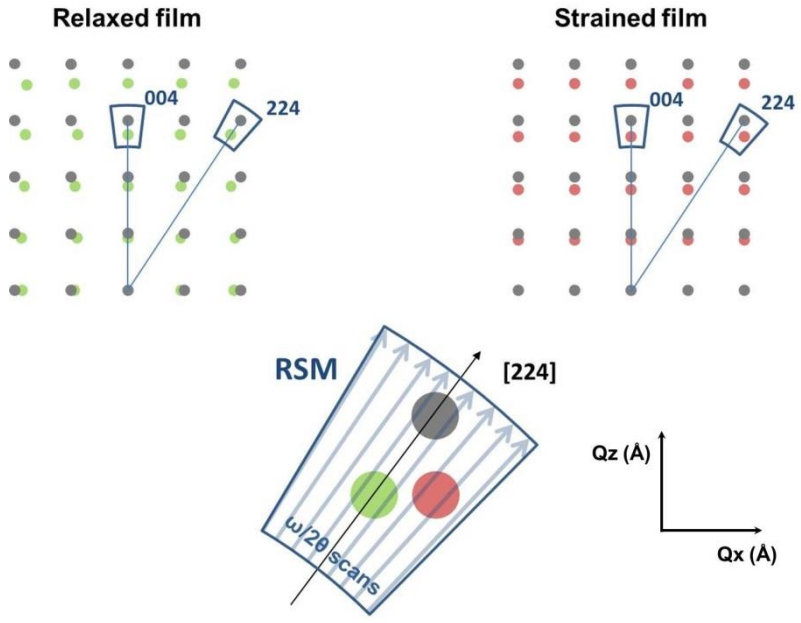

Fig. 2.16 – Representation of fully relaxed and fully strained epitaxial films in the reciprocal space. Below is a zoom in the 224 point and the representation of the reciprocal space mapping (RSM) obtained from multiple ω/2θ scans with different ω at start. The green and red dots respectively features the position of a fully relaxed and fully strained films in the reciprocal space for the (224) orientation.

As an example, Cariou *et al.* performed (004) and (224) RSM on 5.15 µm thick epi-layers grown around 200°C with the SiH_4/H_2 chemistry. Results are shown in Fig. 2.17. The (004) RSM (on the left)

confirms that the lattice parameter of the layer in the direction of growth is different from that of the substrate: $\Delta a_{\perp} \approx 3.10^{-3}$ Å, [43]. Note that our calculations provide a $\Delta a_{\perp} \approx 3.10^{-2}$ Å instead. The (224) RSM, by comparing Q_x positions of the substrate and epi-layers diffraction peak, allows to affirm that the layer is strained. Indeed, with a ΔQ_x (224) = 4.10^{-5} Å, the case is similar to the red case in Fig. 2.16. Thus, they found a low relaxation parameter, defined as R= $(a_{||,epi} - a_s)/(a_{0,epi}-a_s)$, of 5.5%, where $a_{||,epi}$ is the in-plane lattice parameter, a_s the substrate lattice parameter and $a_{0,epi}$ the lattice parameter for the fully relaxed epi-layer with a cubic unit cell.

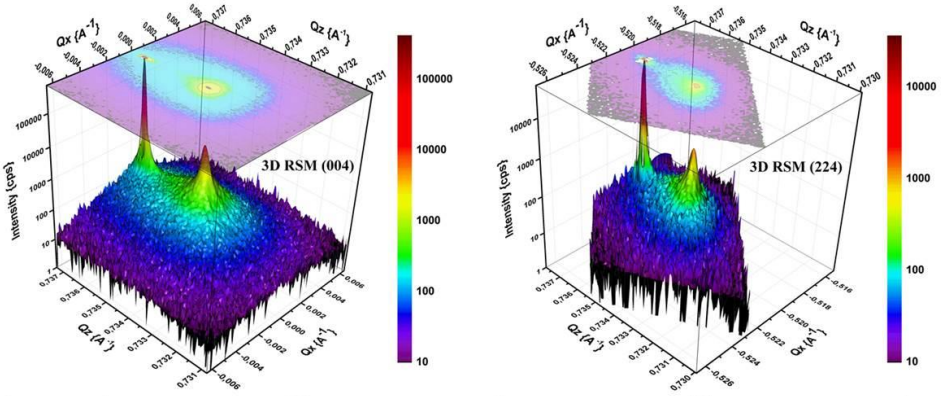

Peaks	004				224			
	Intensity (cps)	FWHM dQx ; dQz (Å⁻¹)	Qx (Å⁻¹)	Qz (Å⁻¹)	Intensity (cps)	FWHM dQx ; dQz (Å⁻¹)	Qx (Å⁻¹)	Qz (Å⁻¹)
c-Si wafer	1,25E6	8.4E-5 ; 6.2E-5	0	0.73675	8.8E4	6.8E-5 ; 1.1E-5	-0,52085	0,73666
Epi-Si layer	1,42E4	2.0E-4 ; 2.8E-4	0	0.73413	1,42E4	5.6E-4 ; 7.3E-4	-0,52089	0,73413

Fig. 2.17 – On the left: (004) RSM and on the right: (224) RSM of 5.15 µm epi-layers grown at 200°C. The low difference in Q_x (ΔQ_x (224) = 4.10^{-5} Å^{-1}) for the (224) RSM indicates that the layer is strained.

2.3. Definition of process conditions for intrinsic epitaxy

2.3.1. Hydrogen influence on material and plasma properties

In this part we study the influence of the hydrogen (H_2) flow rate on the material properties. We will see that the H_2 depletion is a more suitable parameter to describe the behavior of the process conditions, given that to some extent it allows to take into account the variation of the RF power.

The temperature of the substrate is fixed at 200°C and that of the RF electrode at 100°C. The pressure is fixed at 3 Torr and the inter-electrode distance is 2 cm. Thus the product $p \times d$ (pressure multiplied by the inter-electrode distance) is 6 Torr.cm which is the optimum for the deposition rate as observed by Djeridane [49], and more recently Dornstetter [51]. They have shown that for pressures varied between 1.7 Torr and 3.8 Torr, the optimum inter-electrode distance needs to be fixed in such a way that $p \times d$=6 Torr.cm. This also represents the condition for which the H_2 depletion as a function of $p \times d$ reaches a plateau, meaning that this is the optimum to reduce the silicon precursors waste. The SiF_4 and Ar flow rates are respectively fixed at 3.6 and 88 sccm. Such a high flow rate of Ar is necessary to ensure a good dissociation of SiF_4 [51].

The evolution of the imaginary part of the pseudo-dielectric function as a function of H_2 flow rate (f_{H_2}) for a RF power of 10 W (p_{RF}=130 mW/cm^2) is shown in Fig. 2.18.

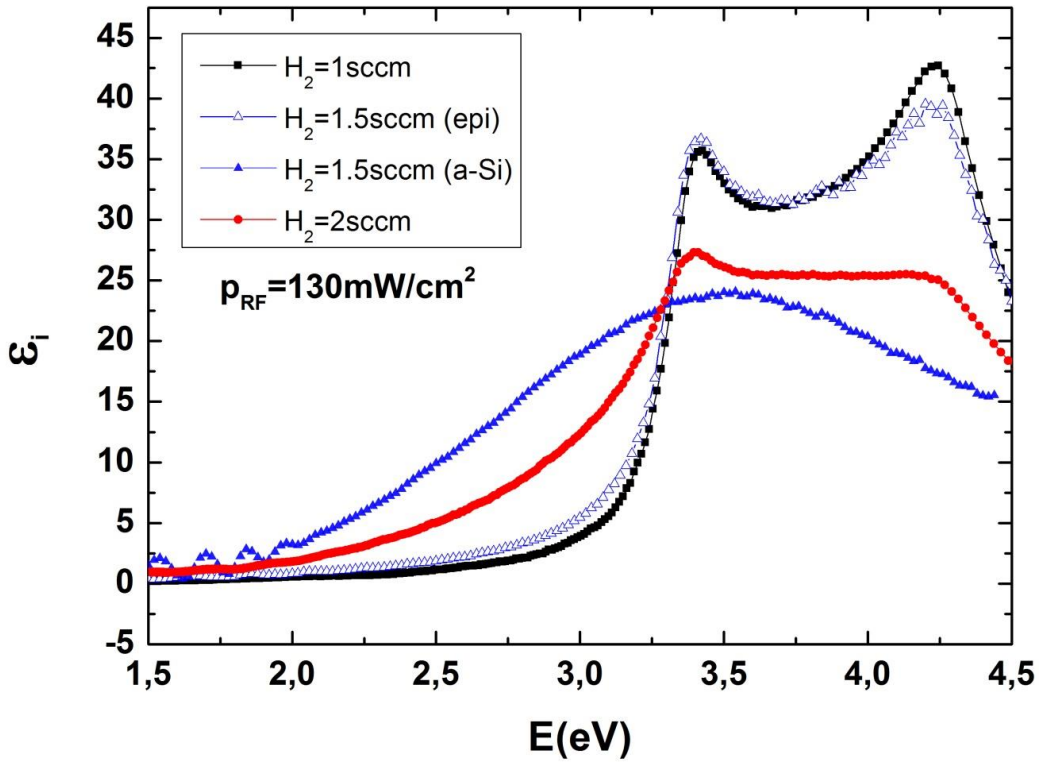

Fig. 2.18 – Imaginary part of the pseudo-dielectric function for different H_2 flow rates (1, 1.5 and 2 sccm) at a RF power of 10 W (p_{RF}=130 mW/cm^2).

It can be seen that for low H_2 flow rate the epitaxy is excellent (in black), both peaks at 3.4 and 4.2 eV are similar to those of a c-Si wafer and a crystalline fraction (F_c) around 100% is found. When the H_2 flow rate is increased to 1.5 sccm, a transition occurs: epitaxy and amorphous silicon appear on the same substrate (in blue) with the same process conditions leading to highly inhomogeneous films. These conditions are highly unstable for epitaxy, either it leads to epitaxy or a-Si:H from the initial stages of deposition or after some deposition time. Finally when the flow rate is increased up to 2 sccm the material becomes microcrystalline.

As shown in Fig. 2.19, when the RF power is increased to 15 W (p_{RF}=200 mW/cm^2) it can be seen that the optimal H_2 flow rate also increases, moving from 1 sccm to 2 sccm. For H_2 = 1 sccm, both ε_i(3.4eV) and ε_i(4.2eV) values decrease with respect to those obtained at p_{RF}=130 mW/cm^2, meaning the sample becomes rougher. In case of H_2 = 2 sccm, ε_i(3.4eV) is above 36 but ε_i(4.2eV) is lower than 40, which could mean that the roughness is also increased; as a matter of fact the measurement has been done two months after the deposition due to technical problems, so a native oxide grew thus affecting ε_i(4.2eV). After modelling the native oxide with a 2 nm thin layer composed of SiO_2 and voids at the top of the stack, we found a crystalline fraction between 95 and 100%, varying with the proportion of each material. The complementary part is only a polycrystalline fraction (no amorphous phase). We know from *in situ* measurements that the spectrum of the layer is similar to that of p_{RF}=130 mW/cm^2 and H_2=1 sccm.

Finally, when the H_2 flow rate reaches 3 sccm, the material is similar at what is obtained with 2 sccm at p_{RF}=130 mW/cm^2. Thus the process conditions for epitaxy do not only depend on the H_2/SiF_4 ratio

given that the optimum changes when the RF power is changed. Indeed, we observe that the H_2 transition from epitaxy to a-Si:H/µc-Si:H shifts when the power is increased. Therefore, another parameter to define the material transition is required. We will see that the H_2 depletion is a much more relevant parameter.

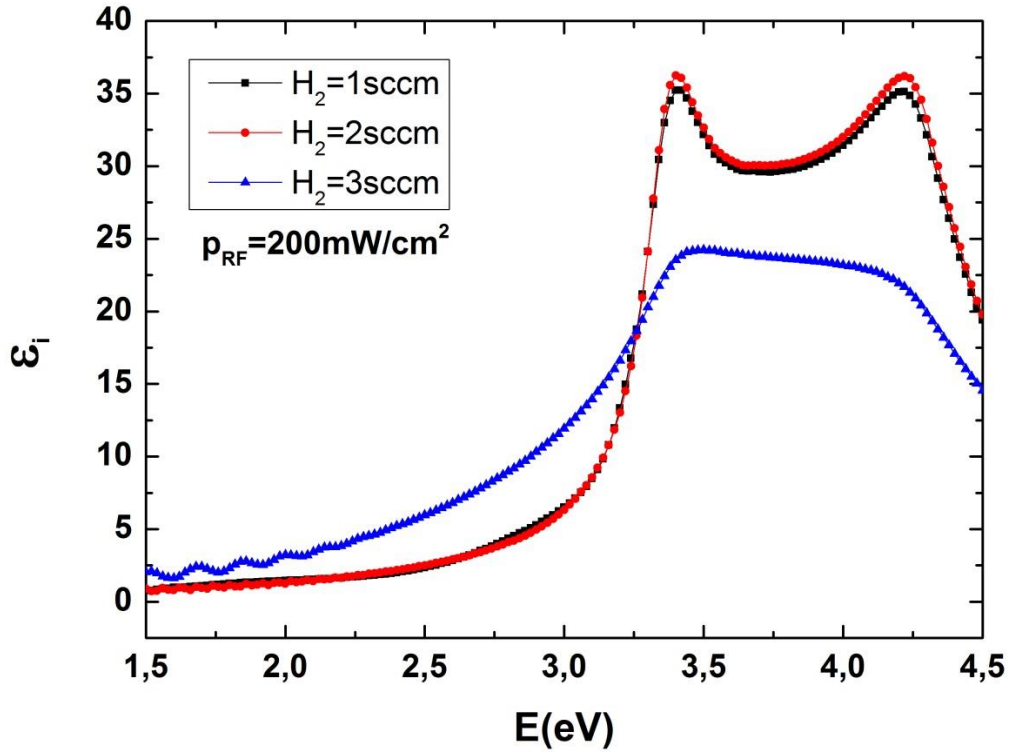

Fig. 2.19 – Imaginary part of the pseudo-dielectric function for different H_2 flow rates (1, 2 and 3 sccm) at a RF power of 15 W (p_{RF}=200 mW/cm^2). At H_2=2 sccm a native oxide has grown before the measurement.

In order to assess the chemical properties of the plasma and the influence of process parameters on the plasma species, OES has been performed. The idea is to find a difference in the spectral signature of the plasma species and to correlate them to the differences observed in the material properties.

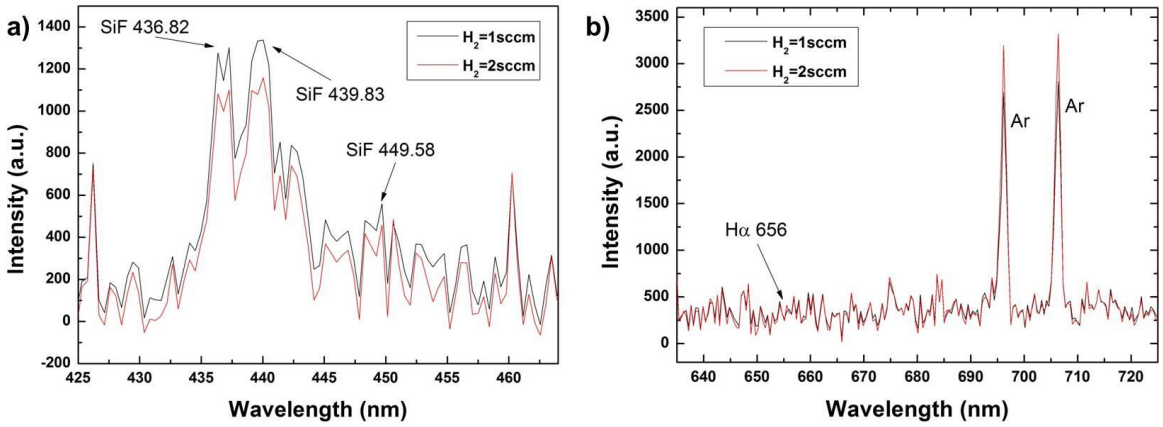

Fig. 2.20 – OES spectra obtained at 10 W (130 mW/cm^2) for H_2=1 sccm and 2 sccm around a) SiF emission peaks and b) Hα and Ar emission peaks.

The power is fixed at 10 W (130 mW/cm^2) and the H_2 flow rate is varied from 1 sccm to 2 sccm, the corresponding material properties are shown in Fig. 2.18**.** The two spectra shown in Fig. 2.20-a) do not present significant differences and from Fig. 2.20-b), the Hα emission peak at 656 nm [64] is not detectable in our measurement conditions. Ar peaks are slightly higher in the case of H_2=2 sccm and this is consistent with the work of Dornstetter [51] but these differences have not been considered to be significant enough to correlate them with material properties. Thus we can see that no significant difference is observable between both spectra while, as seen in Fig. 2.18, material properties are strongly different. OES, at least in the specific conditions we used, is not suitable for the characterization of $SiF_4/H_2/Ar$ plasmas to correlate them to structural properties of epi-layers and another approach has to found. Note that a more detailed characterization of $SiF_4/H_2/Ar$ plasmas by OES can be found in [51].

The residual gas analyzer (RGA) is a powerful and very convenient tool for the reactive plasmas characterization. By comparing the partial pressure of molecular hydrogen (H_2) before and after ignition of the plasma, as shown in Fig. 2.21, we can deduce the H_2 depletion involved in the gas-phase reaction and calculate the total consumption of H_2 for each process conditions. Namely, a full (100%) depletion of H_2 means that the totality of the hydrogen injected has been consumed in the plasma. Conversely, 0% of depletion (same H_2 partial pressure before and after ignition) means that no H_2 molecule has been consumed in the plasma.

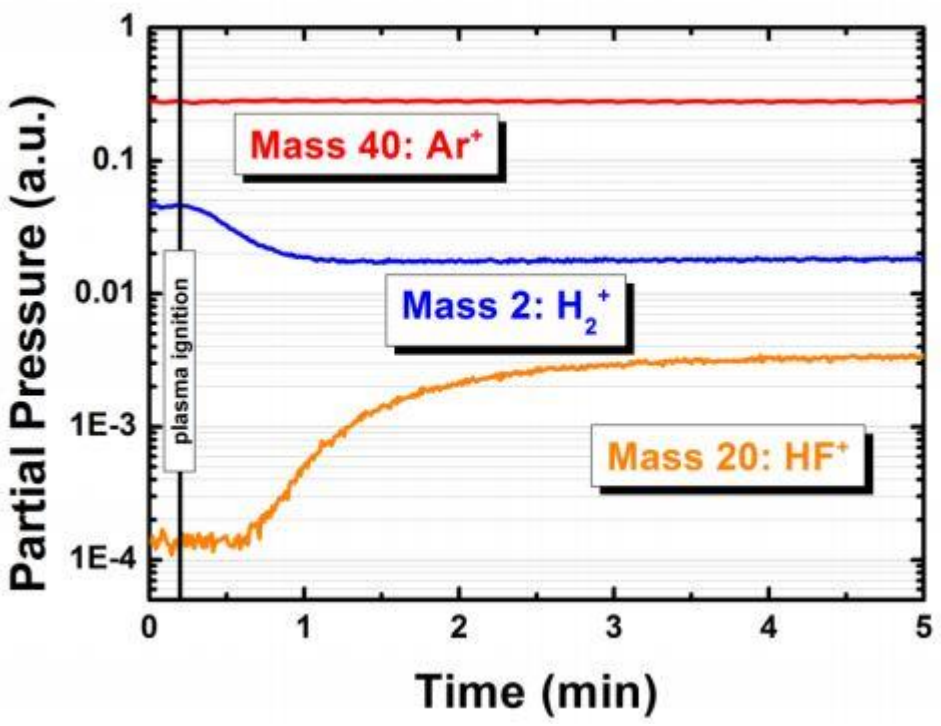

Fig. 2.21 – Example of measurement performed with the RGA. The partial pressure of each species is measured before and after ignition of the plasma. The hydrogen depletion is calculated from the values obtained by the RGA [51].

The collision of SiF_4 molecules and electrons lead to the formation of SiF_x radicals ($x \leq 3$). The deposition of silicon thin films (a-Si:H/µc-Si:H) is ensured by the removal of monoatomic fluorine produced in the decomposition of SiF_4 in the plasma (by-products of SiF_x radicals). Dornstetter *et al.*

have shown in [56] that the deposition of silicon thin films (a-Si:H/µc-Si:H) could be approximated by a phenomenological model which consists of three kinetic equations:

$$SiF_4 \leftrightarrow SiF_3 + F, \quad (1)$$

$$H_2 \leftrightarrow 2H, \quad (2)$$

$$H + F \leftrightarrow HF \quad (3)$$

They demonstrated that the amorphous deposition regime occurs when monoatomic fluorine is in excess (full depletion of H_2) while the microcrystalline regime is obtained when the molecular hydrogen is in excess. The measurement of H_2 depletion is therefore a good indication to know the regime the plasma is in. This is calculated from the partial pressures measured by the RGA before and after plasma ignition:

$$D_{H_2} = \frac{P_{H_2^+}^{off} - P_{H_2^+}^{on}}{P_{H_2^+}^{off}}$$

Fig. 2.22 shows the correlation between H_2 depletion and crystalline fraction extracted from ellipsometry measurements by using the BEMA model described in Fig. 2.5.

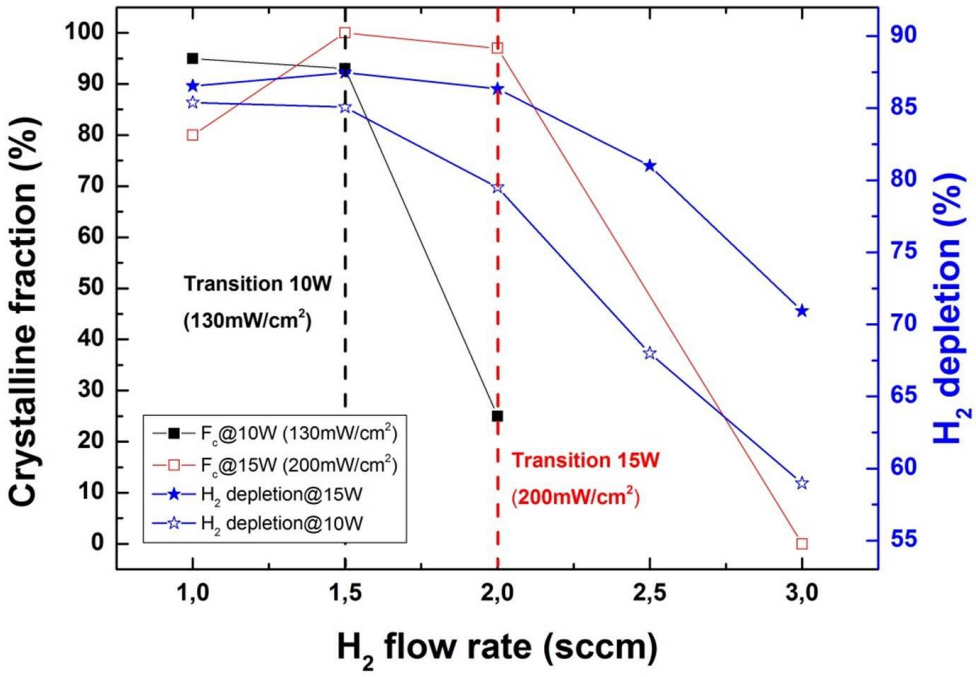

Fig. 2.22 – Evolution of H_2 depletion as a function of H_2 flow rate for a RF power of 10 and 15 W, corresponding to a power density of respectively 130 and 200 mW/cm^2. We can identify two regimes: the epitaxial growth regime corresponding to the full depletion (>85%) of H_2 and the microcrystalline growth regime for which the H_2 depletion is not full.

Interestingly, when the H_2 depletion is maximum, i.e on a plateau, which occurs for the low H_2 flow rates, the crystalline fraction is maximum as well (>80%). After the H_2 depletion transition the crystalline fraction rapidly drops meaning that the deposited layers are no longer epitaxial. Thus

instead of considering the H_2/SiF_4 ratio, the H_2 depletion is a more relevant parameter because, to some extent, it allows to take into account the variation of the RF power.

In the same way as a full depletion is required to deposit a-Si:H from $SiF_4/H_2/Ar$ chemistry on glass, it is thus observed that the full depletion of H_2 is a necessary (but not sufficient, as shown later) condition to perform epitaxy. Based on these observations we can measure the depletion for every (P_{RF} ; f_{H_2}) couple and draw a mapping of H_2 depletion to identify a process window in which we can expect epitaxy. The mapping is shown in Fig. 2.23.

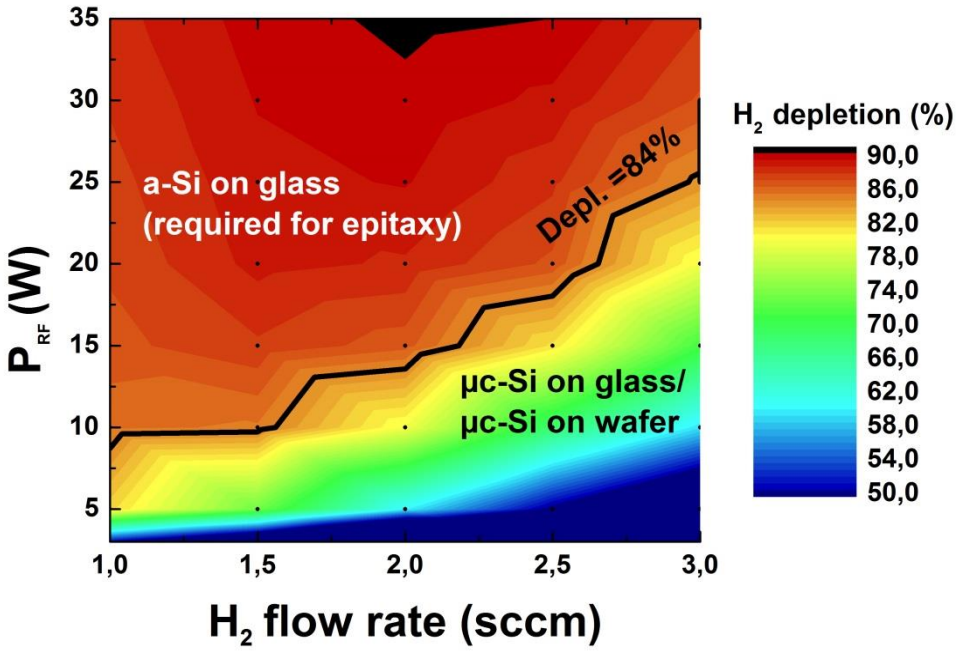

Fig. 2.23 – Mapping of H_2 depletion at given pressure and inter-electrode distance (3 Torr, 2 cm) as a function of the RF power and the H_2 flow rate. Black dots represent the experimental data.

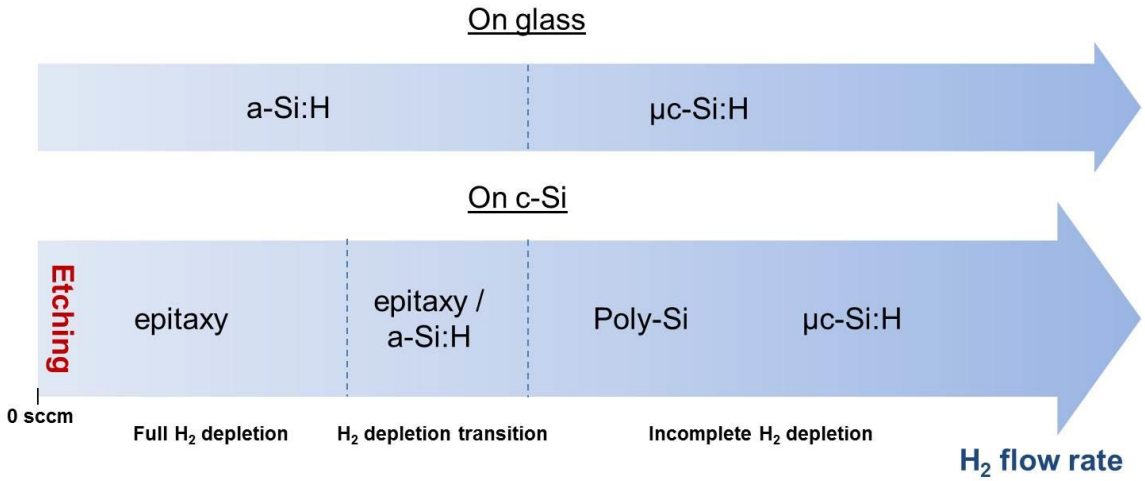

Fig. 2.24 – Illustration of the influence of H_2 flow rate on the evolution of material properties at a given RF power.

The Fig. 2.24 gives an illustrative summary concerning the material properties as a function of the H_2 flow rate. For pure SiF_4/Ar plasmas, no deposition is observable and the plasma is in the etching

regime. When H_2 is added to the gas mixture the plasma is in the epitaxy regime, the quality improves with H_2 flow rate until the conditions approach the H_2 depletion transition. At the transition the films consist of inhomogeneous epitaxial and amorphous area. Note that a full H_2 depletion is a necessary but not sufficient condition. By further increasing the H_2 flow rate, the films become poly-crystalline and then µc-Si. In this regime the results obtained from ellipsometry measurements between deposition on c-Si substrate and glass are similar. The films may be crystalline (not amorphous) but are not epitaxial given that the orientation of the films is no longer determined by the orientation of the substrate. This regime has not been widely studied given that µc-Si:H is already well detailed in the literature. Nevertheless a XRD θ/2θ scan would be interesting to carry out for samples on glass and c-Si to compare the preferential orientations in the films.

2.3.2. Effect of RF power

In order to study the effect of the RF power on the optical properties of the layers the power has been varied during deposition and the imaginary part of the pseudo-dielectric function at 4.2 eV has been monitored by *in situ* ellipsometry. This allows to determine a RF power critical limit for these conditions of SiF_4 flow rate and pressure, namely 3.6 sccm and 3 Torr respectively, as shown in Fig. 2.25. The plasma potential can be evaluated measuring the RF potential and the self-bias voltage, and calculated by:

$$V_{pl} = \frac{V_{RF} + V_{DC}}{2}$$

Note that under our collisional sheath conditions this corresponds to the maximum ion energy.

The plasma is purposely ignited in process conditions leading to epitaxy, namely here a RF power of 15 W for a H_2 flow rate of 1.5 sccm. In these conditions the growth rate is 1.6 Å/s. The RF power is increased and kept constant until the stabilization of ε_i(4.2eV) is achieved, the result is given in Fig. 2.25.

As it can be seen, from 15 W to 17 W the evolution is negligible but when P_{RF} is increased to 19 W, ε_i(4.2eV) slowly decreases (which is due to the roughening of the surface) and a period of almost 20 min, corresponding to more than 200 nm, is necessary to reach the stabilization. Finally, when the power is increased to 21 W, corresponding to a plasma potential of 61 V, ε_i(4.2eV) rapidly decreases indicating an epitaxy breakdown. The drop and the increase of ε_i(4.2eV) at the plasma ignition and stop respectively along with the oscillations observable at 19 W and 21 W will be discussed in Chapter 3. Thus, a RF power around 20 W, corresponding to a plasma potential threshold of 60 V, is identified to be responsible for epitaxy breakdown.

The effect of the RF power on the material properties at H_2=1 sccm has also been investigated by ellipsometry but for 6 different samples, results are shown in Fig. 2.26.

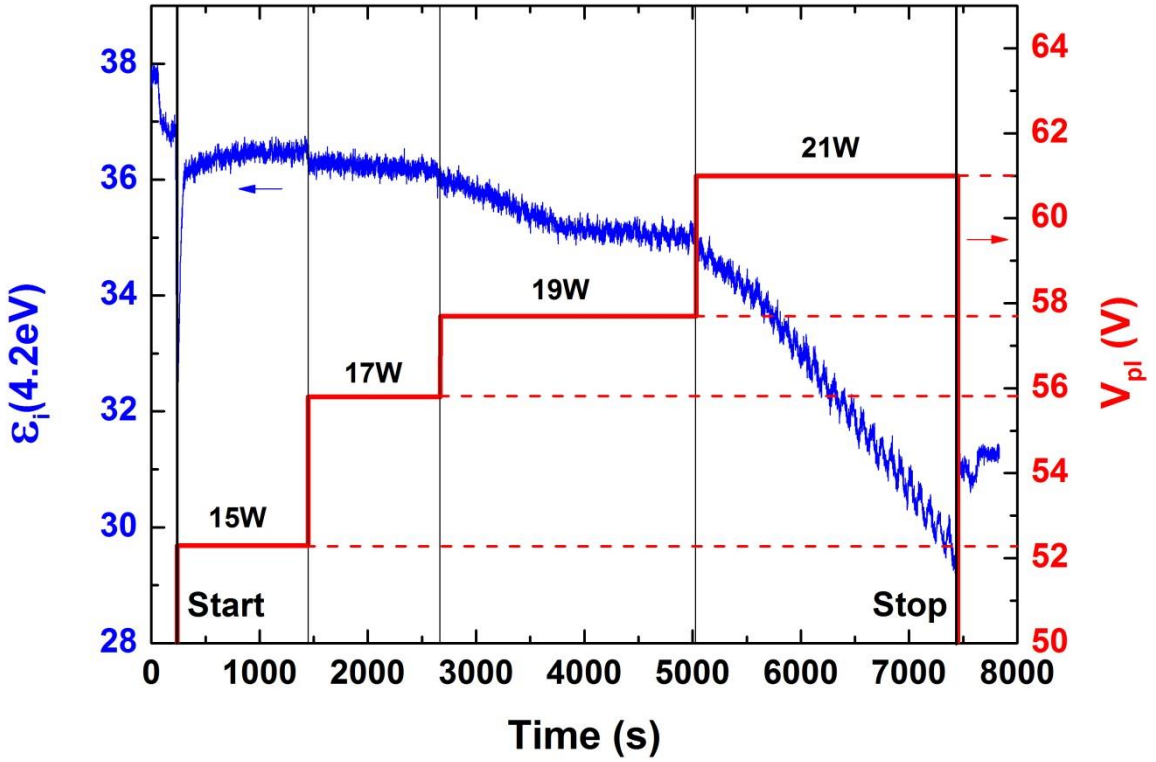

Fig. 2.25 – Evolution of the imaginary part of the pseudo-dielectric function at 4.2 eV as a function of power and related plasma potential V_{pl}. Flow rates are kept constant: $SiF_4/H_2/Ar$ =3.6/1.5/88 sccm and p=3 Torr.

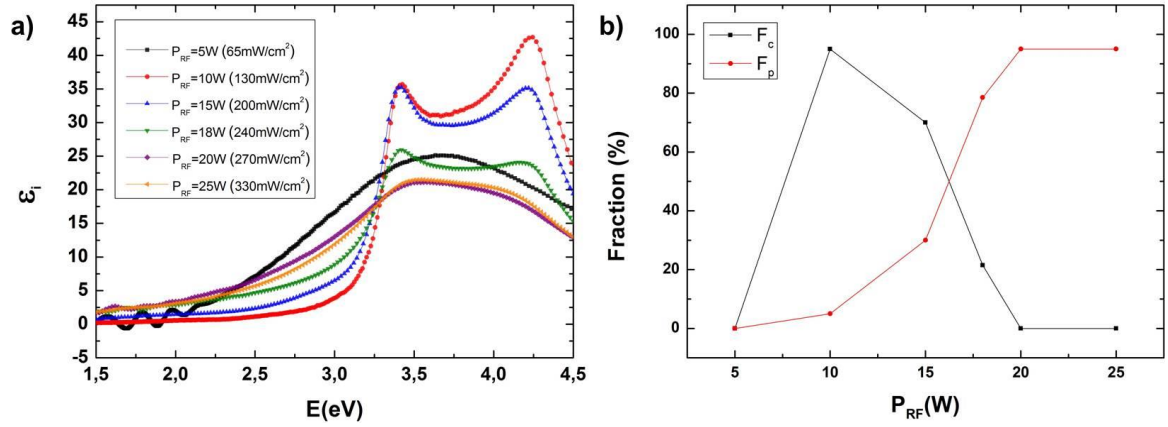

Fig. 2.26 – Ellipsometry spectra for H_2=1 sccm and for various RF power values. The SiF_4 flow rate and pressure are fixed to 3.6 sccm and 3 Torr respectively. By increasing the RF power from 5 W to 25 W, the film goes from amorphous to epitaxial to microcrystalline. b) Evolution of the mono- and polycrystalline fraction as a function of RF power. The transition occurs for a plasma potential between 54 V and 58 V.

Firstly, this decline of the quality by an increase of the RF power confirms the observations based on *in situ* ellipsometry for H_2=1.5 sccm. Secondly, it shows that this second type of transition, promoted by the increase of RF power, is interestingly similar to that observed with the variation of H_2 flow rate. When the RF power is too low the film is amorphous, because the process conditions are close to the transition of H_2 depletion. But an increase of the RF power leads to an increase of the H_2 depletion and allows to reach the stable full depletion regime (See Fig. 2.23). Thus at 10 W the film is epitaxial with a smooth surface given that ε_i(4.2eV) is above 40 in that case, corresponding to a roughness of a few

Å. At 15 W the film is still monocrystalline but ε_i(4.2eV) begins to drop indicating an increase of the roughness, until the threshold of 20 W where it becomes fully microcrystalline.

Thus we observe the same trends on the material properties between the H_2 transition and the P_{RF} transition, if the H_2 is too high or if the P_{RF} is too high the films become poly/microcrystalline. The mechanisms induced in this epitaxy breakdown will be discussed in detail in the next section based on TEM and XRD observations. The evolutions of the crystalline fraction and polycrystalline fraction are summarized in Fig. 2.26-b). The transition occurs for a RF power between 15 W to 20 W corresponding to plasma potentials of 54 V and 58 V respectively. Note that except for the film at P_{RF}=5 W which is fully amorphous, all the depositions are crystalline ($F_c+F_p\approx100\%$).

Besides, a further increase of H_2 flow rate to 2 sccm (See Fig. 2.27) does not have the beneficial effect previously observed. It means that it is not possible to indefinitely increase the H_2 flow rate if P_{RF} is also increased. So the H_2 depletion is a necessary condition but not sufficient. This is a significant issue to improve the deposition rate, since to do so H_2 flow rate needs to be increased and the P_{RF} as well to stay in full H_2 depletion regime. This shows the importance to limit the RF power below 20 W (270 mW/cm^2) in these conditions of pressure and SiF_4 flow rate.

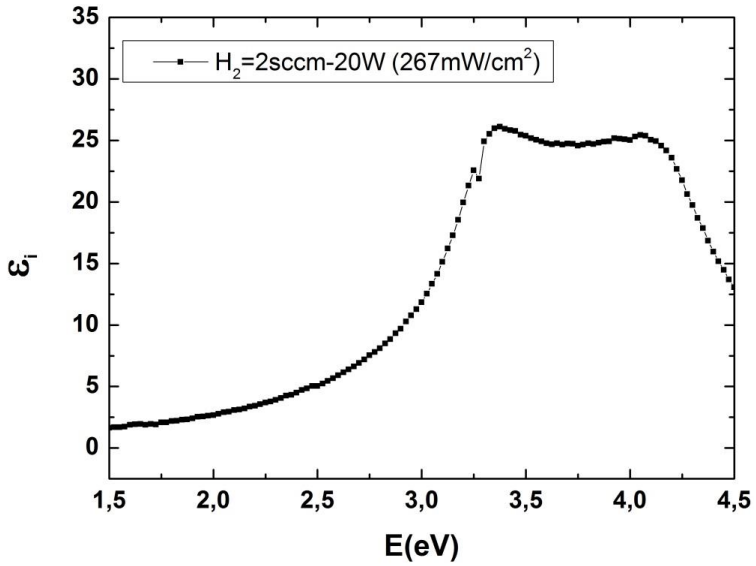

Fig. 2.27 – Imaginary part of the pseudo-dielectric function for a RF power of 20 W (p_{RF}=267 mW/cm^2) and H_2=2 sccm.

Based on this observation, the mapping of H_2 depletion can be updated and the plasma potential threshold can be added to define the process conditions for epitaxy for the fixed conditions of pressure and SiF_4 flow rate (Fig. 2.28).

Interestingly, similar results have been obtained by Bruneau *et al.* [65] for epitaxy using SiH_4/H_2 gas mixtures. They showed that in similar conditions of pressure epitaxial films deposited with a plasma potential above 60 V leads to a significant decrease of ε_i(4.2eV). They assumed that above this threshold, the ion bombardment energy is too high and energetic ions damage the upper layers of the films impeding the good arrangement of atoms. Above all, this threshold is much higher than what was observed so far, Rosenblad *et al.* [17] highlighted a maximum ion energy of 15 eV for epitaxial films grown by DC biased PECVD. Above this threshold, staking faults start to appear. This significant difference between Rosenblad and Bruneau studies is attributed to the different pressure

used for their processes, in case of Rosenblad the pressure is very low (10 mTorr) while it is 2.2 Torr in the study from Bruneau *et al.*. Besides Bruneau *et al.* showed that by reducing the total pressure to 850 mTorr, this threshold shifts to 35 V, confirming that the ion energy threshold is pressure-dependent.

A lot of causes can explain this behavior but the most likely are: i) an increase of pressure induces an increase of the probability of collisions between energetic ions and other species in the collisional sheaths meaning that the ion energy distribution function is shifted towards low values. ii) an increase of pressure promotes the formation of high order silicon precursors (Si_xH_y, with $x > 1$) and/or nanoparticles which reduces the energy per atom of the impinging species which limit the damage in the Si bulk. Brice *et al.* [66] showed that the critical energy of ions to induce damages in the Si bulk reaches a minimum for masses between 10 and 20 atomic mass units (amu) and then increases when mass increases, meaning that heavier species are less likely to damage the Si bulk at constant energy values.

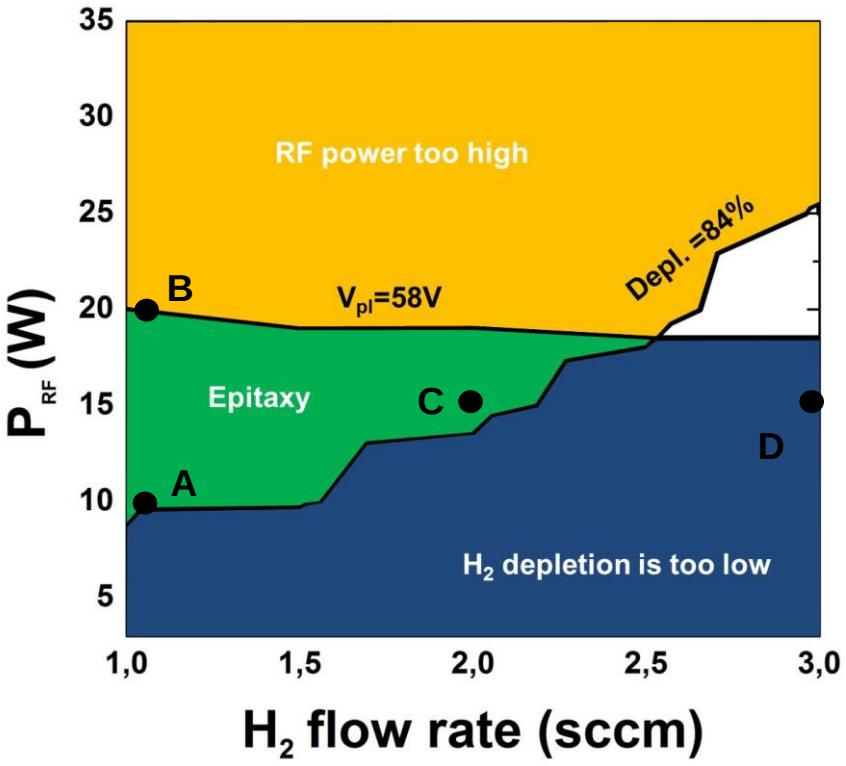

Fig. 2.28 – Process conditions for epitaxy considering ellipsometry results taking into account H_2 depletion and plasma potential threshold for a given pressure (3 Torr) and SiF_4 flow rate (3.6 sccm). The points A, B, C and D correspond to specific process conditions studied in detail in the next section by advanced characterizations.

The fact that the ion bombardment energy threshold is pressure dependent means that an optimum RF power is valid for a given pressure. We also studied the effect of pressure on the pseudo-dielectric function of our epi-layers. The evolution of ε_i(4.2eV) for different values of pressure varied from 3 to 1 Torr is shown in Fig. 2.29. It shows that even at low pressure (1 Torr) the epitaxy is stable in these conditions of RF power. That means that at 3 Torr, a RF power of 20 W, and therefore a V_{pl} of 60 V, should not be the cause of epitaxy breakdown. Thus, the evolution as a function of pressure of optical

properties of $SiF_4/H_2/Ar$ plasma is different from what is observed with SiH_4/H_2 chemistry if the considered figure of merit is the imaginary part of the pseudo-dielectric function. This result should be taken with caution since no additional characterization has been performed on these layers grown at low pressure. In Chapter 4 additional results about the influence of the pressure dependency on the plasma potential critical limit will be provided thanks to XRD characterization.

Thus, the SiF_4 flow rate has been increased to 10 sccm to see if the dilution ratio $[H_2]/[SiF_4]$ ratio needs to satisfy some conditions. The idea is to find other necessary conditions in addition to the full H_2 depletion to define the process window. Hence, the H_2 flow rate is fixed at 2 sccm and the RF power increased at 35 W (p_{RF}=470 mW/cm^2), leading to a plasma potential above 60 V, so normally out of the conditions which lead to epitaxy. The result is given in Fig. 2.30.

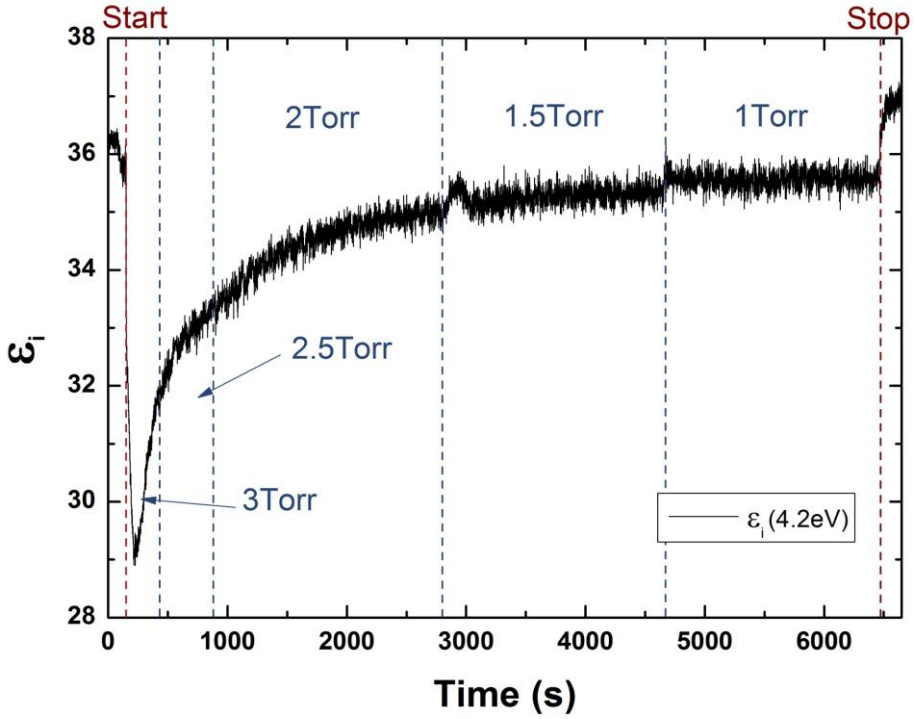

Fig. 2.29 – *In situ* evolution of ε_i(4.2eV) for different conditions of total pressure. P_{RF}=15 W (200 mW/cm^2) and $SiF_4/H_2/Ar$=3.6/1/88 sccm.

The sample is highly inhomogeneous with most of amorphous area but epitaxial growth has been obtained for a power density above 470 mW/cm^2, which leads to a plasma potential of 80 V, i.e. above the limits reported so far to grow epi-layers without defects induced by highly energetic ions. It means that with $SiF_4/H_2/Ar$ chemistry and in some specific process conditions, it is possible to exceed the ion bombardment energy threshold determined before in the literature. Moreover by increasing the H_2 flow rate to 3 sccm the layers are still monocrystalline (not shown here). This is an important result with respect to our objective of reaching deposition rates up to 1 nm/s.

The additional influence of pressure and SiF_4 flow rate on epitaxy clearly shows that the process conditions are a several dimensions space. The evolution of epitaxy as a function of H_2 and P_{RF} only showed a 2D representation of the process conditions (Fig. 2.28). If the H_2 flow rate is increased the P_{RF} also needs to be increased and inversely, if the P_{RF} is increased the H_2 flow rate also needs to be increased. This condition is effective for a certain gas ratio, thus the process window is also dependent from the SiF_4 flow rate. From our experiments we showed that for a stable epitaxy following the [100]

direction on a <100> oriented substrate and according to ellipsometry the $[H_2]/[SiF_4]$ gas ratio needs to be lower than 2/3 for every case. In addition, the increase of P_{RF} if the SiF_4 flow rate is too low leads to an epitaxy breakdown. This phenomenon is not understood yet. Thus for a technology transfer it is recommended to choose a high SiF_4 flow rate to avoid being limited by this condition and to satisfy a $[H_2]/[SiF_4]$ gas ratio below 2/3. Once this condition is met, it is required to take into account the pressure dependency to adapt the P_{RF} from the pressure. The increase of pressure allows the acceptance of an increase of the P_{RF} on the material properties by keeping a high crystalline fraction above the ion bombardment energy threshold. Nevertheless, we will see that this negatively affects the homogeneity of the epitaxial layers, thus we will also see in Chapter 4 that optimizing the gas injection pattern is mandatory to achieve homogenous layers at these high pressures.

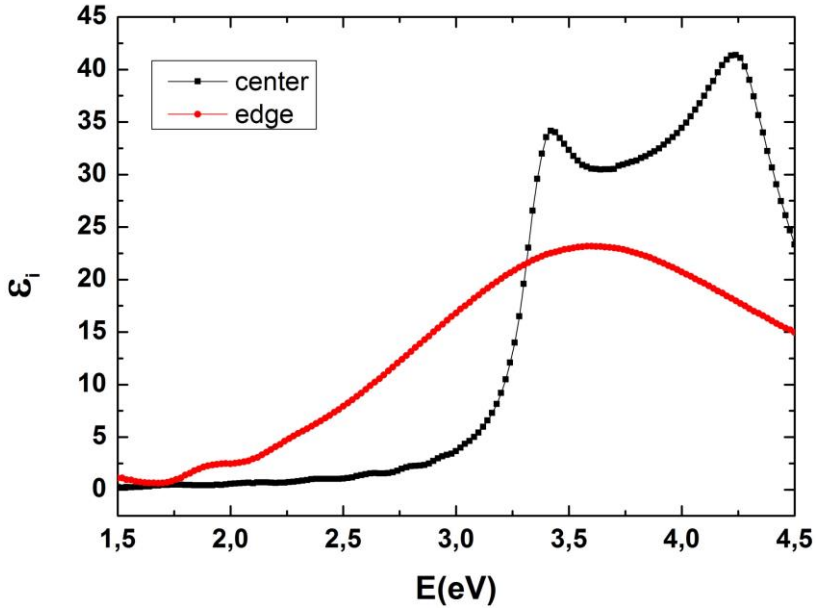

Fig. 2.30 – Ellipsometry spectra for P_{RF}=35 W (p_{RF}=470 mW/cm^2) and $SiF_4/H_2/Ar$=10/2/88 sccm. The film is inhomogeneous and leads to amorphous layers at the edge and epitaxial layers at the center of the quarter of a 4" wafer. The growth rate is 2.7 Å/s for the epi-layer.

Note that while the structural properties will be confirmed by transmission electron microscopy (TEM) and XRD for the conditions represented by the points named A, B, C and D in Fig. 2.28, we are not able to conclude about the structural properties of the epi-layers grown at 1 Torr and for those at 35 W. The properties of these films need to be confirmed by XRD. Indeed we will see in the next part that a high crystalline fraction (F_c+F_p=100%) extracted from ellipsometry is a necessary condition to perform epitaxy with high structural properties but is not sufficient. The structural properties need to be assessed by the values of full width at half maximum (FWHM) extracted from XRD scans.

2.4. Advanced materials characterization

In this part we focus on the structural properties of the layers deduced from transmission electron microscopy, X-ray diffraction and Raman spectroscopy for a few process conditions, inside and

outside the process window. Ellipsometry allows to provide information on the optical properties of the layers and the results of crystalline fraction are extracted from a model. Thus, this section also aims to verify the quality of the layers inside the process window using complementary characterization techniques. Besides, as seen previously, the two different causes observed for epitaxy breakdown (H_2 depletion too low or P_{RF} too high) lead to the same result by ellipsometry, namely a deposition of µc-Si:H. In this part we study more in detail these conditions in order to provide insights on a possible signature of the different cause of the epitaxy breakdown on the material properties. Finally, the use of TEM to identify the cause of epitaxy breakdown during a technology transfer is efficient but long and demanding, thus the objective of this part is also to provide guidelines to make a technology transfer easier using simpler and nondestructive characterization techniques such as XRD and Raman spectroscopy.

2.4.1. Roughness measurement

Prior to study structural properties of the epi-layers, it is interesting to look at the smoothness of the layer to confirm results from ellipsometry. The roughness of the epitaxial layers has been investigated by atomic force microscopy (AFM) and compared to that of a FZ wafer.

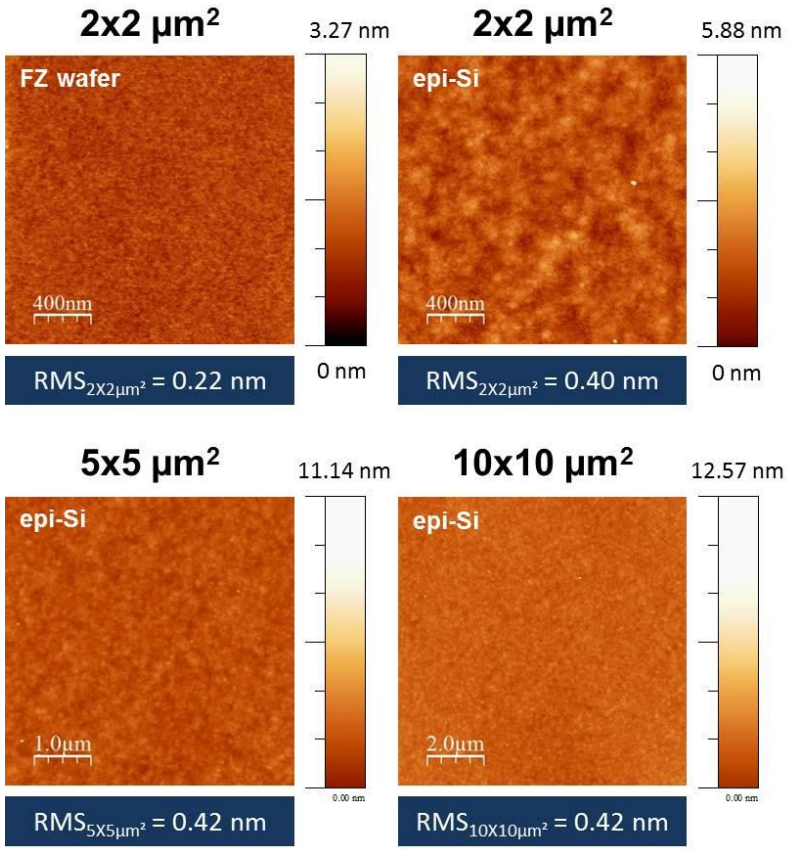

Fig. 2.31 – Topographic images obtained by AFM of a FZ wafer and an epitaxial layer for condition A with scan area of 2x2 µm², 5x5 µm² and 10x10 µm².

The results of AFM scans for 2x2, 5x5 and 10x10 µm² area are shown in Fig. 2.31. The root mean

square (RMS) value of the wafer roughness is 0.2 nm and is only 0.4 nm for a 200 nm thick epitaxial layer grown with the following conditions: p_{RF}=130 mW/cm^2 and H_2=1 sccm, thus confirming the smoothness of the epitaxial film. This value of 0.4 nm is consistent with what has been deduced from ellipsometry modelling for which a roughness of 0.5 nm was determined. As a comparison, 250 nm thick epitaxial layers grown with SiH_4/H_2 gas mixtures have a RMS around 0.5 nm [43].

2.4.2. TEM analysis

The characterization by TEM of selected samples has been done in collaboration with F. Haddad. Further details on TEM characterization can be found in her thesis [67].

Fig. 2.32-a) shows TEM images of a 750 nm thick epitaxial film for process conditions A, namely a full depletion and a low power. It shows an almost free of defects film and suggests that dislocations, if they exist, are in a very low concentration. In addition, we did not observe hydrogen platelets in this film, which can sometimes be observed in low temperature epitaxial silicon due to an excessive hydrogen content. This is a significant difference of the $SiF_4/H_2/Ar$ with respect to SiH_4/H_2 chemistry, for which H platelets are systematically observed for process temperatures below 350°C [25]. Fig. 2.32-b) presents a zoom of the surface region and confirms the observations from ellipsometry and AFM about the smoothness of the surface of the epitaxial films, where we can see that the roughness is comparable to that of a mechanically polished wafer, i.e. atomically smooth.

Fig. 2.33-a) shows a 2.5 µm thick epitaxial layer obtained when the H_2 flow rate is increased to 2 sccm and the power to 15 W (condition C), for which a F_c of 95% was deduced from ellipsometry measurements (Fig. 2.22). Various types of defects appear in that case but the film is still monocrystalline as shown in Fig. 2.34 where the diffraction pattern of the epitaxial film is identical to that of the wafer. We can also see in Fig. 2.34 that at high magnification the interface seems smooth. However at lower magnification the interface is visible as shown in Fig. 2.35-a), most likely due to contamination of the surface before the substrate loading in the reactor, and to a higher concentration of hydrogen at the interface, consistent with the increase of the H_2 flow rate to 2 sccm. In the bulk of the epi-layer, different types of defects are observable. First, dislocations originating from the interface are visible (Fig. 2.33-a) and Fig. 2.35-a)) and spreading up to the surface of the epitaxial film through {110} planes. These dislocations may result from the impurities at the surface of the wafer when loaded into the reactor. They are not visible in the other analyzed samples and may be cleaning process dependent.

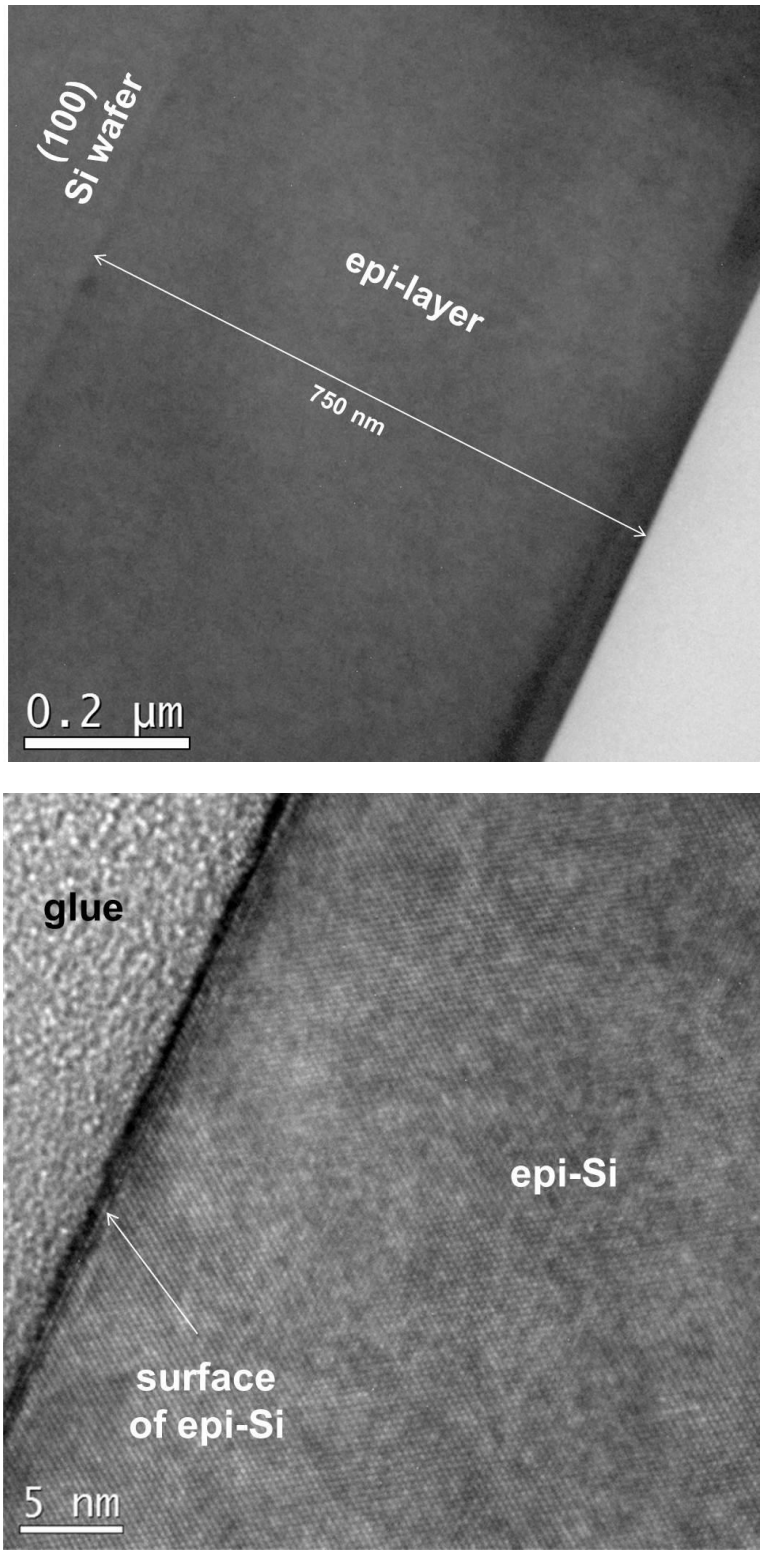

Fig. 2.32 – a) HR-TEM image of a 750 nm thick epi-layer grown at P_{RF}=10 W and 1 sccm of H_2 (condition A). b) Zoom in the surface region of the epi-layer. The growth rate is 0.6 Å/s.

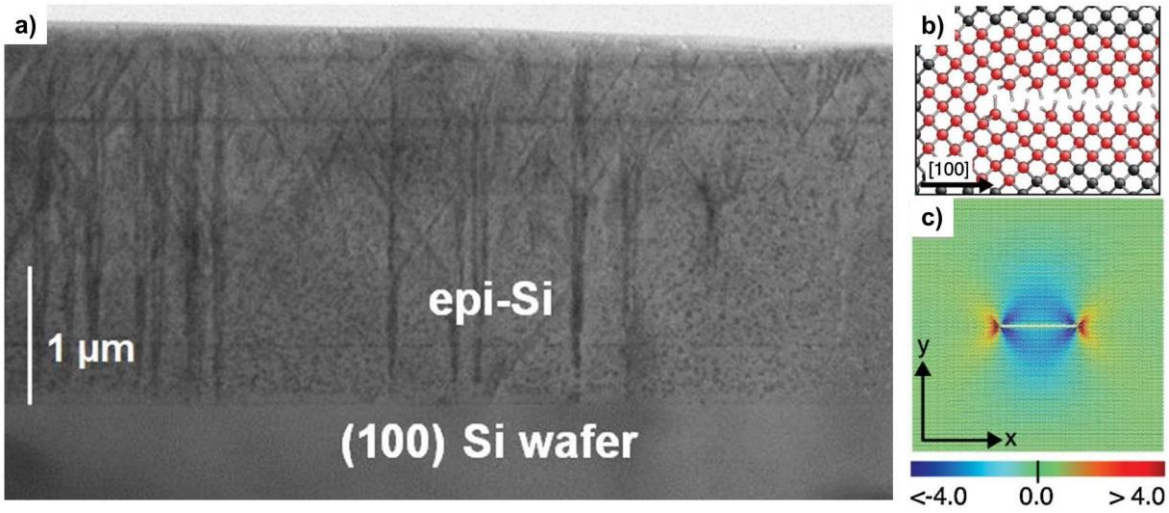

Fig. 2.33 – a) Cross section TEM image taken from a sample deposited at 15 W and 2 sccm of H_2. b) Illustration of the atomistic model of (100) H platelets and c) its simulated distribution of the stress component σ_{yy} [68]. The red area is in tension and the blue one in compression. The unit is the GPa. The growth rate is 1.4 Å/s.

Another possible explanation for the presence of dislocations would be that they could originate from the relaxation due to the accumulation of stress in the layers induced by a higher incorporation of hydrogen than in the previous case at 1 sccm of H_2. Some other dislocations along {110} planes originate from the bulk of the epitaxial film and also spread up to the surface. We think these ones originate from H platelets which are extended defects induced by the segregation of hydrogen in {111} planes. A schematic view of a H platelet is given in Fig. 2.33-b). They are easily recognizable in the films at low resolution by the black spots they form. The higher contrast around the H platelets is due to the stress they induce on the silicon lattice (Fig. 2.33-c) [68]. The presence of H platelets in this case is also consistent with the process conditions for which more hydrogen is injected in the gas mixture, so more hydrogen can be expected in the epitaxial layers. Tsai *et al.* [25] have shown that in the case of SiH_4/H_2 chemistry H platelets were 17 times more likely to result from SiH_4 than from H_2, except when the hydrogen dilution is too high, in which case the H platelets come from the H_2. Interestingly, we can see that we have a similar effect with SiF_4/H_2/Ar gas mixture when the hydrogen flow rate is too high. Thus, even if ellipsometry gives excellent results for this deposition, looking at TEM images shows that the material incorporates a lot of defects.

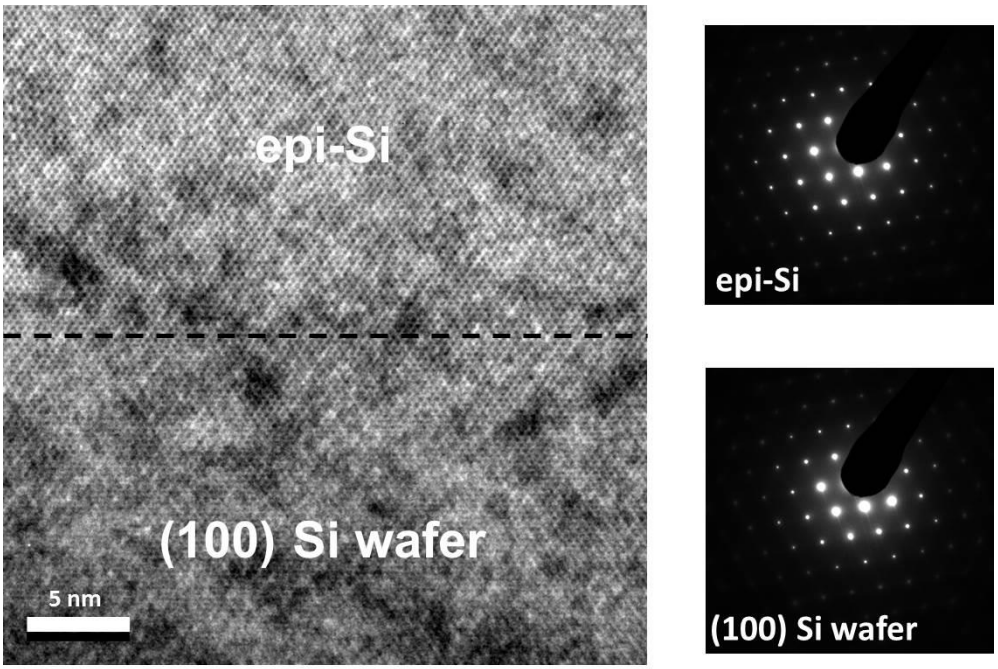

Fig. 2.34 – Zoom in the interface region by HR-TEM between the Si(100) substrate and the epitaxial layers of the same sample as Fig. 2.33 and their associated diffraction patterns.

A high crystalline fraction extracted from ellipsometry is therefore a necessary but not sufficient condition to reach high structural quality. The increase of defects is nevertheless consistent with the fact that the conditions are close to the H_2 depletion transition and that material properties approach polycrystalline deposition, which has been observed in ellipsometry measurements. If the threading dislocations in the {110} planes come from the H platelets, two causes may be identified: either the hydrogen impurities impede to reproduce the silicon lattice or the stress induced by the H platelets makes the film relaxing on top of the H platelets.

Extended defects along {111} planes are also identified, they may originate from segregation of hydrogen and accumulation of H platelets in the {111} planes. Similar planar defects have been observed in hydrogenated silicon obtained by the exposure of a c-Si wafer to a hydrogen plasma [69]. Most of the time they originate from (110) threading dislocations and/or stop in (110) dislocations.

The influence of all these extended defects on electrical properties is difficult to assess, their role is out of scope of this thesis and the investigation of electrical properties will be focused on structural defect-free epitaxial layers. However the effect of the incorporation of hydrogen in the epi-layers on the electrical properties needs to be discussed. On the one hand the incorporation of hydrogen in the layer could have a beneficial effect on its electrical properties by passivating the local defects such as vacancies. It can also act as a hydrogen reservoir for the passivation layer, like highly hydrogenated silicon nitride deposited on top of AlO_x. On the other hand, hydrogen induces some stress in the layers which can lead to a progressive relaxation and dislocation formation. It can also diffuse to the surface or the interface in case of thermal annealing for the passivation or metallization for example, inducing the blistering of passivation layers. In any way, the effect of hydrogen incorporation at this point needs to be taken into account for the integration of this layer in the final solar cell. Finally, marks parallel to the substrate in the {001} planes, observed in Fig. 2.33 at about 500 nm, 2 µm and 2.5 µm may come from variations of H_2 flow rate during the deposition.

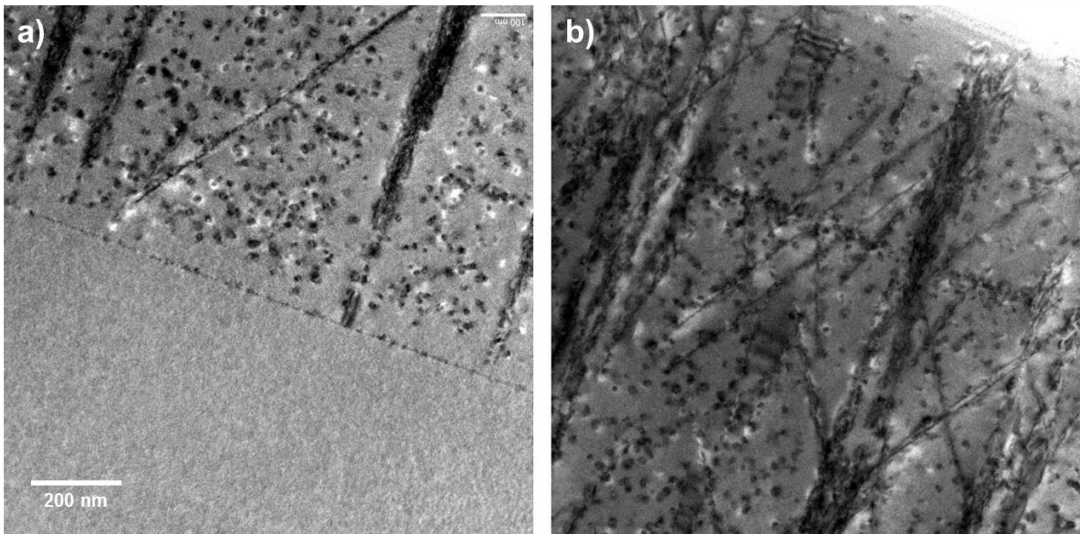

Fig. 2.35 – a) Low resolution TEM image of the interface and b) surface region for P_{RF}=15 W (200 mW/cm^2) and H_2=2 sccm. In both regions H_2 platelets and {111} dislocations are visible. The formation of platelets is consistent with the conditions of relatively high H_2 flow rate. The growth rate is 1.4 Å/s.

It is worth noticing that concerning these conditions TEM images reveal a lot of defects while ellipsometry gives a crystalline fraction (F_c) of 100% (Fig. 2.22), thus a spectrum similar to a wafer and to the epi-layers in conditions A for which TEM images showed defect-free layers. Thus two same crystalline fraction could lead to completely different observations in TEM. Ellipsometry is therefore a very convenient, easy- and quick-to-use tool for the coarse development of epitaxy but is not sufficient because not sensitive to H platelets, {111} planar defects and {001} dislocations.

When the H_2 flow rate is further increased, to 3 sccm ($[H_2]/[SiF_4]$=80%), a new regime of growth is observable and the epitaxial growth is no longer stable. This is consistent with the fact that the process conditions go out from the full depletion region. In these conditions the H_2 depletion is around 70%. The film reveals a three phases growth with at first a defect-free epitaxial growth. After 50 nm, twins appear and a monocrystalline phase with a high density of twins occurs over a thickness of around 200 nm. Finally a transition towards a mix of a-Si:H and µc-Si appears. This case is really interesting in the way that no dislocation is visible contrary to the case at the H_2 depletion transition where the epitaxy is stable but with a larger lattice parameter due to hydrogen which leads to the formation of dislocations. In that case the energy should be released in the stacking faults and twins. Note that in that case the growth rate is up to 4.4 Å/s. Even though, the film is not monocrystalline, it demonstrates the interest of the increase of the H_2 flow rate to improve the growth rate. This is consistent with the observations from Dornstetter [51].

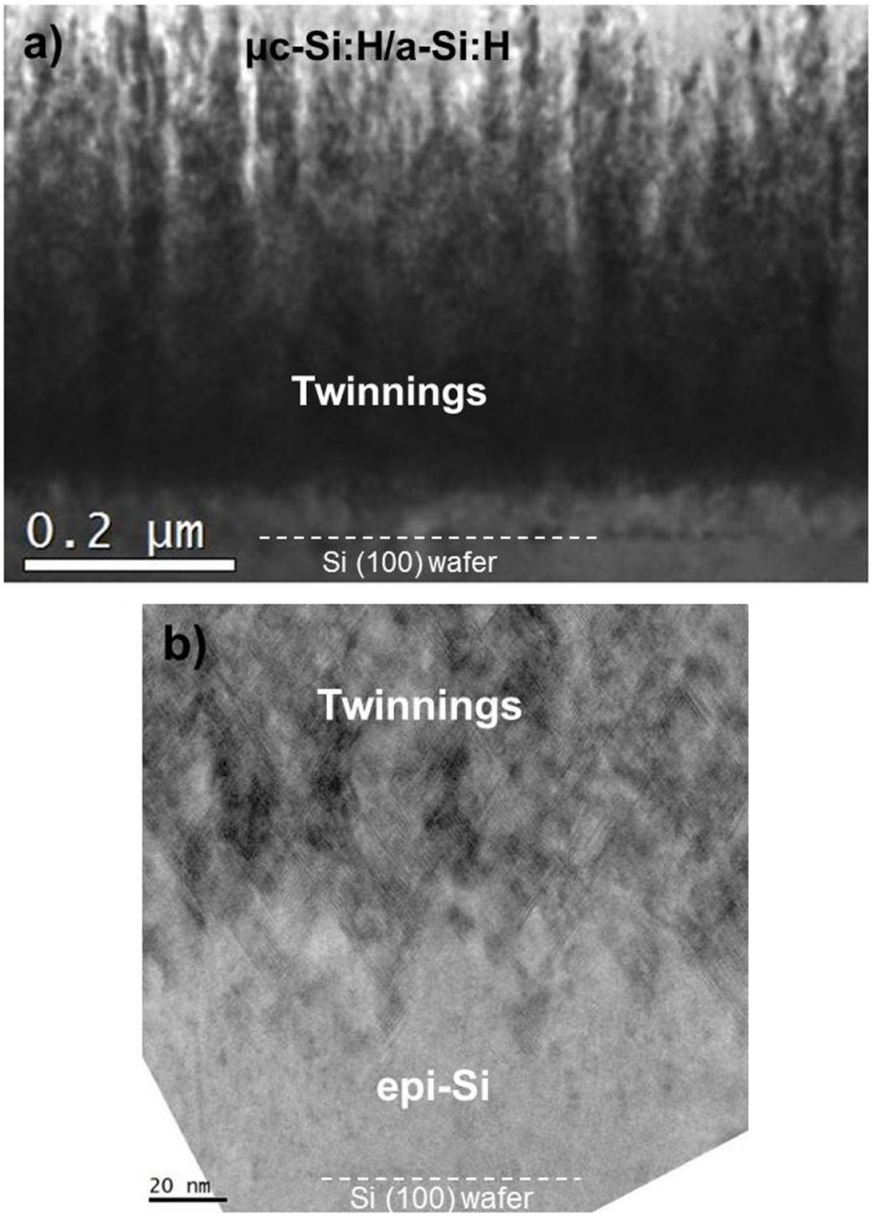

Fig. 2.36 – a) Low resolution TEM image of a film grown at 15 W and 3 sccm of H_2 (condition D). Three phases are distinguishable, a first one of epitaxial growth, a second one of twinned monocrystal growth and a third one of a mix between a-Si:H/µc-Si:H b) Zoom in the interface region and the transition between the first phase (epi-Si) and the second one (twinning) after 50 nm of growth. The growth rate is 4.4 Å/s.

The case of full depletion and high power (H_2=1 sccm, P_{RF}=20 W) is investigated in Fig. 2.37. The power is set at 20 W and the H_2 flow rate is kept low at 1 sccm. Interestingly, this case looks like the previous case of low depletion regime despite the conditions being completely different, confirming the observation obtained by ellipsometry concerning the similar trends with H_2 and P_{RF} increases. A three phase growth scenario is also observed in this case with a first phase of defect-free epitaxial growth over a thickness of around 150 nm, followed by the appearance of twins after. After a certain thickness of growth, the twins formation leads to µc-Si:H deposition. This result is very interesting in the way that these conditions lead to amorphous deposition on glass, and even after epitaxy breakdown the layer is microcrystalline. This also confirms the ellipsometry spectra obtained at high power for which a µc-Si:H signal was observed.

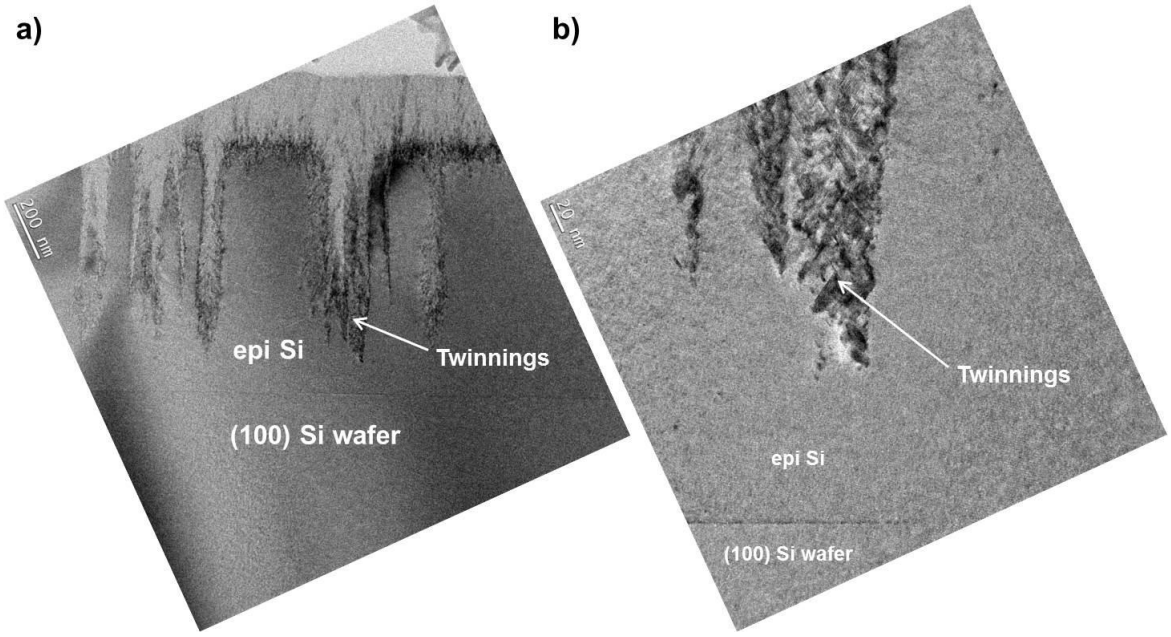

Fig. 2.37 – a) Low resolution TEM image of a film grown at 20 W and 1 sccm of H_2, corresponding to condition B. Three phases are distinguishable, a first one of epitaxial growth, a second one of twinning formation and a third one of µc-Si:H deposition b) Zoom around the interface and the transition between the first phase (epi-Si) and the second one (twins) after 150 nm of growth. The growth rate is 0.7 Å/s.

Keeping the same RF power but increasing the H_2 flow rate is not efficient to recover the material properties as shown in Fig. 2.38. This also confirms the observations obtained by ellipsometry for these conditions. Interestingly, the material is highly defective but still monocrystalline up to a critical thickness of approximatively 1 µm. Above this thickness limit, either grain boundaries appear, meaning that the film becomes polycrystalline (Fig. 2.38-a), or amorphous cones appear (Fig. 2.38-b) depending on the analyzed region. A zoom of the materials in the first phase (defective epitaxial growth) is shown in Fig. 2.39-a) in which a high density of twins can be seen. The diffraction pattern in Fig. 2.39-b) extracted from the first phase of growth shows a monocrystalline phase with extra spots confirming the presence of twins in the films. An interesting feature is that an increase of the RF power alone does not allow to increase the deposition rate, the combination of an increase of the RF power and the H_2 flow rate is required (keeping a full H_2 depletion, i.e. in a H_2-limited regime).

The diffraction pattern (not shown here) of the cone in Fig. 2.38-b) displays a large diffuse spot, characteristic of an amorphous phase. The epitaxy breakdown in case of high P_{RF} therefore seems to be a multi-phase phenomenon in which a first phase of epitaxy is maintained despite the high density of twins and subsequently, after a critical thickness, some grain boundaries appear. The appearance of amorphous cones happens in a similar way. Note that the formation of amorphous cones has also been reported for SiH_4/H_2 epitaxy [70]. They assumed the epitaxy breakdown into amorphous cones was due to the accumulation of strain induced by the coalescence of excess hydrogen and in particular H platelets. The same explanation is not viable in our case where the segregation of hydrogen has not been observed. The amorphous cone broadens along the deposition and the height of the amorphous cone is larger than the height of the epitaxial layers in its vicinity. The higher growth rate of amorphous phase with respect to that of epitaxial phase makes that amorphous cones overcome the epitaxial layers. These phenomena of broadening and random formation suggest that for sufficiently long deposition time, the full film should be amorphous at the top. This case confirms the necessity to

to respect a certain gas ratio (< 1/3) to perform epitaxy on <100> oriented substrates despite a full depletion of H_2.

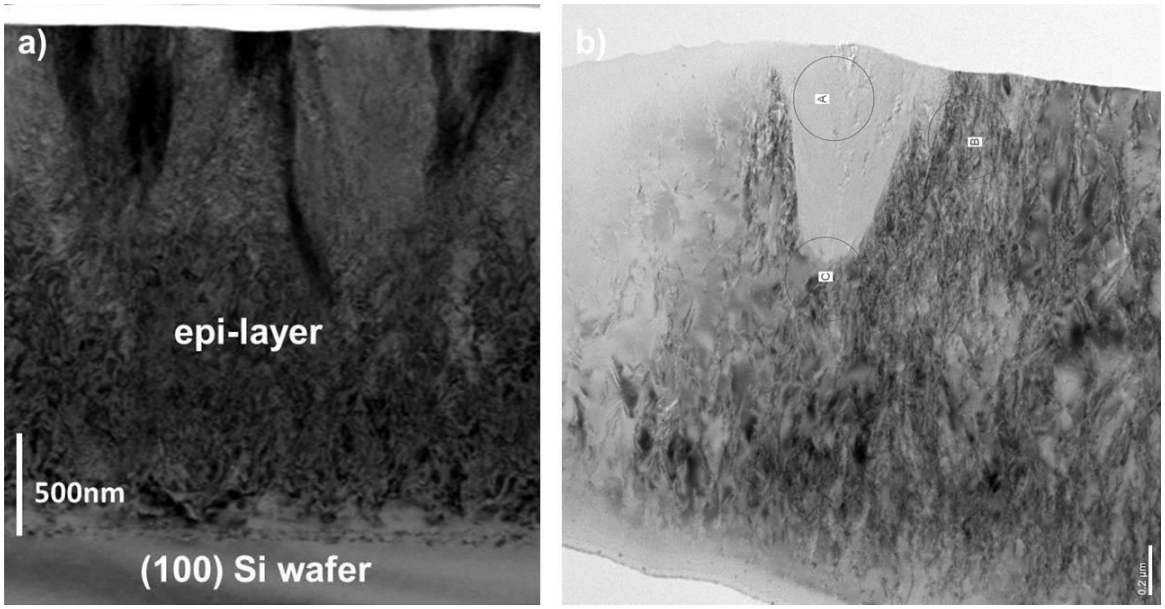

Fig. 2.38 – TEM image of epi-layers grown at 20 W and 2 sccm of H_2 at two different regions on the sample. The growth rate is 1.5 Å/s.

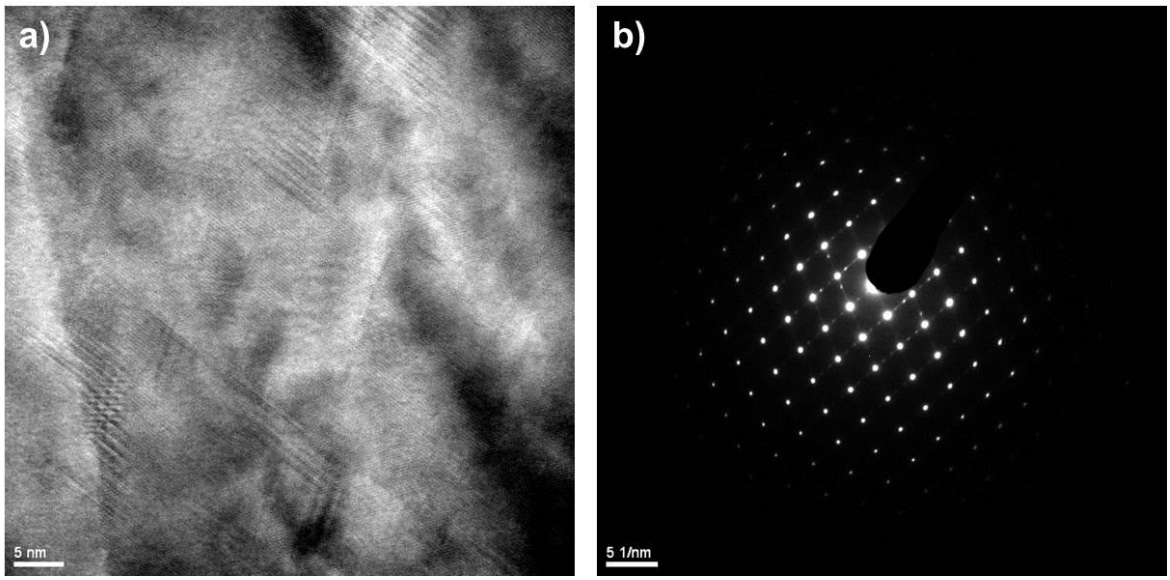

Fig. 2.39 – a) Zoom in the first phase of growth (defective epitaxy) obtained by HR-TEM revealing a high concentration of twins in the layer. b) Associated diffraction pattern showing the monocrystallinity of the film and confirming the presence of twins.

2.4.3. XRD analysis

TEM provides a lot of information but only for small area, XRD is a complementary technique because it allows to measure structural properties on larger area, typically a few cm^2 against μm^2 for TEM. Moreover the dopant impurities necessarily have an effect on the lattice parameter and likely on the mosaicity, thus it is mandatory to assess macroscopic structural properties of intrinsic epitaxial layers before introducing an additional potential source of defects.

Epitaxial thin films have been characterized by X-ray diffraction (XRD) using a Bruker D8 diffractometer. Omega/2theta measurements and rocking curves have been performed to respectively evaluate strain/relaxation and mosaicity of the layers. The analyzed crystallographic planes are (004) and (224), therefore planes parallel and inclined to the surface respectively. The setup is composed of a Cu tube for X-ray generation, a Goebel mirror, a 1 mm large divergence slit, a double reflection Ge(220) monochromator for the primary beam optics (emission side) and a linear detector of 14 mm with a 1 mm large analysis slit for the secondary beam optics (detection side). Measurements are performed using the Kα1 radiation of Cu and at 2 steps per second with a step of 0.0001°.

The ω/2θ scan and the rocking curve (RC) on (004) measured on a wafer and epitaxial layers almost free of defects (cond. A) are given in Fig. 2.40. The results have been normalized and centered on theoretical values of diffraction peak for (004) planes in a <100> oriented silicon substrate, namely ω=34.56°.

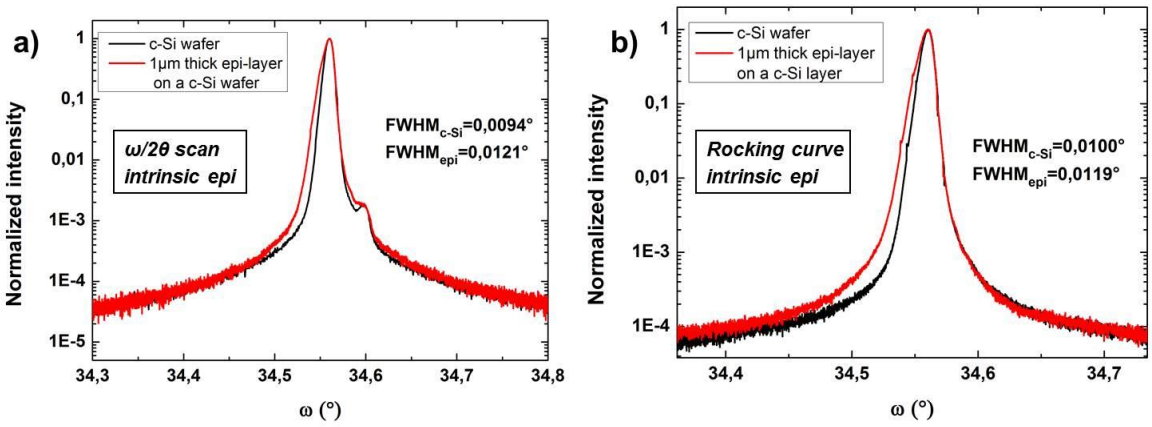

Fig. 2.40 – a) Normalized ω/2θ scan on (004) and b) rocking curve on (004) for a wafer and good quality epitaxy in conditions A.

In both cases the diffraction peak of the epi-layers and that of the substrate overlap, leading to very close FWHM values. Indeed a difference of less than 3.10^{-3} ° in the FWHM is observable for the ω/2θ scan which means that the lattice parameter of epi-layers is very close of that of the substrate, and we are now limited by the resolution of the equipment which, according to our calculations, corresponds to a difference of lattice parameter of 1.10^{-3} Å. The use of a monochromator with a better resolution around ω=34.5° (Ge(004) 2 or 4 reflections) is therefore more suitable for this type of epitaxial layers.

This small difference of lattice parameter limits the potential problem of relaxation in the epi-layers. The slight shoulder at 34.60° on the right of the diffraction peaks is a measurement artefact. This can be avoided by reducing the slit size or the detector size but this detrimentally affects the flux. To our knowledge such close structural properties confirmed by similar diffraction scans between epi-layers and wafer have never been reported so far.

The RC gives also very close values for the FWHM of the wafer and the epi-layers with a difference of 2.10^{-3} °, which means that the epitaxy presents a very low mosaicity. This is an important result for epitaxial emitters because in that case the lateral current in the emitter to reach metallic contacts will not be affected by the grain boundaries or dislocations.

XRD measurements have also been performed on layers grown in conditions B and C. Results are given in Fig. 2.41. Interestingly, whereas electron diffraction pattern shows a perfectly monocrystalline phase for conditions C (in green), XRD shows that the film presents a variation of the lattice parameter along the thickness, related to the large broadening of the diffraction peak at lower angle. It also means that the lattice parameter is larger (in average) than that of the substrate. These results are consistent with the process conditions used for this sample, for which the hydrogen flow rate has been increased. Indeed an increase of the hydrogen incorporated in the layer is expected and is characterized, not exclusively, by the presence of hydrogen platelets in the layers. We will see later that the increase of hydrogen incorporation is confirmed by Raman spectroscopy. The most likely explanation is that the incorporation of hydrogen (especially by the presence of H platelets) distorts the crystal lattice. This case is similar to what is observed with SiH_4/H_2 chemistry where systematic compressive strain is observed in as grown epitaxial layers [71] due to a larger lattice parameter. After annealing above 300°C the strain decreases and the diffraction peak of the epi-layer is shifted towards that of the substrate. This effect is attributed to the desorption of hydrogen which allows the lattice parameter to become closer to that of the substrate.

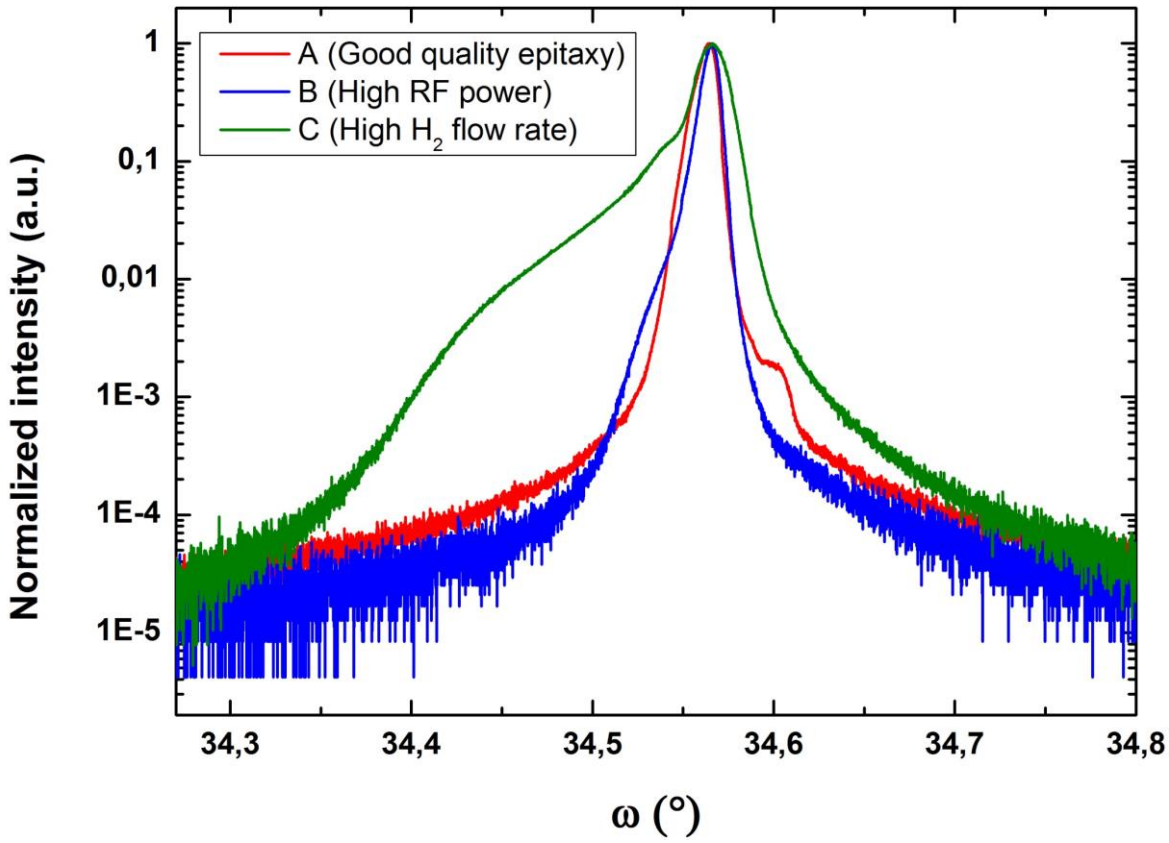

Fig. 2.41 - Normalized ω/2θ scan of (004) diffraction for growth conditions A, B and C, namely low H_2 flow rate/low RF power (10 W, H_2=1 sccm), low H_2 flow rate/high RF power (20 W, H_2=1 sccm) and a higher H_2 flow rate/moderate RF power (15W, H_2=2 sccm).

Although ellipsometry gives similar results between conditions A and C, XRD shows that significant differences appear between these conditions due to the distortion of the film. XRD is therefore an excellent tool to differentiate epitaxy with good structural properties (conditions A) and at the H_2 depletion transition.

In the case of process conditions B, i.e. full depletion and high RF power (20 W), a broadening at lower angle is also observed. It also means that in these conditions the lattice parameter is larger than that of the substrate but its dispersion is reduced, compared to the case of conditions C, due to its smaller FWHM. Given that this diffraction peak of the layer is relatively narrow and similar to what obtain in best case of epitaxy with SiH_4/H_2, we think it only results from the contribution of the first phase of epitaxial growth and not of the µc-Si:H deposition after epitaxy breakdown. In order to further analyse the structural properties of these layers, reciprocal space mappings have been performed, this should allow to determine if the layers are strained or relaxed in conditions B and C due to the larger lattice parameter we observed.

2.4.3.1. Reciprocal space mapping (RSM) on (004) planes

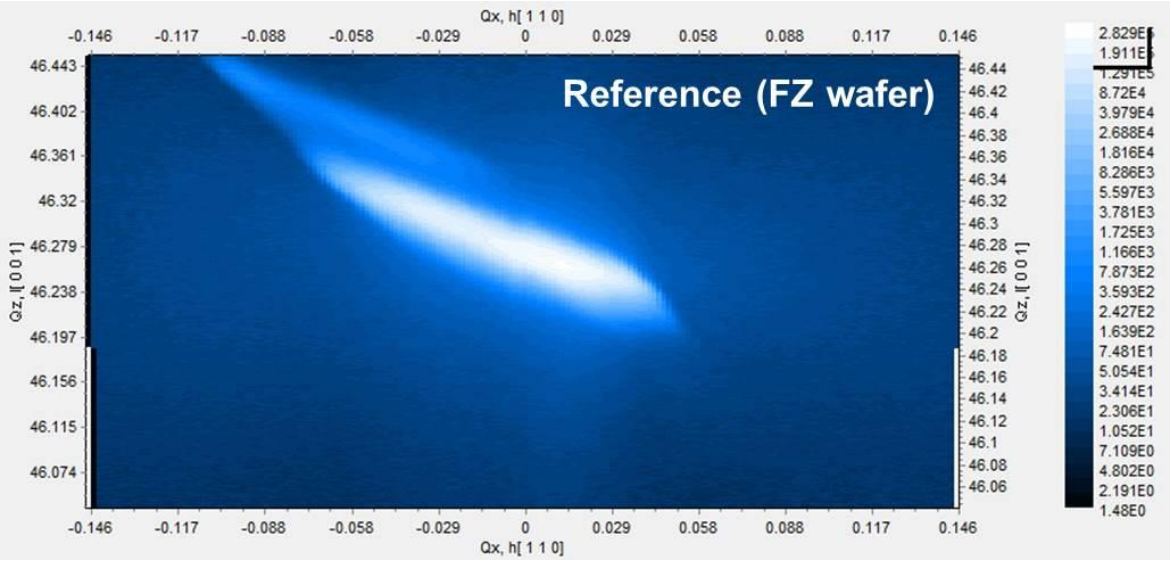

Fig. 2.42 – RSM on (004) planes for a <100> oriented silicon wafer used as reference. The light stain at the top left of the diffraction peak is a measurement artefact.

Fig. 2.42 features the RSM on (004) planes for a FZ n-type (1-5 Ω.cm) wafer. The lengthening of the diffraction peak is due to the lack of crystal analyzer (monochromator on the detection side). By reducing the slit size, these artefacts can be reduced but it induces a dramatic loss of intensity. The resolution is correct enough to clearly distinguish the layer from the substrate in case of epitaxy from SiH_4/H_2 gas mixture, so it has been considered that in this configuration the system would have a sufficient resolution to discriminate conditions by their XRD scans and in particular RSM. The light stain at the top left of the diffraction peak is a measurement artefact, it corresponds to the same artefact at 34.6° previously observed in the scans. This can also be avoided by reducing the slit size or the detector size but, in the same way that for the lengthening of the diffraction peak, this lowers the intensity.

The RSM of good quality epitaxial layers grown in conditions A, in Fig. 2.43, shows that no significant differences are observable with respect to that of a bare FZ Si wafer. Diffraction peaks of the epitaxial layer and that of the substrate overlap, indicating that no significant difference of lattice parameter is observable, thus confirms the excellent structural properties of the epitaxial layers. Thus no strain but especially no relaxation is expected for these conditions. The relaxation of the epi-layers would induce the presence of dislocations which would affect the performance of the device. From these measurements no dislocation at the interface or in the bulk due to an accumulation of stress in the layer should be expected.

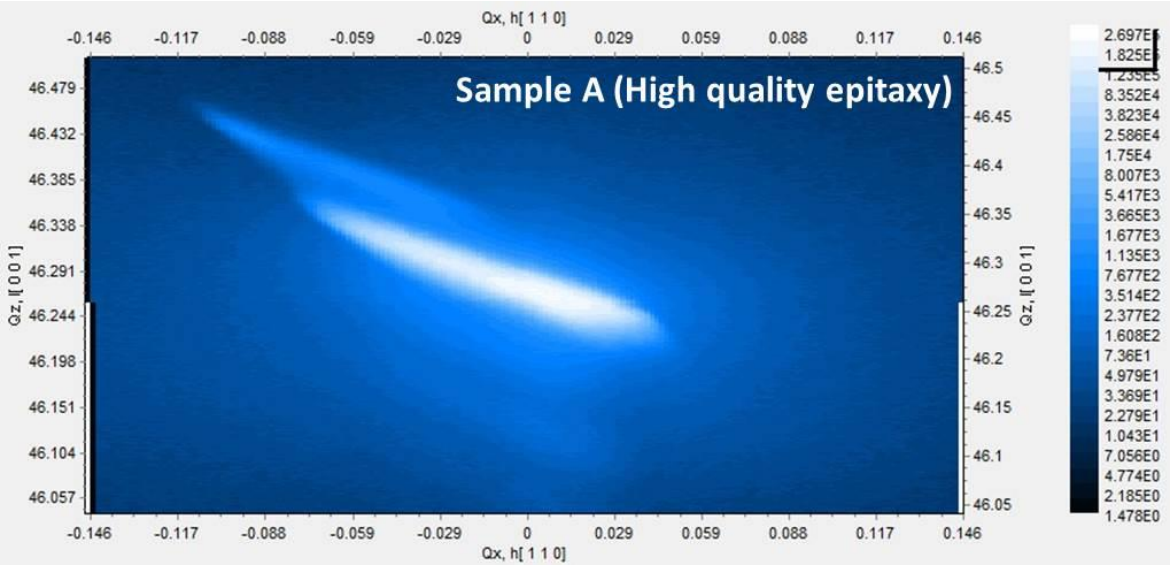

Fig. 2.43 – RSM on (004) planes for epi-layers grown with conditions A (low power and low H_2 flow rate).

When the power is increased, to reach conditions B, the RSM displays a shouldering at low Qz, as shown in Fig. 2.44. This indicates a slight dispersion of the lattice parameter in the direction of growth.

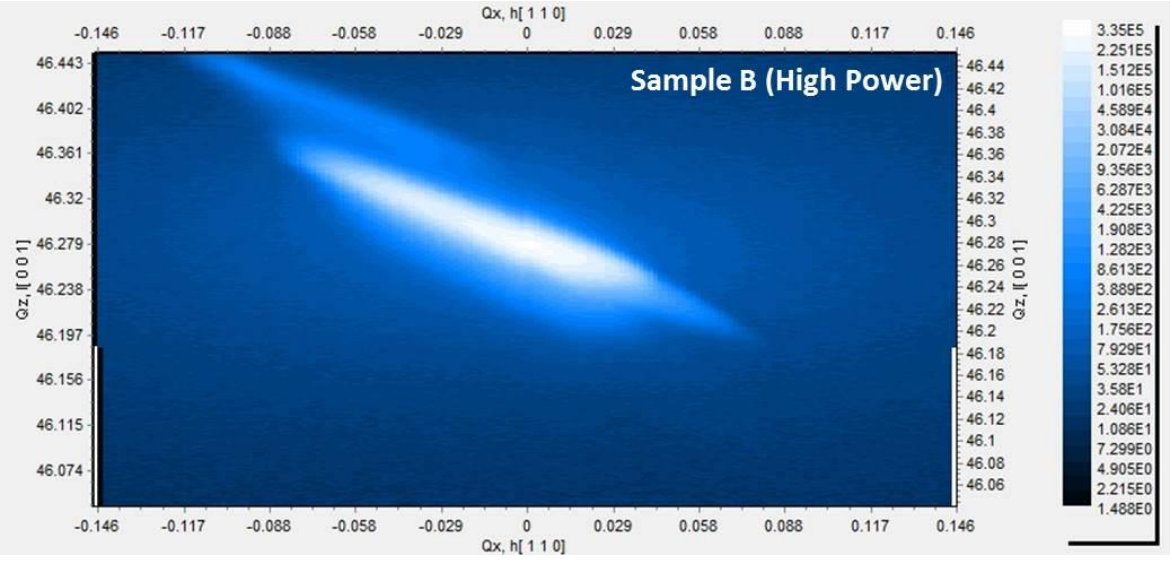

Fig. 2.44 – RSM of (004) planes for epi-layers grown with conditions B (high power and low H_2 flow rate).

The increase of hydrogen flow rate at low power in order to approach the transition has a more pronounced effect on the XRD measurement (Fig. 2.45). The large broadening at low Qz indicates a strong dispersion of lattice parameter in the epitaxial film, consistent with the process conditions. The increase of H_2 flow rate should induce a rise of hydrogen concentration in the layer and thus contributes to the increase of the lattice parameter in the epitaxial layers.

These results, not surprisingly, confirm the conclusions deduced from the ω/2θ scans. To know if as grown layers in the case of conditions B and C are strained or relaxed, RSM on asymmetric planes have been performed.

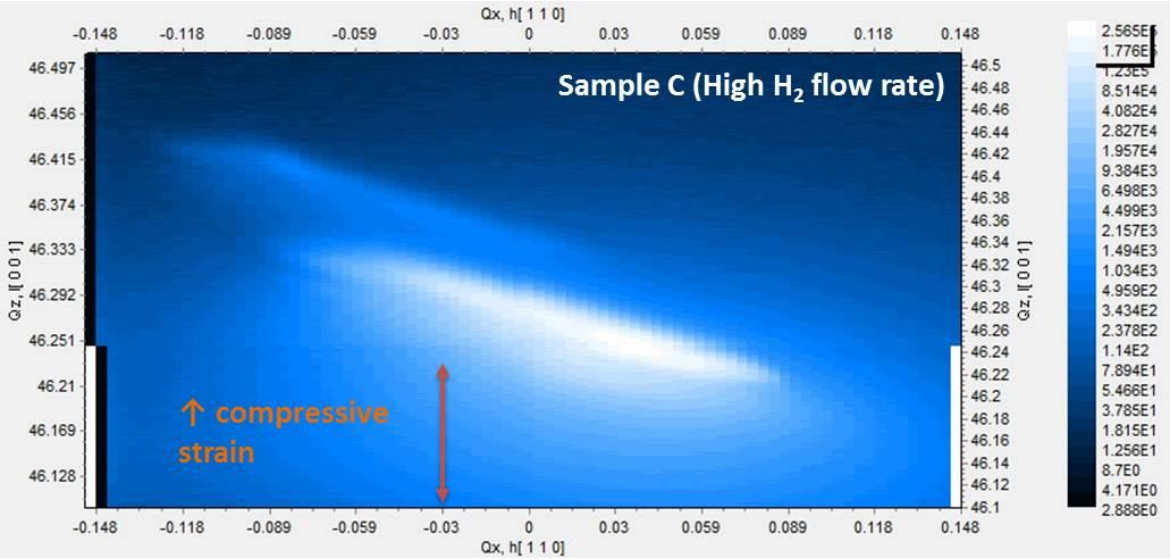

Fig. 2.45 – RSM of (004) planes for epi-layers grown with conditions C (H_2=2 sccm).

2.4.3.2. RSM on (224) planes

Fig. 2.46 shows the RSM on (224) planes for a bare FZ wafer used as a reference for comparison. Once again, measurement artefacts are observed. The same extra spot is observed for which a reduction of the slit size can avoid this effect but again it strongly affects the flux.

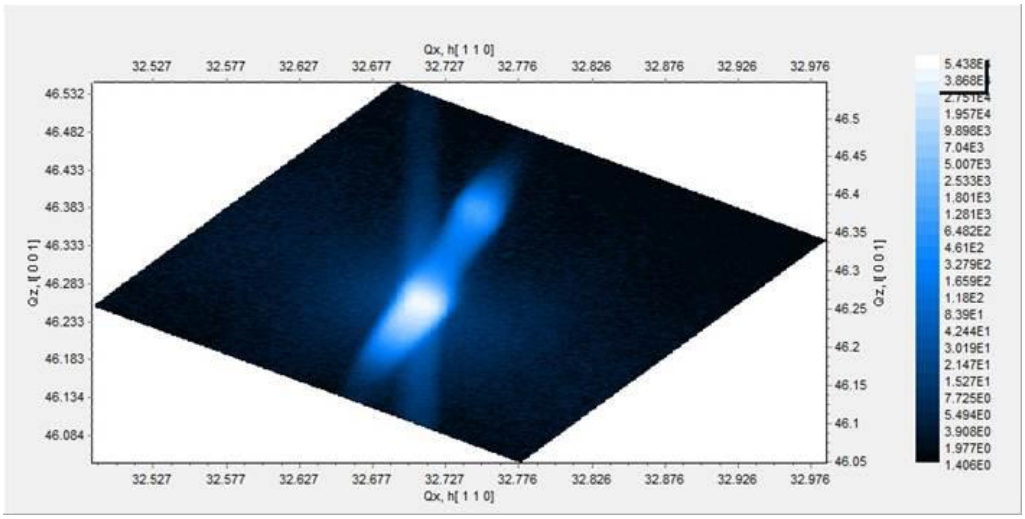

Fig. 2.46 – RSM of (224) planes for a <100> oriented silicon wafer used as reference.

Given that no significant lattice parameter difference has been observed for conditions A, the RSM on (224) has not been performed for this sample.

In Fig. 2.47 the RSM on (224) is detailed. It is difficult to conclude on the strain/relaxation since the broadening in this RSM is similar to that of the reference. However the broadening in the direction normal to the vector $\mathbf{g}_{224}$ is characteristic of a mosaicity following these planes.

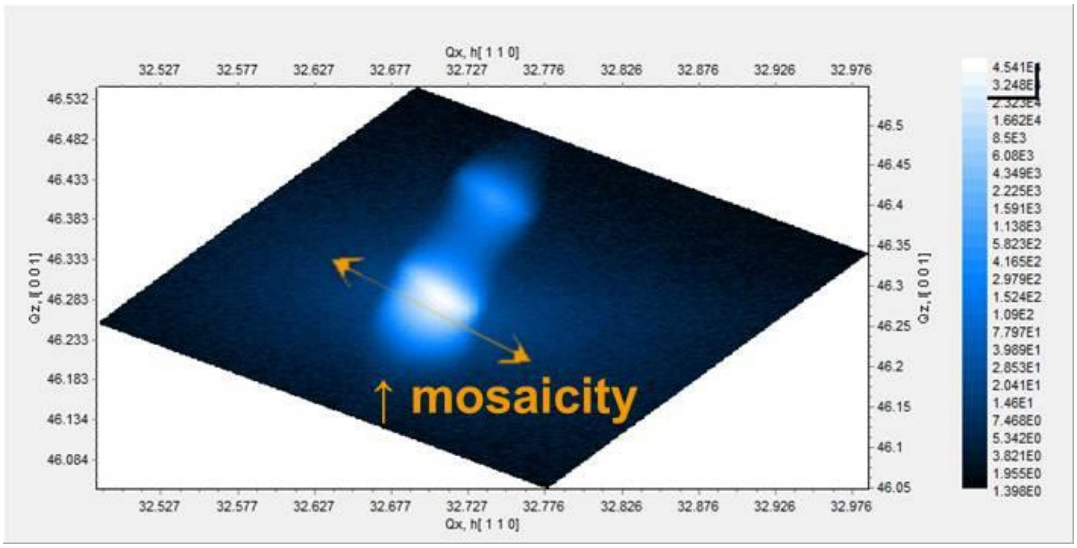

Fig. 2.47 – RSM of (224) planes for epi-layers grown with conditions B (high power and low H_2 flow rate).

Similar observations can be done with the RSM on (224) planes for epitaxy in conditions C, where the effect is even more pronounced. Again, it is difficult to get quantitative information from these results.

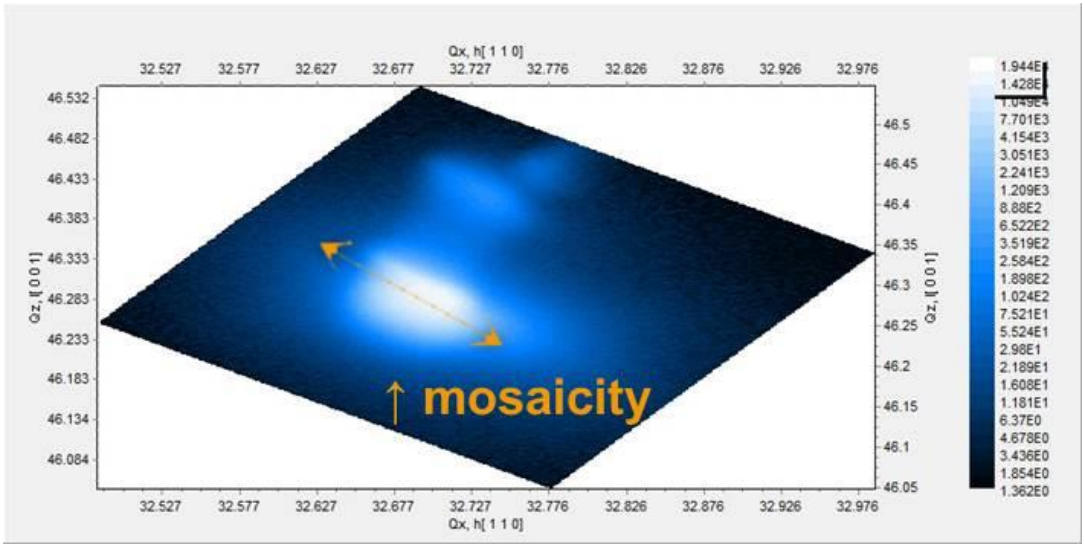

Fig. 2.48 – RSM of (004) planes for epi-layers grown with conditions C (H_2=2 sccm).

Therefore, HR-XRD gives additional information on the epitaxial layer and allows to discriminate high quality epitaxy and epitaxy at the H_2 transition where ellipsometry is unable to differentiate these cases. Nevertheless this type of scan is not reliable to compare results between conditions B and C.

2.4.3.3. Pole figures

In order to focus on the difference between conditions B (high power) and D (high H_2 flow rate), for which ellipsometry spectra gave the same results (µc-Si:H), another approach has been investigated.

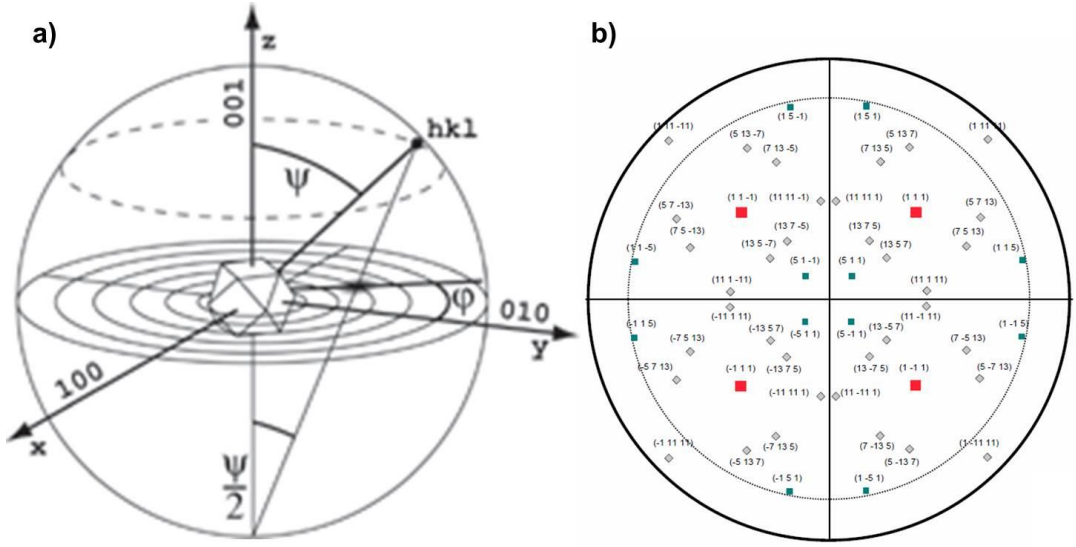

Fig. 2.49 – Representation of the stereographic projection and associated angles ψ and ϕ. b) (111) pole figure of a <100> diamond film with primary orientations (in red), first order twinnings (in blue) and second order twinnings (in grey) [72]. For a perfect monocrystal, only (111) planes at ψ=54.7° (primary orientation) must be observed.

Knowing that the type of defects for both cases are different and as a consequence, electron diffraction patterns are different, pole figures have been performed to try identifying a different signature in order to avoid using a time consuming and destructive characterization technique like TEM.

The principle of a pole figure is given in Fig. 2.49-a). It consists of the representation of the stereographic projection of the diffracted planes for a given crystallographic orientation on a same figure, as a function of ψ (tilt) and φ (azimuth). The (111) pole figure of a <100> oriented film is shown in Fig. 2.49-b) illustrating the 4 (111) planes (in red) and the possible position of the first and second order twins in such a film [72]. Due to the absence of twinning in a perfect FZ wafer no other diffraction peaks that the primary orientations at ψ=54.7°, the 4 (111) planes, should be observed on a (111) pole figure. A (111) pole figure has been performed on layers obtained under conditions C (Fig. 2.50). The absence of extra spots confirms the fact that no twins are formed in these conditions, as observed by TEM.

Comparatively, a pole figure on epitaxial layers in conditions B has been performed for ψ ϵ [0;20°] and [70;85°], results are shown in Fig. 2.51. The 4 spots around ψ=15° (Fig. 2.51-a)) and the 8 spots around ψ=80° (Fig. 2.51-b)) are characteristic of first order twinning. However no second order twinning has been observed in these layers.

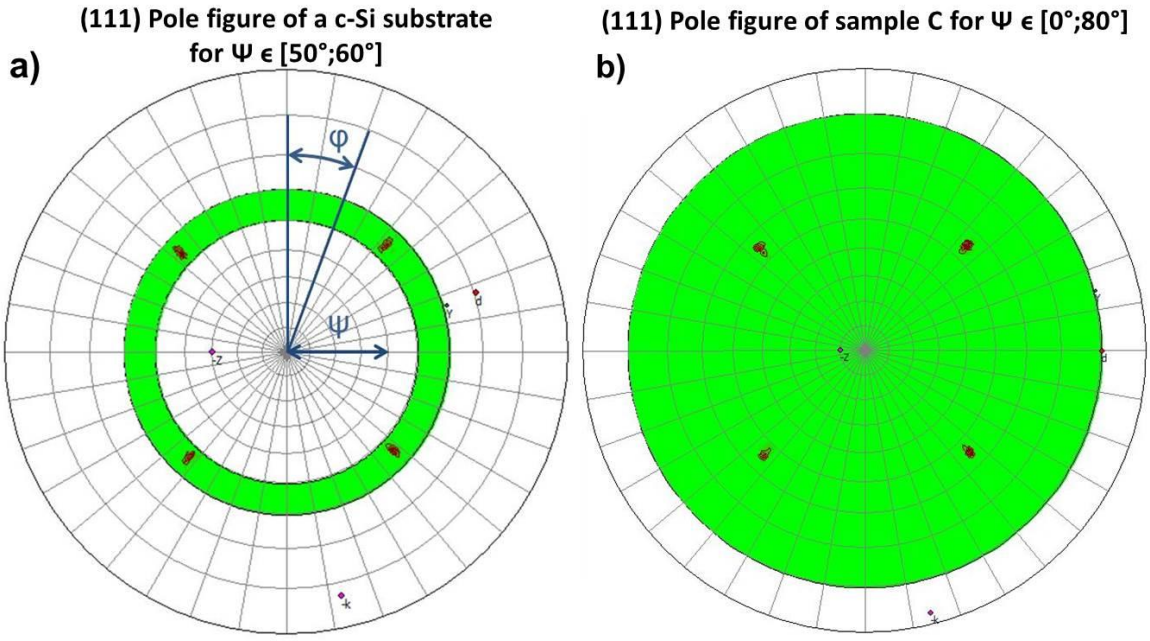

Fig. 2.50 – a) Partial (111) pole figure (ψ ϵ [50;60°]) of a <100> oriented FZ silicon wafer b) (111) pole figure of the <100> oriented film grown in conditions C. The 4 (111) primary orientations are present but no extra spots are observable indicating the absence of twins in these conditions.

When process conditions are in conditions D (15 W, H_2=3 sccm), i.e. out of the full H_2 depletion region, we have seen that after a few tens of nanometers a twinning-induced epitaxy breakdown occurs (Fig. 2.36). This observation is also confirmed by the (111) pole figure performed on this sample as shown in Fig. 2.52. The presence of the 4 spots around ψ=15° and the 8 spots around ψ=80° highlights the formation of twins in the layer.

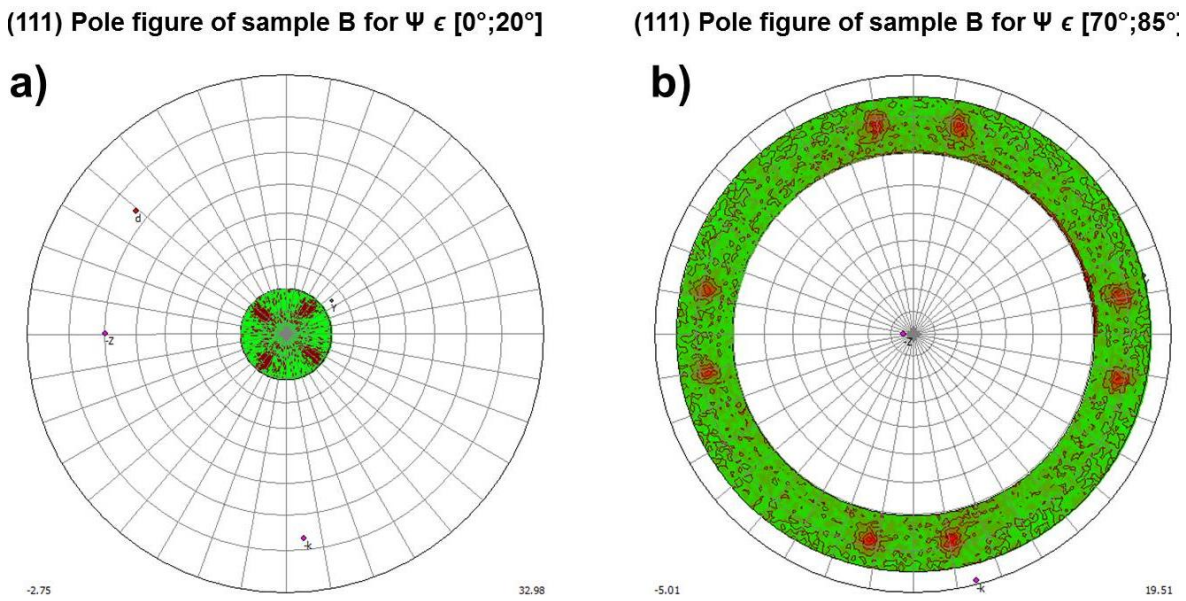

Fig. 2.51 – a) (111) pole figure of a <100> epitaxial Si film grown in process conditions B for ψ between 0° and 20°. b) (111) pole figure of a <100> epitaxial Si film grown in process conditions B for ψ between 70° and 85°. Both pole figures are done for ϕ varied from 0° to 360°.

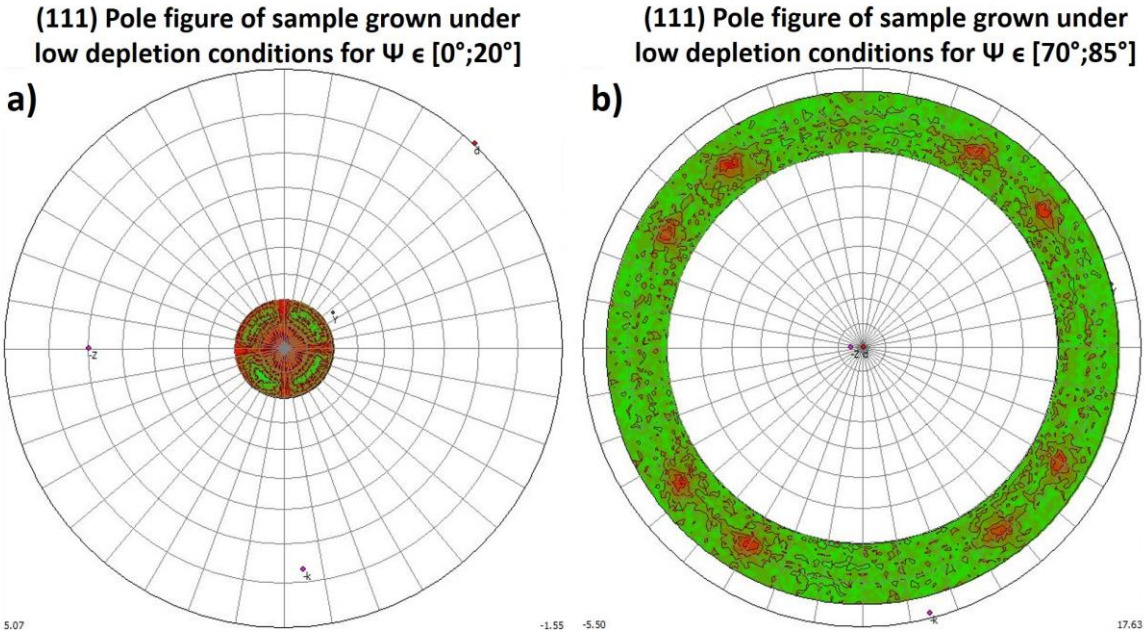

Fig. 2.52 – a) (111) pole figure of a <100> epitaxial Si film grown in conditions D for ψ between 0° and 20°. b) (111) pole figure of a <100> epitaxial Si film grown under low depletion conditions for ψ between 70° and 85°. Both pole figures are done for ϕ varied from 0° to 360°.

Therefore this result is identical to that observed at high P_{RF} and low H_2 flow rate (condition B). However, in contrast with condition B, a diffraction occurs around ψ=0° indicating that some grains are <111> oriented in the direction of growth. Thus, the poly/microcrystalline material obtained from conditions B or and D can be differentiated by their texturation, i.e. the orientation of the grains. It should be noted that these observations do not exclude other orientations in these films, such as <110>

or <311> grains. θ/2θ scans (commonly used in powder diffraction) are required to determine every orientation in the textured films.

As a conclusion, these results are consistent with TEM observations and give an interesting approach for a fast characterization of samples in order to identify the source of epitaxy breakdown and to optimize epi-layers. Ellipsometry, HRXRD and pole figure are complementary characterization technique which allow to differentiate the growth under conditions A, B, C and D. The existence of twins is caused by either a too high RF power or a too low depletion. Nevertheless, these cases can be differentiated by the H_2 depletion, using a RGA, or by the presence of <111> oriented grains in the case of low depletion (cond. D). Besides, conditions A and C can be differentiated by HR-XRD comparing their of ω/2θ scan. Thus ellipsometry, XRD (HR-XRD and/or pole figure) and RGA are complementary techniques for the full development of process conditions in order to determine the optimum conditions for structural defect-free epi-layers and thus succeeding in a technology transfer.

2.4.4. Raman spectroscopy

Raman spectroscopy is an easy way to obtain complementary information on the structural properties of the epitaxial layers. In this part, each spectrum has been obtained for a laser excitation wavelength of 473 nm.

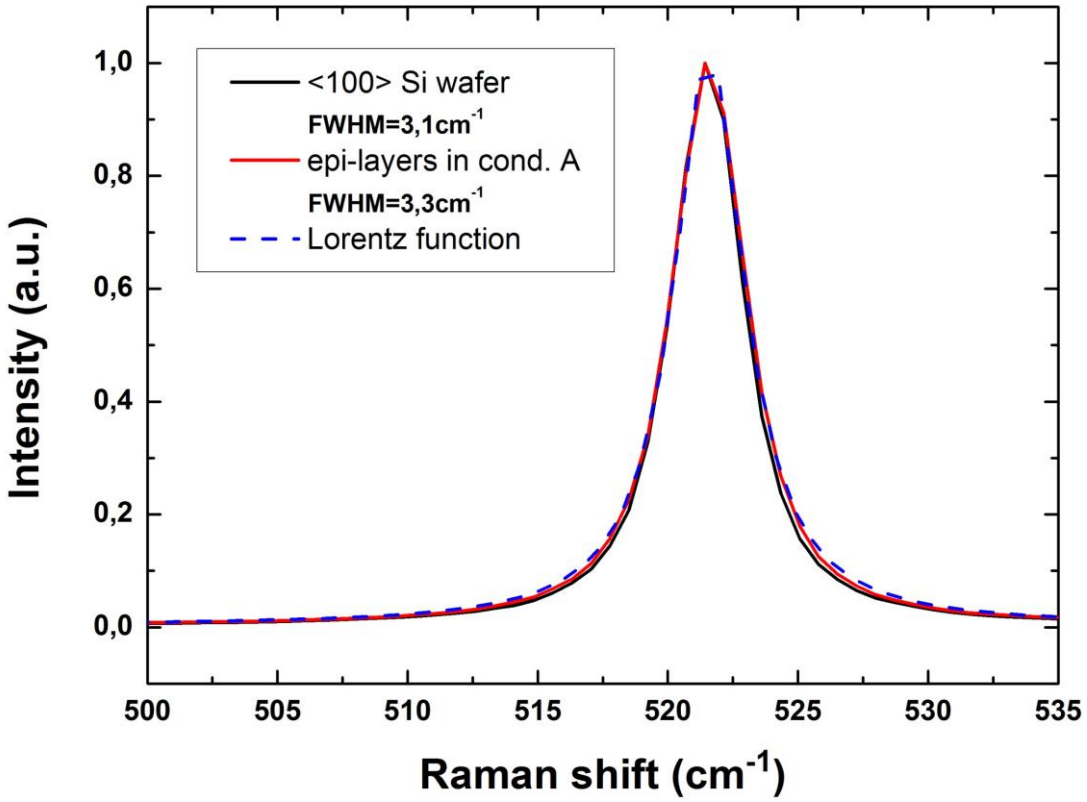

Fig. 2.53 – Comparison of high quality epitaxy (process conditions A) Raman spectrum and that of a <100> c-Si FZ wafer. Spectra have been normalized for a better comparison. FWHM values are extracted from fitting with a Lorentz function. As shown, both peaks excellently fit with a Lorentz function. The position of both peaks is 521.5 cm^{-1}.

The penetration depth in c-Si at this wavelength is less than 600 nm and all the studied films are thicker than that, meaning that the signal is mostly coming from the grown film rather than from the substrate. Moreover the penetration depth in µc-Si:H and a-Si:H is lower than in c-Si, as a result 600 nm is the upper limit of penetration depth for every layer we have studied. Therefore in case of epitaxy breakdown, the contribution from the substrate is even more negligible. Nevertheless it is worth noticing that the contribution of the epi-layers before epitaxy breakdown is also affected. A comparison between Raman spectra of epi-layers, obtained under good conditions (A) and for a wafer is given in Fig. 2.53. Both Raman spectra have been fitted with a Lorentz function and FWHM values of 3.1 cm^{-1} and 3.3 cm^{-1} have been respectively extracted for a wafer and the epi-layer grown under conditions A. The very close value of FWHM obtained from fit with Lorentz function confirms, once more, the quality achievable by LTE with $SiF_4/H_2/Ar$ chemistry. To our knowledge, so close values of FWHM between epi-layers and a FZ wafer have never been reached for epitaxy at 200°C. When the RF power is increased, the Raman peaks broaden and shift towards low Raman shift values which is characteristic of µc-Si:H material.

2.4.4.1. Influence of RF power

Up to 15 W, the Raman spectra are similar to these of a perfect silicon monocrystal. This confirms the ellipsometry results in Fig. 2.26, for P_{RF}=15 W, and shows that the drop of ε_i(4.2eV) is due to the roughening of the surface. From 18 W, and when the RF power is further increased to 20 W and 25 W, a broadening of the Raman peak of c-Si around 520 cm^{-1} appears, associated to a shift towards low Raman shifts values.

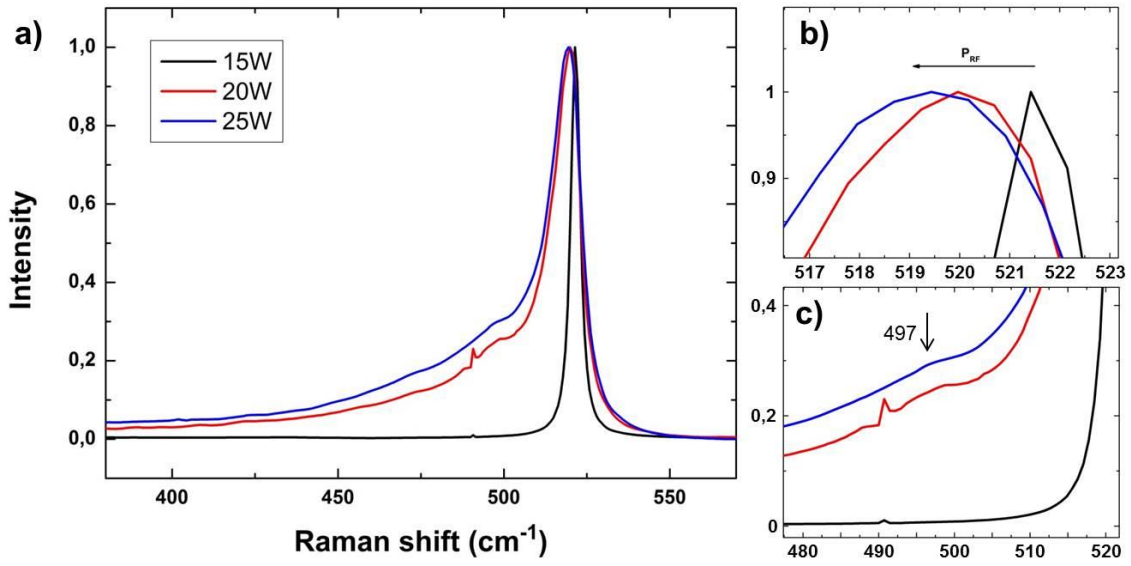

Fig. 2.54 – a) Raman spectra for a constant H_2 flow rate of 1 sccm and various values of P_{RF} b) Zoom in the Raman peak of c-Si around 520 cm^{-1} c) Zoom in the spectra at a Raman shift around 500 cm^{-1} highlighting the hump at 497 cm^{-1}.

The theoretical value for c-Si Raman TO peak is 520 cm^{-1} while in our case the Raman peak for a silicon wafer is at 521.5 cm^{-1}, this is attributed to the lack of control of the temperature in the measurement environment. This shift towards low wavenumbers could be attributed to a tensile strain.

However, this result is not consistent with the conclusions extracted from XRD measurement where an in-plane compressive stress was observed.

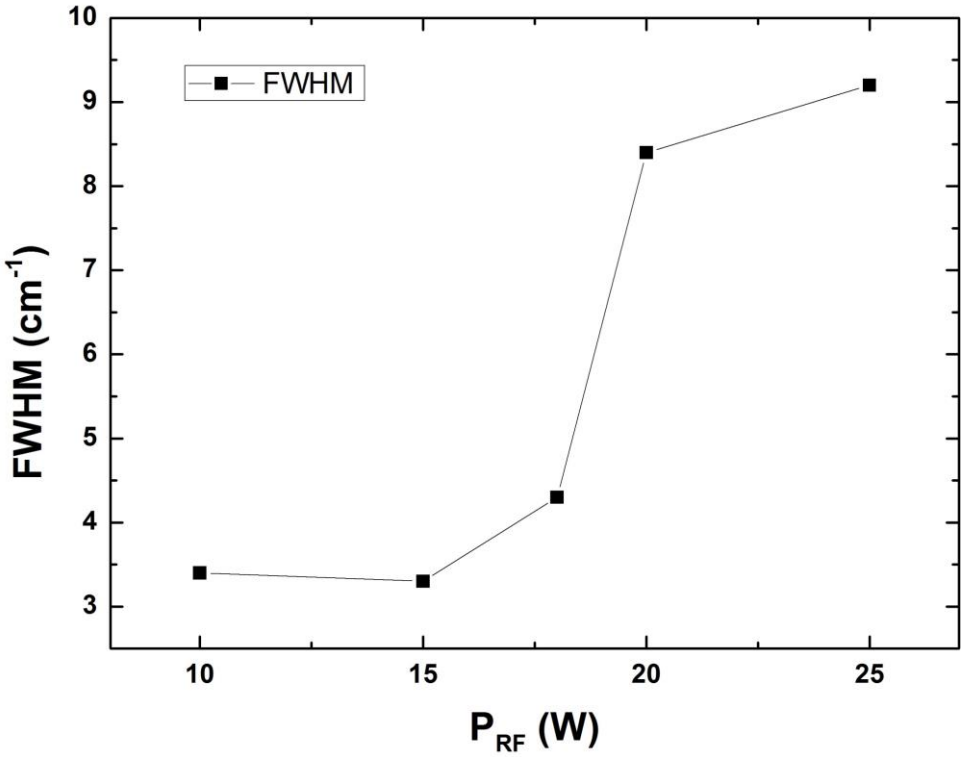

Fig. 2.55 – Evolution of the FWHM of TO mode of c-Si as a function of RF power at H_2=1 sccm. All these samples have been grown under conditions of full H_2 depletion. The gas flow rates are $SiF_4/H_2/Ar$=3.6/1/88 sccm and the pressure is fixed at 3 Torr.

However TEM analysis revealed the presence of µc-Si:H at the top of the layer and the formation of grain boundaries is known to affect the position of the Raman peak, in particular it also shifts towards low values, so the most likely explanation of this shift towards low wavenumbers is the presence of grains boundaries in the µc-Si:H layer. The band at 497 cm^{-1} has been reported to be attributed to faults or dislocation on the nanometer scale in polycrystalline silicon films [73] or to the presence of nanocrystals [74],[75].

The evolution of the FWHM as a function of P_{RF} is shown in Fig. 2.55. The trend in this figure shows that a RF power threshold (here 15 W) for these conditions of $[H_2]/[SiF_4]$ ratio is in accordance with the trend observed by ellipsometry (Fig. 2.26).

2.4.4.2. Influence of H_2

Raman spectra for different H_2 flow rates are shown in Fig. 2.56. As it can be seen, even at H_2=2 sccm, Raman spectra gives low FWHM values, very close to FWHM values of Si wafer, while XRD and TEM shows that defects were present in the layer. Thus looking at the FWHM of the silicon peak at 520 cm^{-1} is not the best figure of merit to assess structural properties of epitaxial layers.

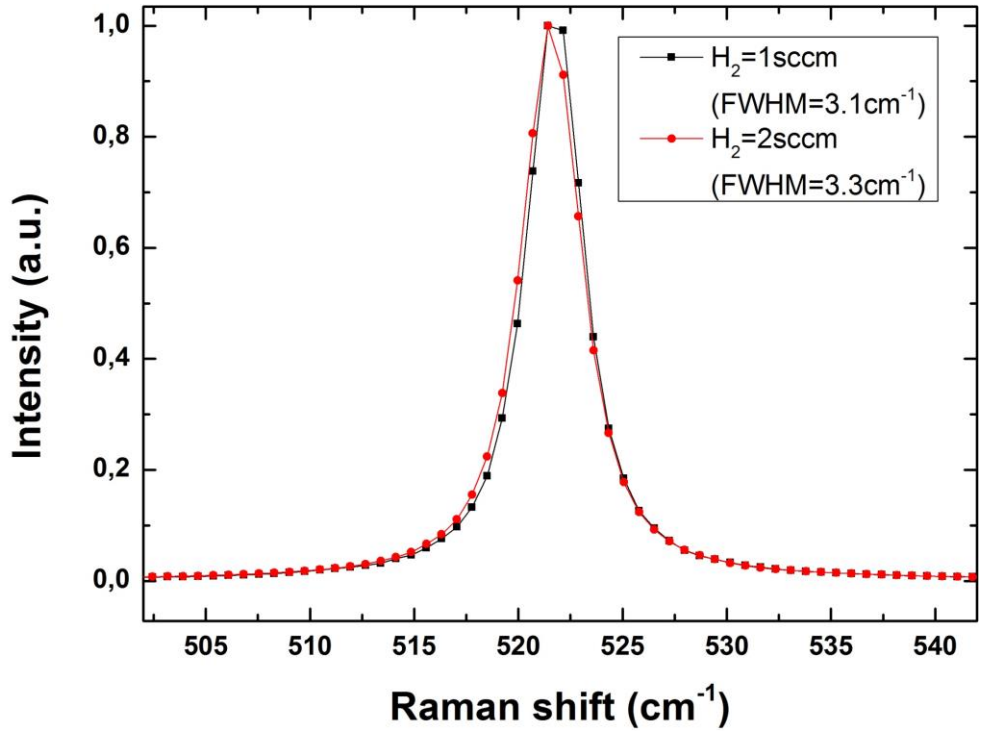

Fig. 2.56 – Raman spectra for epi-layers grown for different H_2 flow rates and at a fixed RF power of 15 W. The FWHM values have been extracted after fitting by Lorentz functions. The spectrum in red corresponds to a layer grown with H_2 depletion at the transition, therefore under conditions C.

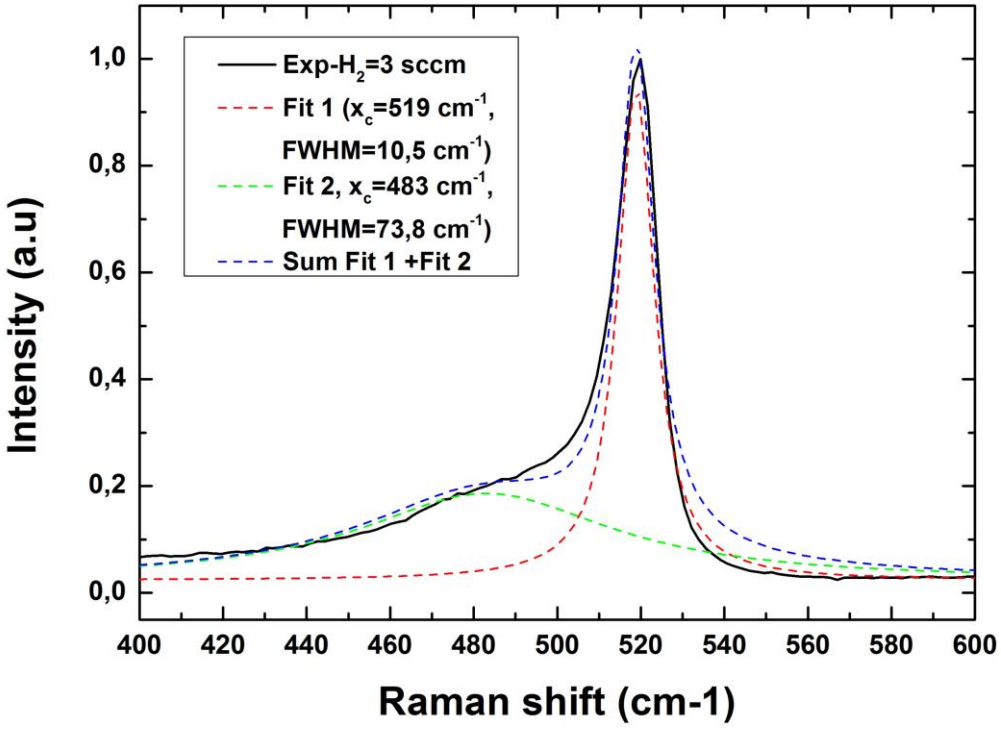

Fig. 2.57 – Raman spectrum around TO modes of a-Si:H and c-Si for epi-layers grown at 15 W with a H_2 flow rate of 3 sccm (condition D). The FWHM values have been extracted after fitting by a Lorentz function for the c-Si contribution and a Gauss function for the a-Si:H contribution.

When the H_2 flow rate is increased to 3 sccm at the same RF power (15 W), the process conditions go out from the full H_2 depletion region and an epitaxy breakdown occurs through the formation of twins. Subsequently the deposited material becomes a mix of a-Si:H and µc-Si:H as deduced from ellipsometry, XRD and TEM. This result is also observed in the Raman spectrum around TO mode of c-Si at 520 cm^{-1}. A peak at 519 cm^{-1} characteristic of µc-Si:H and another around 480 cm^{-1} characteristic of a-Si:H are observed. We purposely fitted the signal by not more than two functions. The best fit is obtained by summing Lorentz and Gaussian functions for the µc-Si:H and a-Si:H contribution, respectively. FWHM values of 10.5 cm^{-1} for the Lorentz function and 73.8 cm^{-1} for the Gaussian function have been found. Interestingly, in these conditions an amorphous phase is observed contrary to the condition B, also leading to µc-Si:H deposition after epitaxy breakdown.

2.4.4.3. Study of the incorporation of hydrogen by Raman spectroscopy

As we can see Raman spectroscopy of c-Si and a-Si TO modes allows to confirm previous observations but does not provide significant additional information. Another approach is to look at the presence of Si-H, $Si-H_2$ and other $Si-H_n$ bonds in the layers. It has been reported in literature that defective layers act as "sinks" for hydrogen [28]. No way of causality has been proved so far but the more defective the layers, the more hydrogen is incorporated. Moreover we saw that most of our defects in TEM images are also associated to hydrogen. Thus by studying the incorporation of hydrogen in the layers we can have a better idea of the introduction of defects.

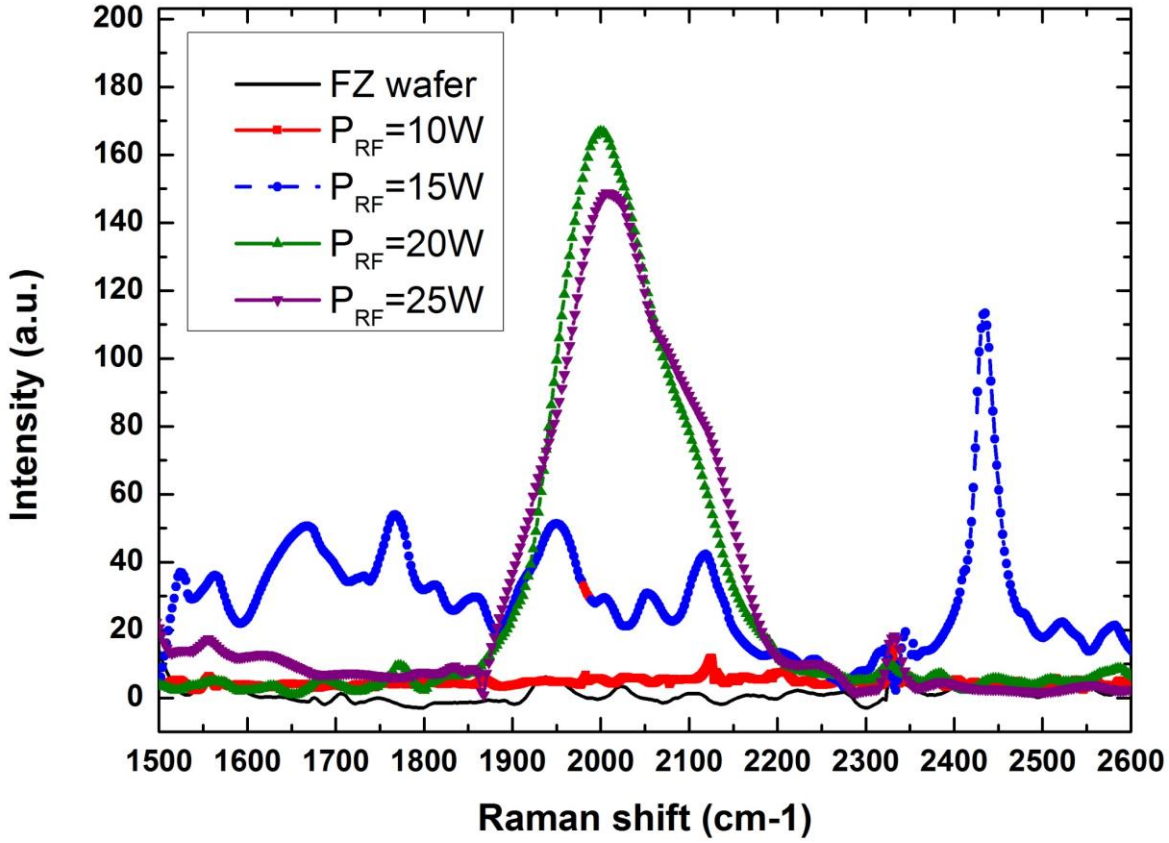

Fig. 2.58 – Raman spectra in the $Si-H_n$ stretching mode region obtained from epi-layers grown at different RF power values. Peaks at 2000 and 2100 cm^{-1} correspond to stretching modes of Si-H and $Si-H_2$ bonds respectively.

The Fig. 2.58 shows the results of Raman spectroscopy for Raman shifts between 1500 and 2600 cm^{-1} to assess the presence of Si-H_n bonds through their vibrational modes. Stretching modes of Si-H, Si-H_2 and Si-H_3 have respective frequencies of 2000, 2100 and 2150 cm^{-1} [76]. The laser wavelength is 473 nm and the acquisition time is 30 s. For every spectrum, the baseline has been extracted. We can see that the spectra of a FZ wafer (in black) and that of epitaxy grown under conditions A (in red), namely 10 W and H_2=1 sccm, are similar. This demonstrates that a small amount of hydrogen is incorporated in the layers for which properties extracted from XRD, TEM, Raman TO modes of c-Si and ellipsometry are close to these of the wafer.

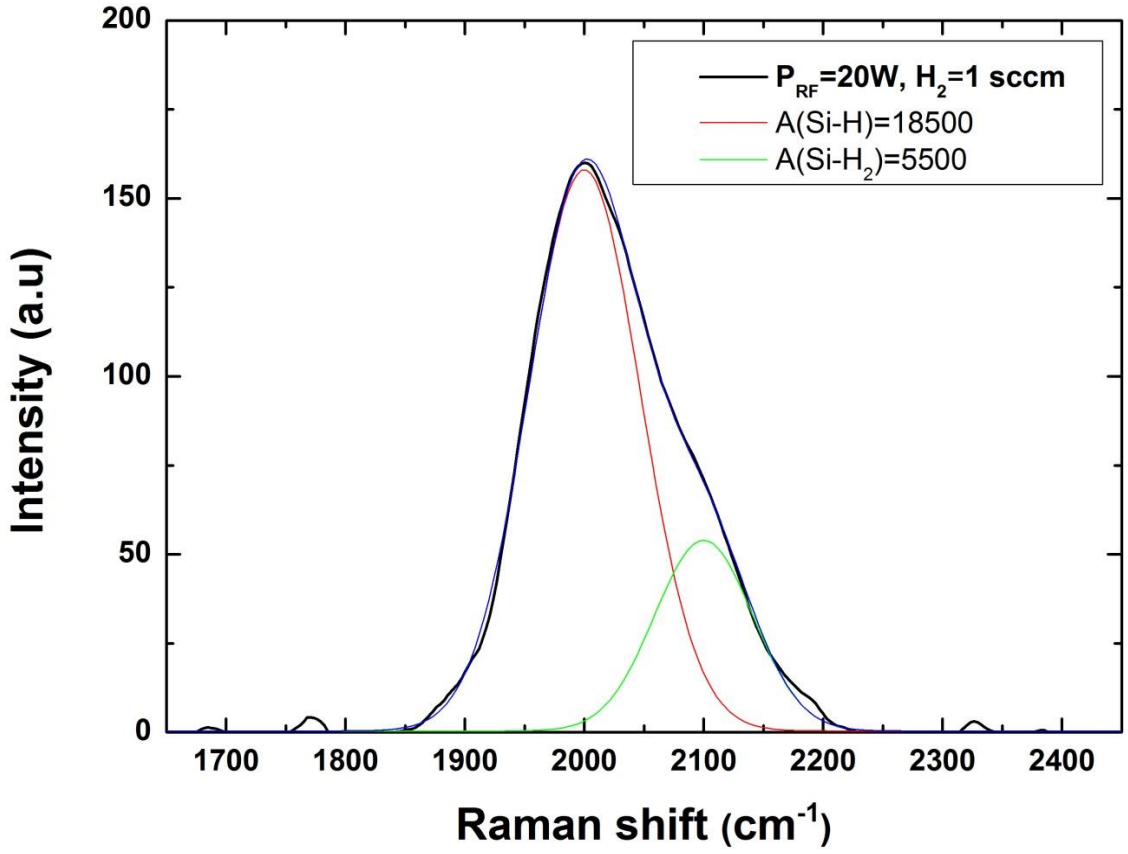

Fig. 2.59 – Deconvolution with Gaussians of Si-H and Si-H_2 stretching modes for a RF power of 20 W (p_{RF}=270 mW/cm^2).

Nevertheless, it can be seen that at 2124 cm^{-1} a sharp peak appears and when the RF power is increased to 15 W the amplitude of this peak increases meaning a rise of higher order Si-H_n bonds in the layers. This peak is not widely reported in the literature but would correspond to the stretching mode of $(SiH_2)_6$ [77]. Moreover Li and Wang [78] reported a Raman signal at 2125 cm^{-1} that they observed in H-implanted Cz silicon wafers annealed at 500 and 700°C and in bare Cz silicon wafers annealed at 700°C. However the correspondence to a specific bond is unclear. This may be associated to segregation of hydrogen in the films and in particular H platelets and would be consistent with our observations. But given that the intensity of the peak is very low for the epi-layers, the density of this type of bonding, and *a fortiori* hydrogen, should be very low as well. This is an important result to finely optimize the quality of epitaxial layers since FWHM values of c-Si TO modes of epi-layers with different defects density are the same as that of the wafer. Interestingly, no peak at 2000 and 2100 cm^{-1} are visible, meaning an absence of Si-H and Si-H_2 bonds in epi-layers. After epitaxy breakdown, at 20

W and 25 W, peaks at 2000 and 2100 cm^{-1} appear which is characteristic of the microcrystalline phase at the top of the layers while no contribution of higher order $Si-H_n$ bonds are observed.

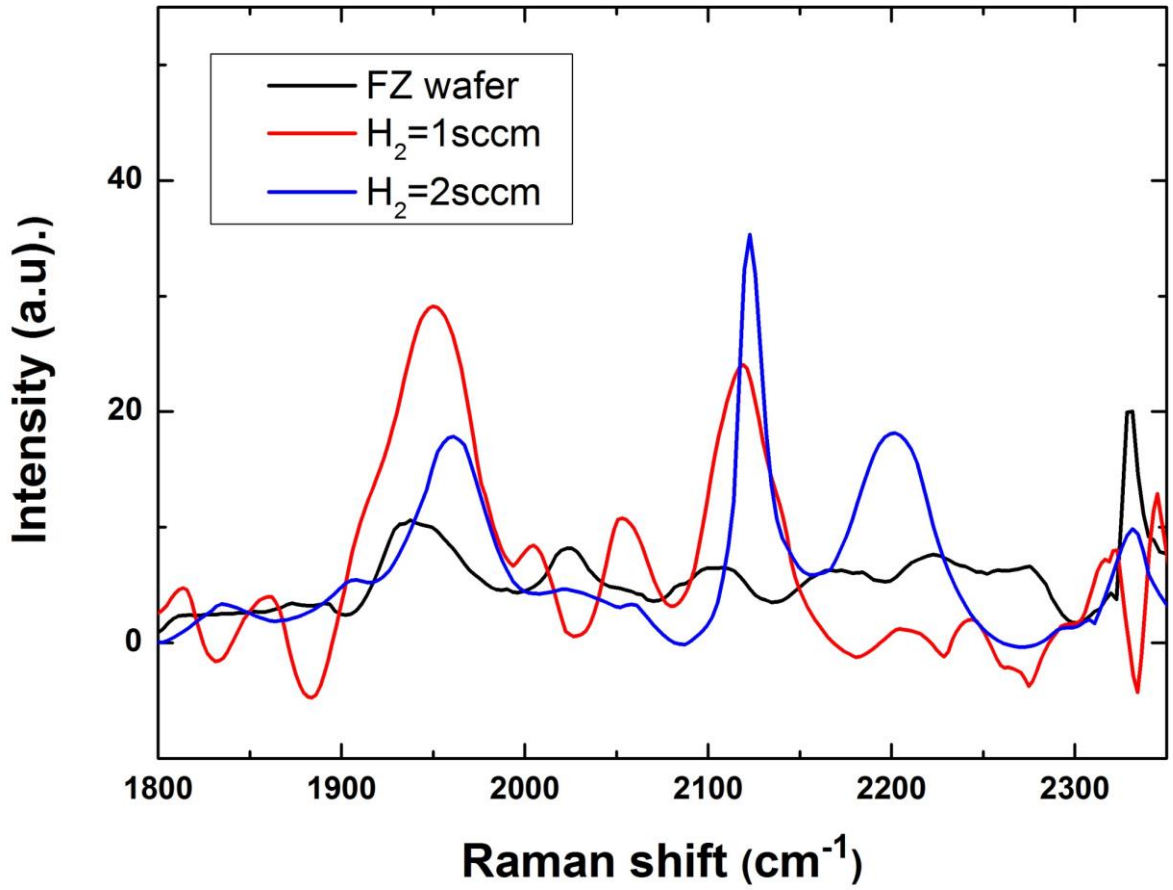

Fig. 2.60 – Raman spectra centered around 2000 cm^{-1} for the observation of stretching modes of $Si-H_n$ bonds obtained from epi-layers grown for different H_2 flow rates at a RF power of 15 W.

The sharp peak at 2433 cm^{-1} for a RF power of 15 W (in blue) is difficult to assign. According to the National Institute of Standards and Technology (NIST), this vibrational energy may correspond to C_2D_2Fe, which is highly unlikely to find in our epi-layers. By integrating each contribution (Si-H and $Si-H_2$) we can see that the Si-H bond is preferential when the RF power is increased.

Conditions	Area Si-H (2000 cm^{-1})	Area $Si-H_2$ (2100 cm^{-1})	Ratio $Si-H_2/Si-H$
FZ wafer (reference)	**0**	**0**	**/**
10 W (A)	**0**	**0**	**/**
15 W	**0**	**0**	**/**
20 W (B)	**18500**	**5500**	**0.30**
25 W	**19630**	**3910**	**0.20**
15 W – 3 sccm (D)	**7260**	**14560**	**2.0**

Table 2 – Area linked to the concentration of Si-H and $Si-H_2$ bonds resulting from the deconvolution of Raman spectra at 2000 and 2100 cm^{-1} respectively.

The result of fitting with Gaussians is given in Fig. 2.59 and the corresponding areas for different process conditions are summarized in Table 2.

Interestingly, for the evolution of Si-H_n bonds with the increase of H_2 flow rate (at fixed RF power of 15 W), similar results are obtained, as shown in Fig. 2.60. When the H_2 flow rate is increased to 2 sccm the peak at 2124 cm^{-1} increases. This is consistent with TEM images given that a lot of H platelets were observed in that case. Again, no Si-H and Si-H_2 bonds are observable at H_2=2 sccm which still corresponds to epitaxy conditions and confirm this remarkable results that hydrogen incorporation in SiF_4/H_2/Ar epitaxy does not rely on Si-H or Si-H_2 bonds.

When the H_2 flow rate is increased to 3 sccm, the deposition is a mix of a-Si:H/µc-Si:H and much more hydrogen is incorporated in the film as shown in Fig. 2.61.

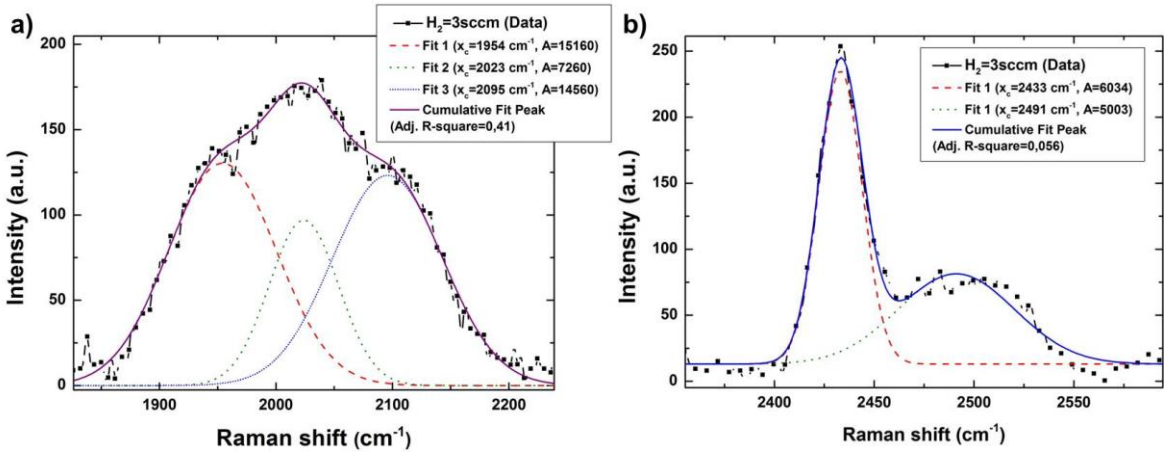

Fig. 2.61 – a) Raman spectra centered around 2000 cm^{-1} for the observation of stretching modes of Si-H_n and b) around 2450 cm^{-1} in layers grown at 15 W with 3 sccm of H_2.

Interestingly, in contrast with µc-Si:H at high P_{RF}, the area of the mode at 2000 cm^{-1} is lower than that at 2100 cm^{-1}. It would mean that, in that case, hydrogen incorporation relies more on Si-H_2 bonds rather than Si-H. However, the contribution at 1954 cm^{-1} has not been successfully determined and corresponding vibrational modes in Raman database do not fit with consistent molecules. Interestingly in Fig. 2.61-b), we can see that for these conditions the sharp peak at 2433 cm^{-1} is present. Once again, we are not able to assign this peak to the vibrational mode of a precise molecule in our layers. Even though we are not able to identify all the Raman peaks, the use of Raman spectroscopy allows to differentiate all the process conditions we investigated.

2.5. Conclusion

First of all, this chapter provides information about the material properties we are able to achieve with LTE at 200°C from SiF_4/H_2/Ar chemistry. For optimized layers, low strain epi-layers with a difference of lattice parameter lower than 1.10^{-3} Å with respect to that of the Si wafer have been obtained. A 100% crystalline fraction extracted from ellipsometry measurement and the same Raman FWHM (3.1 cm^{-1}) in Raman spectroscopy of the TO mode of c-Si are possible to achieve with these layers. Finally, Raman spectroscopy of Si-H_n stretching modes shows that few Si-H_n bonding are present in the layer, indicating that little hydrogen is incorporated in this case of fully optimized layers.

This chapter also allowed to define the process conditions for epitaxy considering RF power and H_2 flow rate through the H_2 depletion parameter. It has been shown that a full H_2 depletion is a necessary condition but not sufficient for epitaxy. A $[H_2]/[SiF_4]$ ratio below 2/3 is also required, under full depletion condition, to avoid the formation of twins. However, a $[H_2]/[SiF_4]$ ratio below 1/3 is required to avoid the formation of H platelets in the layer and to obtain a difference of lattice parameter with respect to that of Si wafer smaller than 1.10^{-3} Å, as shown by HR-XRD. Thus, once proper conditions for epitaxy are found, i.e. H platelets-free, the increase of the growth rate requires an increase of the H_2 flow rate, which requires an increase of the P_{RF}, to stay in the full H_2 depletion regime (or H_2-limited regime), which in turn requires an increase of the SiF_4 flow rate to keep the $[H_2]/[SiF_4]$ gas ratio below 1/3.

Besides, we have shown that for epitaxy breakdown induced by a too high P_{RF} or a too low H_2 depletion, a twinning-induced mechanism is involved in both cases. After epitaxy breakdown, the pursuit of the process leads to the deposition of a mix of a-Si:H and µc-Si:H. Nevertheless, the two cases can be differentiated by the grains orientation. In the case of too low depletion, contrary to the high P_{RF} case, <111> oriented grains have been detected by pole figures. In addition, these two cases can be differentiated by the Si-H_n bondings in the layers after epitaxy breakdown using Raman spectroscopy. The ratio of the contribution of Si-H_2 and Si-H bondings: Si-H_2/Si-H, is one order of magnitude higher in the case of an epitaxy breakdown induced by a too low depletion than that measured in the case of an epitaxy breakdown induced by a too high RF power.

This chapter can be considered as a reference for the technology transfer, development and scale up regarding the influence of each parameter on the material properties assessed by ellipsometry, TEM, XRD and Raman spectroscopy. A good correlation between all these characterization methods has been observed. Finally, this shows that only one or two of these characterizations are required for the full development of the process conditions in terms of structural properties. The electrical properties and the pressure dependency of the process window will be addressed in Chapter 4.

References

[1] S. Suzuki and T. Itoh, “Effect of Si-Ge buffer layer for low-temperature Si epitaxial growth on Si substrate by rf plasma chemical vapor deposition,” *J. Appl. Phys.*, vol. 54, no. 3, p. 1466, 1983.

[2] T. J. Donahue, W. R. Burger, and R. Reif, “Low-temperature silicon epitaxy using low pressure chemical vapor deposition with and without plasma enhancement,” *Appl. Phys. Lett.*, vol. 44, no. 3, p. 346, 1984.

[3] J. H. Comfort and R. Reif, “Plasma-enhanced deposition of high-quality epitaxial silicon at low temperatures,” *Appl. Phys. Lett.*, vol. 51, no. 24, p. 2016, Dec. 1987.

[4] D. J. Eaglesham, H.-J. Gossmann, and M. Cerullo, “Limiting Thickness h for Epitaxial Growth and Room-Temperature Si Growth on Si(100),” *Phys. Rev. Lett.*, 1990.

[5] D. J. Eaglesham, “Semiconductor molecular-beam epitaxy at low temperatures,” *J. Appl. Phys.*, vol. 77, no. 8, p. 3597, Apr. 1995.

[6] R. Cariou *et al.*, “Ultrathin PECVD epitaxial Si solar cells on glass via low-temperature transfer process,” *Prog. Photovoltaics Res. Appl.*, vol. 24, no. 8, pp. 1075–1084, Aug. 2016.

[7] N. Shibata, K. Fukuda, H. Ohtoshi, J. Hanna, S. Oda, and I. Shimizu, “Preparation of Polycrystalline Silicon by Hydrogen-Radical-Enhanced Chemical Vapor Deposition,” *Jpn. J. Appl. Phys.*, vol. 26, no. Part 2, No. 1, pp. L10–L13, Jan. 1987.

[8] H. Shirai, H. Tanabe, T. Uematsu, J. Hanna, and I. Shimizu, “Growth of amorphous, microcrystalline and epitaxial silicon at the same substrate temperature under control of atomic hydrogen,” *J. Non. Cryst. Solids*, vol. 114, pp. 810–812, 1989.

[9] T. Ohmi, K. Matsudo, T. Shibata, T. Ichikawa, and H. Iwabuchi, “Very-Low-Temperature Epitaxial Silicon Growth By Low-Kinetic-Energy Particle Bombardment,” *Jpn. J. Appl. Phys.*, vol. 27, no. Part 2, No. 11, pp. L2146–L2148, Nov. 1988.

[10] T. Ohmi, T. Ichikawa, H. Iwabuchi, and T. Shibata, “Formation of device-grade epitaxial silicon films at extremely low temperatures by low-energy bias sputtering,” *J. Appl. Phys.*, vol. 66, no. 10, p. 4756, 1989.

[11] T. Shibata and T. Ohmi, “Low temperature, defect-free silicon epitaxy using a low kinetic energy particle process,” *J. Electron. Mater.*, vol. 19, no. 10, pp. 1065–1073, Oct. 1990.

[12] W. J. Varhue, J. L. Rogers, P. S. Andry, and E. Adams, “Epitaxial film thickness in the low-temperature growth of Si(100) by plasma enhanced chemical vapor deposition,” *Appl. Phys. Lett.*, vol. 68, no. 3, p. 349, Jan. 1996.

[13] J. Platen, B. Selle, I. Sieber, S. Brehme, U. Zeimer, and W. Fuhs, “Low-temperature epitaxial growth of Si by electron cyclotron resonance chemical vapor deposition,” *Thin Solid Films*, vol. 381, no. 1, pp. 22–30, 2001.

[14] S. J. Deboer, V. L. Dalal, G. Chumanov, and R. Bartels, “Low temperature epitaxial silicon film growth using high vacuum electron-cyclotron-resonance plasma deposition.”

[15] B. Rau *et al.*, “Low-temperature epitaxial Si absorber layers grown by electron-cyclotron resonance chemical vapor deposition,” *Proc. 3rd World Conf. Photovolt. Energy Conversion, Vols a-C*, vol. 1240, no. 100, pp. 1237–1240, 2003.

[16] B. Rau *et al.*, “Low-temperature Si epitaxy on large-grained polycrystalline seed layers by electron-cyclotron resonance chemical vapor deposition,” *J. Cryst. Growth*, vol. 270, no. 3–4, pp. 396–401, 2004.

[17] C. Rosenblad, H. R. Deller, A. Dommann, T. Meyer, P. Schroeter, and H. von Känel, “Silicon epitaxy by low-energy plasma enhanced chemical vapor deposition,” *J. Vac. Sci. Technol. A Vacuum, Surfaces, Film.*, vol. 16, no. 5, p. 2785, Sep. 1998.

[18] T. Oshima, K. Abe, A. Yamada, and M. Konagai, “Heavily B-Doped Epitaxial Si Films Grown by Photochemical Vapor Deposition at Very Low Temperature (<200° C),” *Jpn. J. Appl. Phys.*, vol. 34, no. Part 2, No. 11A, pp. L1425–L1428, Nov. 1995.

[19] Y. Jia, A. Yamada, M. Konagai, and K. Takahashi, “Effects of Deuterium on Low-Temperature Si Epitaxy by Photo-Chemical Vapor Deposition,” *Jpn. J. Appl. Phys.*, vol. 30, no. Part 1, No. 5, pp. 893–896, May 1991.

[20] K. Nagamine, A. Yamada, M. Konagai, and K. Takahashi, “Epitaxial Growth of Silicon by Plasma Chemical Vapor Deposition at a Very Low Temperature of 250°C,” *Jpn. J. Appl. Phys.*, vol. 26, no. 6A, p. L951, 1987.

[21] A. Yamada, A. Satoh, M. Konagai, and K. Takahashi, “Low temperature silicon epitaxy by photo- and plasma-CVD,” in *AIP Conference Proceedings*, 1988, vol. 167, no. 1, pp. 222–236.

[22] N. Gonohe, S. Shimizu, K. Tamagawa, T. Hayashi, and H. Yamakawa, “Low-Temperature Silicon Epitaxial Growth by Photochemical Vapor Deposition Using Vacuum Ultraviolet Light,” *Jpn. J. Appl. Phys.*, vol. 26, no. Part 2, No. 7, pp. L1189–L1192, Jul. 1987.

[23] T. Uematsu, S. Matsubara, M. Kondo, M. Tamura, and T. Saitoh, “Very-Low-Temperature Silicon Epitaxy by Plasma-CVD Using SiH 4 -PH 3 -H 2 Reactants for Bipolar Devices,” *Jpn. J. Appl. Phys.*, vol. 27, no. Part 2, No. 4, pp. L493–L495, Apr. 1988.

[24] C. C. Tsai, G. B. Anderson, R. Thompson, and B. Wacker, “Control of silicon network structure in plasma deposition,” *J. Non. Cryst. Solids*, vol. 114, pp. 151–153, 1989.

[25] C. C. Tsai, G. B. Anderson, and R. Thompson, “Low temperature growth of epitaxial and amorphous silicon in a hydrogen-diluted silane plasma,” *J. Non. Cryst. Solids*, vol. 137, pp. 673–676, 1991.

[26] K. Baert, J. Vanhellemont, W. Vandervorst, J. Nijs, and M. Konagai, “Heavily phosphorus-doped epitaxial Si deposited by low-temperature plasma-enhanced chemical vapor deposition,” *Appl. Phys. Lett.*, vol. 59, no. 7, p. 797, Aug. 1991.

[27] K. Baert, P. Deschepper, J. Poortmans, J. Nijs, and R. Mertens, “Selective Si epitaxial growth by plasma-enhanced chemical vapor deposition at very low temperature,” *Appl. Phys. Lett.*, vol. 60, no. 4, p. 442, Jan. 1992.

[28] J. Schwarzkopf, B. Selle, M. Schmidbauer, and W. Fuhs, “Low-temperature epitaxial growth of B doped Si films on Si(100) and Si(111),” *Thin Solid Films*, vol. 427, no. 1–2, pp. 274–278, Mar. 2003.

[29] J. Plá *et al.*, “Homojunction and heterojunction silicon solar cells deposited by low temperature-high frequency plasma enhanced chemical vapour deposition,” *Thin Solid Films*, vol. 405, no. February, pp. 248–255, 2002.

[30] M. Farrokh-baroughi and S. Sivoththaman, “A Novel Silicon Photovoltaic Cell Using a Low-Temperature Quasi-Epitaxial Silicon Emitter,” *IEEE Electron Device Lett.*, vol. 28, no. 7, pp. 575–577, 2007.

[31] R. Shimokawa, M. Yamanaka, and I. Sakata, “Very Low Temperature Epitaxial Growth of Silicon Films for Solar Cells,” *Jpn. J. Appl. Phys.*, vol. 46, pp. 7612–7618, 2007.

[32] H. El Gohary, “Development of Low-Temperature Epitaxial Silicon Films and Application to Solar Cells,” Univeristy of Waterloo, 2010.

[33] B. Hekmatshoar, D. Shahrjerdi, M. Hopstaken, J. A. Ott, and D. K. Sadana, “Characterization of thin epitaxial emitters for high-efficiency silicon heterojunction solar cells,” *Appl. Phys. Lett.*, vol. 101, no. 10, p. 103906, 2012.

[34] A. Luque and S. Hegedus, *Handbook of Photovoltaic Science and Engineering*, vol. p. 110. 2011.

[35] B. Hekmatshoar, D. Shahrjerdi, and D. K. Sadana, “Application of thin epitaxial hydrogenated si layers to high efficiency heterojunction solar cells on N-type si substrates,” in *Photovoltaic Specialist Conference (PVSC), 40th IEEE*, 2014, pp. 971–972.

[36] T. Carrere, R. Varache, D. Muñoz, and J. P. Kleider, “Insertion of a thin highly doped crystalline layer in silicon heterojunction solar cells: Simulation and perspectives towards a highly efficient cell concept,” *J. Renew. Sustain. Energy*, vol. 7, no. 1, p. 11202, 2015.

[37] T. Carrere, “Procédés d’implantation ionique et structures innovantes pour les cellules photovoltaïques à hétérojonctions de silicium,” *http://www.theses.fr*, 2016.

[38] T. Carrere, R. Varache, J. Le Perchec, C. Denis, D. Muñoz, and J.-P. Kleider, “Silicon Bulk Issues during Processing of Homo-heterojunction Solar cells,” *Energy Procedia*, vol. 77, pp. 451–457, Aug. 2015.

[39] A. Fontcuberta i Morral, H. Hofmeister, and P. Roca i Cabarrocas, “Structure of plasma-deposited polymorphous silicon,” *J. Non. Cryst. Solids*, vol. 299, pp. 284–289, 2002.

[40] J. Damon-Lacoste and P. Roca i Cabarrocas, “Toward a better physical understanding of a-Si:H/c-Si heterojunction solar cells,” *J. Appl. Phys.*, vol. 105, no. 6, p. 63712, 2009.

[41] S. De Wolf and M. Kondo, “Abruptness of a-Si:H⁄c-Si interface revealed by carrier lifetime measurements,” *Appl. Phys. Lett.*, vol. 90, no. 4, p. 42111, Jan. 2007.

[42] H. Fujiwara and M. Kondo, “Effects of a-Si:H layer thicknesses on the performance of a-Si:H⁄c-Si heterojunction solar cells,” *J. Appl. Phys.*, vol. 101, no. 5, p. 54516, Mar. 2007.

[43] R. Cariou, “Epitaxial growth of Si(Ge) materials on Si and GaAs by low temperature PECVD: towards tandem devices,” PhD thesis, Ecole Polytechnique, 2015.

[44] R. Cariou, R. Ruggeri, X. Tan, G. Mannino, J. Nassar, and P. Roca I Cabarrocas, “Structural properties of relaxed thin film germanium layers grown by low temperature RF-PECVD epitaxy on Si and Ge (100) substrates,” *AIP Adv.*, vol. 4, no. 7, pp. 0–7, 2014.

[45] R. Cariou *et al.*, “Low temperature plasma enhanced CVD epitaxial growth of silicon on GaAs: a new paradigm for III-V/Si integration,” *Sci. Rep.*, vol. 6, no. April, p. 25674, 2016.

[46] R. Cariou, R. Ruggieri, and P. Roca i Cabarrocas, “Silicon epitaxy below 200°C: Towards thin crystalline solar cells,” *SPIE Proc.*, 2012.

[47] P. Narchi, R. Cariou, M. Foldyna, P. Prodhomme, and P. Roca i Cabarrocas, “Nanoscale Investigation of Carrier Lifetime on the Cross Section of Epitaxial Silicon Solar Cells Using Kelvin Probe Force Microscopy,” *IEEE J. Photovoltaics*, vol. 6, no. 6, pp. 1576–1580, Nov. 2016.

[48] M. Labrune, M. Moreno, and P. Roca i Cabarrocas, “Ultra-shallow junctions formed by quasi-epitaxial growth of boron and phosphorous-doped silicon films at 175°C by RF-PECVD,” *Thin Solid Films*, 2010.

[49] Y. Djeridane, A. Abramov, and P. Roca i Cabarrocas, “Silane versus silicon tetrafluoride in the growth of microcrystalline silicon films by standard radio frequency glow discharge,” *Thin Solid Films*, vol. 515, no. 19, pp. 7451–7454, Jul. 2007.

[50] J.-C. Dornstetter, J. Wang, B. Bruneau, E. V. Johnson, and P. Roca i Cabarrocas, “Material and growth mechanism studies of microcrystalline silicon deposited from SiF_4/H_2/Ar gas mixtures,” *Can. J. Phys.*, vol. 92, no. 7/8, pp. 740–743, Jul. 2014.

[51] J.-C. Dornstetter, “Microcrystalline silicon deposited from SiF_4/H_2/Ar plasmas and its application to photovoltaics,” PhD thesis, Ecole Polytechnique, 2015.

[52] A. Abramov and P. Roca i Cabarrocas, “Addition of SiF_4 to standard SiH_4+H_2 plasma an effective way to reduce oxygen contamination in μc-SiH films,” *Phys. Status Solidi*, 2010.

[53] M. Moreno, G. Patriarche, and P. Roca i Cabarrocas, “Fine-tuning of the interface in high-quality epitaxial silicon films deposited by plasma-enhanced chemical vapor deposition at 200 °C,” *J. Mater. Res.*, 2013.

[54] J.-C. Dornstetter, “Microcrystalline Silicon Deposited from SiF_4/H_2/Ar Gas Mixtures: Material Properties and Growth Mechanisms Studies,” *ICANS Proc.*, 2013.

[55] J.-C. Dornstetter *et al.*, “Deposition of High-Efficiency Microcrystalline Silicon Solar Cells Using SiF_4/H_2/Ar Mixtures,” *IEEE J. Photovoltaics*, 2012.

[56] J.-C. Dornstetter, B. Bruneau, P. Bulkin, E. V. Johnson, and P. Roca i Cabarrocas, “Understanding the amorphous-to-microcrystalline silicon transition in SiF_4/H_2/Ar gas mixtures,” *J. Chem. Phys.*, 2014.

[57] J. W. Coburn and M. Chen, “Optical emission spectroscopy of reactive plasmas: A method for correlating emission intensities to reactive particle density,” *J. Appl. Phys.*, vol. 51, no. 6, p. 3134, 1980.

[58] G. E. Jellison, M. F. Chisholm, and S. M. Gorbatkin, “Optical functions of chemical vapor deposited thin-film silicon determined by spectroscopic ellipsometry,” *Appl. Phys. Lett.*, vol. 62, no. 25, pp. 3348–3350, Jun. 1993.

[59] M. H. Brodsky, M. Cardona, and J. J. Cuomo, “Infrared and Raman spectra of the silicon-hydrogen bonds in amorphous silicon prepared by glow discharge and sputtering,” *Phys. Rev. B*, vol. 16, no. 8, pp. 3556–3571, Oct. 1977.

[60] Z. Iqbal and S. Veprek, “Raman scattering from hydrogenated microcrystalline and amorphous silicon,” *J. Phys. C Solid State Phys.*, vol. 15, no. 2, p. 19, Jan. 1982.

[61] J. H. Parker, D. W. Feldman, and M. Ashkin, “Raman Scattering by Silicon and Germanium,” *Phys. Rev.*, vol. 155, no. 3, pp. 712–714, Mar. 1967.

[62] S. Lebib and P. Roca i Cabarrocas, “Effects of ion energy on the crystal size and hydrogen bonding in plasma-deposited nanocrystalline silicon thin films,” *J. Appl. Phys.*, vol. 97, no. 10, p. 104334, May 2005.

[63] B. E. Warren, *X-ray Diffraction*, Courier Co. 1969.

[64] V. Suendo and P. Roca i Cabarrocas, “Plasma diagnostics in silane–methane–hydrogen plasmas under pm-Si1−xCx:H deposition conditions: Correlation with film properties,” *J. Non.*

Cryst. Solids, vol. 352, no. 9, pp. 959–963, 2006.

[65] B. Bruneau *et al.*, "Ion Energy Threshold in Low-Temperature Silicon Epitaxy for Thin-Film Crystalline Photovoltaics," *IEEE J. Photovoltaics*, vol. 4, no. 6, pp. 1361–1367, Nov. 2014.

[66] D. K. Brice, J. Y. Tsao, and S. T. Picraux, "Partitioning of ion-induced surface and bulk displacements," *Nucl. Inst. Methods Phys. Res. B*, vol. 44, no. 1, pp. 68–78, 1989.

[67] F. Haddad, "Transmission electron microscopy study of low-temperature silicon epitaxy by plasma enhanced chemical vapor deposition," University of Paris-Saclay, 2016.

[68] G. Moras, L. C. Ciacchi, C. Elsässer, P. Gumbsch, and A. De Vita, "Atomically Smooth Stress-Corrosion Cleavage of a Hydrogen-Implanted Crystal," *Phys. Rev. Lett.*, vol. 105, no. 7, p. 75502, Aug. 2010.

[69] C. Ghica, L. C. Nistor, H. Bender, O. Richard, G. Van Tendeloo, and A. Ulyashin, "Characterization of {111} planar defects induced in silicon by hydrogen plasma treatments," *Philos. Mag.*, vol. 86, no. 32, pp. 5137–5151, Nov. 2006.

[70] W. Chen, R. Cariou, G. Hamon, R. Léal, J.-L. Maurice, and P. R. i Cabarrocas, "Influence of deposition rate on the structural properties of plasma-enhanced CVD epitaxial silicon," *Sci. Rep.*, vol. 7, p. 43968, Mar. 2017.

[71] D. Shahrjerdi, B. Hekmatshoar, S. W. Bedell, M. Hopstaken, and D. K. Sadana, "Low-Temperature Epitaxy of Compressively Strained Silicon Directly on Silicon Substrates," *J. Electron. Mater.*, vol. 41, no. 3, pp. 494–497, Nov. 2011.

[72] F. Silva, "Maitrise dela croissance et de la texture de films de diamant polycristallins, réalisés par dépôt chimique en phase vapeur assisté par plasma micro-onde," Paris 13, 1998.

[73] D. R. Tallant, T. J. Headley, J. W. Medernach, and F. Geyling, "Characterization of Polysilicon Films by Raman Spectroscopy and Transmission Electron Microscopy: a Comparative Study," *MRS Proc.*, vol. 324, p. 255, Jan. 1993.

[74] C. M. Hessel, J. Wei, D. Reid, H. Fujii, M. C. Downer, and B. A. Korgel, "Raman Spectroscopy of Oxide-Embedded and Ligand-Stabilized Silicon Nanocrystals," *J. Phys. Chem. Lett.*, vol. 3, no. 9, pp. 1089–1093, May 2012.

[75] B. Ghosh *et al.*, "Origin of the Photoluminescence Quantum Yields Enhanced by Alkane-Termination of Freestanding Silicon Nanocrystals: Temperature-Dependence of Optical Properties," *Sci. Rep.*, vol. 6, no. 1, p. 36951, Dec. 2016.

[76] G. Lucovsky, R. J. Nemanich, and J. C. Knights, "Structural interpretation of the vibrational spectra of a-Si:H alloys," *Phys. Rev. B*, vol. 19, no. 4, pp. 2064–2073, Feb. 1979.

[77] M. Cardona, "Vibrational Spectra of Hydrogen in Silicon and Germanium," *Phys. status solidi*, vol. 118, no. 2, pp. 463–481, Aug. 1983.

[78] B. S. Li and Z. G. Wang, "Effects of the surface oxide layer on platelet growth in H2+-implanted Si," *Vacuum*, vol. 102, pp. 5–11, Apr. 2014.

[79] K. Köhler, J. W. Coburn, D. E. Horne, E. Kay, and J. H. Keller, "Plasma potentials of 13.56-MHz rf argon glow discharges in a planar system," *J. Appl. Phys.*, vol. 57, no. 1, p. 59, 1985.

[80] W. Chen, G. Hamon, R. Léal, J.-L. Maurice, L. Largeau, and P. Roca i Cabarrocas, "Plasma-enhanced epitaxial growth of stable tetragonal Si," *Prep.*

3. Growth mechanism in low-temperature epitaxy by PECVD from $SiF_4/H_2/Ar$ gas mixtures

3.1. Growth modes in epitaxy and standard techniques of surface analysis

This chapter deals with the growth mechanisms involved in low temperature epitaxy (LTE) by PECVD. The possibility to grow monocrystalline silicon layers at temperatures below 300°C is not fully understood yet. In this chapter we will provide insights on the mechanisms by combining ellipsometry and TEM analyses at early stages of growth. This study has been led in collaboration with F. Haddad; additional information on the growth mechanisms can be found in her thesis [1].

Three primary growth modes have been identified so far to explain the different mechanisms involved in the deposition of thin films. The schematics in Fig.1 present the primary modes encountered in epitaxial growth, which refers to most of processes used in thin film deposition techniques, and were first classified by Bauer [2] in 1958.

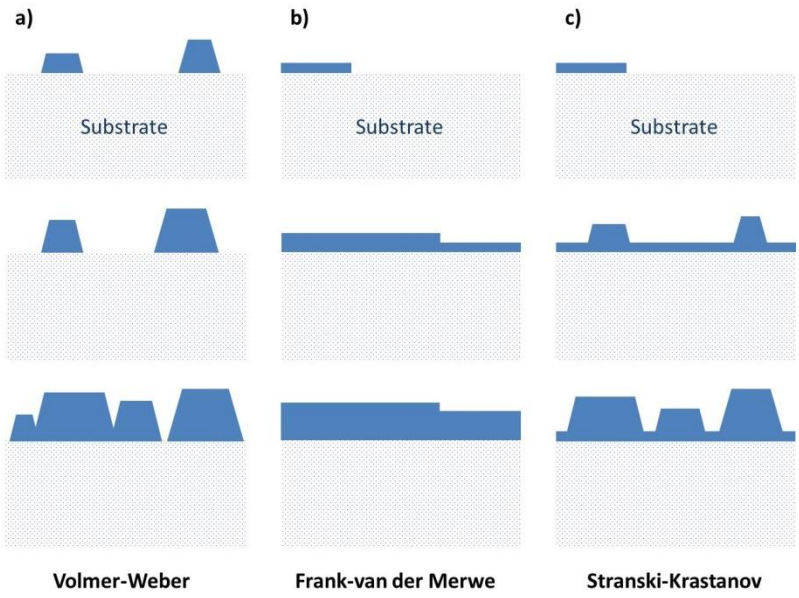

Fig. 3.1 – Representation of primary modes of thin film deposition: a) Volmer-Weber or island growth mode, b) Frank-van der Merwe or layer-by-layer growth mode and c) Stranski-Krastanov or layer-plus-island growth mode [2].

The Volmer-Weber or island growth mode, represented in Fig. 3.1-a), relies on nucleation of islands composed of several atoms at the surface of the substrate. These nuclei grow and coalesce with each other to form a full continuous layer. In that case the interaction is stronger between the adatoms than between the adatom and the substrate surface. This 3D growth mode is common in low-temperature processes due to the low surface diffusion of adatoms. This mode is reported as providing reduced electric properties of films due to the possible presence of grain boundaries formed at the interface

between islands and to an increase of the roughness. This growth mode is for example found in the homoepitaxial growth of iron by MBE at low temperature [3], as shown in Fig. 3.2.

The Frank-van der Merwe or layer-by-layer growth mode, represented in Fig. 3.1-b), as its name suggests, is based on the growth of films monoatomic layer by monoatomic layer. In that case the adatoms preferentially interact with the surface than between each other. This growth mode is possible if adatoms have enough energy to diffuse at the surface of the sample to reach preferential sites of adsorption. This 2D growth mode usually occurs for high temperature epitaxy. Due to the high mobility of adatoms provided by the high temperature of the substrate, they can diffuse at the surface towards the closest terrace and form thin films with an atomically smooth surface.

The Stranski-Krastanov or layer-plus-island growth mode, represented in Fig. 3.1-c), is a combination of these two growth modes. The first layers of the film are grown through a layer-by-layer growth mode. Afterwards, from a critical layer thickness, the growth is ensured by an island growth mode and follows its mechanism (nucleation and coalescence). The critical thickness depends, not exclusively, on the surface energy and the difference of lattice parameter between that of the substrate and that of the film. This growth mode appears when the interface energy increases as the layer thickness increases [4], for example through an accumulation of stress.

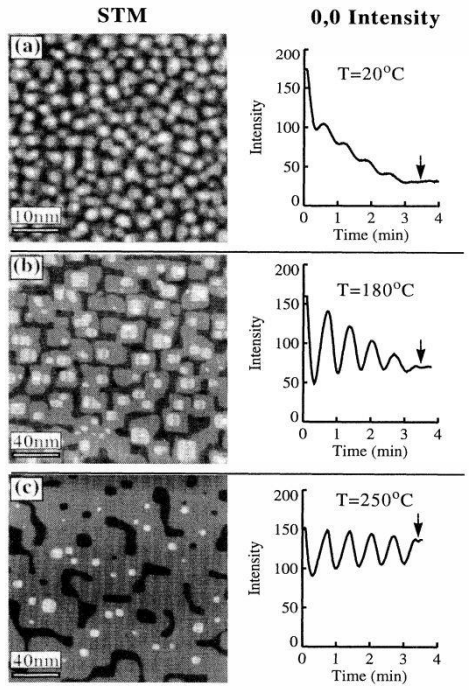

Fig. 3.2 – STM images of Fe layers (white) on Fe(001) (black) deposited by MBE and their corresponding RHEED beam intensity measurements for different sample temperatures: a) 20°, b) 180°C and c) 250°C [3]. The contrast depends on the film thickness: light regions are thicker than the dark ones. In c) major changes in grey level indicate a monoatomic step. The STM images have been taken after 5 RHEED oscillations, represented by the black arrow in the RHEED plots.

To identify which growth mode a specific thin film deposition process is associated with, different surface analyses techniques are used. Most developed and reported techniques are low-energy electron diffraction (LEED), reflection high-energy electron diffraction (RHEED) and Auger electron spectroscopy (AES). However these techniques require high or even ultra-high vacuum ($<10^{-9}$ mbar) conditions, for LEED especially. Thus, these techniques can be suitable for *in situ* analysis in the case

of MBE, for which the working pressure is in the same range of pressure as that required for the analysis. As an example, a correlation between scanning tunneling microscopy (STM) images and RHEED beam intensity measurements for Fe layers deposited on Fe(001) by MBE [3],[5] is shown in Fig. 3.2. The STM images indicate that when the sample temperature is increased the density of islands decreases while their size increases until forming terraces at 250°C. The latter case is therefore approaching the layer-by-layer growth mode. This behavior can be observed during the process with the RHEED intensity which in the case of a deposition at 250°C shows well defined oscillations corresponding to the variation of electron scattering induced by the periodicity of the morphological changes from rough (low intensity) to smooth (high intensity) surfaces. This indicates that the layer grows in a layer-by-layer growth mode; one oscillation corresponds to the filling of one single monoatomic layer. In the case of the island growth, at 20°C, the RHEED beam intensity progressively decreases with low amplitude oscillations, typical of an island growth mode. Thus *in situ* techniques such as RHEED can differentiate the growth mode during the process. However these techniques are much more difficult to implement for PECVD, due to the high working pressure, especially in our case around 3 Torr.

The PECVD reactors in which low-temperature epitaxy (LTE) has been processed are equipped with *in situ* ellipsometers (See schematic in Fig. 2.7). This allows to monitor the evolution of growth of the layers in real time and to verify if the growth is stable or if an epitaxy breakdown happens. Optical characterization techniques are less invasive than electron spectroscopy techniques since in the latter case the source and detector are placed inside the reactor, inducing possible contaminations. Moreover due to the "high" energy of incident electrons used in electron spectroscopy techniques, from tens of eV for LEED up to a few tens of keV for RHEED, the measurement can affect the growth. Besides, to answer to an increased demand of *in situ* monitoring for industrial applications, i.e. different from MBE, the development of optical diagnostics (Raman spectroscopy, laser light scattering, photoreflectance,…) suitable for high pressure processes, such as CVD, earned a significant interest.

3.2. Initial stages of growth in low-temperature epitaxy

3.2.1. *In situ* ellipsometry analysis

In this chapter, the ellipsometric analysis is focused on the early stages of growth. Even if a complementary study involving electron spectroscopy techniques is required, we can already provide insights on the growth mechanisms of LTE.

By purposely selecting the appropriate wavelength of the ellipsometry signal, the optical response is either more bulk- or surface-sensitive. Obviously, this study aims to use wavelengths more sensitive to the surface (short wavelength) rather than the bulk (long wavelength), knowing that the range of the ellipsometer used in this section goes from 1.5 to 4.5 eV for Philix and 0.7 to 6.4 eV for Cluster. For that, monitoring the imaginary part of the pseudo-dielectric function at 4.2 eV ($\varepsilon_i(4.2eV)$) is suitable for the study of the surface properties. At 4.2 eV, which corresponds to the energy of the second Van Hove singularity of c-Si, the absorption coefficient is close to the maximum ($\alpha|_{Si}(4.2eV)=1.94\times10^6$ cm^{-1}) which leads to a penetration depth of 5 nm. The "typical" evolution over time of the imaginary part of the pseudo-dielectric function at 3, 3.4 and 4.2 eV in the initial stages of growth is shown in Fig. 3.3. The process conditions for this experiment are a RF power of 40 W (180 mW/cm^2), an inter-

electrode distance of 20 mm and a pressure of 2.5 Torr. The SiF_4, H_2 and Ar flow rates are respectively fixed at 20, 3 and 300 sccm.

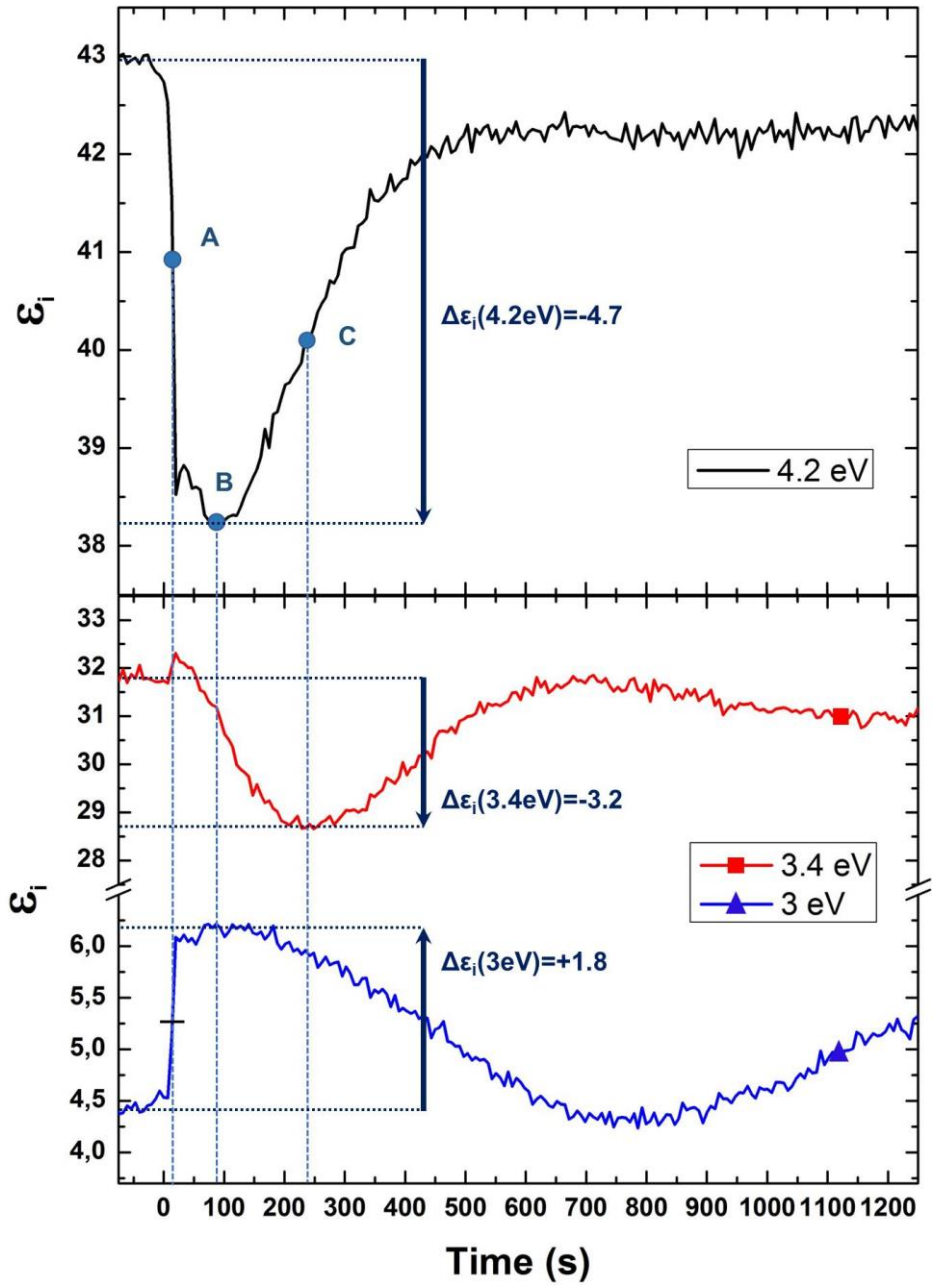

Fig. 3.3 – *In situ* evolution of the imaginary part of the pseudo-dielectric function at 3, 3.4 and 4.2 eV as a function of time during the initial phases of growth. The plasma is ignited at t=0s. Points A, B and C, corresponding to growth time of 12, 90 and 240 s respectively, represent specific stages of growth. The growth has been performed in Cluster. The SiF_4, H_2 and Ar flow rate are respectively 20, 3 and 300 sccm. The inter-electrode distance and pressure are fixed at 20 mm and 2.5 Torr. The RF power is 40 W (180 mW/cm^2), the substrate and RF electrode temperature are both fixed at 200°C. The deposition rate is 0.2 Å/s. The ellipsometer used for this *in situ* measurement is a Woollam M-2000.

Prior to the ignition of the plasma, ε_i(4.2eV) is (unsurprisingly) stable around 43. When the plasma is ignited a strong decrease of ε_i(4.2eV) is observed and it drops to 38.3 after 90 s of process reaching its minimum. From then on, ε_i(4.2eV) slowly increases for about 400 s before stabilization. If no epitaxy breakdown happens afterwards, then, ε_i(4.2eV) stays stable. It is worth noticing that for every epitaxial

growth performed in our process conditions, taking into account the environment, the cleaning and the plasma parameters, the evolution of ε_i(4.2eV) is associated to this shape. Nevertheless, amplitude variations and stabilization time may change.

Interestingly, the evolution of ε_i(3.4eV) has the same shape but drops by 3.2 points and reaches its minimum after 240 s of growth. Thus, the evolution of ε_i(3.4eV) is delayed with respect to that of ε_i(4.2eV) by around 120 s. This might be attributed to the different penetration depth of light at 3.4 and 4.2 eV: $1/\alpha|_{Si}$(3.4eV)=11 nm and $1/\alpha|_{Si}$(4.2eV)=5 nm. As a result, ε_i(3.4eV) is less sensitive to the first stages of growth. However, it may not be the only reason as detailed below.

These drops of ε_i(3.4eV) and ε_i(4.2eV) can be attributed to different causes. The most likely explanations are:

- An increase of roughness in the early stages of growth. The roughness strongly affects ε_i(4.2eV) from a few Å while it affects ε_i(3.2eV) from a few nm. This roughness can either be induced by a deposition or an etching process.

- An increase of the temperature of the surface of the sample induced by the plasma.

- A variation of the crystallinity in the early stages of growth.

In Fig. 3.4 are shown simulation results of the evolution of the imaginary part of the pseudo-dielectric function at 4.2 eV, 3.4 eV (Fig. 3.4-a)) and 3 eV (Fig. 3.4-b)) as a function of roughness for a mix composed of 50% of c-Si and 50% of void. Note that the choice of this mix is a strong assumption and can be restrictive for the simulated values but for different mixes the trends remain the same, the effect of roughness on ε_i(4.2eV) is much stronger than on ε_i(4.2eV). The substrate and the layer representing the roughness, are both fixed at 200°C. For that, a temperature dependent model is used. In this graph are reported the drop of ε_i(4.2eV), ε_i(3.4eV) and ε_i(3eV) measured by *in situ* ellipsometry during the initial stages of growth as shown in Fig. 3.3.

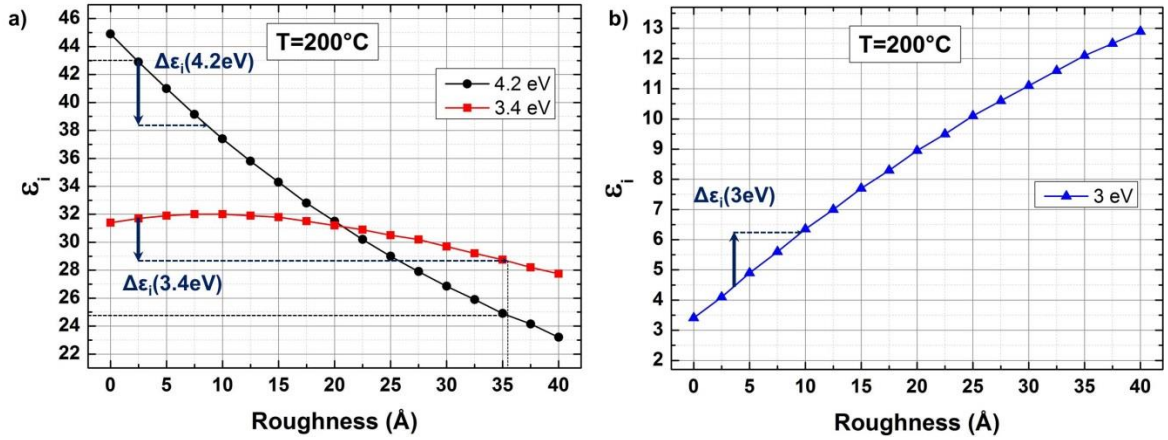

Fig. 3.4 – Simulated evolution of the imaginary part of the pseudo-dielectric function at a) 4.2 eV, 3.4 eV and b) 3 eV as a function of roughness for a mix composed of 50% of c-Si and 50% of void at 200°C. The vertical arrows correspond to the maximum variation $\Delta\varepsilon_i$(4.2eV)=-4.7, $\Delta\varepsilon_i$(3.4eV)=-3.2 and $\Delta\varepsilon_i$(3eV)=+1.8 measured by *in situ* ellipsometry in the initial stages of growth as shown in Fig. 3.3. The roughness values deduced from these drops do not match.

The idea is to verify if roughening alone can be responsible for the trend observed for ε_i at different wavelengths. Initial values of roughness are considered with respect to *in situ* initial values of ε_i at

200°C prior to epitaxy. The drop at 4.2 eV would lead to a roughening between 5 and 7 Å and coincides with the roughening corresponding to the drop at 3 eV. Therefore, the stage A would be in a phase corresponding to a slight roughening of the surface. This is also consistent with the small increase of ε_i(3.4eV) in this phase observed in Fig. 3.3. Indeed, up to a roughness of 10 Å, simulations show that ε_i(3.4eV) increases up to roughly 0.5 points.

However the drop at 3.4 eV observed in stage C would indicate a surface roughening of 30 Å. These values of roughness would strongly affect the signal at 4.2 eV. In that case ε_i(4.2eV) would drop by up to 18 points while in the experimental data, when ε_i(3.4eV) reaches its minimum, ε_i(4.2eV) only loses 3 points with respect to its initial value at 43. Similarly, a roughening of 30 Å would involve an increase of ε_i(3eV) up to 12 while its value in stage C is only 5.8. The drop of ε_i(3.4eV) thus cannot be explained by an increase of the roughness.

As shown in Fig. 3.5-a), and as reported in [6], the increase of the temperature also induces important variations of ε_i. In addition, the increase of temperature causes a shift of the Van Hove singularities towards low energy, which further affects the height of ε_i(4.2eV) [6]. The evolution of simulated ε_i(4.2eV), ε_i(3.4eV) and ε_i(3eV) as a function of substrate temperature is shown in Fig. 3.5-a). For these simulations, the roughness of the sample is fixed at 5 Å. A drop of ε_i(3.4eV) of 3.2 points would imply at least an increase of the temperature to 500°C, if we assume a measurement error of 0.3. Thus, the drop of ε_i(3.4eV) cannot be associated to a unique increase of temperature since corresponding values of ε_i(4.2eV) and ε_i(3eV) at 500°C do not match experimental data. If we consider a higher roughness, the increase of temperature exacerbates this behavior, i.e. the increase in absolute value of the slope of ε_i at 3 and 4.2 eV as a function of the temperature is significantly higher than that at 3.4 eV. Note that the linear behavior of ε_i(4.2eV) up to 550°C ($a=2.5\times10^{-2}$ K^{-1}) and ε_i(3eV) up to minimum 700°C ($a=2.2\times10^{-2}$ K^{-1}) allows to measure the temperature of a sample *in situ*. Besides, this is not limited to crystalline silicon, the temperature of amorphous silicon-based materials can also be determined *in situ* [7].

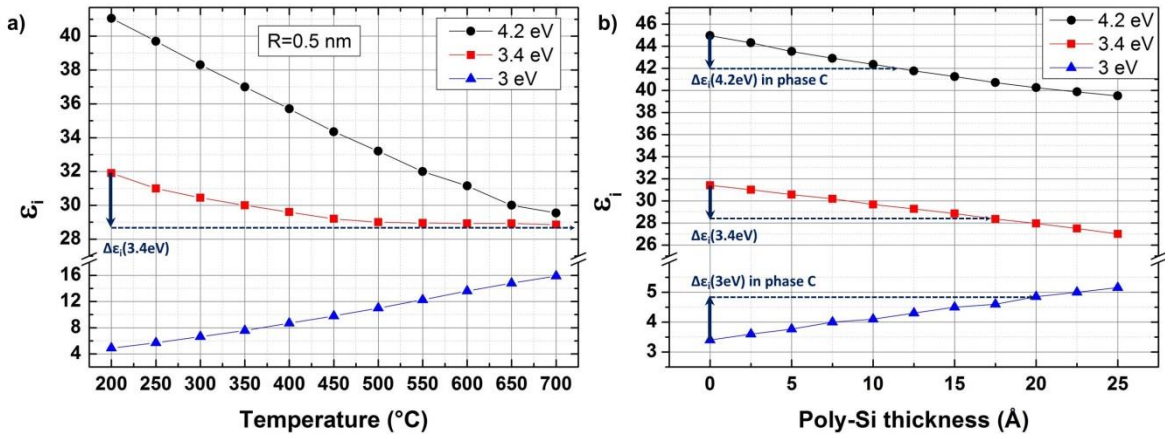

Fig. 3.5 – a) Simulated evolution of the imaginary part of the pseudo-dielectric function at 4.2, 3.4 and 3 eV for different substrate temperature. b) Simulated evolution of the imaginary part of the pseudo-dielectric function at 4.2, 3.4 and 3 eV for different thickness of a poly-Si layer deposited on a c-Si substrate at 200°C. In stage C: $\Delta\varepsilon_i$(4.2eV)=-3 and $\Delta\varepsilon_i$(3eV)=-1.5.

Finally, the dependence of ε_i on the crystallinity of the grown layer is shown in Fig. 3.5-b). To consider the growth of a defective layer in the early stages of growth, the first grown atomic layers have been modeled by a poly-Si layer. If we consider a defective material in the first stages of growth, the values measured *in situ* at a growth time of 240 s reasonably coincide with those modeled with a

dense poly-Si layer. The drops of ε_i at 4.2, 3.4 and 3 eV reported would correspond to a poly-Si layer with a thickness of 12, 17 and 20 Å respectively, i.e. to values in the same order of magnitude and quite close. The cause of the growth of a defective layer between stage A and C is therefore more consistent than a further increase of roughness or an increase of temperature. Note that no direct fitting provides relevant results, due to the complexity of the case and likely to a combination of the three phenomena detailed above. However, we can identify some trends: ε_i(4.2eV) and ε_i(3eV) are more sensitive to the roughness while ε_i(3.4eV) is more sensitive to the crystalline quality.

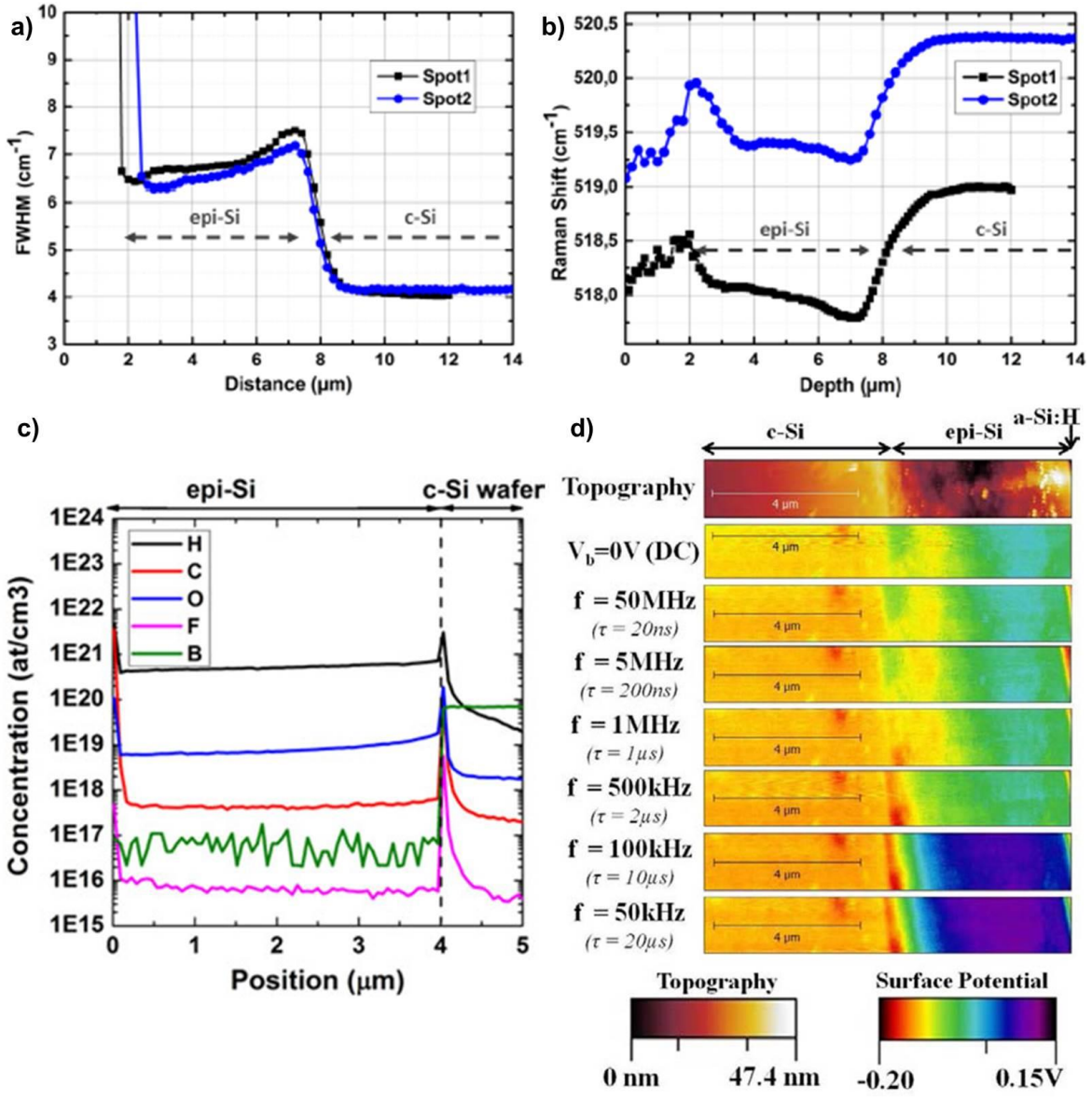

Fig. 3.6 –Raman cross section measurement performed on a 4 µm epitaxial sample grown by PECVD from SiH_4/H_2 gas mixture [8]. In a) is represented the FWHM of the TO mode of c-Si and b) its position. The surface is positioned at 2 µm. The measurements have been performed on two areas on the sample (spots 1 and 2). c) SIMS profile of a 4 µm thick epitaxial sample grown on a p^{++} wafer by PECVD from SiH_4/H_2 gas mixture and d) topography and surface potential mapping of a solar cell with a 5 µm thick epitaxial absorber grown on a p^{++} wafer by PECVD from SiH_4/H_2 gas mixture [10]. The measurements are carried out by KPFM under frequency-modulated voltage bias for different frequencies. The analyzed region is the same for each frequency.

The explanation of the drop of ε_i(3.4eV) at 240 s by the formation of a defective layer is also

supported by observations made in the case of epi-layers grown by PECVD from SiH_4/H_2. A similar evolution of $\varepsilon_i(4.2eV)$ and $\varepsilon_i(3.4eV)$ over time has been observed by Cariou [8] for LTE using SiH_4/H_2 gas mixtures. As a result, an analogy between both chemistries is relevant, even though larger drops are measured in the case of SiH_4/H_2 gas mixtures, with $\varepsilon_i(4.2eV)$ decreasing by up to 8 points in the initial stages of growth. In addition, Cariou investigated the evolution of the Raman signal on a 4 µm epitaxial layer in cross section [8]. The average scan line for the FWHM and the Raman shift position of the TO mode of c-Si over the epi-layer and the substrate are shown in Fig. 3.6-a) and -b).

The FWHM measured in the substrate region far from the interface (by at least 2 µm) is 4 cm^{-1}. At the interface the FWHM strongly increases to 7.5 cm^{-1} for spot 1 and to 7 cm^{-1} for spot 2 indicating that the interface is defective. In the bulk of the epi-layer the FWHM slowly decreases to reach FWHM values of 6.5 cm^{-1} for spot 1 and 6.3 cm^{-1} for spot 2. Thus, the author suggests that the quality of the epi-layers increase with the epi-layer thickness. This conclusion is also supported by the evolution of the Raman shift position over the sample. As shown in Fig. 3.6-b), the Raman shift position at the interface drops by 1.2 points with respect to that of the substrate. This peak shift is either attributed to a tensile strain in the layer or to the formation of grains. Given that XRD measurements indicate a compressive strain for these layers [8], the second explanation is more likely even though HR-TEM images do not show grain boundaries at the interface of these layers but only dislocations. These observations are consistent with our ellipsometry curves and their comparison to results of simulations. At some stage, a defective layer is formed followed by a recovery of the structural properties. Similarly to the evolution of the FWHM along the epi-layer, the Raman peak position shifts towards higher values indicating the recovery of the structural properties. The author suggests that these evolutions of FWHM and Raman peak position, indicating the recovery of structural properties along the layer, is the result of defects healing induced by hydrogen [9].

Even though the scales related in these experiments are micrometric and in our case nanometric, it appears that the interface is a critical issue affecting the structural properties of the whole epi-layer. Indeed, in addition to featuring a FWHM at the interface almost twice that of the substrate, it influences the growth at least over 2.5 µm. Thus focusing on the early stages of growth does not only provide insights to understand the growth mechanisms but also to improve the structural properties in the bulk of the epi-layer.

Besides, Narchi *et al.* [10] investigated minority carriers lifetime in LTE layers at the nanoscale by correlating SIMS measurement (Fig. 3.6-c)) with Kelvin probe force microscopy (KPFM) under frequency modulated voltage bias measurement (Fig. 3.6-d). They showed that the epi/wafer interface in a solar cell with a 4 µm epitaxial layer grown on a p^{++} wafer by PECVD from SiH_4/H_2 gas mixture has a lifetime shorter than in the bulk of the epi-layer. The objective of this technique detailed in [10], is to determine a difference of surface potential between various regions of the sample via their different response to a frequency modulated electrical bias. This allows to assess the minority carriers lifetime in the layer and to compare it with that of the substrate. The principle is to apply an AC voltage to the cell to switch from forward bias, for which there is an excess of minority carriers at the junction, to reverse bias, for which there is a lack of minority carriers at the junction. The time to go from forward to reverse bias is longer than the time to go from reverse to forward bias due to the fact that the injection of minority carriers is faster than the recombination of the excess minority carriers. Based on this, the reverse and forward recovery times depend on the minority carriers lifetime. For the mapping showed in (Fig. 3.6-d), the surface potential of the p^{++} wafer is not affected by the bias because it is grounded. For frequencies of 5 and 50 MHz, the frequency is too high to observe a distinction in lifetime between the different regions of the sample because one full period is shorter than the lifetime in every region of the epi-layer. At 1 MHz and 500 kHz, the epi/wafer interface is the

only region of the sample where the surface potential changes, indicating that the lifetime in this region is shorter than in the rest of the epi-layer, which is likely due to a higher defect density. When the frequency is further decreased to 100 kHz, the frequency is sufficiently low to observe change in the epi-layer. In light of this, a lifetime around 1 µs and 10 µs can be deduced in the near interface region and the bulk of the epi-layer respectively.

From these measurements we can conclude that an electrically active defective layer is observed at the epi/wafer interface. To explain its origin and to provide a clear explanation of the involved mechanisms, the interpretation of the evolution of ε_i over time in the early stages is not sufficient. Additional characterizations at the nanoscale are required.

3.2.2. Analysis of early stages of growth by HR-TEM

In order to gain further insight on the growth mechanisms, a complementary study by HR-TEM has been led. To correlate with ellipsometry measurements, three samples after the specific growth times represented in Fig. 3.3 by the points labelled A, B and C, have been analyzed by HR-TEM. The images are shown in Fig. 3.7.

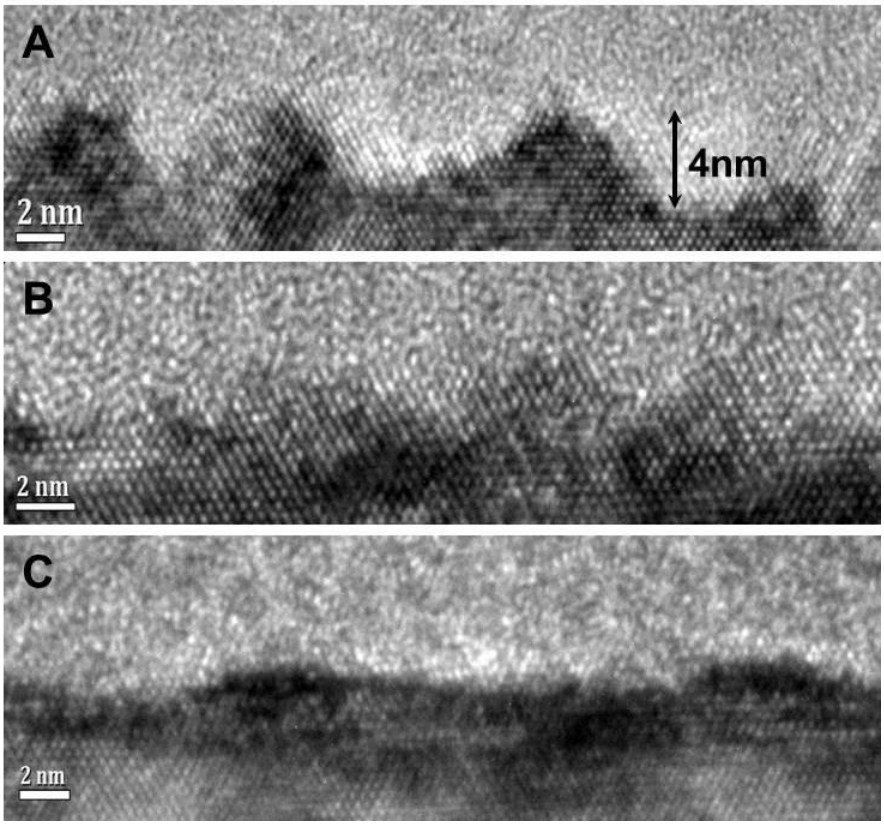

Fig. 3.7 – HR-TEM images of the surface in cross section for initial stages of epitaxial growth on a Si(100) substrate after an HF dip of 30 s. A, B and C images correspond to three different growth times represented by their respective point in the ellipsometry curve in Fig. 3.3. Process conditions are detailed in Fig. 3.3. Images: courtesy of F. Haddad

The HR-TEM images indicate that the stage A, which corresponds to the period for which ε_i(4.2eV) rapidly decreases and ε_i(3eV) rapidly increases, features a roughening of the layer in the form of a few nm high islands. A significant result is that these islands are crystalline and no defects are visible at this stage. This increase of roughness of a fully monocrystalline layer during the phase in which the stage A is contained correlates with the deduction made by the interpretation of the ellipsometry curves concerning the roughening. But a roughness of 4 nm is much too high compared to the 6 Å deduced from ellipsometry simulations (where we assumed a void fraction F_v=50%), such a difference could be explained by the restrictive condition on the roughness represented by a c-Si/void mix of 50%/50%. When the growth time is increased up to stage B, the layer becomes smoother which does not correlate with the evolution of ε_i(4.2eV). Logically, the stage B (minimum of ε_i(4.2eV)) should show the largest roughness, instead of stage A. This may be attributed to the fact that at the moment the plasma was stopped, ε_i(4.2eV) may have already reached its minimum. Indeed the time after which ε_i(4.2eV) reaches values below 39 is very short (16 s), so very close from the targeted time of 12 s, knowing that the acquisition time of the *in situ* ellipsometer is 5 s.

The epi-layer in stage B is smoother than in stage A which corresponds to the phase of coalescence of the islands. Regarding the HR-TEM images, the slow decrease of ε_i(3.4eV) between stages A and C can be attributed to the increase of the thickness of this defective layer associated to a progressive relaxation. This would be consistent with the cross section Raman measurement performed by Cariou and cross-sectional KPFM measurement by Narchi. Moreover the thicker the layer the more sensitive to its properties is ε_i(3.4eV) due to its penetration depth of 11 nm. In stage B the layer thickness varies from 4 to 6 nm. Therefore it is difficult to decorrelate the decrease of the structural properties from the increase of the thickness of a layer already defective. In the meantime, between stages B and C the HR-TEM images show that the layer smoothens, which correlates with the increase of ε_i(4.2eV) in the same phase. Afterwards, in stage C the layer looks more defective which could be the result of a relaxation, which induced the formation of defects. This would match with the drop of ε_i(3.4eV) at this stage which indicates the formation of a poly-Si layer. After stage C, the structural properties of the upper layers improve as observed with the increase of ε_i(3.4eV). This recovery of structural properties can be explained by the healing of defects (those defects being induced by the relaxation). The phase after stage C is also associated to a smoothening of the surface as observed by the increase of ε_i(4.2eV) up to 500 s to finally reach an atomically smooth surface as seen in HR-TEM images in Chapter 2. ε_i(3.4eV) reaches its maximum after 700 s and finally stabilizes after 1200 s, these differences with respect to ε_i(4.2eV) can be associated in that case to their different penetration depth. All the steps in the early stages are not fully understood yet. Nevertheless we can affirm from HR-TEM images associated to ellipsometry that LTE by PECVD relies on a Volmer-Weber growth mode.

To sum up the stages of growth, a model can be suggested as follows:

i) Roughening of the surface through strained monocrystalline islands corresponding to the nucleation (Phase up to stage A).

ii) Coalescence of islands and relaxation leading to a defective layer (Phase from stage A to C).

iii) Smoothing and recovery of structural properties due to defects healing (Phase after stage C up to stabilization of ε_i(4.2eV) ε_i(3.4eV)). This phase can be divided in two periods as observed in Fig. 3.9 and in [8]:

   1. Fast increase of ε_i(4.2eV) and ε_i(3.4eV) corresponding to a fast recovery of structural properties.

2. Slow increase of ε_i(4.2eV) and ε_i(3.4eV) corresponding to a slow recovery of structural properties.

iv) Smooth and stable epitaxy.

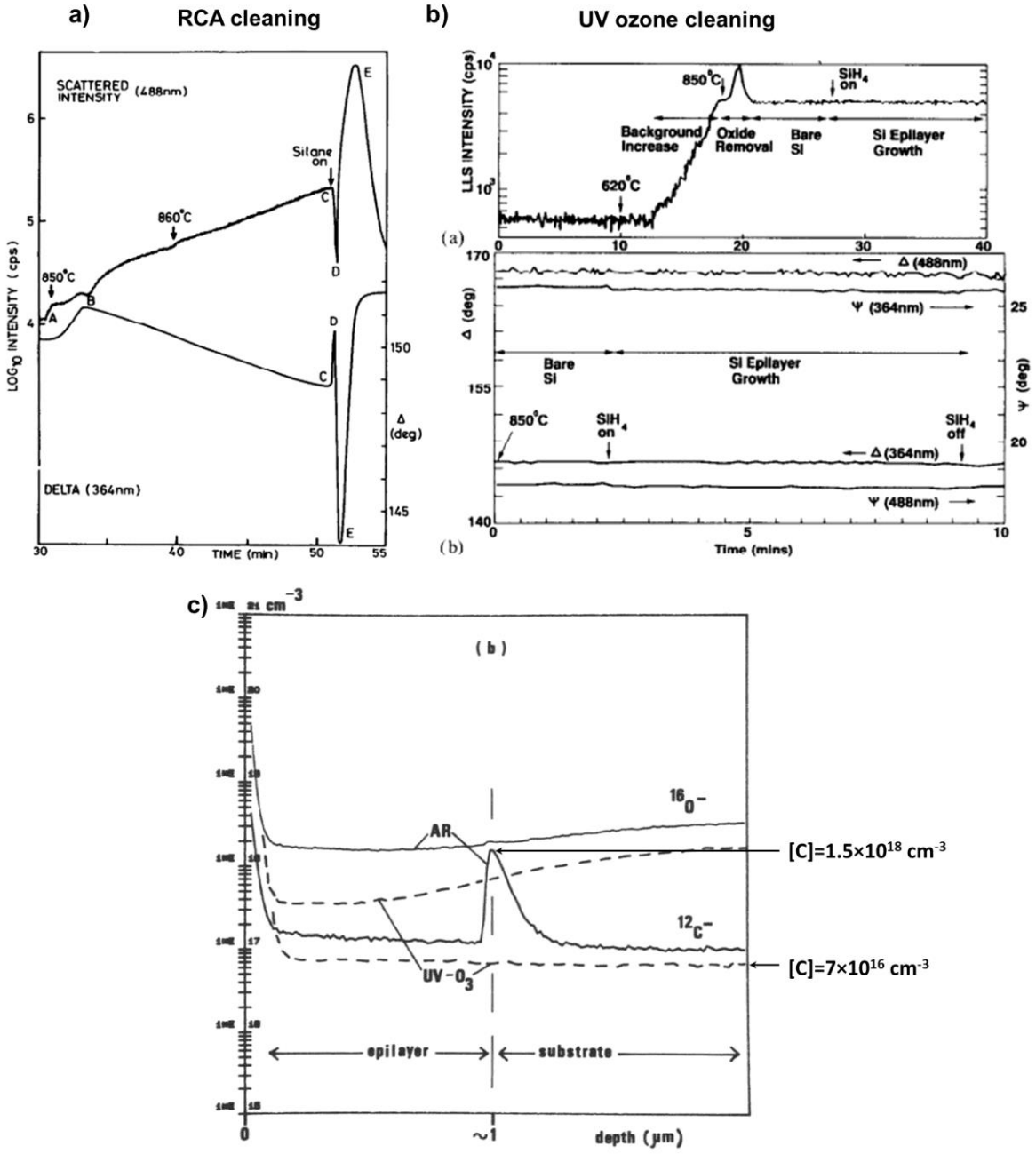

Fig. 3.8 – Evolution over time of ellipsometry signal (Δ) at 364 nm (3.4 eV) and LLS signal at 488 nm (2.54 eV) before and during initial stages of epitaxial growth by VPE at T°C=850°C (SiH_4/H_2 chemistry and p=0.1-1 Torr) for a) RCA cleaning and b) UV ozone cleaning prior to epitaxy [11]. The beginning of growth is represented by a black arrow and "Silane/SiH_4 on". c) SIMS profiles of samples with epitaxy after RCA cleaning (AR) and after UV ozone cleaning (UV-O_3) [15].

However the roughening and the formation of islands in initial stages of growth must be related to the process itself but also to the surface state prior to epitaxy. Pickering showed in [11] that the surface

state and especially the carbon contamination of the wafer substrate prior to the epitaxy was extremely critical on the Δ angle measured by ellipsometry. The evolution of laser light scattering (LLS) and ellipsometry (Δ) signals for the homoepitaxy of silicon by UHV-VPE at 850°C using SiH_4/H_2 gas mixtures at a working pressure between 0.1 and 1 Torr is shown in Fig. 3.8. Note that Ψ and Δ are used in these graphs, to compare with our data ε_i follows the same trend as Δ.

As shown in the case of RCA cleaning in Fig. 3.8-a), a decrease of Δ is observed in the initial stages of growth indicating an increase of the roughness. Conversely, in the case of UV ozone cleaning (Fig. 3.8-b)), which efficiently removes carbon contaminations contrary to their RCA cleaning as shown in the SIMS profiles in Fig. 3.8-c), the Δ signal is constant indicating that the growth does not feature an increase of roughness at the beginning.

The epitaxy by CVD at 850°C relies on Frank-van der Merwe growth mode. When the surface of the substrate has been submitted to a proper cleaning, unsurprisingly, no variation of both LLS and ellipsometry signals is observed meaning no increase of the roughness during the initial stages of growth, at least not observable by ellipsometry and LLS. However when the surface is contaminated with carbon, it shows a roughening of the sample surface. Consequently, in the RCA cleaning case, the growth does not rely on a Frank-van der Merwe mode in the early stages of growth. Note that the recovery of a stable signal is faster for ellipsometry than LLS, this is due to the fact that ellipsometry is more sensitive to nano/microscopic roughness than LLS and inversely [12]. It is worth noticing that the initial value of Δ prior the epitaxy is 149° for the sample after RCA cleaning and 147°, so the UV ozone cleaning may slightly roughen the substrate surface. But this roughening should not be significant enough to affect the growth mechanisms since ellipsometry simulations show that a loss of 2° for Δ corresponds to an increase of roughness of 5 Å (mix: 50% c-Si/50% void).

Therefore, this raises the issue of the dependence of the growth mechanisms on the surface state. To rigorously tackle this question, the same study with a proper cleaning prior to epitaxy should have been led but we have not been able to develop it during this PhD. To reduce surface contamination effects, a rerun of epitaxy after stabilization has been performed to get rid of the surface state (fluorinated surface due to HF dip, carbon and oxygen contaminations, …). This epitaxy has been carried out in Philix, contrary to the experiments detailed above. However the same shape of ellipsometry curves are observed in both reactors. The process conditions used for this experiment are: a RF power of 15 W (200 mW/cm^2), SiF_4, H_2 and Ar flow rates of 3.6, 1 and 88 sccm respectively. The inter-electrode distance is fixed at 2 cm and the pressure at 3 Torr. Substrate and RF electrode temperatures are set to 200 and 100°C respectively. The ellipsometer implemented on Philix, a Uvisel 1 from Horiba Jobin Yvon, allows to monitor ε_i at one single wavelength. The result of the evolution of ε_i(4.2eV) over time in these conditions is shown in Fig. 3.9. Between the first and the second epitaxy the gas has been pumped and the reactor has been put back under turbo pumping to reach a vacuum below 10^{-6} Torr, with the sample remaining in the reactor.

For the first epitaxy, ε_i(4.2eV) drops by 4 points while it only drops by 2 points for the regrowth, indicating that the roughness in the initial stages of growth is smaller in the case of the second epitaxy. A second observation is that the minimum of ε_i(4.2eV), i.e. the maximum of roughness, is reached after 35 s for the first epitaxy while it takes 125 s for the second one. These differences can be attributed to the difference of surface state and, in particular, contaminations at the surface. Despite these differences, the same behavior of ε_i(4.2eV) is observed on the regrowth, i.e on a clean and smooth surface (ε_i(4.2eV) is even higher after epitaxy than before), which bring us to the same conclusion about the causes of this drop of ε_i(4.2eV), namely a Volmer-Weber growth mode. This also shows that this drop is due to a variation of material properties rather than an effect of plasma itself

(e.g. through optical emissions) on the ellipsometry measurement. Besides, even though we showed that the lattice mismatch was less than 1.10^{-3} Å between the epi-layer grown in these conditions and a c-Si substrate, it is necessarily smaller for the regrowth than for the first growth. Thus, the difference between the *in situ* ellipsometry spectra of the first epitaxy and the second one can also likely be explained by their different lattice mismatch with their respective substrate.

Another interesting feature in this ellipsometry curve is the systematic increase of ε_i(4.2eV) when the plasma is stopped. In the case presented in Fig. 3.9-a), this increase is around 1 point but in some cases it can increase of a few points. This may be associated to an increase of the sample temperature when the process is ongoing and its cooling when the plasma is stopped.

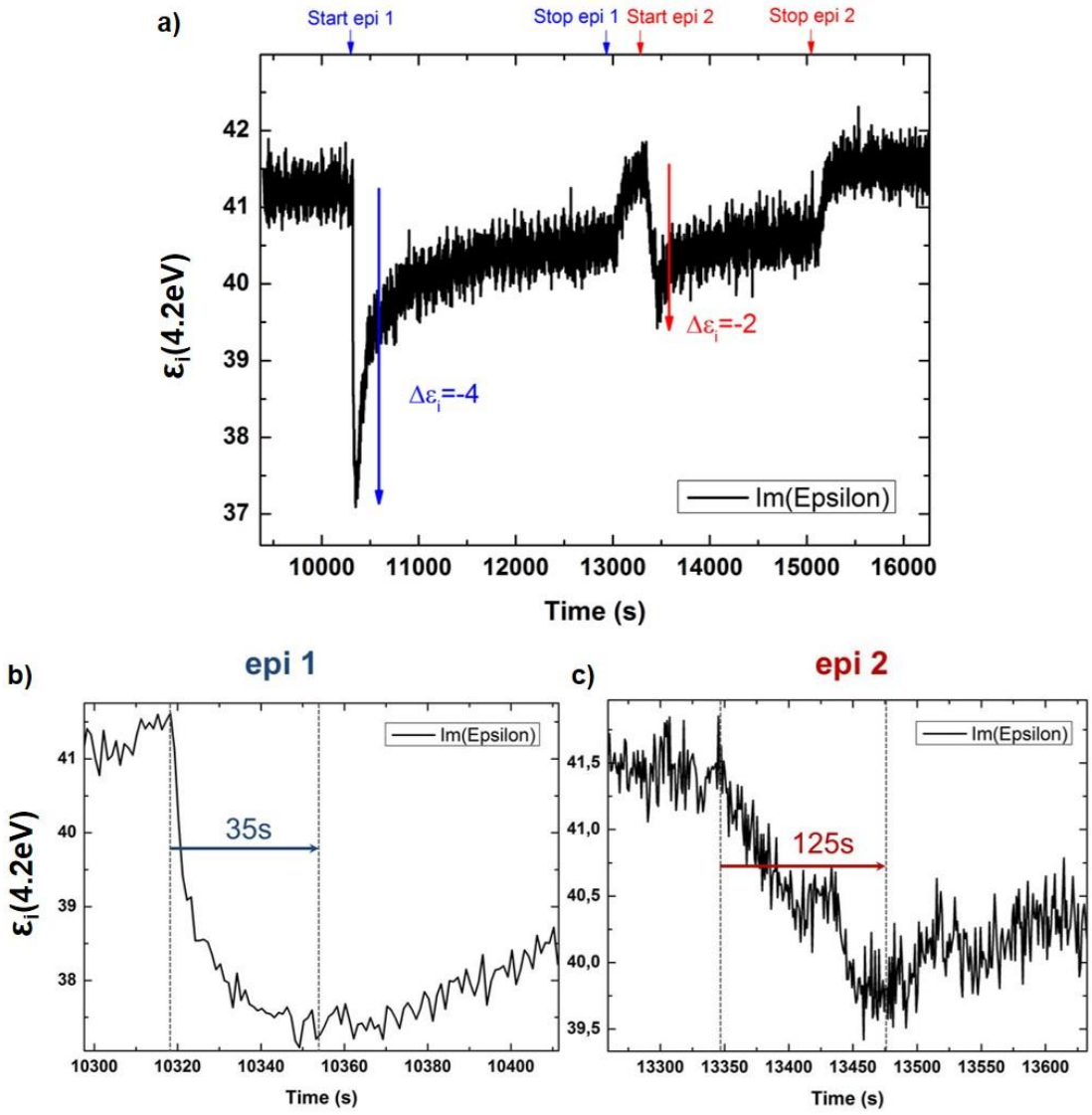

Fig. 3.9 – a) Evolution of the imaginary part of the pseudo-dielectric function at 4.2 eV (ε_i(4.2eV)) as a function of time for two epitaxial growths performed on the same sample. b) Zoom in the initial stages of growth for the first epitaxy and c) the second epitaxy.

It is worth noticing that a sharp increase is only observed when the plasma is stopped after a high (above 35) and stable signal of ε_i(4.2eV), i.e. when a layer with a high crystallinity is obtained. When epitaxy breakdown occurs, the increase of ε_i(4.2eV) is very slight indicating that this is not a single effect of the plasma but a material effect instead. This interestingly correlates with the study of

Abolmasov *et al.* [13] about the effect of SiH_4/H_2 dusty plasmas on the temperature of the sample. They measured thanks to a heat flux microsensor the energy flux on samples exposed to a plasma composed of either Ar, H_2 or SiH_4/H_2 for different pressures and RF power. For Ar plasma no significant difference is observed when the RF power and pressure are respectively varied from 10 to 50 W and from 0.68 Torr to 3 Torr. In contrast, for SiH_4/H_2 plasma, under a pressure of 2 Torr the energy flux is 10 times higher at 50 W with respect to that at 10 W, while at 0.5 Torr the energy flux is only doubled. They suggest that in the case of a high pressure the ion sheath becomes thinner and as a result the ion bombardment is enhanced, which would explain a higher energy loads and as a consequence the increase of temperature. However, the increase of pressure also favors the formation of nanoparticles, and the reaction of these nanoparticles with the substrate could also heat the sample through chemical annealing. This hypothesis has been studied by Thi Le *et al.* [9], they showed by *ab initio* molecular dynamics simulations that under the effect of H-atom reactions, some amorphous and crystalline nanoparticles may reach temperatures above 1400 K, leading to a solid to liquid phase transition. Thus, this raises the question of the main precursors involved in the LTE process.

3.3. Identification of precursors in low-temperature epitaxy

Three main types of precursor can be identified to be involved in LTE by PECVD: radicals (Si_nH_x, $Si_nF_mH_x$, …), ions, and nanoparticles. The question of the main type of precursor in LTE by PECVD remains unclear. The existence of nanoparticles in reactive plasma for the deposition of Si thin films is known since a long time but their effect on the actual deposition remains not fully understood [14]. To verify the hypothesis of a growth mainly ensured by nanoparticles we compared the pattern of the initial stages of growth obtained on c-Si substrates and on TEM copper grids with carbon membranes, for which the surface reactions should be completely different. For that, energy filtered transmission electron microscopy (EFTEM) is used, it allows to select specific energies of electrons and thus specific chemical species. By doing so, carbon and silicon maps can be obtained. EFTEM images of TEM grids for stage A are shown in Fig. 3.10, they are taken from F. Haddad's thesis. The TEM grid has been stuck to the wafer and placed close to the region analyzed by HR-TEM.

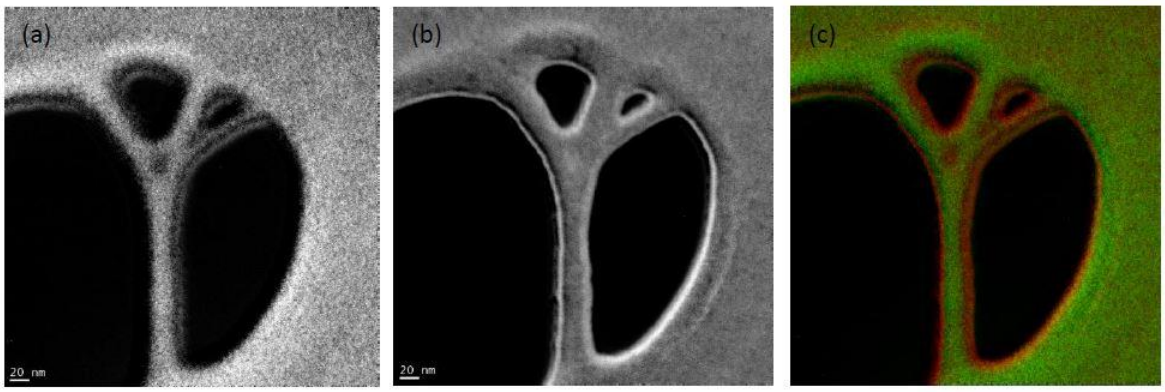

Fig. 3.10 – a) Carbon map, b) silicon map and c) map combining contribution of both carbon (in green) and silicon (in red) obtained by EFTEM at the stage of maximum roughness on the c-Si substrate [1]. In a) and b) the higher intensity areas correspond to the areas with the higher concentration of the analyzed element.

Fig. 3.10 shows that silicon is preferentially deposited on the edge of the holes of the TEM grid and that only few traces of silicon are observed on the top of the TEM grid. This phenomenon is not

understood yet. It may come from electrostatic interactions between silicon precursors and the carbon membrane. In the case of a growth mainly ensured by nanoparticles we should expect red spots, representing silicon nanoparticles, on a green continuum.

The existence of nanoparticles in the plasma is not questioned since some have also been observed on the TEM grids as shown in Fig. 3.11. All the nanoparticles observed are amorphous. This result is consistent with the fact that epitaxial conditions processed on glass lead to amorphous silicon deposition, and not microcrystalline. At stage A, nanoparticles with a diameter around 10 nm are observed, they have the particularity to stick to each other leading to the formation of clusters composed of tens of nanoparticles. Thus, the contribution of these nanoparticles to the deposition is difficult to assess since they do not respect the pattern described by the islands on the c-Si substrate observed in the HR-TEM images in stage A.

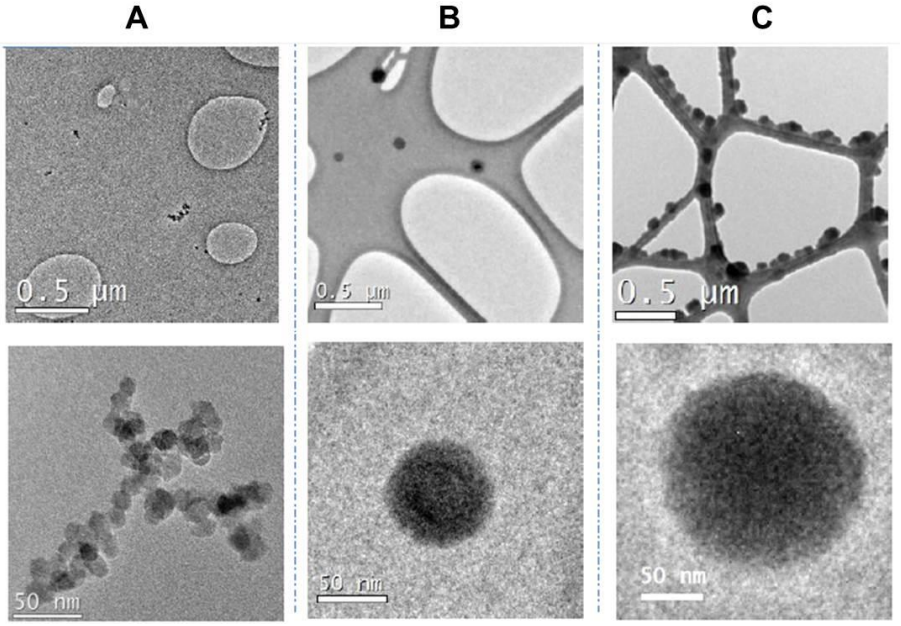

Fig. 3.11 – TEM and HR-TEM images obtained on TEM copper grids with carbon membrane for stages A, B and C. Bottom images are zoomed in the top images. These depositions on TEM grids have been carried out in the same respective run as those on c-Si and analyzed by HR-TEM (Fig. 3.7).

In stage B, the size of nanoparticles increases and reaches diameters superior to 50 nm for most of them. Finally at stage C, up to 200 nm large aggregates are observed. Therefore, the increase of the deposition time induces an increase of the size of nanoparticles observed on the TEM grids. It is unlikely that the particles observed in stage B and C are involved in the growth of epi-layer due to their large diameter. The contribution to the growth of smaller size nanoparticles, as those observed in stages A and potentially smaller nanoparticles that we do not observe, remains unclear. A better way to compare the pattern of the initial stages of growth to identify if nanoparticles are the main precursors would be to deposit on a carbon coated c-Si substrate and to compare HR-TEM images in cross section to those shown previously in Fig. 3.7.

3.4. Conclusion

From the correlation of *in situ* ellipsometry measurement and HR-TEM images in the early stages of growth we have been able to demonstrate that low temperature epitaxy by SiF_4/H_2/Ar chemistry, and likely SiH_4/H_2 chemistry, relies on a Volmer-Weber growth mode. The evolution of growth over time can be suggested as the following:

i) Roughening of the surface through strained monocrystalline islands corresponding to the nucleation.

ii) Coalescence of islands and relaxation leading to a defective layer at the epi/wafer interface.

iii) Smoothing and recovery of structural properties due to defects healing. This phase can be divided in two periods: a fast (~ a few min) followed by a slow (~ tens of minutes to hours) recovery of structural properties.

iv) Smooth and stable epitaxy.

We also demonstrated that the surface state has a strong influence on the initial stages of growth since a regrowth on an epi-layer shows lower values for the drop of ε_i(4.2eV), which can be attributed to a lower roughening. To further analyze the effect of the surface state on the growth mechanisms, epi-layers grown on an interface with fewer contamination, thanks to a proper wafer cleaning prior to epitaxy, should be processed and analyzed by HR-TEM in order to verify the cause of the increase of roughness in the early stages of growth.

Finally, the study of the co-deposition on TEM copper grids with carbon membranes aimed to provide insight on the identification of the main precursors involved in LTE. The analysis of TEM grids led to the observation of amorphous nanoparticles whose diameter increases with the deposition time. The amorphous properties of the nanoparticles are consistent with the fact that, during an epitaxial growth (on c-Si), a co-deposition on glass leads to amorphous silicon layers. However the patterns described by the nanoparticles and the EFTEM images do not match with that described by the crystalline islands observed on the c-Si substrate in the early stages of growth. Additional investigations are required to identify the main precursors, the co-deposition on a carbon coated c-Si substrate is suggested.

References

[1] F. Haddad, “Transmission electron microscopy study of low-temperature silicon epitaxy by plasma enhanced chemical vapor deposition,” University of Paris-Saclay, 2016.

[2] E. Bauer, “Phänomenologische Theorie der Kristallabscheidung an Oberflächen. I,” *Zeitschrift für Krist.*, vol. 110, no. 1–6, pp. 372–394, Jan. 1958.

[3] J. A. Stroscio, D. T. Pierce, and R. A. Dragoset, “Homoepitaxial growth of iron and a real space view of reflection-high-energy-electron diffraction,” *Phys. Rev. Lett.*, vol. 70, no. 23, pp. 3615–3618, Jun. 1993.

[4] J. Venables, *Introduction to surface and thin film processes*. Cambridge University Press, 2000.

[5] J. A. Stroscio and D. T. Pierce, “Scaling of diffusion-mediated island growth in iron-on-iron homoepitaxy,” *Phys. Rev. B*, vol. 49, no. 15, 1994.

[6] G. Vuye, S. Fisson, V. Nguyen Van, Y. Wang, J. Rivory, and F. Abelès, “Temperature dependence of the dielectric function of silicon using in situ spectroscopic ellipsometry,” *Thin Solid Films*, vol. 233, no. 1–2, pp. 166–170, Oct. 1993.

[7] D. Daineka, V. Suendo, and P. Roca i Cabarrocas, “Temperature dependence of the optical functions of amorphous silicon-based materials: application to in situ temperature measurements by spectroscopic ellipsometry,” *Thin Solid Films*, vol. 468, no. 1, pp. 298–302, 2004.

[8] R. Cariou, “Epitaxial growth of Si(Ge) materials on Si and GaAs by low temperature PECVD: towards tandem devices,” PhD thesis, Ecole Polytechnique, 2015.

[9] H.-L. Thi Le, N. C. Forero-Martinez, and H. Vach, “Heating and melting of plasma-born hydrogenated silicon clusters by reactions with atomic hydrogen,” *Phys. status solidi*, vol. 211, no. 2, pp. 294–300, 2014.

[10] P. Narchi, R. Cariou, M. Foldyna, P. Prodhomme, and P. Roca i Cabarrocas, “Nanoscale Investigation of Carrier Lifetime on the Cross Section of Epitaxial Silicon Solar Cells Using Kelvin Probe Force Microscopy,” *IEEE J. Photovoltaics*, vol. 6, no. 6, pp. 1576–1580, Nov. 2016.

[11] C. Pickering, “Correlation of in situ ellipsometric and light scattering data of silicon-based materials with post-deposition diagnostics,” *Thin Solid Films*, vol. 206, no. 1–2, pp. 275–282, Dec. 1991.

[12] D. T. J. Hurle, *Handbook of crystal growth*. 1994.

[13] S. N. Abolmasov, P.A. Cormier, A. Torres Rios, R. Dussart, N. Semmar, A.L. Thomann and P. Roca i Cabarrocas, “Probing dusty-plasma/surface interactions with a heat flux microsensor,” *Appl. Phys. Lett.*, vol. 100, no. 1, p. 11601, Jan. 2012.

[14] P. Roca i Cabarrocas, K.H. Kim, R. Cariou, M. Labrune, E.V. Johnson, M. Moreno, A. Torres Rios, S. Abolmasov and S. Kasouit, “Low Temperature Plasma Synthesis of Nanocrystals and their

Application to the Growth of Crystalline Silicon and Germanium Thin Films," *MRS Proc.*, vol. 1426, p. mrss12-1426-a12-01, Jan. 2012.

[15] D. J. Robbins, A. J. Pidduck, C. Pickering, I. M. Young, and J. L. Glasper, "In-Situ Study Of Silicon Vapour Phase Epitaxy Using Laser Light Scattering," 1989, pp. 25–34.

4. Boron and phosphorus doped low-temperature epitaxy – From process transfer to lifetime test samples

In this chapter we detail the process conditions to produce boron and phosphorus-doped epitaxial layers at 200°C to 300°C. The first part deals with the transfer of the epitaxial process from Philix to Cluster, a pre-pilot line tool, and the characterization of the boron and phosphorus-doped epi-layers. In the second part we discuss the modifications of the shower head necessary to obtain uniform epi-layers and to increase the deposition rate for the purpose of succeeding the scale-up to 4 and 6-inch wafers. Based on the fluidics simulation for the optimization of the shower head, the influence of several parameters (pressure, P_{RF},…) on the homogeneity of structural and electrical properties of the epi-layers will be investigated. Finally, the passivation of the epi-layers will be studied.

4.1. Process transfer

In this part we address the transfer of the process conditions optimized in Chapter 2 on a small scale (4 inches) laboratory research reactor (Philix) to a pre-pilot (6 inches) semi-industrial reactor (Cluster). It should be noted that the heating on the Cluster is performed by a non-contact method via a heater well. The monitored temperature is that of the heater well, the actual substrate holder temperature is deduced from an abacus provided by the manufacturer. The substrate holder temperature is roughly 100°C lower than that of the heater well.

The first experiments consist in defining the lower and upper limit for most process parameters, even if we know they are linked. The first parameter we will study is the electrode temperature. In Fig. 4.1-a) the H_2 depletion, and the consequent H_2 consumption, as a function of the H_2 flow rate are shown for two electrode temperatures. The substrate temperature is fixed at 200°C, like for the definition of the process window in Chapter 2, while the temperature of the RF electrode is varied from 100°C to 200°C (its maximum value). We keep the RF power density close to that leading to the best epitaxy in Philix (same properties between epi-layers and wafer by ellipsometry, XRD and Raman spectroscopy), namely between 130 mW/cm^2 and 200 mW/cm^2. Given that the RF electrode area in Cluster is 225 cm^2, i.e 3 times larger than that of Philix, the RF power will be fixed at 40 W, corresponding to a RF power density of 180 mW/cm^2. For this experiment the pressure and the SiF_4 flow rate have been fixed at 2.5 Torr and 20 sccm, respectively. The same trend obtained in Philix is observed. At low H_2 flow rate the depletion is higher than 80% and follows a plateau. After a certain threshold (here around 5 sccm) the H_2 depletion drops. As detailed in Chapter 2, the process conditions for epitaxy are necessarily in the plateau at low H_2 flow rates. Even if there are no significant differences on H_2 depletion for the low H_2 flow rates between a RF electrode at 100°C and 200°C, the transition is smoother at 200°C compared to 100°C. At 6 sccm the H_2 depletion at 200°C is around 15% higher than that at 100°C. Thus at 200°C the epi-Si/a-Si:H transition should be less abrupt limiting the risk of an epitaxy breakdown when the H_2 flow rate is increased. In light of this, a RF electrode temperature of 200°C is preferable.

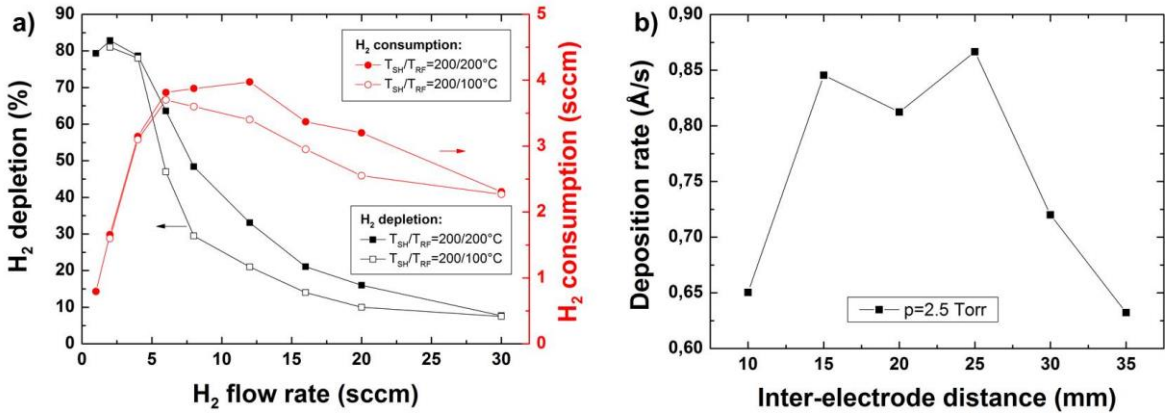

Fig. 4.1 – a) H_2 depletion and the related H_2 consumption as a function of H_2 flow rate for a substrate holder temperature (T_{SH}) of 200°C and a RF electrode temperature (T_{RF}) of 100°C and 200°C. The SiF_4 and Ar flow rates are fixed at 20 and 300 sccm, respectively. Inter-electrode distance, pressure and RF power are respectively fixed at 20 mm, 2.5 Torr and 40 W. b) Evolution of the average deposition rate of a-Si:H on glass, for process conditions leading to epitaxy on a c-Si substrate, as a function of the inter-electrode distance. The H_2 flow rate is fixed at 3 sccm, the rest of process conditions are the same as those used for a).

Given that the thickness of the layers deposited on a c-Si wafer is sometimes difficult to measure, depending on the chosen H_2 flow rate as detailed previously, a first study on glass has been led to determine a coarse range of inter-electrode distances to investigate. The results of the average deposition rate calculated from 5 ellipsometry spectra measured at the center and the corner of 5x5 cm^2 samples are given in Fig. 4.1. While the deposition rate is rather constant between 15 mm and 25 mm, it drops by 30% at 10 mm and 35 mm. However, a short inter-electrode distance leads to highly inhomogeneous layers. In order to limit the effect of gas injection on the homogeneity but keeping a reasonable deposition rate, a good tradeoff is to study the properties of the materials for an inter-electrode distance varied from 20 mm to 30 mm.

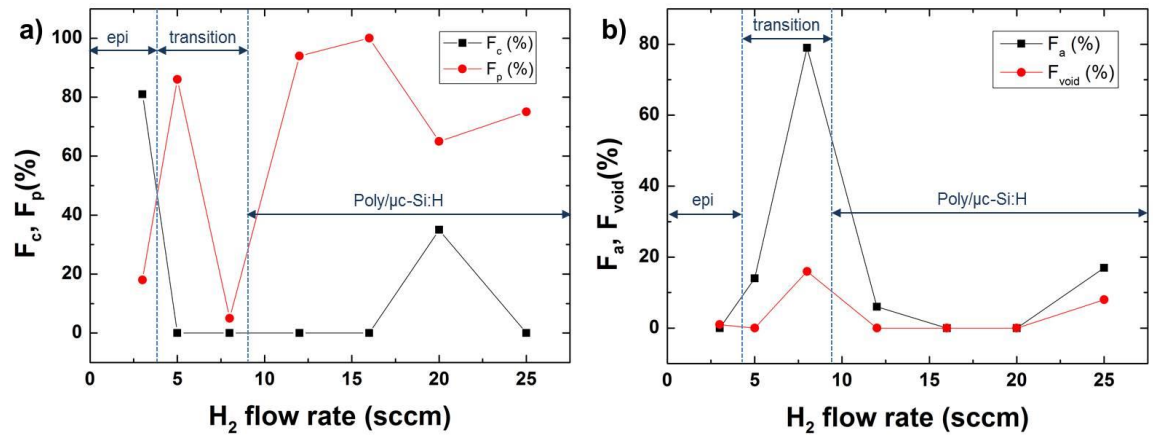

Fig. 4.2 – a) Average crystalline, polycrystalline, b) amorphous and void fractions of epi-layers deduced from the modelling of ellipsometric spectra for different H_2 flow rates, varied from 3 to 25 sccm. The SiF_4 and Ar flow rates are fixed at 20 and 300 sccm, respectively. The inter-electrode distance is 20 mm and the pressure 2.5 Torr. The RF power is 40 W.

In the same way as what has been done in Chapter 2, a series of samples has been produced at various

H_2 flow rates and characterized in terms of their crystalline, polycrystalline, amorphous and void fractions. Results are shown in Fig. 4.2.

Interestingly, the same transition around 5 sccm is found in the H_2 depletion (see Fig. 4.1-a) and the material component fractions. This is fully consistent with Chapter 2, validating the process transfer. Up to 3 sccm of H_2, the regime is epitaxial while the material becomes polycrystalline at 5 sccm. When the H_2 flow rate is further increased the regime is amorphous up to 12 sccm of H_2 and becomes microcrystalline for flow rates above 12 sccm. This epi-Si:H/a-Si:H/µc-Si:H transition confirms the observations detailed in Chapter 2. It is worth noticing that in Cluster, the H_2 depletion appears to be more difficult to achieve than in Philix. Even though the full H_2 depletion condition on the epitaxial growth is also applicable in Cluster, the requirement on the gas ratio is strongly different: 0.33 for Philix against 0.06 for Cluster. This might be attributed to the presence of a plasma box in Philix ensuring a better dissociation of SiF_4. As a result more fluorine would be formed which allows to inject higher H_2 flow rates while remaining in the H_2-limited regime.

As the substrate temperature range on the cluster is larger than on Philix, we could study the effect of the substrate temperature on the pseudo-dielectric function from 150°C to 300°C. As shown in Fig. 4.4, from 200°C to 300°C no significant difference is observable on the spectra, but at 150°C, a significant decrease on the amplitude of the Van Hove singularities is observed, decreasing by 2 points at 3.4 eV and by around 5 points at 4.2 eV, which reveals an increase of the sample roughness. This could be attributed to the fact that the mobility of adatoms at the surface is lower at this temperature and this threshold may be due to a critical reduction of surface diffusion at temperatures lower than 200°C.

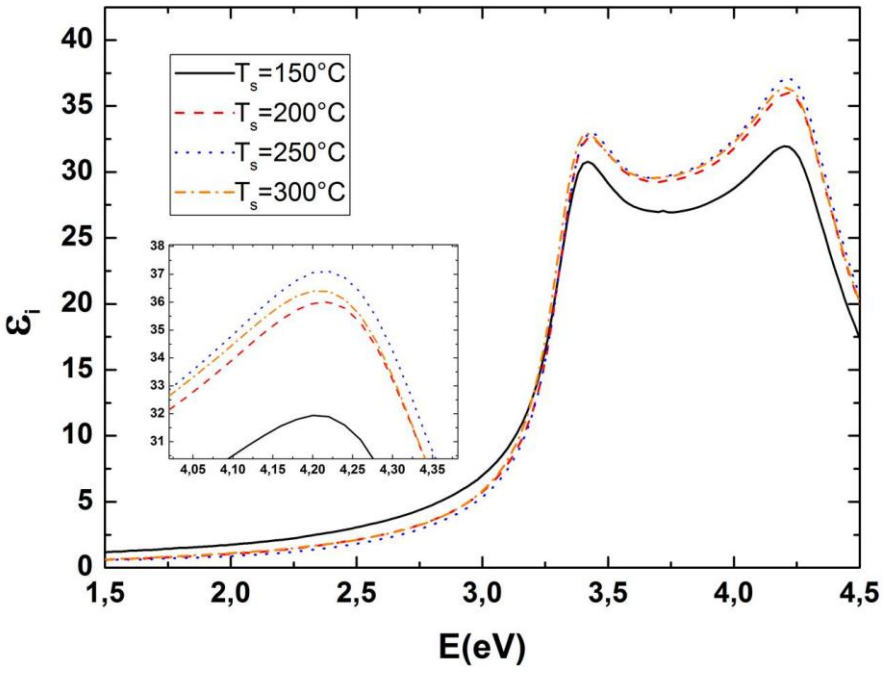

Fig. 4.3 – Pseudo-dielectric function of epitaxial films deposited at different substrate temperatures. The temperature of the RF electrode is fixed at 200°C. The RF power is fixed at 40 W (180 mW/cm^2) and the SiF_4, H_2 and Ar flow rates are fixed at 20, 3 and 300 sccm respectively.

A major difficulty of epitaxial films produced from $SiF_4/H_2/Ar$ gas mixtures is to determine their growth rate. As seen in Chapter 2 and Fig. 4.3, the absence in most cases of interference fringes in the ellipsometry spectra at low energy makes the calculation of epi-layers thickness impossible.

Nevertheless these interferences can be observed during deposition. As shown in Fig. 4.4 the monitoring of the pseudo-dielectric function at 3 eV (ε_i(3eV)) allows to assess the thickness of the film during deposition. We choose 3 eV because this photon energy is sufficiently low to allow observing the interferences fringes due to a penetration depth larger than the thickness targeted for our applications ($\leq$ 500 nm) and sufficiently high to have the best resolution on the determination of the thickness given that it is necessarily linked to the used wavelength. Fig. 4.4-a) shows that in case of a mixed phase (crystalline/polycrystalline) growth, the period and the phase of the oscillations are identical, so that model can be used in this type of growth. However, in case of a mix of crystalline, polycrystalline and amorphous phases, although the period is the same, the oscillations are in opposition of phase with respect to crystalline and crystalline/polycrystalline deposition. As a result, a progressive epitaxy breakdown can induce a disappearance of these oscillations. This explains why in case of a progressive epitaxy breakdown no interferences are visible on the full spectrum. By comparing the model experimental data, in Fig. 4.4-a), to the experimental data, in Fig. 4.4b-), we are able to *in situ* determine the thickness of the layer knowing that one oscillation corresponds to a thickness of 40 nm. Thus we can see that 60 min of growth corresponds to two full periods of ε_i(3eV) indicating that the layer is 80 nm thick. This leads to a growth rate for intrinsic epi-layers of 0.2 Å/s, i.e. 4 times slower than for a-Si:H deposition on glass with the same process conditions (see Fig. 4.1-b).

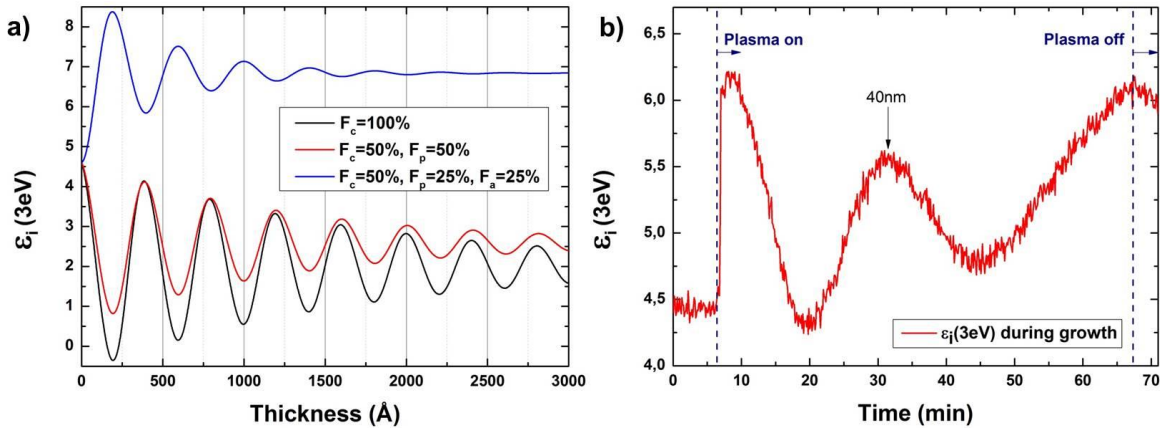

Fig. 4.4 – a) Modeled evolution of the imaginary part of the pseudo-dielectric function at 3 eV (ε_i(3eV)) as a function of epi-layer thickness for different film compositions. b) Experimental results of the monitoring of ε_i(3eV)) during epitaxial growth.The SiF_4,H_2 and Ar flow rates are fixed to 20, 3 and 300 sccm respectively. The RF power is 40 W and the pressure 2.5 Torr. The inter-electrode distance is 20 mm.

Fig. 4.4-b) also shows that in case of epitaxial growth by PECVD the behavior of ε_i(3eV) is different at the beginning of growth. Instead of decreasing, ε_i(3eV) quickly increases which might be interpreted as the deposition of amorphous silicon at the beginning of the growth, as observed in Fig. 4.4-a), but this explanation is unsatisfactory. Indeed, this abrupt change of ε_i(3eV) correlates with the drop of ε_i(4.2eV) previously explained in Chapter 3 and is therefore associated to an increase of the roughness in the early stages of epitaxial growth. In these conditions, the fitting of the ellipsometry spectrum at 200°C, shows an increase of the sample roughness up to 10 Å during the early stages of growth.

4.2. Phosphorus doping

Once the conditions for epitaxy have been transferred to the Cluster reactor the behavior of the doped epitaxy has been investigated. This part deals with the n-type doping of epi-layers by introducing phosphine (PH_3) in the gas mixtures. From the conditions detailed above, namely a substrate temperature of 200°C and an electrode temperature of 200°C, the effect of the PH_3 flow rate on the epitaxy has been investigated by ellipsometry. The results are shown in Fig. 4.5. All the phosphorus doped epi-layers detailed in this part are grown with an inter-electrode distance of 20 mm. The SiF_4 and Ar flow rates are respectively fixed at 20 sccm and 300 sccm. It is worth noticing here that PH_3 is highly diluted in H_2 (0.1%) so that it is not possible to indefinitely increase the PH_3 flow rate, else the condition of full H_2 depletion would not be respected. As a consequence, process conditions would exit from the process window allowing epitaxy, and would lead to amorphous deposition and then microcrystalline deposition if the H_2 flow rate is further increased as explained in Chapter 2. Thus the H_2 flow rate is fixed in such a way that the addition of the H_2 and PH_3 flow rates is equal to 3 sccm ($f_{H2}+f_{PH3}$=3 sccm), given that phosphine is diluted at 0.1% in hydrogen.

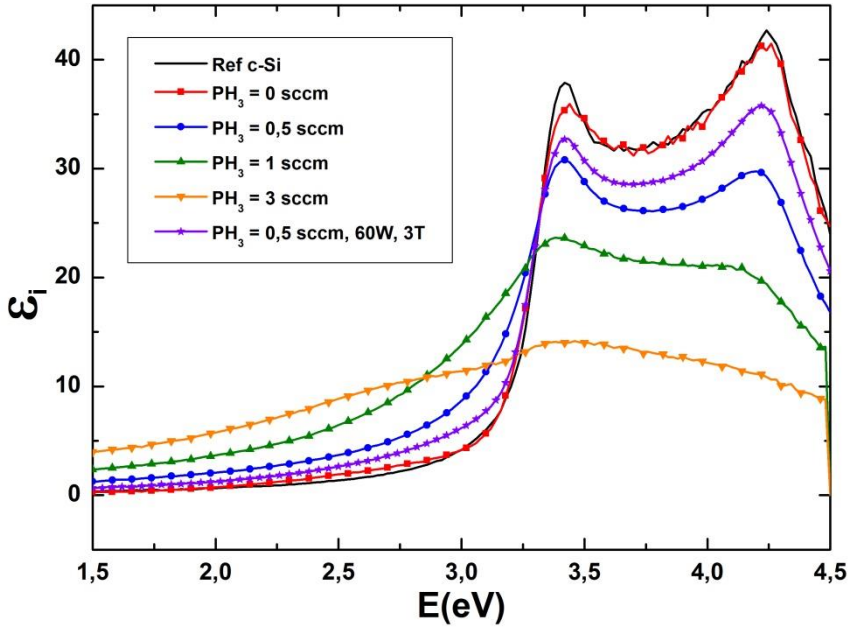

Fig. 4.5 – Imaginary part of the pseudo-dielectric function of epitaxial films grown with different PH_3 flow rates. The measurements have been performed at the center of a quarter of 4" wafer. PH_3 is diluted in H_2 at a concentration of 0.1 %. The deposition time is 600s except for the sample at 3 Torr (900s).

From Fig. 4.5, we can clearly see that the PH_3 flow rate has a very strong effect on the crystalline quality of the layers even though they are less than 20 nm thick and the deposition time is 600s in the case of layers grown under a pressure of 2.5 Torr. For a PH_3 flow rate as low as 0.5 sccm, corresponding to a $[PH_3]/[SiF_4]$ ratio of 2.5×10^{-5}, the imaginary part of the pseudo-dielectric function at 4.2 eV drops to 30 and further decreases for higher PH_3 flow rates, leading to a very poor quality material, no longer crystalline (F_c and F_p decrease) and porous (F_{void} increases). When the deposition is continued after 600s, the material becomes fully amorphous. A way to improve the crystallinity is to increase both power and pressure as shown in Fig. 4.5 with the sample grown at 3 Torr and 60 W, however this results in inhomogeneity issues as shown in Fig. 4.6.

Fig. 4.6 shows the evolution of the crystalline (F_c), polycrystalline (F_p), amorphous (F_a) and void (F_{void}) fractions as functions of the PH_3 flow rate. The H_2 flow rate is adjusted in such a way that $f_{H2}+f_{PH3}$=3 sccm.

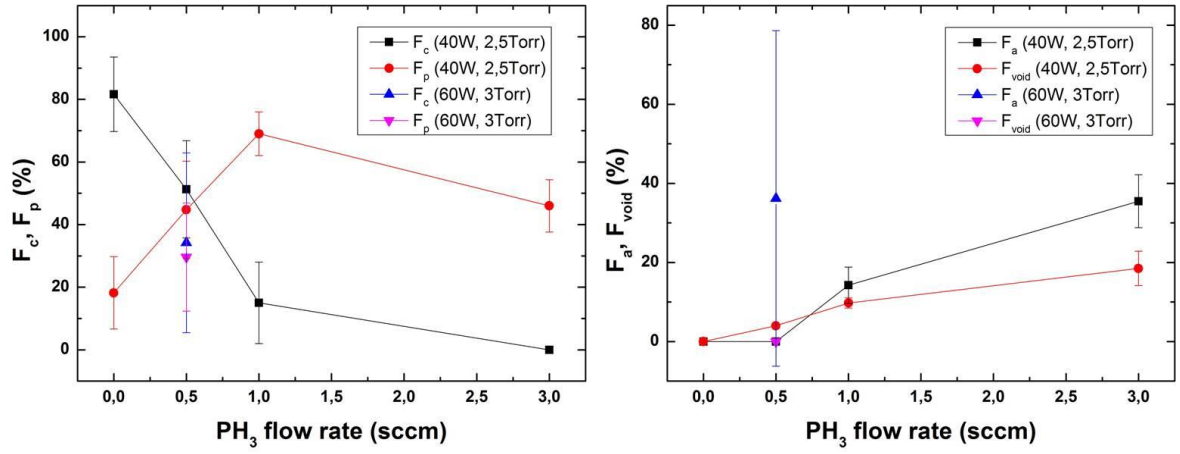

Fig. 4.6 – a) Evolution of the crystalline and polycrystalline fraction (F_c and F_p) and b) evolution of the amorphous and void fraction (F_a and F_{void}) deduced from ellipsometry measurements as functions of PH_3 flow rate. The amplitude of error bars is the standard deviation of 5 measurements done on a quarter of a 4" wafer.

Firstly, as expected, we can see that the higher the PH_3 flow rate, the less crystalline is the material. However we can note that at 1 sccm of PH_3, even if F_c is below 20%, F_p is around 70%, so $F_c+F_p \approx 85\%$ meaning that the material is highly crystalline. However at 3 sccm F_p is lower than 50% and F_c is equal to 0% whatever the position on the quarter of wafer and the void fraction approaches 20% meaning that the material is porous.

Secondly, the high standard deviation on the measurement carried out on the layers grown at 60 W and 3 Torr indicates that the layer is highly inhomogeneous. However the increase of pressure and RF power can be beneficial in some areas of the wafer. To explicit the strong differences of material properties, the ellipsometry spectra measured on different areas of this layer are shown in Fig. 4.7. For the area defined by the green triangle, purple square and orange diamond symbols, F_c+F_p is higher than 90%. This same part leads to sheet resistance values varying between 190 and 300 Ω for around 45 nm thick layers. It should be noted that these values must be considered with precaution given that the substrates used for this series are n-type (1-5 Ω.cm) FZ wafers, so the current lines can go through the wafer. But this does not alter the fact that these conditions of high pressure lead to efficient dopant activation. Note that all the R_{sheet} detailed in this chapter are measured on as-deposited layers, no annealing has been performed after the growth.

However, in the same quarter of wafer we can see that amorphous and amorphous/microcrystalline areas are also present (red star and blue triangle). In these regions, no sheet resistance is measurable. These poorly crystalline areas are visible to the naked eye and correspond to the regions in front of the injection nozzles of the shower head. The requirement of working at high pressure shows that a good control of gas flow in the PECVD chamber is mandatory if one expects to obtain homogenous doped epitaxial layers. The improvement of the gas injection will be detailed later.

To elucidate the reason for the epitaxy breakdown in the case of high PH_3 flow rate, plasma profiling time of flight mass spectrometry (PP-TOFMS) has been carried out on the layer obtained with the highest PH_3 flow rate, namely 3 sccm. In the same way as secondary ion mass spectrometry (SIMS), the PP-TOFMS measurement provides information on the incorporation of phosphorus atoms in the layer. The results are shown in Fig. 4.8.

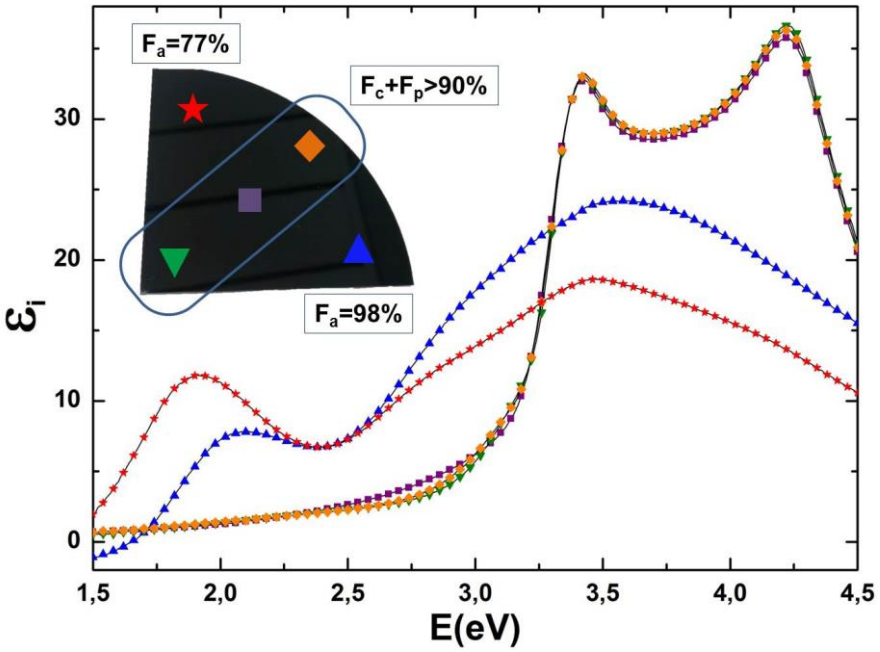

Fig. 4.7 – a) Imaginary part of the pseudo-dielectric function measured at 5 points on a quarter of a 4" wafer for a film deposited at 60 W and 3 Torr. Each curve is labelled with symbols corresponding to the area represented on the quarter of wafer. The sheet resistance varies from 190 Ω to 300 Ω in the region where F_c+F_p>90%.

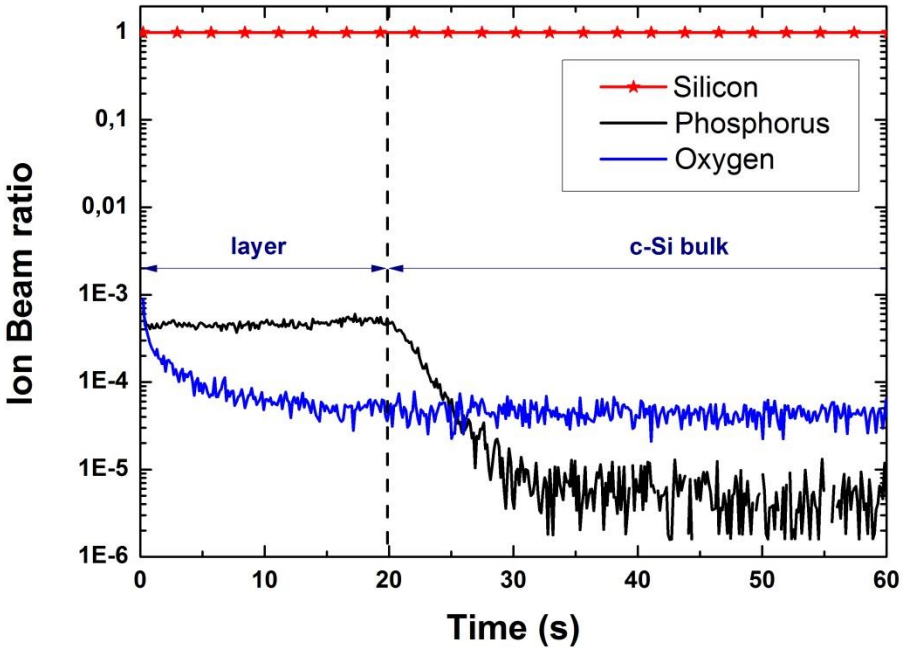

Fig. 4.8 – PP-TOFMS measurement performed on a phosphorus doped layer with a PH_3 flow rate of 3 sccm at 2.5 Torr and 40 W.

The PP-TOFMS output is the ion beam ratio (IBR), it corresponds to the ratio between the signal of a species corrected by its isotopic abundance and the sum of ion matrix signals corrected by their isotopic abundance. Thus for doped silicon layers the data is normalized by the silicon signal. Because in the case of phosphorus, the PP-TOFMS sensitivity is similar to that of silicon, we can just multiply the ion beam ratio (IBR) by the atomic density of silicon to know the concentration of P. As a result

IBR(P)=5.10^{-4} should correspond to a phosphorus concentration around 3.10^{19} at/cm^3. Thus the epitaxy breakdown does not come from a too high phosphorus concentration since concentrations of 10^{20} at/cm^3 [1],[2] and even 10^{21} at/cm^3 [3] in epitaxial layers grown at low temperature have already been reported in literature.

Nevertheless numerous issues associated to phosphorus doping using PH_3 have been reported in the literature. In 1984, Meyerson and Lu [4],[5] discussed their difficulty in LPCVD technique (620°C) to transfer the deposition of intrinsic polycrystalline silicon layers to phosphorus doped ones. They showed that the addition of PH_3 induces a reduction of the growth rate by a factor 20 with respect to undoped growth and causes serious homogeneity problems. To explain such a drop in growth rate, they suggest a preferential adsorption of phosphine at the growth surface, which limits silicon precursors decomposition by chemical surface reactions. Although LPCVD is performed at more than 600°C, they also showed that phosphine is easily adsorbed even at room temperature. They found that phosphine has a sticking coefficient at least 40 times higher than silane (SiH_4). In our case, we do not use SiH_4 but SiF_4 and PECVD instead of LPCVD. However, reasonable analogies can be made. In our case of phosphorus-doped silicon films, the deposition rate does not seem to be significantly affected since a deposition rate of 0.5 Å/s is achieved i.e. in the same order of magnitude that the deposition rate of intrinsic epi-layers. Contrary to LPCVD which mostly relies on surface interactions, in PECVD the dissociation of gas molecules occurs in the gas phase which means that incident species have already reacted and can directly lead to deposition. Thus the most reasonable explanation in our case of phosphorus doped PECVD epitaxy is the occupation of adsorption sites by PH_3 inhibiting silicon precursors to reproduce crystal lattice, which associated to the continuous flux of matter (ions, radicals, nanoparticles, …) makes the material poorly crystalline and finally amorphous.

Moreover, issues on P coverage of Si surface have also been reported latter. The formation of P-P dimers due to surface segregation has been highlighted as a reason for a reduction of the deposition rate in MBE [6] but can also be considered as a cause for epitaxy breakdown since they occupy adsorption sites for Si precursors in the same way that they passivate dangling bonds and impede epitaxy. Kipp *et al.* [7] have also shown that on Si(100) at 200°C P surface coverage of around 0.2 ML was reached (ML denotes monolayer, 1 ML corresponding to the maximum surface concentration that the adsorbed species can reach at the surface of a substrate) and that at even such low temperature, clusters formation of P-P dimers was observed.

More recently Cho *et al.* [8] confirmed by temperature programed desorption a P surface coverage of 0.25 ML in the same range of temperature (300°C) and also revealed phenomena of surface roughening due to P segregation. These issues of phosphorus surface coverage and segregation leading to surface roughening may also be the cause of the epitaxy breakdown we encounter, since even after only 20 nm of growth a roughness of a few nm is already observed on our layers.

It should be noted that similar observations have been made on Si(100) and Si(111) [9], a sticking coefficient for phosphine near 1 has been found in both cases. Therefore the development of n-type doped epi-layers requires some strict conditions whatever the surface state (mirror polished, SDR, textured surfaces,…). The incorporation of phosphorus in the layers grown from by PECVD from $SiF_4/H_2/Ar$ seems to be very efficient since a $[PH_3]/[SiF_4]$ ratio as low as $2.5x10^{-5}$ leads to phosphorus concentration around above 10^{19} cm^{-3}. Thus a higher dilution of PH_3 in H_2 to reduce even more the gas ratio is necessary to perform epitaxy with phosphine. Moreover the inhomogeneity observed at higher pressure requires a better management of gas injection, this is a crucial point since even in semi-industrial tools phosphine induces uniformity issues [4].

To tackle this issue three main studies have to be made. Firstly, complementary structural characterization (XRD, Raman, TEM,…) needs to be carried out on these layers for a better understanding of the effect of phosphorus on the crystal lattice. Secondly, once thick and homogenous layers will be obtained, electrical characterization to assess the active dopant concentration should be performed. Thirdly, a comprehensive study on the effect of phosphine on plasma and plasma-surface interactions needs to be carried out and by doing so explaining the reasons of this epitaxy breakdown. However this implies to use very sensitive characterization techniques such as low energy electron diffraction (LEED) and Auger electron spectroscopy (AES) which are difficult to implement *in situ* in the case of PECVD.

However from our point of view the development of n-type epitaxy is not as important as that of boron epitaxy due to the beneficial effect of phosphorus diffusion during standard process using $POCl_3$ at high temperature. Indeed, even if a perfect phosphorus doped epitaxy was achieved, from a technological point of view it would be more appropriate to choose phosphorus diffusion to benefit from its gettering effect to reduce the impurity concentration in the wafer. Therefore, we have not extensively investigated phosphorus-doped epitaxy and preferred to focus on boron-doped epitaxy.

4.3. Boron doping

4.3.1. Optical and structural properties

The process parameters for boron-doped epitaxy are the same as those used for intrinsic and phosphorus-doped epitaxy, namely a pressure of 2.5 Torr, a P_{RF} of 40 W (180 mW/cm^2), a substrate and RF electrode temperature of 200°C, and an inter-electrode distance of 20 mm. Diborane (B_2H_6) has been added to the gas mixture with flow rates in the range from 0.2 sccm to 3 sccm. Similarly to PH_3, B_2H_6 is highly diluted in hydrogen, with a concentration of 0.9%. Thus, the total flow rate $f_{H2}+f_{B2H6}$ is maintained at 3 sccm for all the samples whose properties are shown in this part. The quality of the films deposited at various B_2H_6 flow rates has been assessed by ellipsometry as shown in Fig. 4.9.

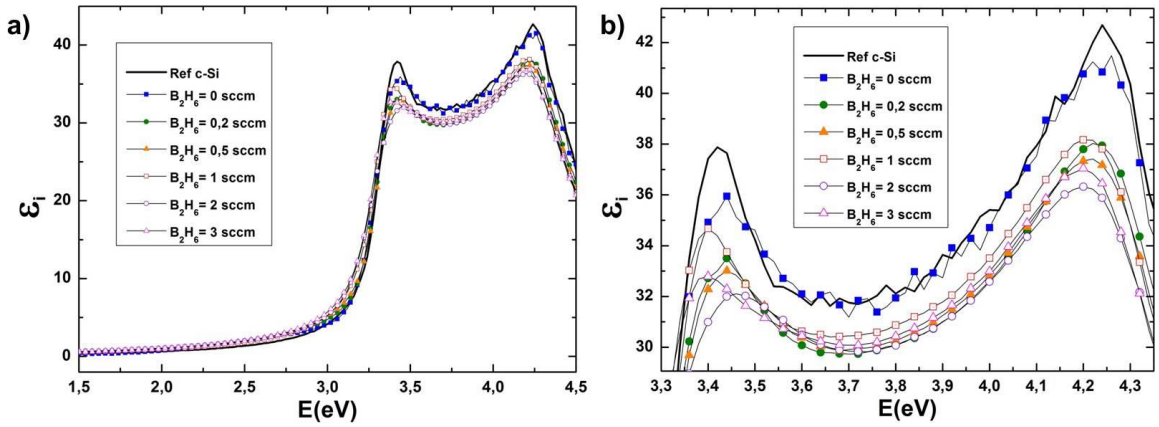

Fig. 4.9 – a) Average pseudo-dielectric function of boron-doped epi-layers obtained for different B_2H_6 flow rates from 0 to 3 sccm. b) Zoom on the Van Hove singularities at 3.4 and 4.2 eV. The RF power is 40 W and the pressure is 2.5 Torr. SiF_4 and Ar flow rates are respectively 20 and 300 sccm.

While PH_3 strongly changes the material properties, Fig. 4.9 reveals that diborane has a moderate effect on the crystallinity of the layers given that the Van Hove singularities at 3.4 and 4.2 eV are well defined even for the film obtained with a high B_2H_6 flow rate (3 sccm). Nevertheless, the intensity of the peaks is slightly lower when the B_2H_6 flow rate is increased.

The evolution of the crystalline (F_c) and the polycrystalline (F_p) fraction deduced from the ellipsometry spectra is shown in Fig. 4.10. From 0 to 0.5 sccm of B_2H_6, F_c decreases until around 50% while F_p increases up to around 50%. It should be noted that the amorphous phase fitted for all spectra is 0%, therefore there is always $F_c+F_p=100\%$. From 0.5 to 3 sccm F_c and F_p do not vary a lot, except for the sample at 2 sccm, but the standard deviation strongly increases. Thus, the increase of the B_2H_6 flow rate does not have a significant effect on the crystallinity of the layers but negatively affects their homogeneity. Given that the height of the second Van Hove singularity at 4.2 eV does not change a lot, the increase of the B_2H_6 flow rate in these conditions does not induce a dramatic increase of the roughness. The roughness values deduced from ellipsometry show a variation of roughness going from 7 to 12 Å without indicating a clear trend when the dopant gas flow rate is changed. It has been shown by Bardet *et al.* [10] that the grain size in polycrystalline films has an effect on the position of the Van Hove singularities. They showed that the difference of position of the Van Hove singularities $\Delta E=E_2-E_1$, with E_1 the first Van Hove singularity at 3.4 eV and E_2 the second one at 4.2 eV, is reduced when the grains are getting smaller than 20 nm, with a decrease of ΔE of 0.3 eV when the grains size drops to 10 nm. We also observe a shift in E_1 and E_2 positions but their difference is roughly constant from 0 to 3 sccm of B_2H_6 as shown in Fig. 4.10-b). Therefore the shift of E_1 and E_2 is not attributed to the decrease of grain size below 20 nm.

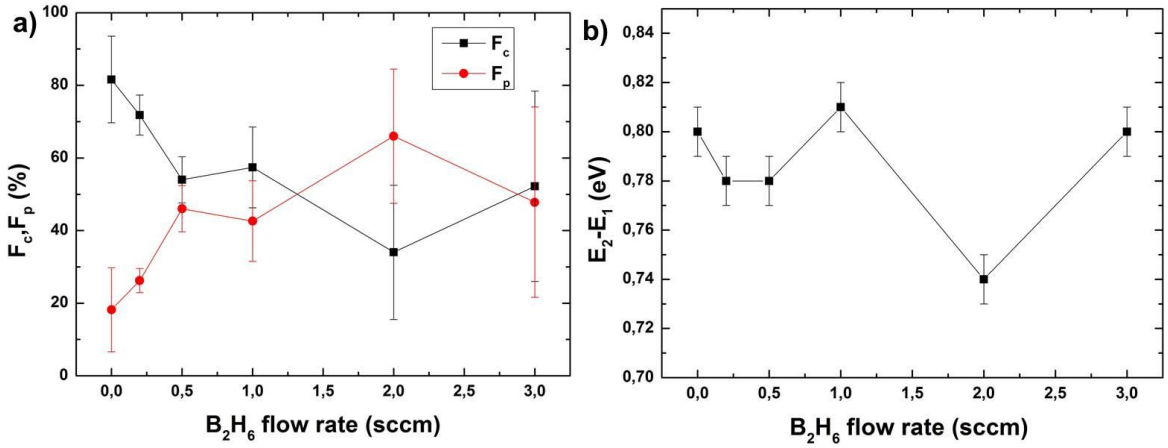

Fig. 4.10 – a) Evolution of crystalline (F_c) and polycrystalline (F_p) fractions deduced from ellipsometry spectra as functions of B_2H_6 flow rate. The RF power is 40 W and the pressure is 2.5 Torr. The error bar corresponds to the standard deviation calculated from 5 measurements on a quarter of a 4" wafer. Note that $F_c+F_p=100$ % whatever the B_2H_6 flow rate. b) Difference E_2-E_1 as a function of the B_2H_6 flow rate where E_1 and E_2 are the first (3.4 eV) and the second (4.2 eV) Van Hove singularities respectively.

Viña and Cardona studied the effect of high doping in silicon on ellipsometry spectra [11]. They observed for highly doped c-Si wafers with a boron concentration of 4.10^{20} cm^{-3}, a red shift of 0.05 eV for both E_1 and E_2. For our layers, we observed a shift of Van Hove singularities of 0.04 eV for the epi-layers grown with the highest B_2H_6 flow rate (3 sccm) with respect to intrinsic epi-layers ones. This is consistent with our observations for which hole concentration above 10^{20} cm^{-3} is deduced from sheet resistance measurements in the case of the epi-layers grown with the highest B_2H_6 flow rate. To investigate the incorporation of boron in the epi-layer, PP-TOFMS [12] measurements on boron-doped

layers have been performed. The profile is shown in Fig. 4.12. Given that the equipment sensitivity for boron is different from that for silicon, we firstly used a highly boron-doped wafer with a boron concentration of 2.10^{19} at/cm^3 as a reference to measure the IBR corresponding to a boron concentration of 2.10^{19} at/cm^3. The corresponding IBR for boron is 1.10^{-5} and is represented in green in Fig. 4.12. Secondly, we measured the IBR of different elements for the doped epi-layers grown on an n-type FZ wafer. The 50 nm thick boron-doped epi-layer is etched during the first 20s, during which the boron IBR from the epi-layers (in orange) is above that of the reference wafer, indicating that the concentration of boron in the epi-layers is above 2.10^{19} at/cm^3 in case of a diborane flow rate of 3 sccm.

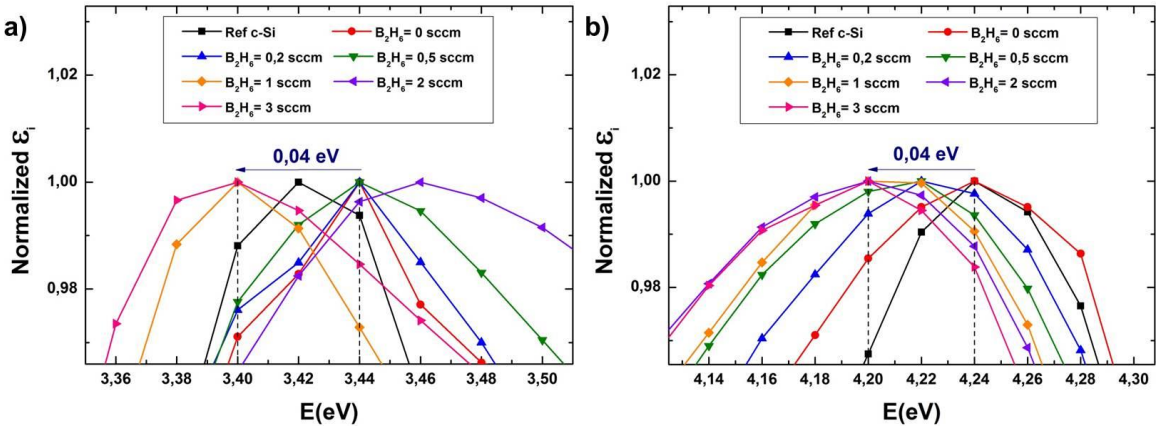

Fig. 4.11 – a) Evolution of the position of the Van Hove singularities as functions of B_2H_6 flow rate at a) 3.4 eV and b) 4.2 eV. All spectra have ben normalized.

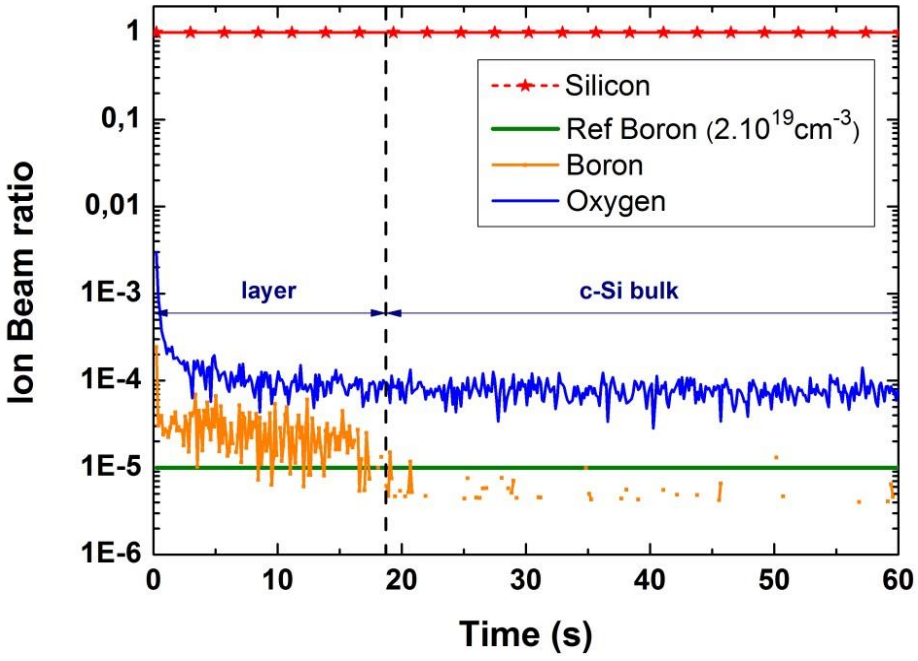

Fig. 4.12 – a) PP-TOFMS measurement performed on a highly boron-doped epi-layer for a diborane flow rate of 3 sccm. The IBR of boron for the reference silicon wafer with a boron concentration of 2.10^{19} cm^{-3} is represented in green ($IBR_{ref}=1.10^{-5}$). Note that the IBR of oxygen is almost constant indicating that it corresponds to the background signal from the system. The RF power is 40 W and the pressure is 2.5 Torr. SiF_4, B_2H_6 and Ar flow rates are respectively 20, 3 and 300 sccm. The H_2 comes with the B_2H_6 diluted at 0.9%.

PP-TOFMS allows us to determine the concentration of boron atoms in the epi-layers. To evaluate the concentration of active dopants, Hall effect measurements have been performed. To do so, boron-doped epi-layers have been grown on SOI (Silicon On Insulator) wafers with B_2H_6 flow rates of 0.5 sccm and 3 sccm. The upper silicon layer on the SOI substrates, on which epi-layers have been grown is 700 nm thick and has a resistivity of 50 Ω.cm. Therefore, the current going through the substrate is negligible. Silver paste has been used for metallic contacts and a 30 min long annealing at 200°C has been performed to improve the ohmic contact. For a flow rate of 0.5 sccm, the hole concentration and mobility μ_h are respectively 10^{16} cm^{-3} and 280 $cm^2.V^{-1}.s^{-1}$. This can be compared to the theoretical mobility calculated by Masetti *et al.* [13] which is 425 $cm^2.V^{-1}.s^{-1}$ for this doping level. Increasing the diborane flow rate to 3 sccm resulted in $p = 2.10^{19}$ cm^{-3} and μ_h = 40 $cm^2.V^{-1}.s^{-1}$, while the theoretical mobility, calculated using the same model, is 73 $cm^2.V^{-1}.s^{-1}$.

To cross check the results, these values have been compared to four-point probe measurements. For the epi-layers grown with 3 sccm of B_2H_6, a sheet resistance of 105 Ω has been measured. It is important to note that the doping concentration measured by Hall effect should be underestimated given that a sheet resistance of 105 Ω for a thickness of 50 nm (measured by TEM) leads to a doping concentration of 2.10^{20} cm^{-3} for a uniform doping profile. Thus a diborane flow rate of 3 sccm leads to good electrical properties in addition to excellent structural properties as deduced from ellipsometry results. Nevertheless, additional characterization techniques need to be used to confirm these results.

To assess the crystalline quality of the boron-doped epi-layers HR-TEM has been carried out. A HR-TEM image of the epi-layer grown with the highest diborane flow rate (3 sccm), therefore for which one may expect the worst crystalline quality, and having a sheet resistance of 105 Ω is shown in Fig. 4.13.

The same observations as for the intrinsic layers in Chapter 2 can be made. No grain boundary is detectable and the boron-doped epi-layer presents a low density of dislocations in the area of interest, which is an excellent result for such low temperature growth of highly doped layers. No H platelets are visible neither. Nevertheless a difference with the intrinsic growth is that the surface is a few nanometers rough.

The fact that the interface is hardly detectable in the high resolution images, as it was the case for intrinsic epitaxy (see Chapter 2) is a sign of a good arrangement of atoms at the interface. The smoothness of the interface can be due to a competition between growth and etching during the process induced by fluorine since pure SiF_4 plasma is also used to remove native silicon oxide from c-Si wafers showing excellent results [14]. However, a too long exposure to the SiF_4 plasma leads to etching of the silicon. The electron diffraction pattern of the doped layer is shown by the inset in Fig. 4.13-b) and is identical to that of the c-Si substrate in Fig. 4.13-c), which further assesses the monocristallinity of the doped epi-layer.

The interface uniformity on the full wafer is difficult to assess by HR-TEM due to the small analyzed area. However a strong correlation between the smoothness of the interface and the oscillations in the low energy range (1.5 - 3 eV) in ellipsometry spectra for low temperature silicon homoepitaxy has already been reported [14]. The results for epi-layers grown under these conditions, namely a RF power of 40 W, a pressure of 2.5 Torr and a gas mixture $SiF_4/H_2/B_2H_6$/Ar=20/0/3/300 sccm, do not show any oscillations over the 5 measurements points on a quarter of a 4” wafer meaning a high quality of this interface on the full quarter of wafer.

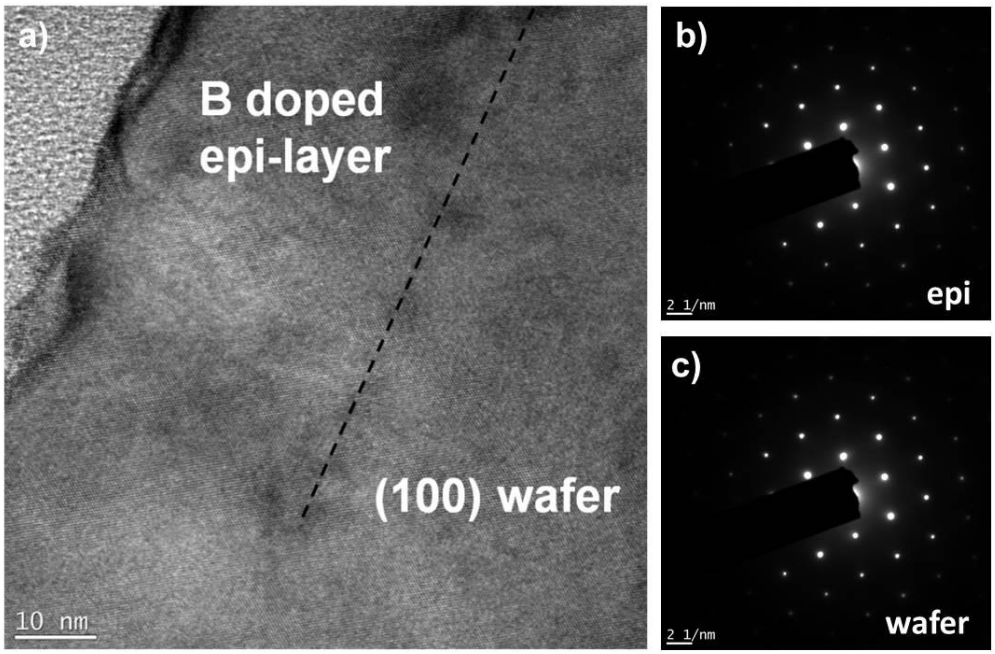

a

Fig. 4.13 – a) HR-TEM image of a 50 nm thick boron-doped epi-layer grown with a 3 sccm diborane flow rate leading to a hole concentration of a few 10^{19} cm^{-3} b) Diffraction pattern of the boron-doped epi-layer, which is identical to that of the substrate shown in c). This demonstrates that the film is in perfect epitaxial relationship with the substrate. The RF power is 40 W (180 $mW.cm^{-2}$) and the pressure is 2.5 Torr. SiF_4, B_2H_6 and Ar flow rates are respectively 20, 3 and 300 sccm.

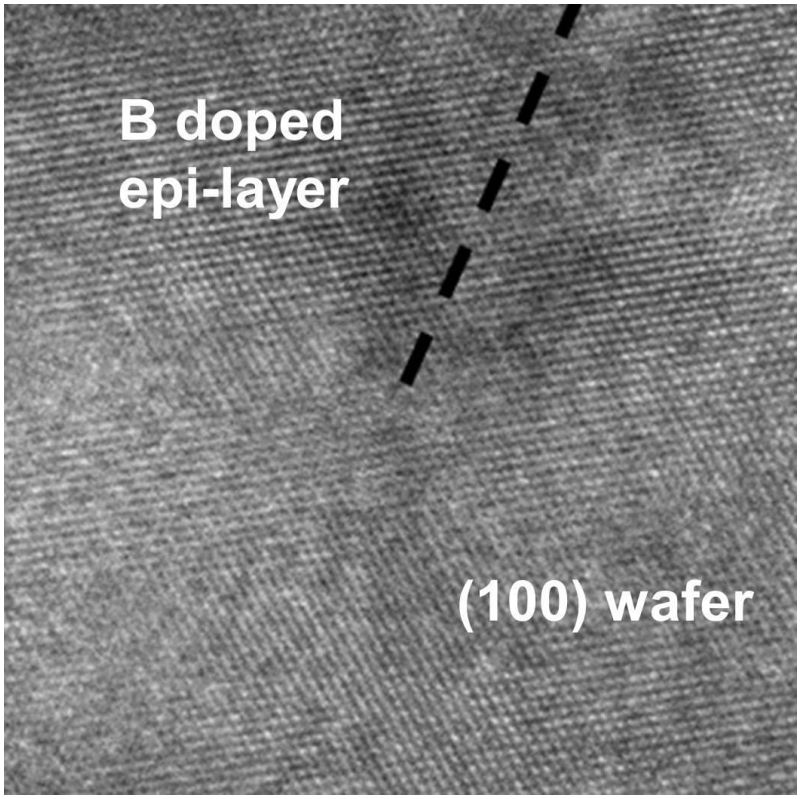

Fig. 4.14 – a) HR-TEM image of the interface between a highly boron-doped layer (p>$10^{19}cm^{-3}$) and the substrate, a Si(100) wafer.

In order to obtain macroscopic properties of the epi-layers, X-ray diffraction (XRD) measurements have been performed. In particular one may expect a potential stress in the epi-layer, as observed in the case of epi-layers produced from SiH_4/H_2 gas precursors. Moreover the incorporation of impurities in the crystal has an effect on its lattice parameter, XRD gives crucial information on these properties.

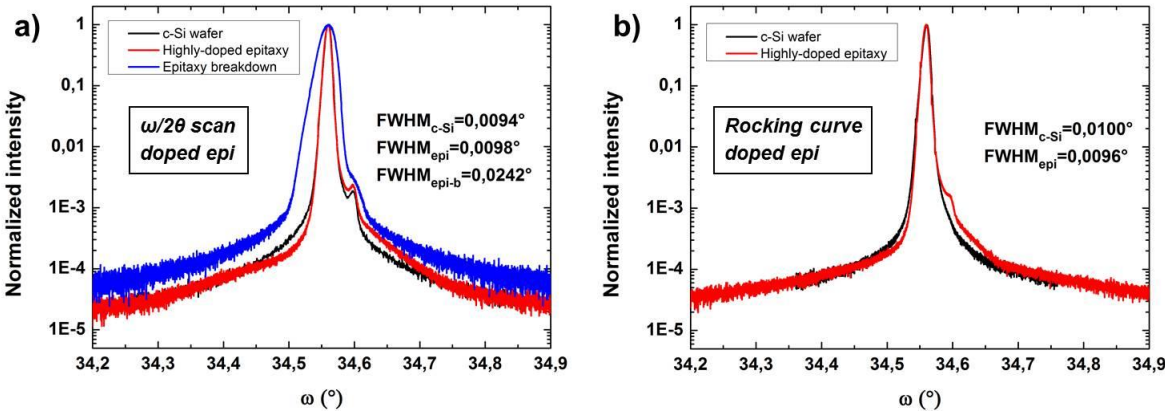

Fig. 4.15 – a) XRD measurement in ω/2θ configuration for (400) planes of a bare c-Si wafer, highly boron-doped epi-layers (p >10^{19}cm^{-3}) and a layer after epitaxy breakdown. b) Rocking curve of a bare c-Si wafer and of highly boron-doped epi-layers for (400) planes. FWHM values are equivalent showing a low mosaicity in the epi-layers. The number of counts has been normalized for every scan. The small peak at 34.60° is an artefact due to the detector.

Results from XRD measurements in ω/2θ configuration and rocking curves for highly boron-doped layers are shown in Fig. 4.15. In that case their diffraction peaks do not completely overlap compared to that of intrinsic epi-layers. The diffraction peak from doped epi-layers is slightly shifted towards larger angles, which means that the lattice parameter of the epi-layers is smaller than that of the substrate in the growth direction. An approximation of the boron concentration using the Vegard's law is difficult in our case because it is not high enough, which causes the overlapping of epi-layers and wafer diffraction peaks.

To compare between high and low quality doped epi-layers, the scan for a layer of the same thickness obtained in a different area of the same sample but after epitaxy breakdown has been added, for which the FWHM is more than twice larger than that of good quality epi-layers and c-Si substrate. In addition, rocking curves reveal the same FWHM between the substrate and the layer grown on it, the proof of a very low mosaicity of the epi-layers.

Several publications address the determination of the boron concentration from XRD in Si single crystals [15]–[17] and epi-layers [18]–[21]. Kucytowski and Wokulska [17] succeeded to differentiate doped silicon with B concentration below 6.10^{17} cm^{-3}, corresponding to a variation of a few 10^{-6} Å. However, because of instrumental limits, in most cases reported in the literature, the difference of lattice parameter for B concentrations below 1.10^{19} cm^{-3} is not significant enough to detect a variation. Hence, B concentrations above this value should be observable in most XRD systems featuring an adapted monochromator. From simulations correlated to our experimental results, we found that the detection limit for our XRD system in case of a 200 nm thick layer corresponds roughly to a variation of 1.10^{-3} Å of the lattice parameter of the epi-layers with respect to that of the substrate. To estimate the limit of detection regarding B concentration, the evolutions of out-of-plane lattice parameter as a function of boron concentration determined by Horn [15] and Celotti [16] have been plotted in Fig. 4.16. These studies show different values of the lattice parameter of intrinsic or lowly doped silicon ($a_{0,i}$ (Celotti)=5.431 Å and $a_{0,i}$ (Horn)=5.4295 Å) but a similar evolution of the lattice parameter as a

function of B concentration. A linear dependence of the lattice parameter as a function of B concentration is observed up to 2.25×10^{20} cm^{-3}. The blue arrows represent the shift induced by the detection limit of our system, namely 1.10^{-3} Å, and thus correspond to the difference of lattice parameter between that of the substrate and that of the epi-layers measurable by the system. The corresponding detectable B concentration we expect is shown by the green arrows with respect to both data series. It shows that a (fully activated) B concentration above 3.10^{19} cm^{-3} should be detected by our system.

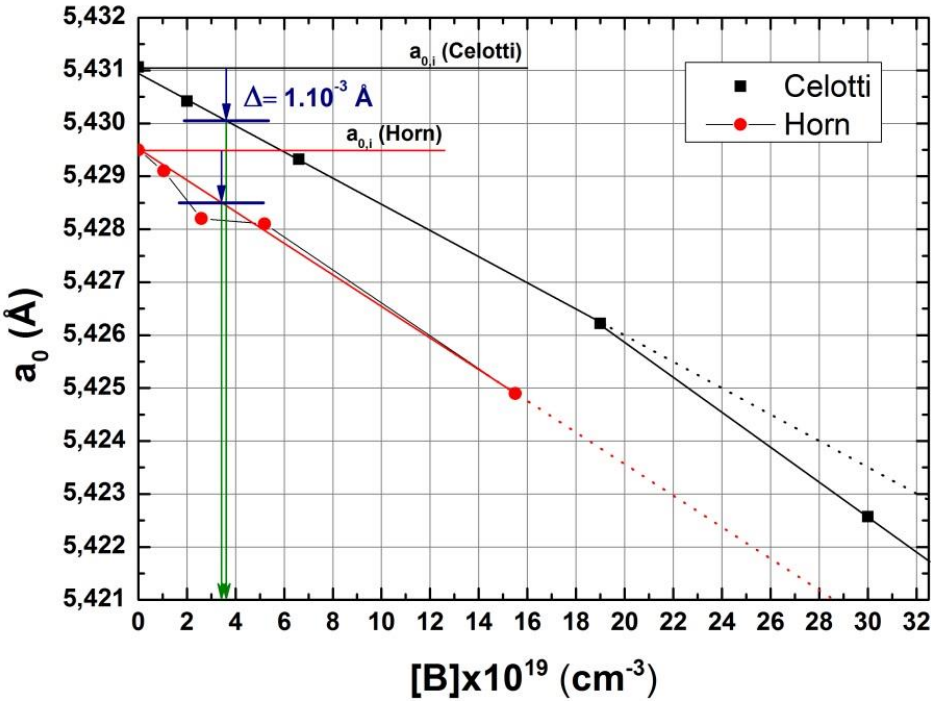

Fig. 4.16 – a) Influence of the boron concentration on the boron-doped crystal lattice parameter a_0. Data are extracted from Horn, 1955 [15] and Celotti, 1974 [16]. A linear behavior is observed up to a B concentration of 2.25×10^{20} cm^{-3} [16]. The blue arrows represent the instrumental limit of the diffractometer used for our experiments, it correspond to a shift of 1.10^{-3} Å with respect to the lattice parameter measured in lowly doped Si wafers for both references. The green arrows show the corresponding B concentration measurable with our diffractometer, namely above 3.10^{19} cm^{-3}.

Thus, the fact that the 50 nm thick layer is observable by XRD suggests that most likely the B concentration is closer to the values deduced from 4-point probe measurements (2.10^{20} cm^{-3}) than to these deduced from Hall effect ($2.10^{19}cm^{-3}$). A difficult point to discuss is the different influence of substitutional and interstitial boron on the lattice parameter. In the literature, high temperature epitaxy is used, meaning that the boron is fully activated except for doping concentrations above 10^{21} cm^{-3}. In our case a detailed study should be carried out to distinguish both cases considering boron incorporation. In addition, the incorporation of hydrogen increases the lattice parameter while the incorporation of boron decreases it, which can favor the formation of defects and therefore the incorporation of hydrogen. Thus two opposite phenomena are competing which makes the analysis even more difficult.

This uncertainty on boron concentration in the epi-layers is also due to serious problems of homogeneity we constantly encountered. As an example, Fig. 4.17 shows the variation of carrier concentration measured by Hall effect on a quarter of a 4" wafer. On the same quarter of wafer the hole concentration varies by two orders of magnitude, from 1.5×10^{17} cm^{-3} to 2.10^{19} cm^{-3}.

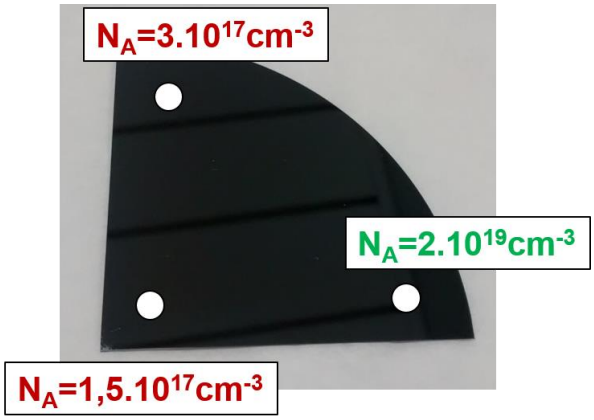

Fig. 4.17 – a) Variation of the doping concentration over a quarter of a 4" wafer.

Moreover, the deposition rate at 3 sccm of B_2H_6, for a layer with a hole concentration between 2.10^{19} and 2.10^{20} cm^{-3}, is only 0.07 Å/s. This low deposition rate is unacceptable from an industrial point of view. An increase of the gas flow rates is therefore necessary to favor the formation of reactive species and enhance the deposition rate. However, this leads to even worse uniformity of the films. As a conclusion both phosphorus- and boron-doped epitaxial growth raise the issues of gas management. To tackle this problem, the chamber of the PECVD reactor has been designed and fluid dynamics simulations have been performed with different designs of shower head. This allows to determine the best configuration in terms of nozzle density considering our process conditions for epitaxy.

4.4. Fluid dynamics simulations: optimization of the shower head design

This part has been performed with the help of F. Silva, research engineer at LPICM. The simulations have been carried out with the ANSYS software.

Fig. 4.18 represents the PECVD chamber in which depositions are performed. As we can see from the velocity streamlines, the velocity of gas is higher (in red) at the level of the gas injection nozzles, while it quickly slows down once in the chamber, the pumping port is easily recognizable on the right of the picture where all the gas streamlines are directed, towards the exhaust.

No chemistry has been used in these simulations, the idea is to provide a coarse optimization of the shower head. Given that argon (Ar) is the diluting gas, it seemed to be the most consistent choice to use it for simulations. The pressure and inter-electrode distance have been fixed to the corresponding best conditions so far, namely 2.5 Torr and 2 cm respectively, and for which structural properties of boron-doped epi-layers have been previously detailed. The dimensions of the shower head are 15x15cm^2, it features 24 nozzles with a diameter of 0.8 mm. The design of the nozzles has not been changed, only the nozzles density and the total Ar flow rate have been varied. The number of holes simulated is 24, 48 and 143 for 350 and 700 sccm of Ar. For a better understanding a 2D view in cross section of the reactor is shown in Fig. 4.19.

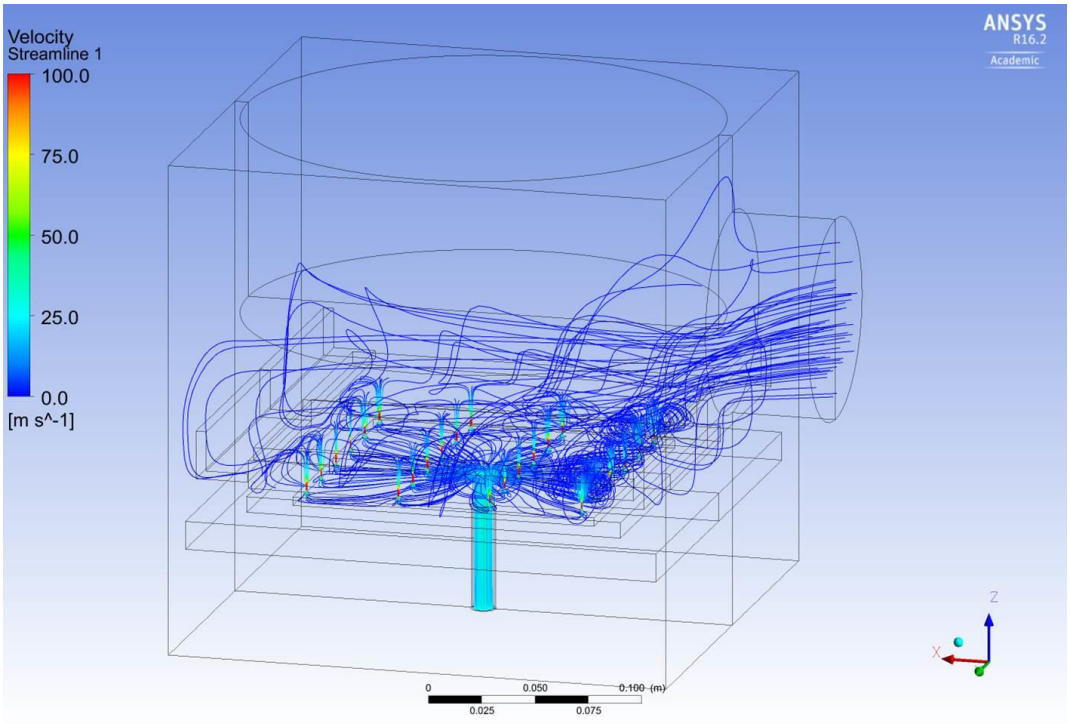

Fig. 4.18 – 3D design of the PECVD chamber (PL8 on the Cluster tool) and the resulting gas velocity streamlines for the existing shower head with 24 nozzles.

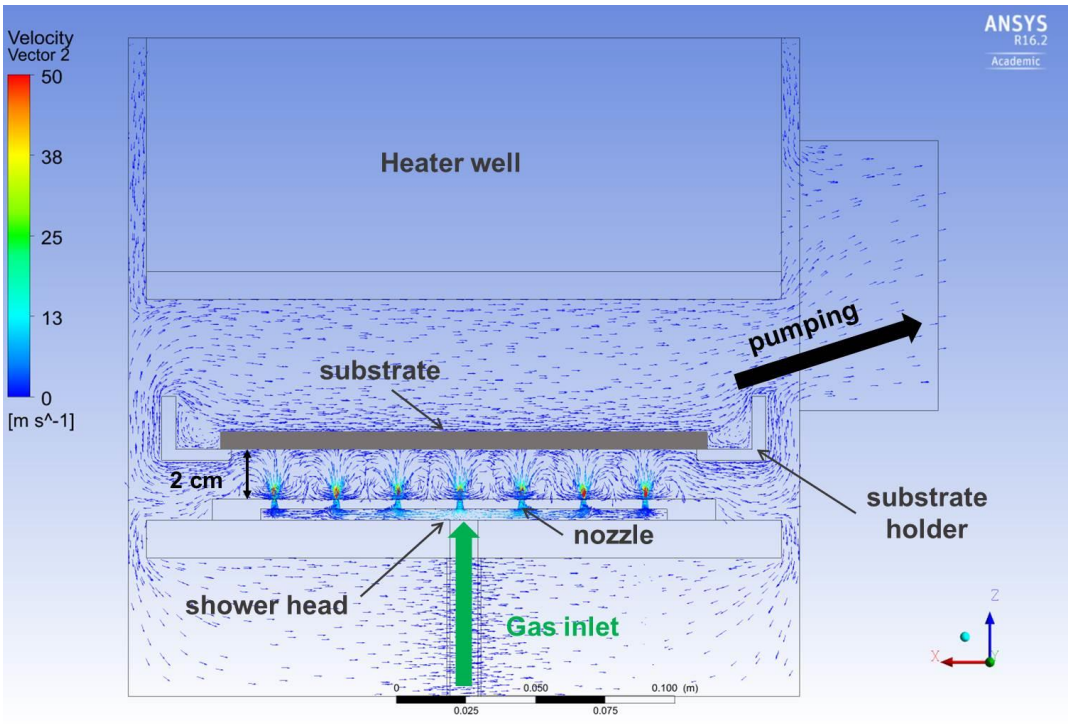

Fig. 4.19 – Cross section of the modeled PECVD chamber (PL8 on the Cluster tool) and the resulting gas velocity streamlines for the initial shower head (24 nozzles).

Fig. 4.20 represents for these different numbers of nozzles in the shower head, the gas velocity isovalues at the surface of the substrate, i.e 2 cm above the shower head. The projection of the nozzles pattern of the shower head on the substrate is clearly visible, the diameter of the spots on the pattern

are around 3 cm large in diameter. From these simulations, the spots visible by the naked eye on phosphorus doped epi-layers and the inhomogeneity in sheet resistance for boron-doped layers are easily understandable. Thus the initial gas injection (Fig. 4.20-a)) is not optimized for the process conditions we use, this is mainly due to the relatively high pressure and the gas species we use for epitaxy. The density of Ar being strongly different from that of H_2, the usual diluting gas used in this reactor, this influences the injection and so the growth homogeneity. Indeed, the density of Ar is 1.78 $g.L^{-1}$ while it is only 0.0899 $g.L^{-1}$ for H_2, at standard temperature and pressure (0°C, 101.3 kPa). Therefore, Ar is 20 times heavier than H_2. While this design of shower head is acceptable for amorphous silicon deposition (low pressure) and SiH_4/H_2 chemistry (epitaxy from SiH_4/H_2 chemistry at around 2 Torr is homogenous), this is not the case for SiF_4/H_2/Ar chemistry at high pressure and for high flow rates.

By increasing the number of nozzles, the spots visible in gas velocity isovalues start to partially vanish (Fig. 4.20-b): 48 nozzles) and then to completely disappear (Fig. 4.20-c): 143 nozzles). In the latter case it is worth noticing that the injection follows a global pattern, contrary to the other case where a pattern is repeated locally in front of every hole. Therefore, this global behavior is more suitable to obtain uniform films. In addition, a simple requirement for shower head design is to have a nozzle spacing smaller than the inter-electrode distance. In case of the 143 nozzles design this spacing is around 5 mm, i.e. 4 times smaller than the inter electrode distance, thus this design satisfies this condition.

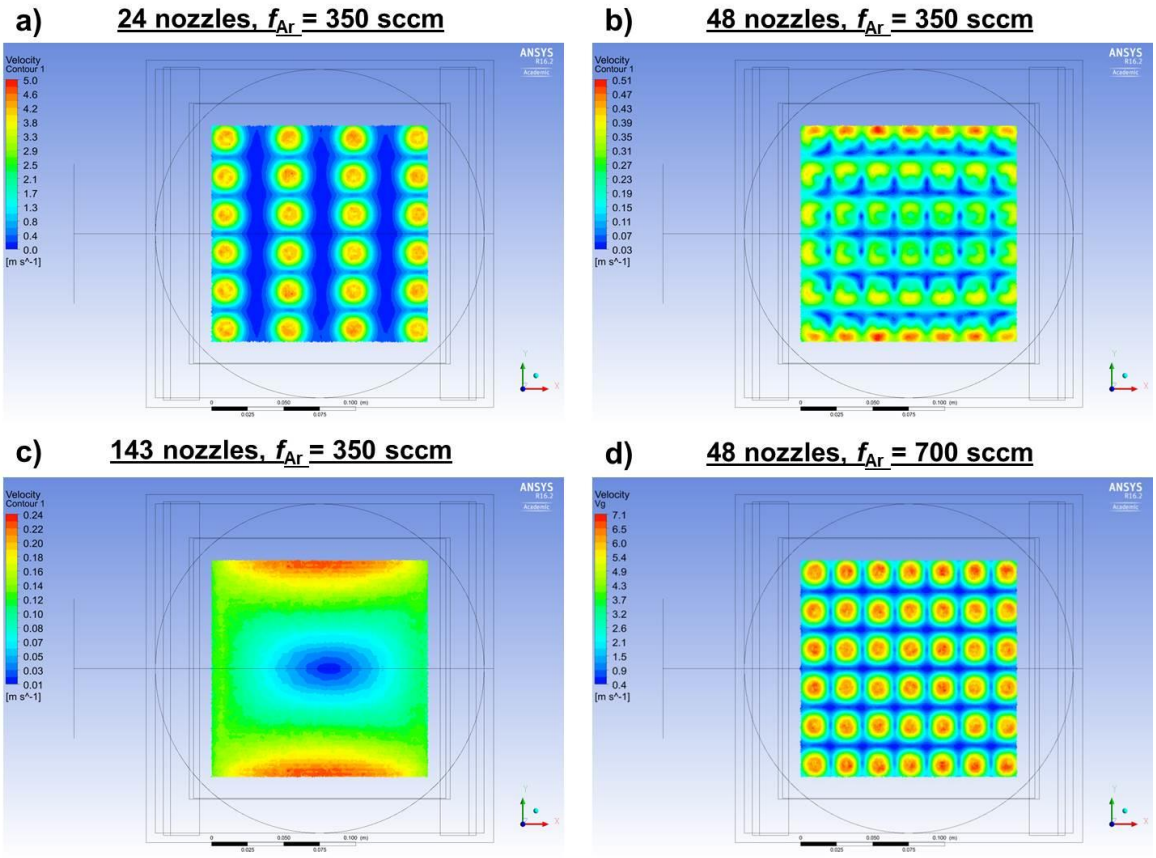

Fig. 4.20 – Gas velocity isovalues at the surface of the substrate ((XY) plane 2 cm above the shower head) for various nozzles density at 2.5 Torr and d=2cm.

Besides, it is worth noticing that when the flow rate is increased the spots reappear, as shown in Fig.

4.20-d) where the number of nozzles is kept at 48 but the flow rate is doubled to 700 sccm. Thus a particular care is required on the total flow rate for the improvement of the film uniformity, although knowing that this is necessary to increase the deposition rate. We will see later that the global pattern obtained in simulations can also be observed in the material properties for some process conditions.

The profile of the gas velocity vectors in cross section of the shower head (Fig. 4.21) gives a crucial information about the behavior of gas flow pattern leading to these homogeneity issues. Convection-like cells appear to be responsible for these spots. At 24 nozzles (Fig. 4.21-a)), the gas from the injection does not mix before reaching the substrate, instead it collides with the substrate and then goes down. At 48 nozzles (Fig. 4.21-b)), the gas starts to mix once it reaches the surface of the substrate, this represents the limit between the two modes of gas injection. When there are 143 holes (Fig. 4.21-c)), the gas from each nozzle mixes with the gas coming from adjacent nozzles, which is a mandatory requirement to obtain a uniform film deposition. This occurs at around 5 mm above the exit of the nozzle which corresponds to one quarter of the inter-electrode distance and to the same distance as the inter-nozzle spacing.

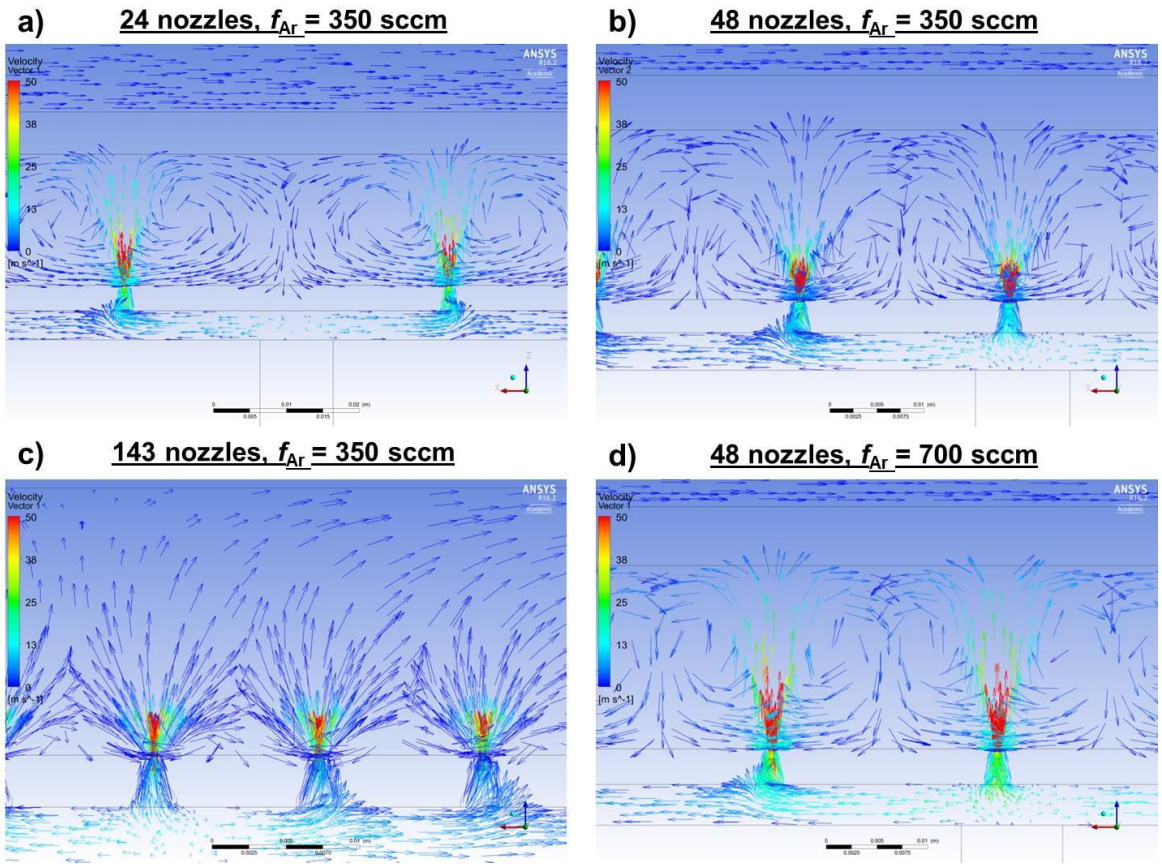

Fig. 4.21 – Velocity vectors profile in cross section of the shower head for different nozzle densities.

When the flow rate is increased (Fig. 4.21-d)), the problem is similar to that of a low flow rate with a lower nozzle density, such as (Fig. 4.21-a)). The homogeneity of the film deposition therefore depends on the inter-electrode distance, the nozzle spacing and the gas flow rate, which strongly influences the gas velocity at the outlet of the nozzle.

Finally, to affirm that the design of a gas injection can be considered as a shower head, the radial velocity must follow a linear evolution as a function of the distance from the center of the shower head [22], in such a way that:

$$v_r(r)=(v_{in}/2H_c).\,r$$

where v_{in} is the constant entrance velocity, H_c the height of the chamber and r the distance from the center of the shower head. The radial velocity as a function of the distance from the center of the shower head for a design with 143 nozzles has been plotted in Fig. 4.22, it shows that the condition of linearity is satisfied.

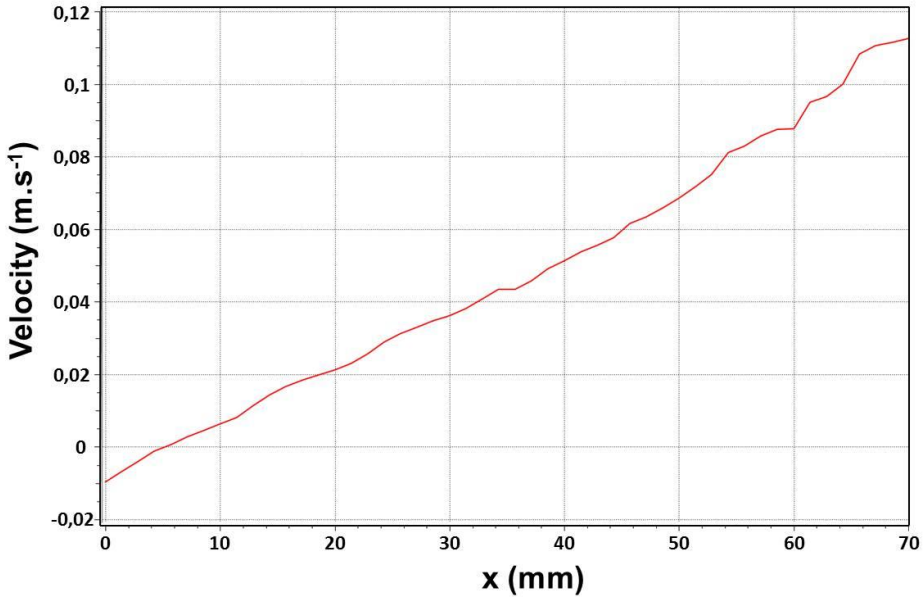

Fig. 4.22 – Evolution of the radial velocity as a function of the distance from the center of the shower head.

As a conclusion, the design with 143 nozzles is satisfactory regarding its behavior in simulation, even though these simulations are not sufficient for the full optimization of the design of the shower head to meet industrial requirements. Other parameters have to be taken into account to obtain uniform films such as: the design of the nozzle itself [23],[24] the variation of pressure along the reactor [25], the reaction kinetics and the enhanced depletion in the direction of the gas flow, the electronegativity of the plasma which favors electron attachment [26]. Nevertheless, it allows to reach satisfactory conditions for the study at the present research stage of development.

4.5. Scale-up

4.5.1. Intrinsic epi-layers

The objective of this part is to analyze trends for providing the best conditions to reach an optimum doping concentration on the largest area. For that, the former shower head with 24 nozzles has been

changed to a shower head with 143 nozzles to improve the gas injection homogeneity as detailed previously in the simulation results.

The substrates are 4-inch wafers and except if specified otherwise, the wafers are n-type FZ. The deposition rate will also be evaluated in order to improve it and reach deposition rates higher than 0.07 Å/s for boron-doped layers.

Given that the fluidics simulations have been performed for a pressure of 2.5 Torr and an inter-electrode distance of 20 mm, the studied conditions will be varied in a range around these values, namely from 2 Torr to 3 Torr. Even after optimization of the shower head, reaching process conditions with satisfactory properties in terms of crystallinity, homogeneity, smoothness, coherency of the lattice parameter along the direction of growth of epi-layers, is not an easy task and the process window remains tight. Nevertheless, the development of intrinsic epi-layers, which will be used as a basis for the development of boron-doped layers, allowed to achieve homogeneous layers on a full 4" wafer with high crystalline fraction and a satisfactory deposition rate. The necessary conditions are detailed below.

As shown in simulations results, the increase of gas flow rates keeping a good uniformity of the gas flow is possible when the nozzle density is increased. Thus the gas flow rates have been increased to 50 sccm of SiF_4, 4 sccm of H_2 and 500 sccm of Ar ($SiF_4/H_2/Ar$=50/4/500), compared to 20/3/300 with the former design. The former shower head design allowed growth rate of 0.2 Å/s with a substrate temperature of 200°C. As shown in Fig. 4.23, for a same temperature of 200°C, the new shower head design and the increase of the gas flow rates allows to obtain an average deposition rate three times higher (0.6 Å/s) than with the previous configuration.

Besides the substrate temperature has a strong influence on both the structural properties and the deposition rate. When the substrate temperature is increased to 300°C the deposition rate is 50% higher than that at 200°C. Moreover, the average crystalline fraction and the homogeneity are strongly enhanced when the substrate temperature is increased to 300°C.

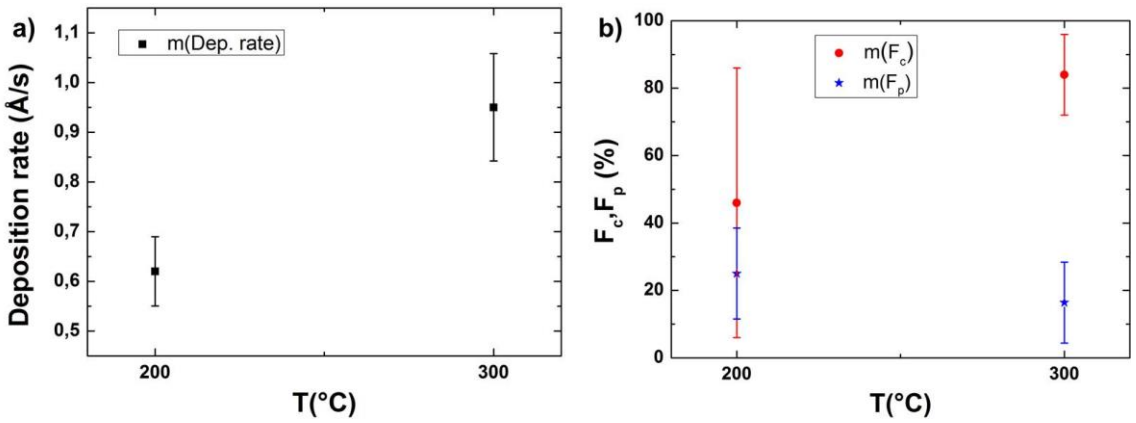

Fig. 4.23 – a) Evolution of the deposition rate and b) the crystalline and polycrystalline fraction as a function of substrate temperature. The inter-electrode distance is 20 mm, the pressure 2.5 Torr, the RF power 40 W and $SiF_4/H_2/Ar$=50/4/500 sccm.

Thus, in the following the substrate and RF electrode temperature will be respectively fixed at 300°C and 200°C. Note that the samples detailed until the end of this chapter do not present any amorphous phase: F_c+F_p=100%.

To further improve the homogeneity, the pressure has been reduced to 2 Torr and the inter-electrode distance has been increased to 30 mm. The gas mixture is composed of $SiF_4/H_2/Ar$=50/4/500 sccm. The RF power is 70 W, i.e. a power density of 311 mW/cm^2, which leads to a V_{pl} of 56 V. Thus, the plasma potential is purposely kept below 60 V, the critical limit observed in epitaxy using SiH_4/H_2 chemistry at 2.2 Torr [27]. The crystalline fraction mapping and roughness mapping are shown in Fig. 4.24. From Fig. 4.24-a), one can see that in these conditions of growth the epi-layer has an excellent crystalline fraction and is highly homogenous with an average crystalline fraction up to 99.8% and a standard deviation σ_{Fc} of 0.14% (absolute).

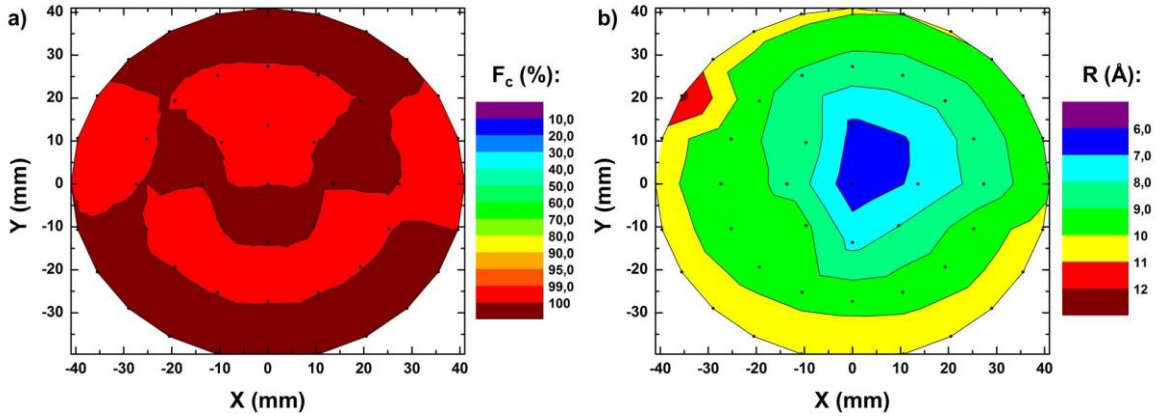

Fig. 4.24 – a) Crystalline fraction (F_c) mapping and b) roughness (R) mapping deduced from ellipsometry measurements. Data points are represented by black dots (48 points). The crystalline fraction varies from 99% to 100% indicating the excellent homogeneity obtained in these conditions of growth, namely a pressure of 2 Torr, an inter-electrode distance of 30 mm, a RF power of 70 W (311 mW/cm^2) leading to a V_{pl} of 56 V, SiF_4, H_2 and Ar flow rates of 50, 4 and 500 sccm respectively.

To further assess the crystalline quality of the epi-layer grown under these conditions, a ω/2θ scan has been performed on this sample to study the lattice parameter in the direction of growth [001], written as $a_{\perp,epi}$ or c_{epi}. The experimental data and the result of simulation obtained using the software LEPTOS from Bruker is shown in Fig. 4.25. The presence of interference fringes on the right and the left of the substrate peak is worth noticing. They are Pendellösung fringes and indicate the coherency of the diffracted beam and therefore the spatial coherency of the epi-layer. This is a proof of the monocrystallinity of the layers. This also allows to determine the thickness of the film. However the significant shift towards low angles of the position of the epi-layer diffraction peak indicates that this layer has an important difference of its lattice parameter with respect to that of the substrate, i.e. bulk silicon.

The lattice parameter $a_{\perp,epi}$ obtained from simulation is equal to 5.4336 Å. The variation of this lattice parameter with respect to that of the substrate is expressed below:

$$\frac{dc}{c} = \frac{c_{epi} - c_s}{c_s} = \frac{c_{epi} - a_s}{a_s} \quad (1)$$

where a_s is the substrate lattice parameter: a_s = 5.431020 Å and given that its lattice is cubic: a_s=c_s. Here, this leads to a variation *dc/c* of 0.048%.

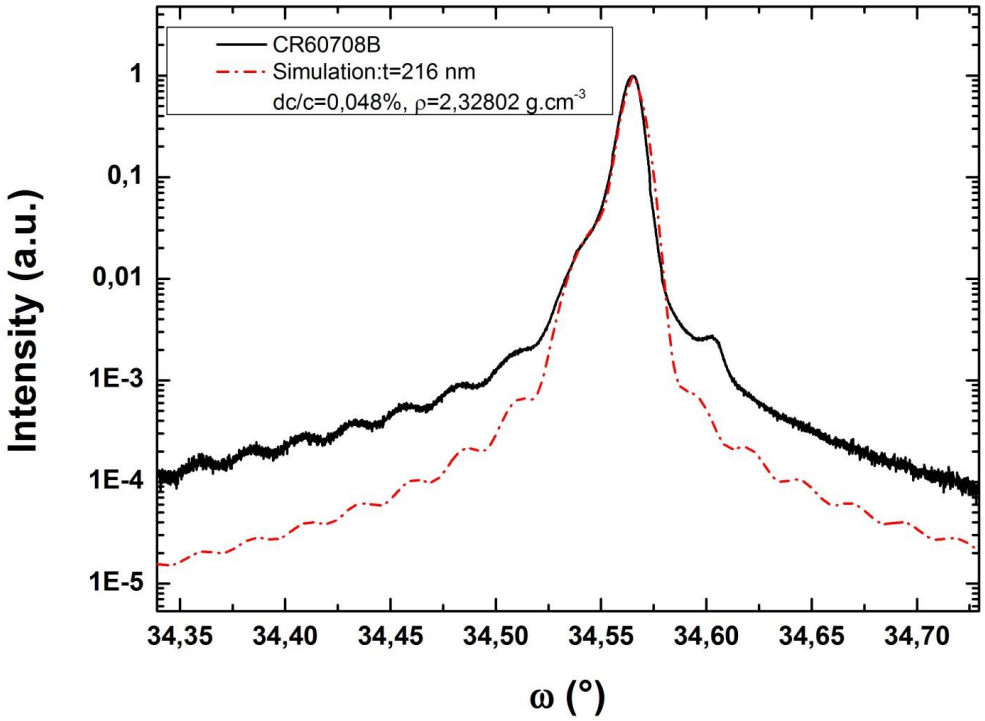

Fig. 4.25 – Experimental data of a ω/2θ scan for epi-layers grown at a RF power of 70 W (311 mW/cm^2) and 2 Torr and result of simulation for a 216 nm c-Si:H layer with a variation of lattice parameter in the direction of growth [001] with respect to that of the substrate (dc/c) of 0.048%. Pendellösung fringes indicate the spatial coherency of the epi-layer and allow to determine its thickness. This leads to a deposition rate of 1.2 Å/s for these conditions.

The values of $a_{\perp,epi}$ (the lattice parameter in the direction of growth [001]) obtained by the results of simulation using LEPTOS are compared to the results obtained from the equation detailed below [28]:

$$c_{epi} = a_{\perp,epi} = a_s.\left(1 + \frac{\Delta q_z{}^{(004)}}{\frac{4}{a_s} + \Delta q_z{}^{(004)}}\right) \quad (2)$$

where $\Delta q_z{}^{(004)} = q_{z,s}{}^{(004)} - q_{z,epi}{}^{(004)}$, i.e. the difference of position of the epi-layer diffraction peaks with respect to that of the substrate in the reciprocal space along [001] direction. The expressions for the calculation of q_z and q_x from Δω are detailed in [28]. In the case of the layer for which the ω/2θ scan is shown in Fig. 4.25, $\Delta q_z{}^{(004)}$=3.5×10^{-3} nm^{-1}. The resulting $a_{\perp,epi}$ obtained from each technique have a difference of only 1.10^{-4} Å indicating the viability of this model for our samples. In these process conditions, even if diffraction peaks do not perfectly overlap, the difference of lattice parameter is only about 2.10^{-3} Å. It is worth noticing that this is the upper limit of the lattice parameter calculated from XRD experiments on the samples obtained with our process conditions.

However, as shown in Fig. 4.26, the variation of the thickness over the full area of the wafer is not as homogeneous as F_c and R. The thickness of the epi-layer varies from 2090 Å to 3150 Å, for an average thickness of 2610 Å with a standard deviation of 330 Å. This leads to an average growth rate around 1.5 Å/s. Note that it is 7 times higher than the growth rate obtained with the initial shower

head. The pattern described by the mapping shows a correlation between the area with the lower thickness (on the right) and the position of the main entry gas as detailed in Fig. 4.19. This pattern is often observed on the samples, either in terms of F_c, R or thickness. Interestingly this reminds the pattern represented by the isovalues of velocity obtained in the results of fluidics simulations, shown in Fig. 4.20-c. Compared to the former shower head the behavior of the gas injection is therefore global instead of local. Even if these results of homogeneity are not fully satisfactory it represents a good base for the study of doped layers on 4" wafers.

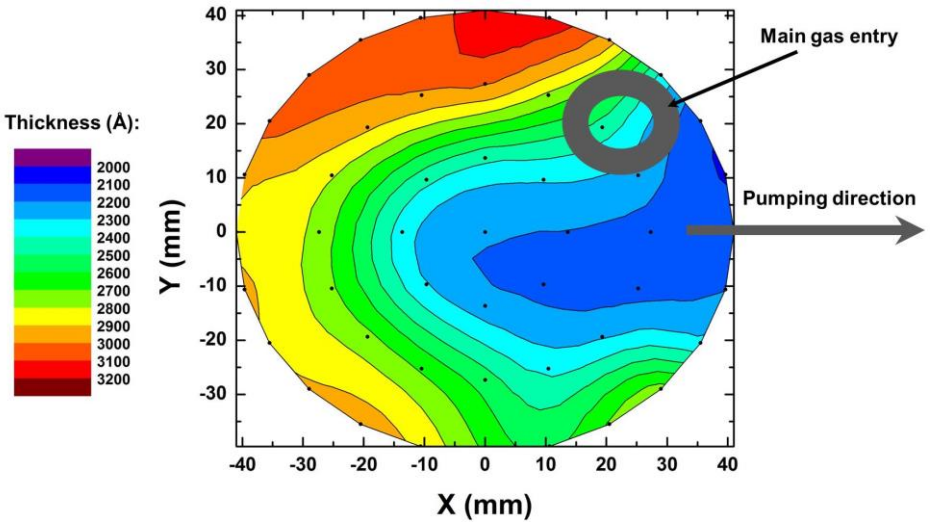

Fig. 4.26 – Thickness mapping deduced from ellipsometry measurements. Data points are represented by black dots (48 points). The thickness of the epi-layer varies from 2090 Å to 3150 Å, for an average thickness of 2610 Å with a standard deviation of 330 Å. This leads to an average deposition rate around 1.5 Å/s. Process conditions of growth are detailed in Fig. 4.24. Note that the area with low thickness roughly matches with the position of the main gas entry, i.e. upstream the shower head.

4.5.2. Effect of B_2H_6 flow rate

The effect of diborane flow rate on the epi-layers structural properties has been investigated in these conditions of low pressure (2 Torr), the process conditions are given in Table 3. Note that the B_2H_6 and H_2 flow rate, respectively $f_{B_2H_6}$ and f_{H_2}, are varied in such a way that $f_{B_2H_6} + f_{H_2} = 4$ sccm.

Sample	Temp. (°C)	Pressure (Torr)	Power (W)	Ar (sccm)	SiF_4 (sccm)	H_2 (sccm)	B_2H_6 (sccm)
CR60708B	300	2	70	500	50	4	0
CR60708C						3	1
CR60708D						2	2
CR60708E						1	3
CR60708F						0	4

Table 3 – Process conditions for B_2H_6 series at 70 W. The inter-electrode distance is 30 mm.

The results of ellipsometry mapping allowing to determine the crystalline fraction (F_c) and the roughness (R) for different B_2H_6 flow rates are shown in Fig. 4.27 and Fig. 4.28. In case of low pressure (2 Torr), the average crystalline fraction is higher than 94% up to 1 sccm of diborane and the layers are still uniform with a standard deviation σ_{Fc} of 2.8% absolute. The layer remains smooth with an average roughness of 11 Å with a standard deviation σ_R of 0.5 Å. At 2 sccm, F_c decreases to 57% and the layers are reasonably uniform with σ_{Fc}=7.9%. The roughness remains low as well with an average value of 14 Å and σ_R=1.4 Å. However from 3 sccm, the crystalline fraction strongly decreases and only reaches 8% and the layer becomes strongly inhomogeneous with σ_{Fc}=14.6%. Besides, the layer becomes rough, the average roughness reaches 29 Å and σ_R also increases to 5 Å. Finally at 4 sccm the same features are observed, the average F_c keeps decreasing and drops to 0%, the crystallinity is that time homogenously low with σ_{Fc}=0.48%. The roughness stays around 30 Å but its homogeneity slightly decreases with a σ_R of almost 8 Å. The evolutions of F_c and R as a function of the B_2H_6 flow rate are shown in Fig. 4.29.

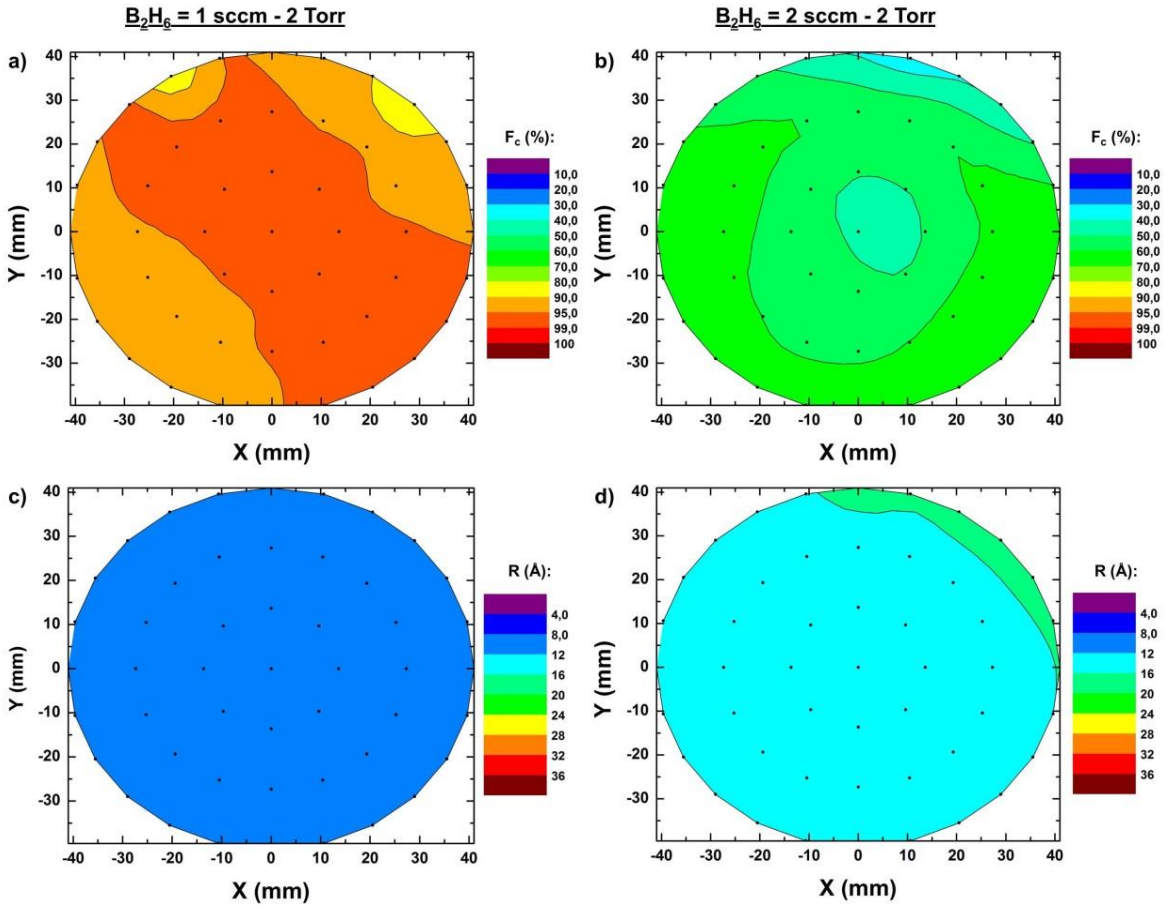

Fig. 4.27 – Mapping of F_c and R for different B_2H_6 flow rates under a pressure of 2 Torr and a RF power of 70 W. Data points are represented by black dots. No amorphous phase has been measured in these samples.

In Fig. 4.29-b) is shown the evolution of the deposition rate as a function of B_2H_6 flow rate. One can see that, in addition to an increase of the roughness and a decrease of the crystalline fraction, the B_2H_6 flow rate has a strong effect on the deposition rate. It is almost divided by 2 when only 1 sccm is added to the gas mixture, going from 1.5 Å/s to 0.8 Å/s, and reaches a plateau around 0.2 Å/s from 3 sccm. Note that in this case, the assessment of the growth rate is possible due to the presence of

interference fringes, this is in particular due to the "low" pressure (2 Torr) used in these process conditions.

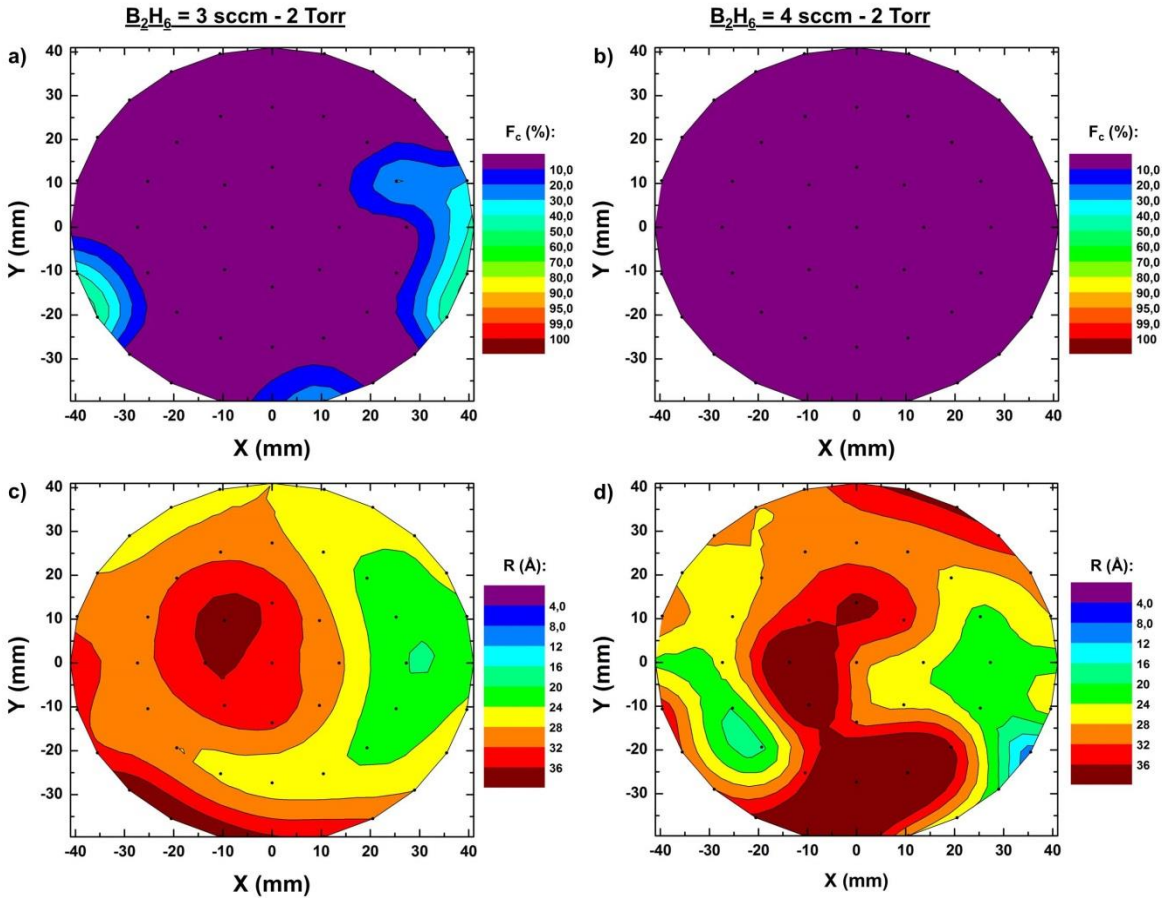

Fig. 4.28 – Mapping of F_c and R for different B_2H_6 flow rates under a pressure of 2 Torr and a RF power of 70 W. Data points are represented by black dots. No amorphous phase has been measured in these samples.

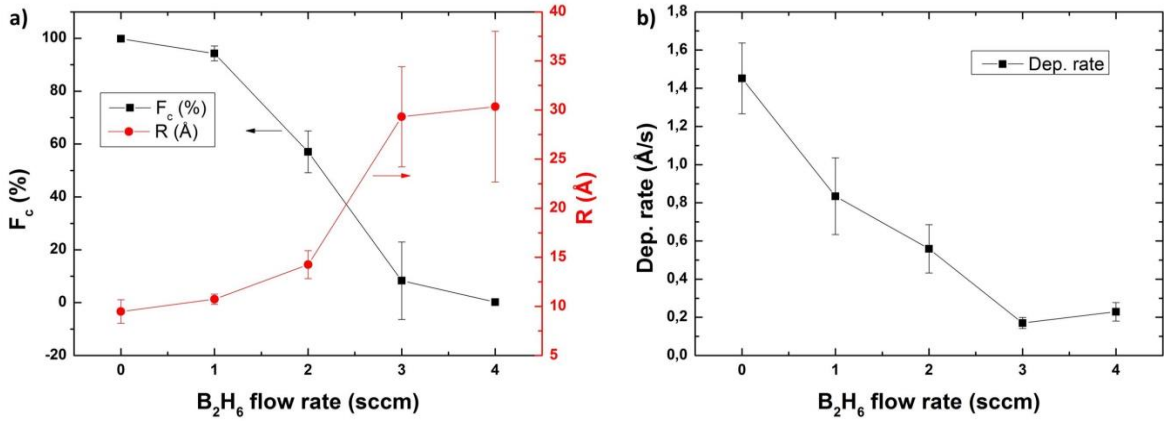

Fig. 4.29 – a) Evolution of F_c and R as a function of B_2H_6 flow rate. b) Evolution of the deposition rate as a function of B_2H_6 flow rate. Error bars are the standard deviation calculated from the 48 measurement points represented on the ellipsometry mappings above.

It is important to note that from 1 sccm to 4 sccm, no R_{sheet} lower than 400 Ω have been measured. In principle, the increase of the diborane flow rate should significantly lower the values of R_{sheet} but this

trend is not observed at 2 Torr – 70 W due to a strong deterioration of the structural properties of the epi-layers from 3 sccm. It seems that at 2 Torr – 70 W the addition of a high B_2H_6 flow rate is not desirable. A B_2H_6 flow rate of 2 sccm seems to be the best trade-off between homogeneity, F_c, deposition rate and B_2H_6 flow rate added to the gas mixture.

4.5.3. Effect of RF power at 2 Torr

From these conditions (70W, 2 Torr, 2 sccm of B_2H_6), the power has been varied and the evolution of the structural properties has been assessed by ellipsometry and XRD. The electrical properties have been studied by sheet resistance mappings. The details of the process conditions are shown in Table 4. Note that the hydrogen flow rate is changed, it has been purposely increased with the RF power in such a way that the conditions of H_2 depletion are equivalent, namely just before the transition towards a-Si:H.

Sample	Temp. (°C)	Pressure (Torr)	Power (W)	Ar (sccm)	SiF_4 (sccm)	H_2 (sccm)	B_2H_6 (sccm)
CR60727E	**300**	**2**	**50**	**500**	**50**	**1**	**2**
CR60801B			**60**			**1**	**2**
CR60708D			**70**			**2**	**2**
CR60727F			**90**			**3**	**2**

Table 4 – Process conditions for RF power series at B_2H_6=2 sccm under a pressure of 2 Torr. The inter-electrode distance is 3 cm.

The results of sheet resistance (R_{sheet}), crystalline fraction (F_c) and roughness (R) mappings for a RF power of 50 W and 60 W are shown in Fig. 4.30. F_c and R are deduced from ellipsometry measurements performed at 48 different points on the samples (4" wafers). R_{sheet} mappings are formed from 81 measurement points.

At 50 W and 60 W the R_{sheet} mappings are similar, a large region on the left of the wafer representing about two thirds of the full area shows a high R_{sheet} from, roughly, 300 to 700 Ω. While another part, on the right and close to the main gas entry, shows values between 73 and 147 Ω at 50 W, and between 99 Ω and 136 Ω at 60W. Average R_{sheet} is 295 Ω at 50 W and 248 Ω at 60 W with a standard deviation of 76% and 72%, respectively. Surprisingly for a RF power of 50 W, F_c is higher in the high R_{sheet} regions (from 90% to 100%) than in the low R_{sheet} region (from 50% to 70%). All the more so as shown in Fig. 4.26 the epi-layer is thinner in the right region therefore one should expect a higher R_{sheet}. At 60 W the homogeneity of F_c is improved and mainly varies from 60 to 80%, this could be attributed to a better dissociation of gas at 60 W with respect to 50 W.

Concerning the roughness of the layers, one can see that at 50 W the high R_{sheet} region is slightly rougher than the low R_{sheet} one. Surprisingly, the opposite observation is made on the layer grown at 60 W where the high R_{sheet} region shows a roughness between 8 and 12 Å while it increases up to 28 Å

on the low doped region. We are not able to explain such a difference with respect of such a slight increase of the RF power.

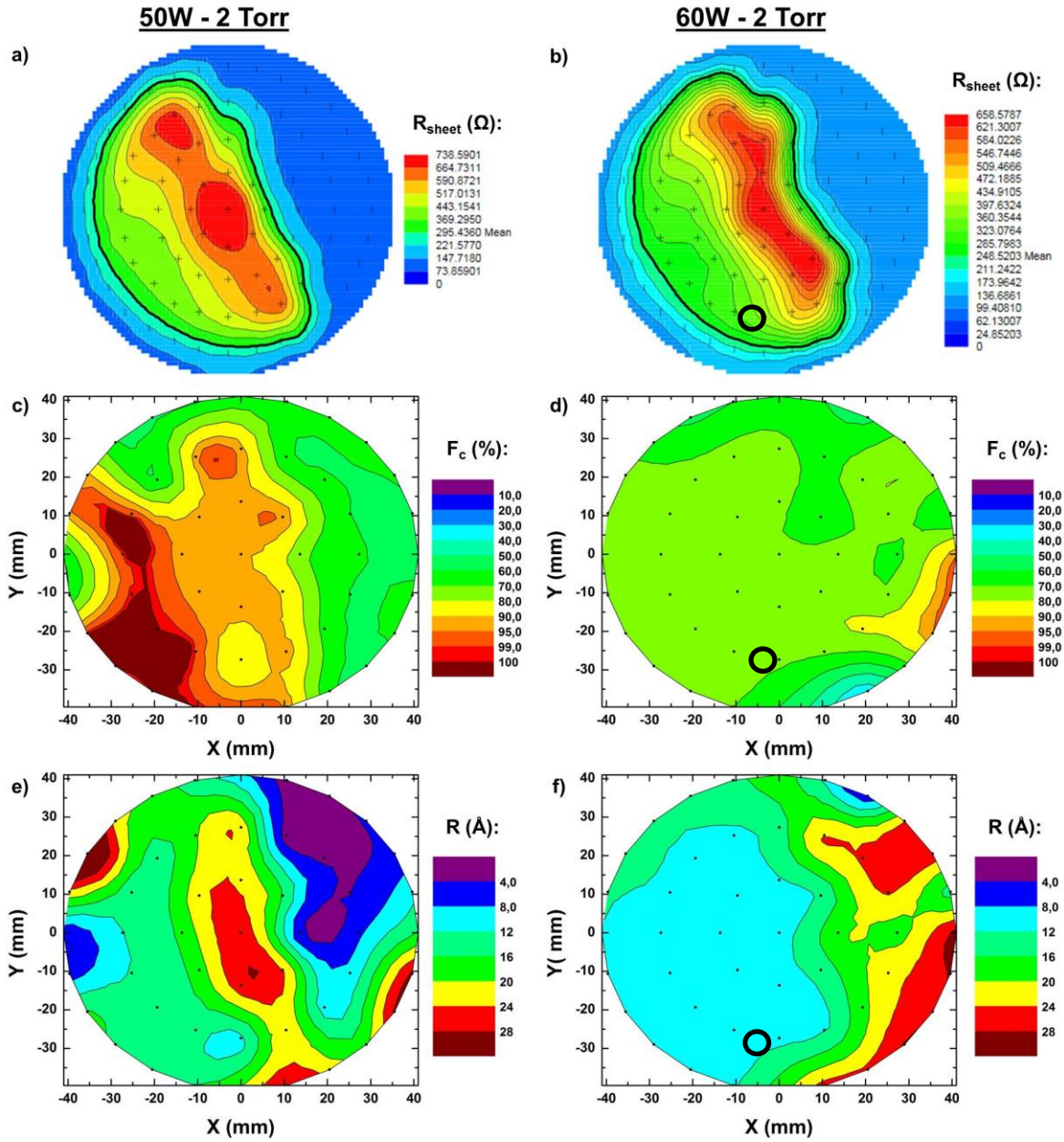

Fig. 4.30 – a) Sheet resistance (R_{sheet}), crystalline fraction (F_c) and roughness (R) mappings for epi-layers grown under a pressure of 2 Torr, at 50 W (a),c),e)) and 60 W (b),d),f)). The B_2H_6 flow rate is fixed to 2 sccm. F_c and R are deduced from ellipsometry measurements. Data points are represented by black dots (48 points). The black circles in b),d) and f) represent the region in which the SIMS and ECV analyses have been carried out. No amorphous phase has been measured in these samples. The R_{sheet} are measured on as-deposited layers.

When the RF power is increased to 70 W and 90 W (Fig. 4.31), keeping the same conditions of H_2 depletion, hence an increase of the H_2 flow rate, the average R_{sheet} tends to increase. Given that the layers are necessarily thicker, the R_{sheet} should actually decrease. However the trend is reversed and the average R_{sheet} at 70 W and 90 W are 431 Ω with a standard deviation of 70% and 620 Ω with a standard deviation of 77%, respectively. Even if F_c stays in the same range than those measured at 50

W and 60 W, namely at 70 W between 60% and 80% and at 90 W between 70 and 80% for the high R_{sheet} region and from 60% down to 0% for the low R_{sheet} region, we attributed the rise of R_{sheet} to a decrease of the structural properties of the layers as shown later by XRD measurement. Note that the R_{sheet} are measured on as-deposited layers, no post-growth annealing has been performed. While the roughness varies from 12 to 16 Å and is homogenous at 70 W, it goes up to 28 Å at 90 W. As a result, reaching low R_{sheet} values and high F_c when the RF power is increased, is difficult at 2 Torr.

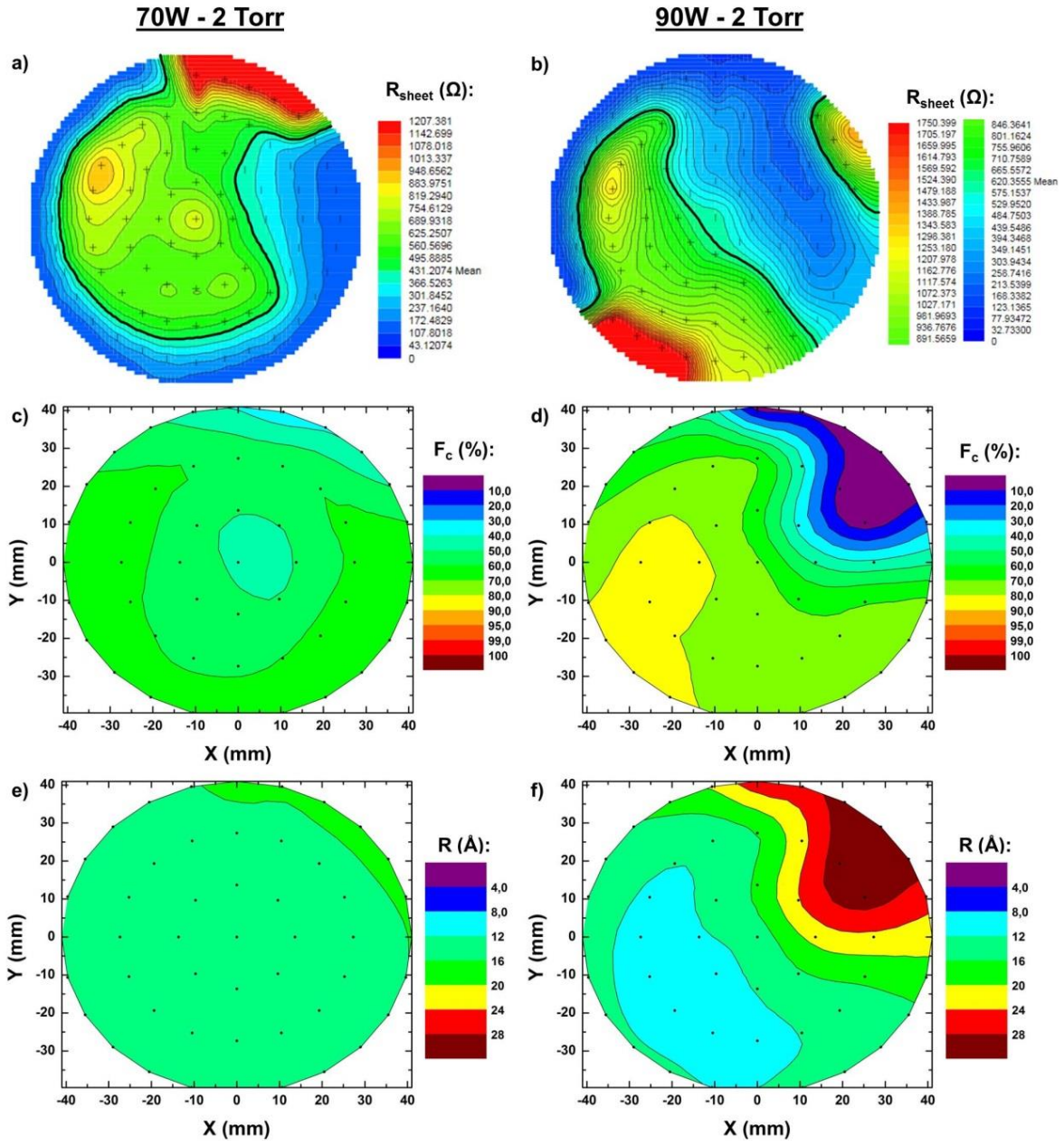

Fig. 4.31 – a) Sheet resistance (R_{sheet}), crystalline fraction (F_c) and roughness (R) mappings for epi-layers grown under a pressure of 2 Torr, at 70 W (a),c),e)) and 90 W (b),d),f)). The B_2H_6 flow rate is fixed to 2 sccm. F_c and R are deduced from ellipsometry measurements. Data points are represented by black dots (48 points). No amorphous phase has been measured in these samples. The R_{sheet} are measured on as-deposited layers.

The effect of the RF power on the same epi-layers has thus been investigated by XRD. The results of ω/2θ scans and rocking curves (ω scan) are shown in Fig. 4.32 and Fig. 4.35, respectively. From the

ω/2θ scans we can see that for RF powers of 50 W and 60 W, the lattice parameter of the epi-layers is similar to that of the substrate or at least the difference with respect to that of the substrate is less than 1.10^{-3} Å, the detection limit of our diffractometer. However at 70 W a shoulder starts to appear on the left of the diffraction peak of the substrate. Thus, the difference of lattice parameter of the epi-layers with that of the substrate is significant enough to be detected by the diffractometer. Moreover, in these conditions, Pendellösung fringes are observed indicating the spatial coherency of the epi-layer. Interestingly, no interference fringes are observed by ellipsometry on this sample. Thus in some specific cases, XRD can be complementary to ellipsometry to determine the thickness of epi-layers.

The analysis of the ω/2θ scan obtained on epi-layers grown at 70 W shows a layer thickness of 145 nm and a variation of the lattice parameter in the direction of growth [001] (dc/c) of 0.037% with respect to that of the substrate. Finally when the RF power is increased to 90 W, the FWHM of the ω/2θ scan of epi-layers significantly broadens and the fringes vanish. That indicates a dispersion of the lattice parameter along the epi-layers in the direction of growth, which points out a likely high defect density.

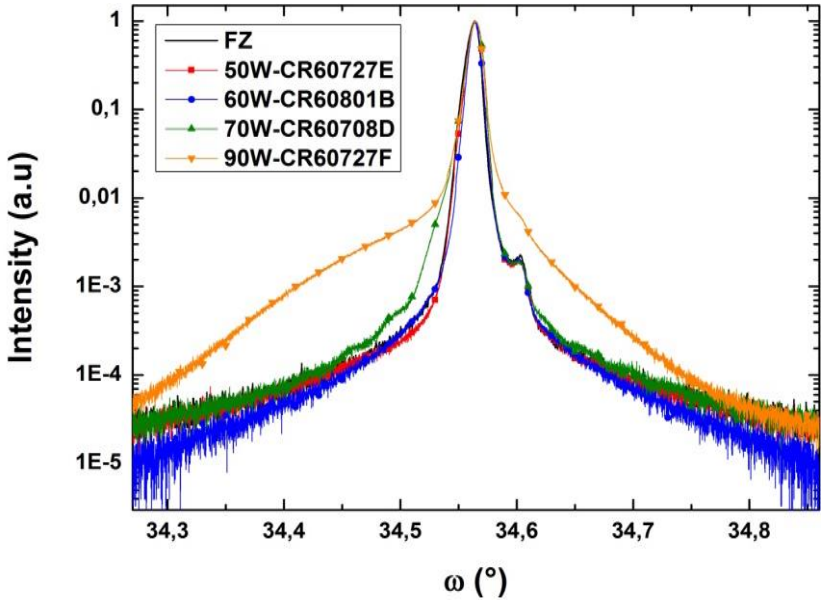

Fig. 4.32 – ω/2θ scans performed on epi-layers grown at 2 Torr under different conditions of RF power, namely 50 W (220 mW/cm^2), 60 W (266 mW/cm^2), 70 W (311 mW/cm^2) and 90 W (400 mW/cm^2). The growth conditions are shown in Table 4.

The FWHM and dc/c as a function of the RF power is plotted in Fig. 4.34. For layers grown at 50 W and 60 W, the FWHM and dc/c are identical to that of the substrate indicating that the variation of the lattice parameter in the epi-layers is lower than the detection limit of the diffractometer. When the RF power is increased to 70 W, the FWHM is twice larger than that of layers grown at 50 W and 60 W and as shown previously dc/c= 0.037%. Finally, at 90 W the FWHM is one order of magnitude higher than that of epi-layers grown at lower RF power. The average dc/c is 0.16%, therefore, also one order of magnitude higher than that of epi-layers grown at lower RF power. It should be noted that for the case at 90W the value of dc/c is an average and is calculated from the center of the Gaussian used to fit the scan. The large FWHM indicates an important variation of the lattice parameter along the growth direction which should be associated to a high defect density.

The same trend is observed with the rocking curve. At 50 W and 60 W the FWHM are the same as that of the substrate indicating a very low mosaicity around the [010] direction. At 70 W, in addition to a

different lattice parameter with respect to that of the substrate, a broadening at low angles is observed meaning that a mosaicity begins to appear. Finally the conditions at 90 W lead to an important mosaicity as deduced from the large FWHM of scan performed on the layer. While ellipsometry indicates similar crystalline fraction between the layers grown with different RF power, XRD shows that the higher the RF power, the less monocrystalline is the epitaxial layer. This would explain the increase of the sheet resistance when the RF power is increased.

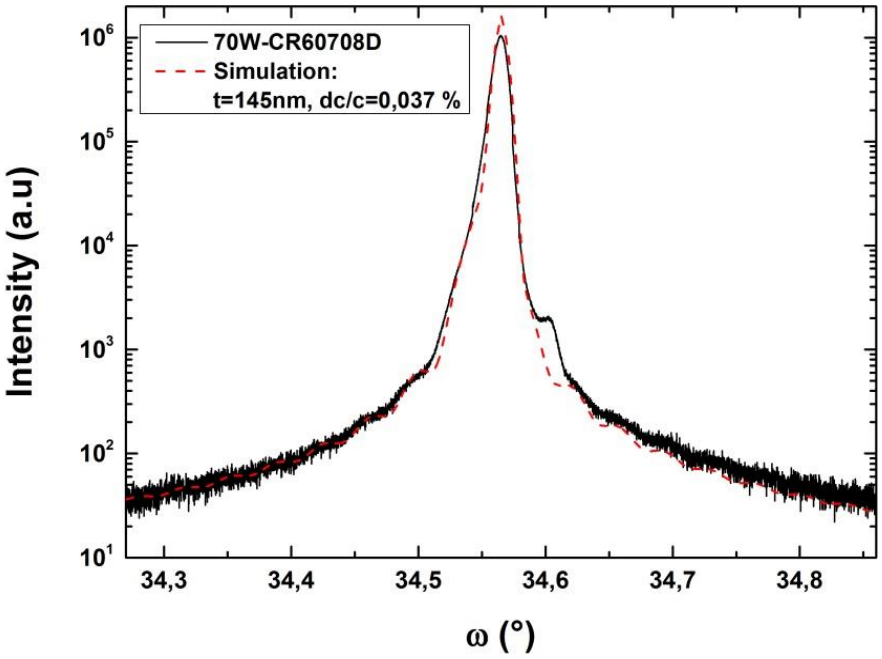

Fig. 4.33 – Experimental data of a ω/2θ scan performed on epi-layers grown at a RF power of 70W (311 mW/cm^2) and 2 Torr and result of simulation for a c-Si:H layer of 145 nm with a variation of lattice parameter in the direction of growth [001] dc/c of 0.037% with respect to that of the substrate. Pendellösung fringes show the spatial coherency of the epi-layer and allow to determine its thickness.

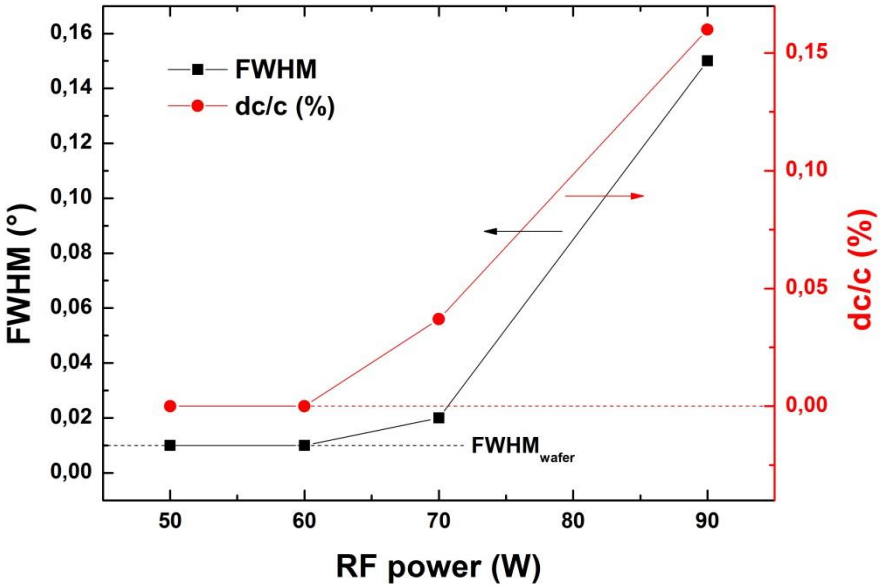

Fig. 4.34 – Evolution of the FWHM and the variation of lattice parameter in growth direction [001] measured by XRD for epi-layers grown under different conditions of RF power. Up to 60 W the FWHM and the lattice parameter are the same as that measured on a FZ wafer.

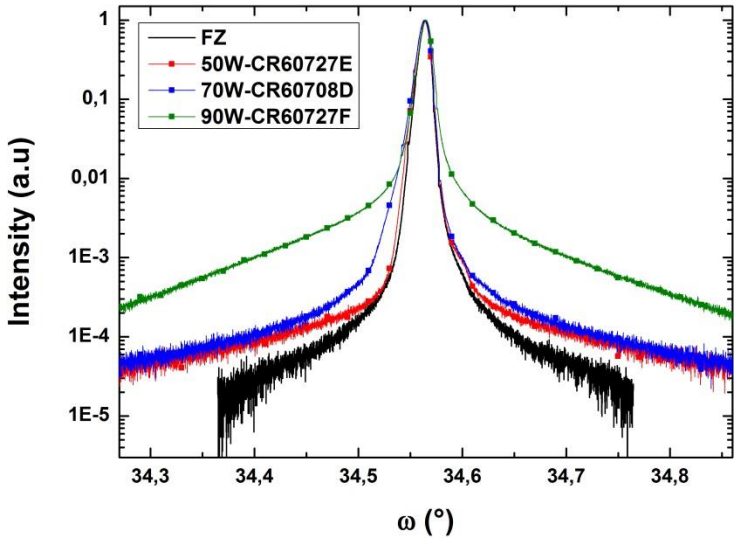

Fig. 4.35 – Rocking curves (ω scans) performed on epi-layers grown at 2 Torr under different conditions of RF power, namely 50 W (220 mW/cm^2), 60 W (266 mW/cm^2), 70 W (311 mW/cm^2) and 90 W (400 mW/cm^2). The detail of conditions is shown in Table 4.

Secondary ion mass spectrometry (SIMS) has been applied to epi-layers grown at 60 W to determine the concentration of boron and other impurities such as oxygen, carbon and fluorine. Moreover, the electrochemical capacitance-voltage (ECV) technique has also been used to determine the doping profile and to assess the doping efficiency; results are shown in Fig. 4.36. The region analyzed by SIMS is represented by a black circle in Fig. 4.30.

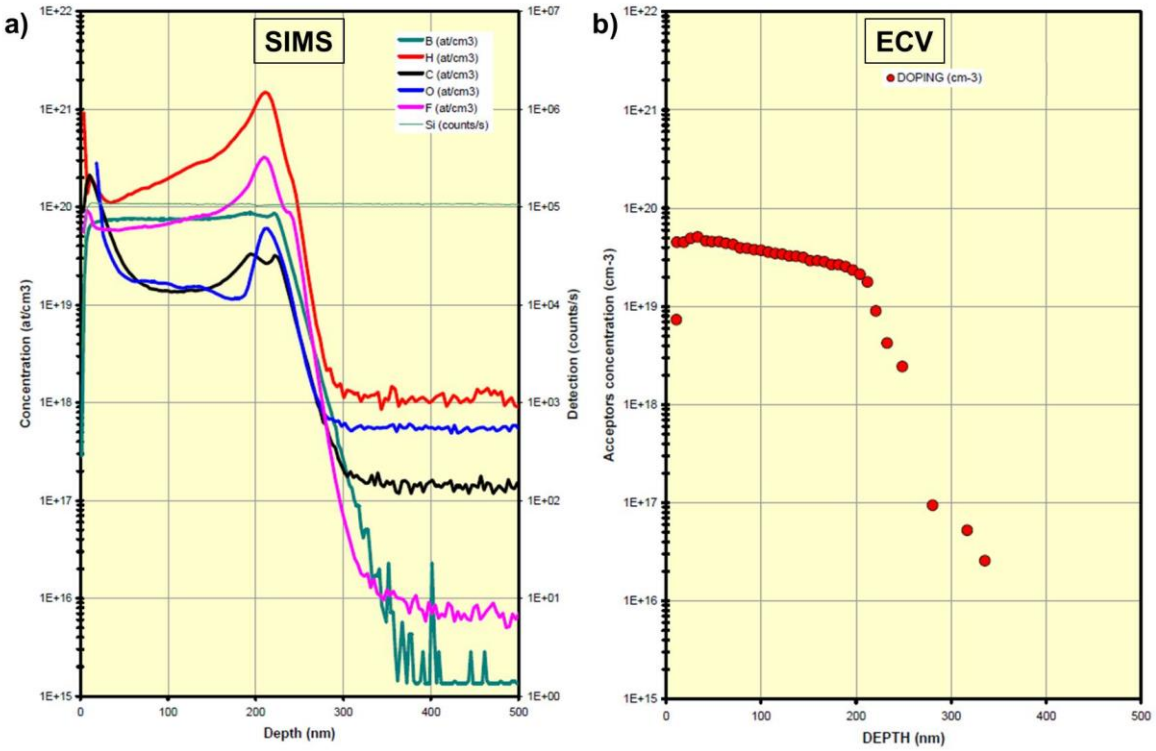

Fig. 4.36 – a) SIMS profile and b) ECV profile obtained on as-deposited epi-layers grown at 60 W under a pressure of 2 Torr, an inter-electrode distance of 30 mm and $SiF_4/H_2/Ar/B_2H_6$=50/2/500/2 sccm. The deposition rate is 1.1 Å/s.

The first observation one can make on the SIMS profile is the evolution of the concentration of impurities along the layer. In the bulk of the layer the concentrations are rather constant except for hydrogen. However there is a strong contamination at the interface between the epi-layers and the wafer characterized by the peak of oxygen, carbon, fluorine and hydrogen. The increase of oxygen and carbon at the interface, reaching respectively 7.10^{19} $cm^{-3}$and 3.10^{19} cm^{-3}, must be due to the lack of proper cleaning prior to epitaxy. Indeed only HF dips were performed on these layers, meaning that the silicon oxide is surely removed (without it no epitaxy could occur) but organic and metallic impurities are not removed. Piranha etching, HF/HNO_3 or UV/O_3 etching are a strong requirement to the development of epi-layers in order to expect performant devices. The increase of hydrogen is probably due to the increase of defects at the interface which favors the formation of sites for hydrogen or a segregation of hydrogen, the hydrogen contained in the bulk of the epi-layer may diffuse during the process and accumulate at the defective interface. The latter would explain the decrease of hydrogen towards the surface. Another explanation is that hydrogen is linked to the defect density. The decrease of hydrogen concentration towards the surface can be associated to a decrease of defect density along the layer. Another notable feature is the high concentration of fluorine in the bulk of the layer above 6.10^{19} cm^{-3}, this high concentration should come from the process itself due to the use of SiF_4 in the gas mixture.

Two reasons can explain the increase of fluorine at the interface (3.10^{20} cm^{-3}). The first one is linked to the HF dip done prior to epitaxy. In epi-layers grown using SiH_4/H_2 chemistry after a HF dip, a peak of fluorine is also measured at the epi/wafer interface indicating that even in fluorine-free plasma processes, fluorine is present at the interface. However, the concentration of fluorine measured at the interface of our layers is higher than that of measured in epi-layers grown using SiH_4/H_2 (6.10^{19} cm^{-3}). In addition, the fluorine concentration follows that of hydrogen. In a similar way that defects act as sinks for hydrogen, it has been reported that in fluorine-implanted silicon, fluorine can passivate the defects [29]. Thus, the increase of defects at the epi/wafer interface may also increase the fluorine concentration. The effect of fluorine on minority carriers lifetime remains unclear and its interaction with silicon can be, depending on cases, beneficial or detrimental. In boron-implanted silicon the fluorine co-implantation allows to terminate some of the defects created by the implantation and to inactivate them [29]. It is also reported that fluorine co-implantation improves the boron activation of boron-implanted silicon layers [30].

Nevertheless, in our case the increase of fluorine does not increase the boron activation. The SIMS profiles shows that the boron concentration is constant along the layer reaching 7.10^{19} cm^{-3}. An interesting feature is the difference between the shape in boron and hole concentration profile. While it is constant for boron, the hole concentration decreases when approaching the epi-wafer interface. The ECV profile shows a hole concentration varying from 2.10^{19} cm^{-3} at the epi-wafer interface to 5.10^{19} cm^{-3} at the surface. This leads to a doping efficiency of 30% at the interface and 70% at the surface. This difference is likely due to the increase of defects at the interface or the compensation by oxygen (donor dopant) and hydrogen known to affect the doping efficiency of boron as well [31]. Nevertheless, it is worth noticing that the SIMS profile indicates a drop of the oxygen concentration between 150 and 190 nm which should induce an increase of the hole concentration in this region, which is not observed. Thus, the compensation by hydrogen is the most likely explanation of the increase of doping efficiency with the thickness.

The R_{sheet} calculated from the doping concentration and emitter thickness deduced from ECV profile, respectively 3.5×10^{19} cm^{-3} and 200 nm for a mobility corresponding to the maximum theoretical value at this range of hole concentration (56 $cm^2.V^{-1}.s^{-1}$), leads to a value of 160 Ω, i.e almost twice lower than the R_{sheet} measured by the 4-point probe technique in the same area (≈320 Ω). This indicates that

the mobility should be twice lower than the maximum theoretical value, i.e. between 25 and 30 $cm^2.V^{-1}.s^{-1}$.

Finally, from these measurements we can deduce a growth rate of 1.1 Å/s. This is 15 times higher than the deposition rate obtained with the former shower head.

4.5.4. Effect of RF power at 3 Torr

In the following, we detail the electrical and structural properties of epi-layers grown under a pressure of 3 Torr, for which the RF power has been varied. The detail of the studied conditions is shown in Table 5.

Sample	Temp. (°C)	Pressure (Torr)	Power (W)	Ar (sccm)	SiF_4 (sccm)	H_2 (sccm)	B_2H_6 (sccm)
CR60803B	**300**	**3**	**50**	**500**	**50**	**1**	**3**
CR60727C			**90**			**3**	**2**

Table 5 – Process conditions for RF power series at 3 Torr. The inter-electrode distance is 3 cm.

As one can see in Fig. 4.37 the R_{sheet} is much more homogenous at 3 Torr than 2 Torr. Moreover R_{sheet} values are significantly reduced and approach targeted values, namely an average R_{sheet} between 100 and 200 Ω. At 50 W, the average R_{sheet} is 226 Ω with a standard deviation of 70%. In spite of a high standard deviation on the full sample the R_{sheet} only varies from 98 to 158 Ω on the two thirds of the wafer (blue part on the left). In addition, the F_c mapping shows high values for this same region with F_c varying from 90% to 100%. Finally an obvious similarity between the low R_{sheet}, high F_c and high roughness regions is observed in this sample, compared to previous results. It is worth noticing that no interference fringes are observed for these process conditions, which makes the thickness measurement difficult.

When the RF power is increased to 90 W, the R_{sheet} mapping results are close to meet the objective with an average R_{sheet} of 125 Ω and a standard deviation of 7%. The result of F_c mapping shows a strong inhomogeneity with F_c varying from 0% to 70%, however we doubt about the reliability of the fit given that the roughness measured on this sample is very important and the fitted values of the bulk layer may corresponds in reality to the roughness. To better understand the effect of RF power and the difference of structural properties between low and high R_{sheet} regions, ω/2θ scans and rocking curves have been performed.

The results are shown in Fig. 4.38. Interestingly the ω/2θ scans of the low and high R_{sheet} regions obtained on the same sample at 50 W are significantly different. In the high R_{sheet} region, a shoulder on the right of the substrate diffraction peak is observed. This represents the diffraction peak of the layer in this region. A shift towards large angles indicates a decrease of the lattice parameter in the direction of growth [001]. This is not surprising given that the boron-doped silicon has a lattice parameter smaller than that of the lowly phosphorus-doped substrate.

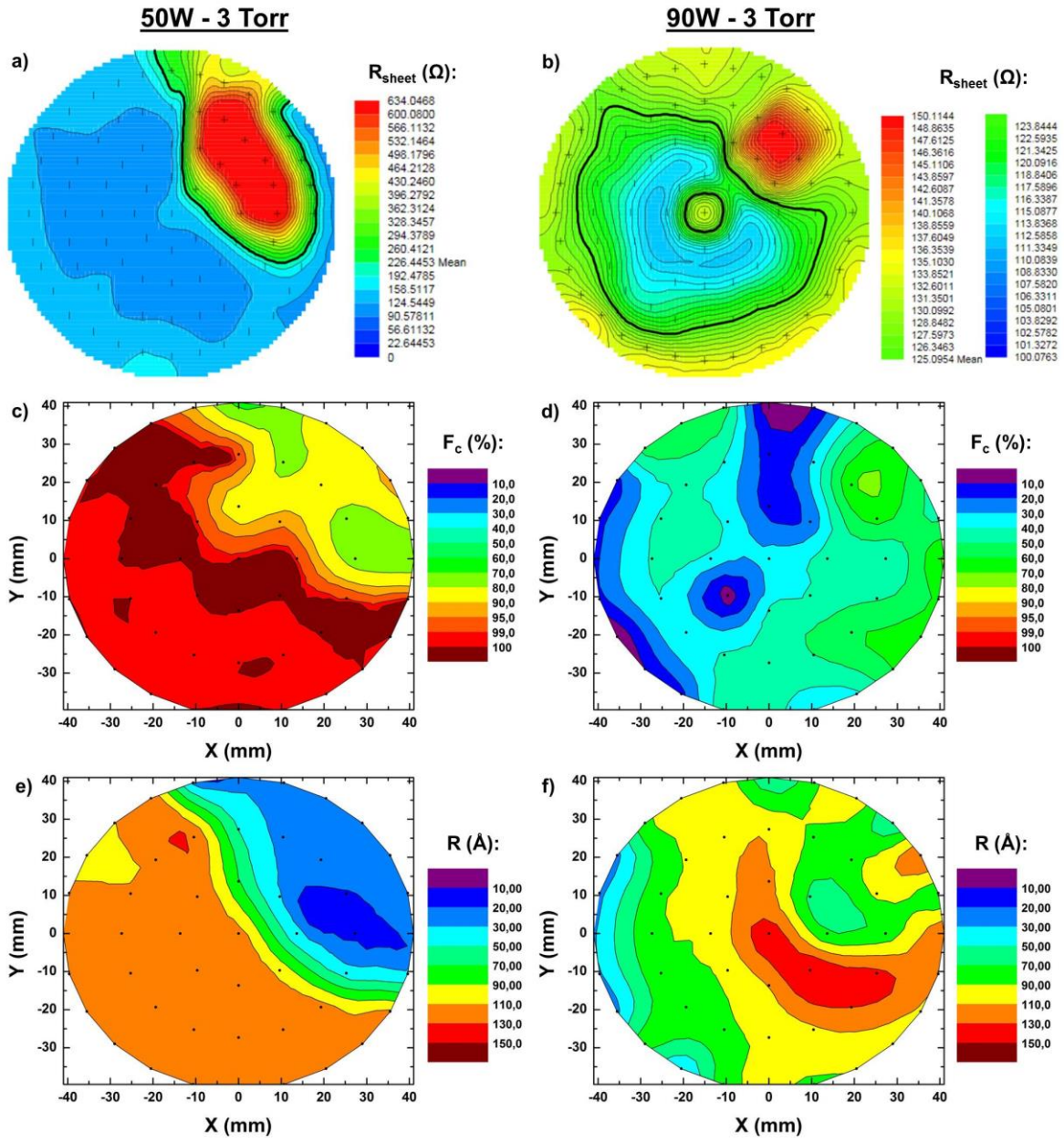

Fig. 4.37 – R_{sheet} mappings for epi-layers grown at 3 Torr and a RF power of a) 50 W and b) 90 W. F_c mappings deduced from ellipsometry measurements (48 points) for c) 50 W and d) 90 W. Roughness mappings deduced from ellipsometry measurements (48 points) for e) 50 W and f) 90 W. No amorphous phase has been measured on these samples. The R_{sheet} are measured on as-deposited layers.

However in the low R_{sheet} region, where one should expect higher doped layers, and therefore layers with a smaller lattice parameter which in turn should induce a shift of the diffraction peak towards even larger angles, surprisingly the diffraction peak of the layer completely overlaps with that of the substrate, indicating that the difference of lattice parameter is below 1.10^{-3} Å. At 90 W the ω/2θ scan is similar to that of the substrate indicating that at 3 Torr, the increase of the RF power up to 90 W keeping the same structural properties as those below is possible. It would indicate that a high pressure favors the acceptance of high RF power on the quality of the epitaxy, as deduced from the structural properties.

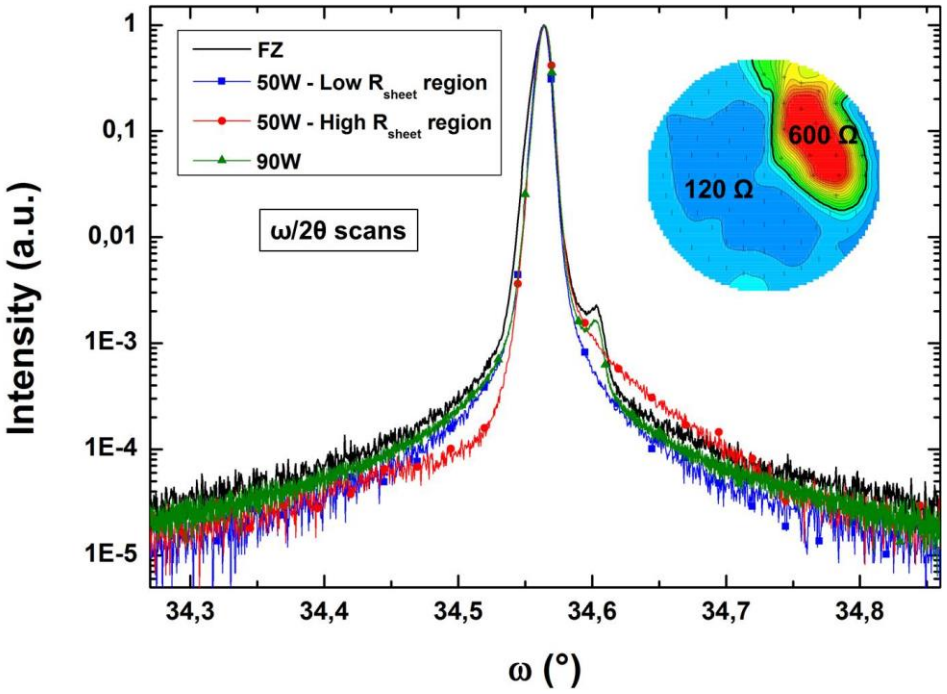

Fig. 4.38 – ω/2θ scans performed on epi-layers grown at 3 Torr under different conditions of RF power, namely 50 W (220 mW/cm^2) and 90 W (400 mW/cm^2). The detail of conditions is shown in Table 5 .

For the rocking curves, shown in Fig. 4.39, no significant differences are observed between the different analyzed samples indicating the low mosaicity of the epi-layers grown at 3 Torr from 50 W to 90 W.

This raises the question concerning the effective growth of epi-layers in the low R_{sheet} region at 50 W and 90 W, actually we may face an epitaxial growth in front of the main gas entry and an etching far from this area. Especially because by increasing the pressure, at a fixed inter-electrode distance that one cannot reduce because of dramatic homogeneity effect, the product $p \times d$ is 9 Torr.cm. Therefore the plasma regime approaches the powder formation and drastically decreases the deposition rate. Above all, it has been observed that when the surface of the wafer is deteriorated and that the process at 3 Torr and 50 W is performed, a 200 nm thick epi-layer is measured by ellipsometry. The deterioration of the surface thus allows to create a defective interface which is detectable by ellipsometry. However in these conditions, the roughness of the layer is only a few Å compared to the tens of Å for a "clean" interface, indicating that the layer did not grow the same way.

To clarify this question of actual epitaxial growth and to provide additional information about the structural properties and in particular out-of-plane properties of the layers in case of low power and to also discriminate the cases between high and low R_{sheet} regions, grazing incidence XRD (GI-XRD) has been performed. This experiment has been carried out with the help of F. Maroun from PMC, Ecole polytechnique. The variation of phi, which is the azimuth angle, around the position corresponding to the Bragg condition for a given interplanar spacing, i.e. here for (hkl)=(111) and (-220), corresponds to a rocking curve for these planes. The scans shown in Fig. 4.40 and Fig. 4.41 thus allow to determine the mosaicity around these planes.

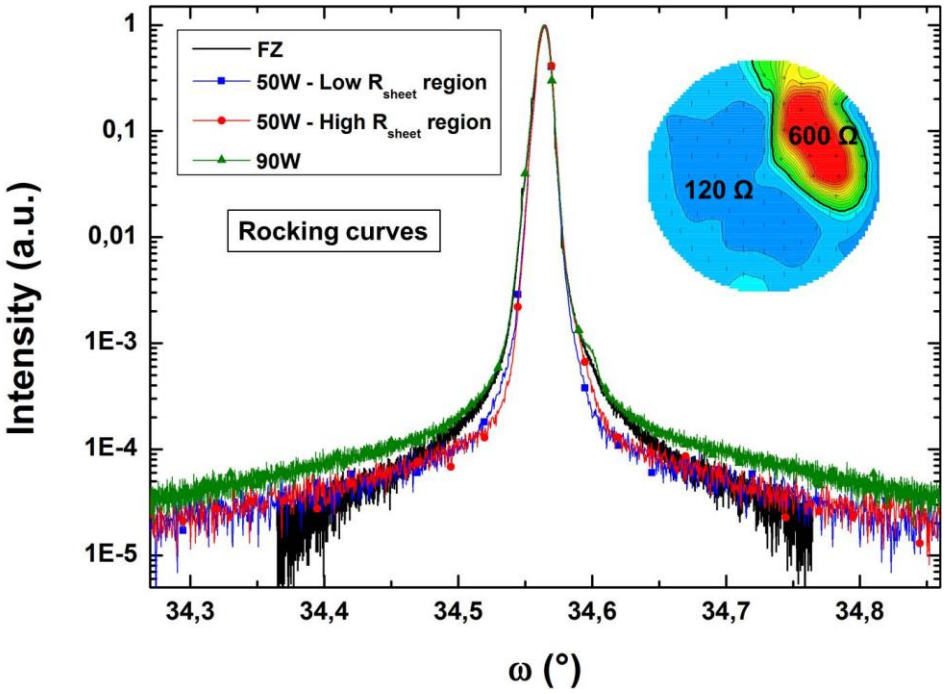

Fig. 4.39 – Rocking curves (ω scans) performed on epi-layers grown at 3 Torr under different conditions of RF power, namely 50 W (220 mW/cm^2) and 90 W (400 mW/cm^2). The detail of conditions is shown inTable 5. Two scans have been performed on the samples grown at 50 W, one in the low R_{sheet} region (≈120 Ω) and another in the high R_{sheet} region (≈600 Ω).

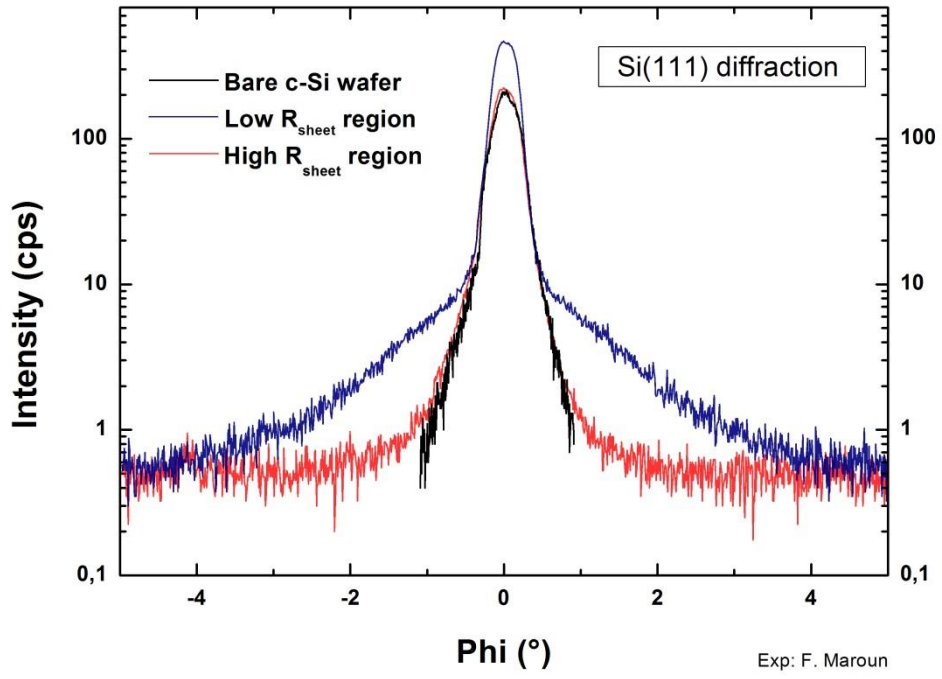

Fig. 4.40 – Phi scan (azimuth angle variation) in GI-XRD at Bragg angle for the Si(111) diffraction. The blue curve corresponds to the low R_{sheet} region and the red curve to the high R_{sheet} region in mappings in Fig. 4.37-a).

While the determination of the layer crystallinity is limited by the instrumental function for the high R_{sheet} area of the sample, a significant broadening of the FWHM is observed for the low R_{sheet} area. It

indicates, that contrary to the low mosaicity obtained on the (004) diffraction, an important mosaicity is observed around the (111) diffraction in GI-XRD for the low R_{sheet} region doped layers. Even if this result is not fully satisfactory for the performances of a solar cell, because it indicates the existence of separated domains between which one may expect recombination, it shows that a layer is effectively grown in this region. The same observations can be deduced from the phi scan for the (-220) diffraction indicating a mosaicity around (-220) planes for the highly doped part while the mosaicity in the lowly doped part is limited by the instrumental broadening.

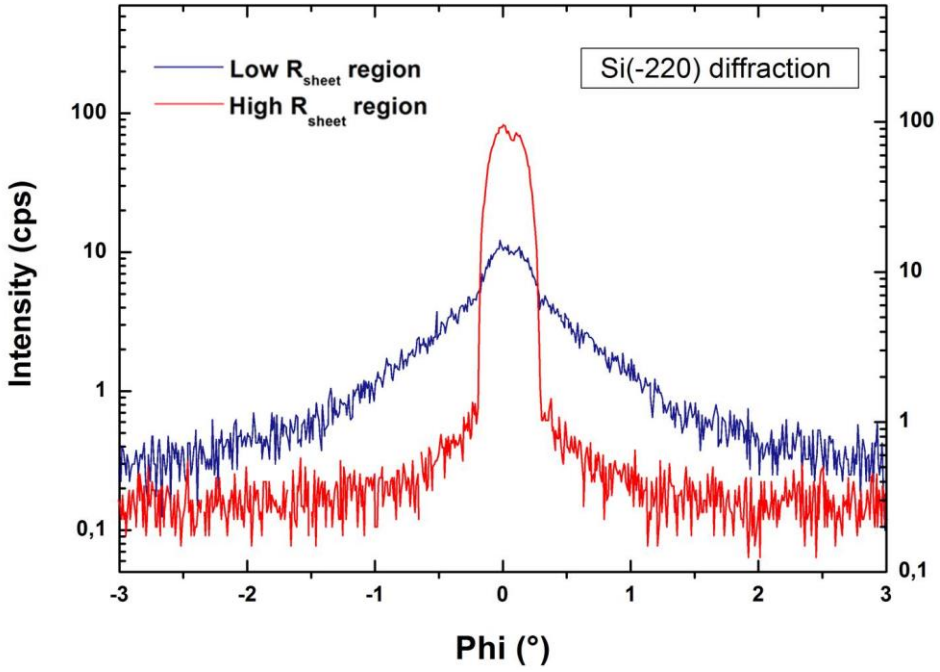

Fig. 4.41 – Phi scan (azimuth angle variation) in GI-XRD at Bragg angle for the Si(-220) diffraction. The blue curve corresponds to the low R_{sheet} region and the red curve to the high R_{sheet} region in mappings in Fig. 4.37-a).

In addition, cross section Kelvin probe force microscopy (KPFM) measurements under frequency modulated electrical bias have been performed over the epi-layer and a few microns in the wafer.

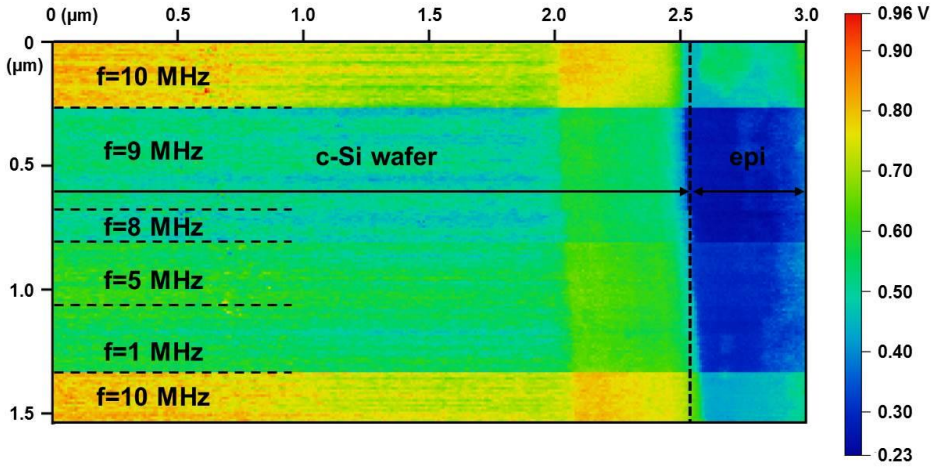

Fig. 4.42 – Cross section surface potential mapping obtained by KPFM for different frequencies of electrical bias obtained on low R_{sheet} region. A layer is recognizable between 2.5 and 3 µm by its lower surface potential than that of the substrate. The deposition time is 3600 s.

Note that scanning electron microscopy has been performed on the same epi-layer, but no contrast between the epi-layer and the wafer has been observed. The principle of the measurement has already been detailed in Chapter 3 and can be found in [32]. Because cross section KPFM requires layers with thicknesses above 300 nm for a proper characterization, the deposition time has been increased to one hour to be sure to observe the layer. From ellipsometry measurement with degraded interface, as a result the layer should be about 400 nm thick. The KPFM result is shown in Fig. 4.42.

As one can see, a layer is easily identifiable on the right side where a clear contrast of surface potential with the left part, corresponding to the wafer region, is observed. This allows to determine a thickness around 400 nm for the layer, which is consistent with the estimations. The frequencies have been varied, from the top to the bottom, from 10 to 9, 8, 5, 1 and 10 MHz again (the maximum of the generator). Whatever the frequency, there is a systematic difference between the surface potential of the wafer and that of the epi-layer indicating that the period for the maximum frequency $T=\frac{1}{10\ MHz}$ =100 ns is higher than the effective lifetime in the epi-layer. According to PV Lighthouse, at an injection level $\Delta n=1.10^{15}$ cm^{-3}, the theoretical lifetime of "perfect" boron-doped silicon with an acceptor concentration $N_A=1.10^{19}$ cm^{-3} is 150 ns and for $N_A=5.10^{19}$ cm^{-3} it goes down to 5 ns. Thus, the used frequencies are not suitable for the doped epi-layers since the maximum frequency corresponds to the upper limit of the lifetime expected for layers with such doping level. It would be more appropriate to either use a very high frequency generator or to use this technique for intrinsic layer in the first place, to separate the problem of lifetime (as one will see after) in the bulk of the epi-layers and at the interface. From the SIMS results obtained on the layer grown at 2 Torr and as shown in [32] one may expect strong differences between these two regions. But this technique requires strong differences of doping between the substrate and the layer. Thus, layers grown on n^{++} or p^{++} wafers would be more appropriate.

To assess the boron and carriers concentration in the epi-layer, SIMS and ECV technique have been performed. The deposition time is 1800 s, the same as the layer characterized by ellipsometry, XRD, GI-XRD. Results are shown in Fig. 4.43. The SIMS profile shows a surface peak extending over less than 100 nm. The boron concentration at the surface is only 4.10^{18} cm^{-3} and further decreases with the depth. It means that the R_{sheet} value (120 Ω) in the low R_{sheet} region is that of the substrate and not that of the layer. Moreover the ECV profiles show that, for the as deposited layer, no carrier concentration is measured until 300 nm, indicating that the carrier concentration is fewer than 5.10^{14} cm^{-3}. After 300 nm, the measured carrier concentration is that of the wafer. After an annealing at 310°C during 10 min the ECV profile indicates that the sample features a 150 nm thick n-type layer with a carrier concentration of 1.10^{15} cm^{-3}. Note that this value should be overestimated given that the measured electron concentration in the wafer is around 4.10^{16} cm^{-3} while the wafer resistivity is 1-5 Ω.cm, which normally leads to an electron concentration between 9.10^{14} cm^{-3} and 5.10^{15} cm^{-3}. This shows that instead of growing a p-type boron-doped epi-layer, a doping compensation might be observed in the first hundreds of nanometers.

Such a behavior might be explained by a high density of defects induced by the plasma; to clarify this, HR-TEM has been performed to analyze the crystallinity of this layer. HR-TEM images are shown in Fig. 4.44, Fig. 4.45 and Fig. 4.46. The deposition time is 3600 s, thus the layer should be around 400 nm thick. However Fig. 4.44 shows that no interface is visible over a thickness of 500 nm. The black spot corresponds to the damaged area induced by the energetic electron used for the HR-TEM in this region of the sample. From the Fig. 4.45 one can see that the surface is rough, which is consistent with the ellipsometry spectra obtained in this region (See Fig. 4.37). A slight contrast can be observed

between the first 20 nm and the region below. This could be attributed to a 20 nm thick epi-layer with a perfect interface however no other characterization showed this eventuality.

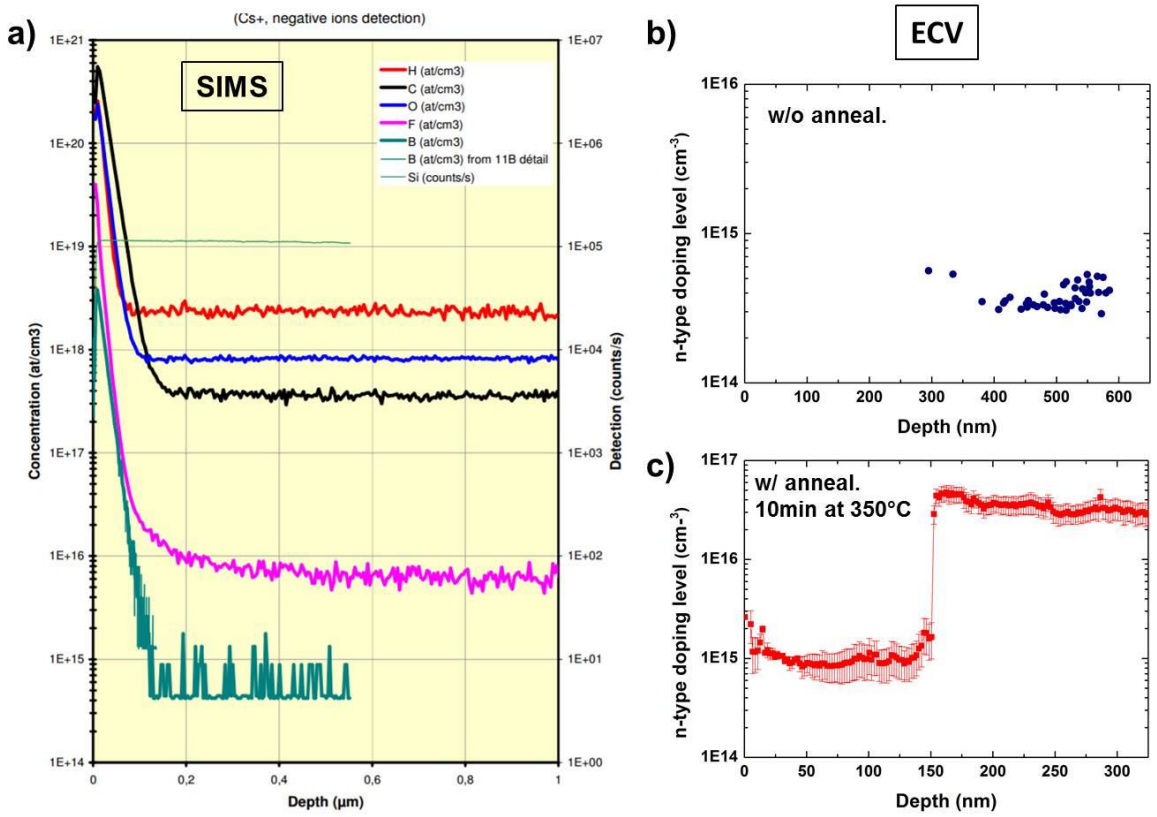

Fig. 4.43 – a) SIMS profile b) ECV profile performed in the low R_{sheet} region. c) ECV profile obtained on the same layer after an annealing at 350°C during 10 min. The deposition time is 1800 s. The electrolyte used for ECV is composed of HCl at 0.5 mole/L and NH_4HF at 0.1 mole/L.

Finally, Fig. 4.46 indicates that the roughness at the top of the sample is induced by the presence of perfectly monocrystalline islands. The height of these islands varies from 5 to 10 nm. This is below what we measured with ellipsometry, which indicates a roughness between 11 nm and 13 nm. Besides, the region below the islands is also perfectly monocrystalline, defect-free on the full analyzed area and no interface is visible. The most likely explanation is that these islands correspond to the nuclei observed in the early stages of growth (see Chapter 3). However in this case, islands are twice higher than those observed in the early stages of growth. Thus the roughness induced in the early stages of growth by these specific process conditions and in particular a $p \times d$ of 9 Torr.cm can impede the growth of the layer after its incubation phase.

Conclusions deduced from each characterization performed on the sample with conditions CR60803B detailed above are gathered in Table 6. However, in spite of these results, no clear conclusion on the effective epitaxial growth can be drawn. The most likely explanation is a plasma-induced doping compensation.

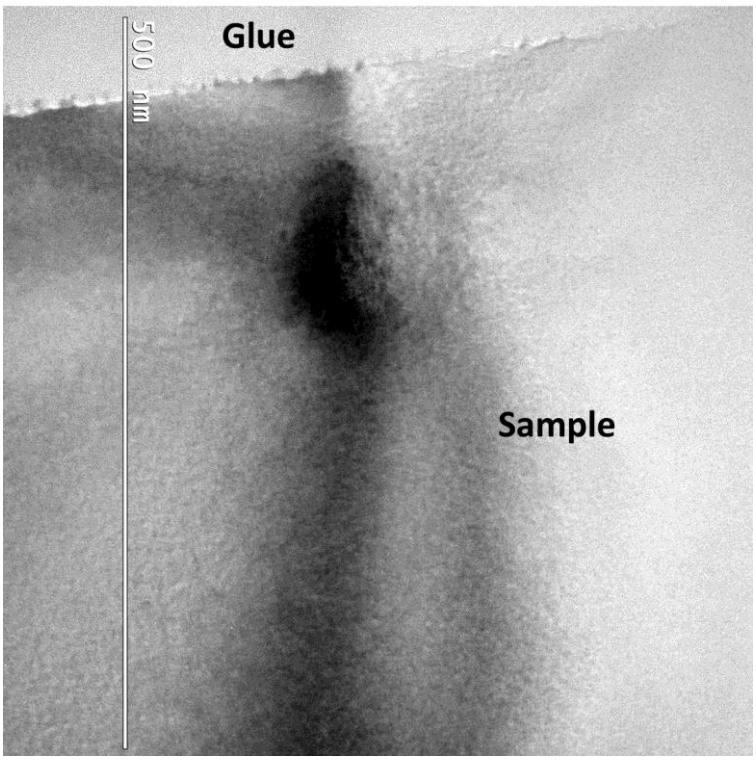

Fig. 4.44 – TEM image of the first 500 nm at the top of a sample for the low R_{sheet} region (process conditions: CR60803B in Table 5). The black spot corresponds to the damaged area induced by the energetic electrons used for the HR-TEM in this region of the sample.

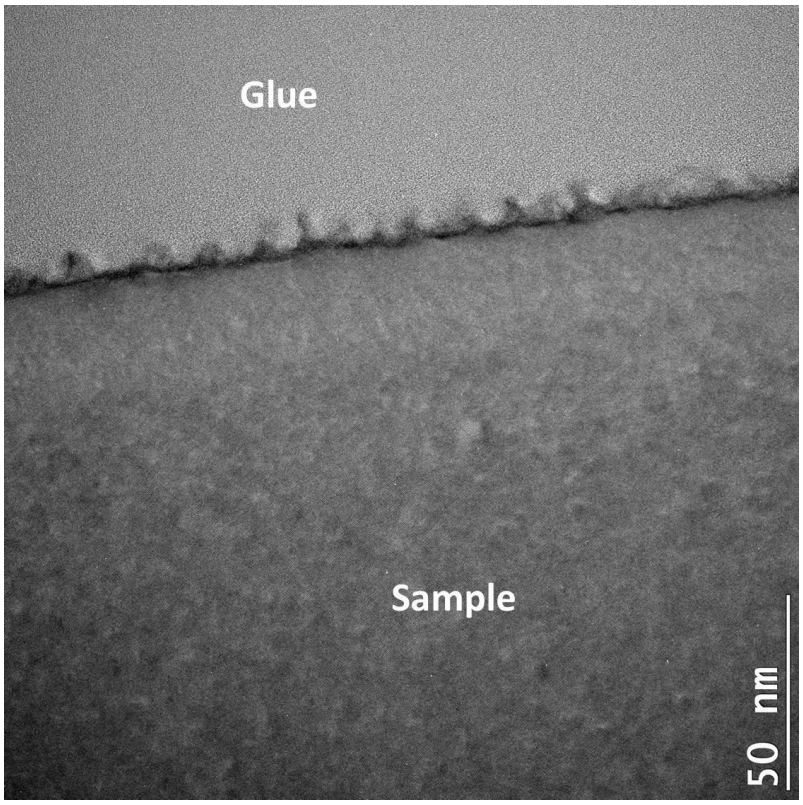

Fig. 4.45 – TEM image zoomed in the surface for the low R_{sheet} region (process conditions: CR60803B in Table 5). A few nm high islands are observed everywhere on the surface of the analyzed sample.

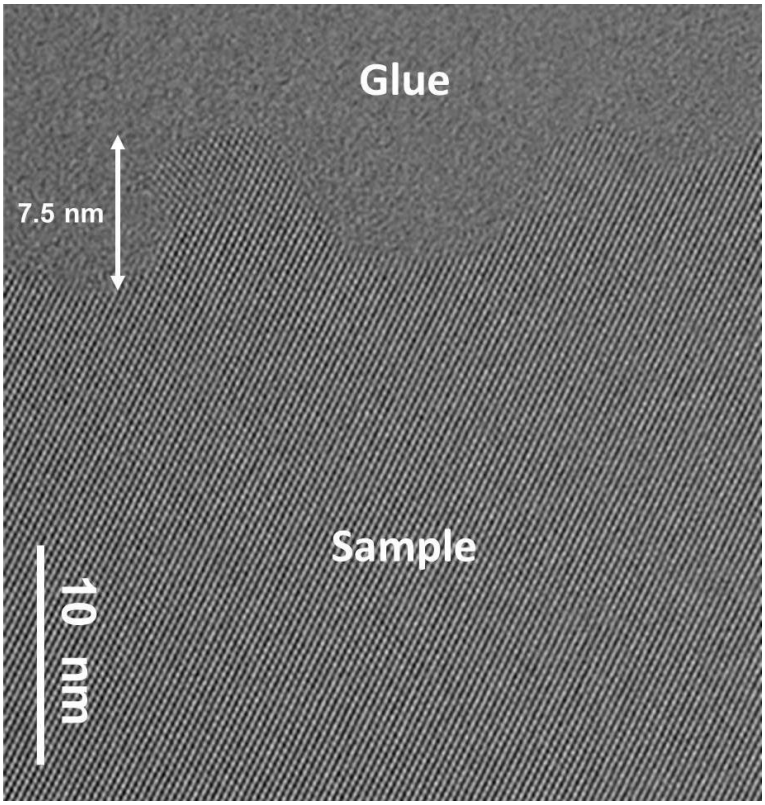

Fig. 4.46 – HR-TEM image at the surface of the low R_{sheet} region showing that the islands are perfectly monocrystalline. The height of islands at the surface of the sample varies from 5 to 10 nm.

Characterization technique	Result
4-point probe	No R_{sheet} measured before growth. After growth R_{sheet} of 120 Ω.
Ellipsometry with damaged interface	Epi-layer with a growth rate of 1 Å/s and high R_{sheet}. Roughness of a few Å.
Ellipsometry with clean interface	Impossible to measure a thickness. Roughness up to 12 nm.
SEM	No layer is observed.
XRD	No layer measured or difference of lattice parameter with respect to the substrate lower than 1.10^{-3} Å.
GI-XRD	Layer with an important mosaicity.
KPFM	400 nm thick layer with a different surface potential than that of the substrate (would correspond to a growth rate of 1.1 Å/s).
SIMS	Tail of fluorine, boron and hydrogen at the surface.
ECV	Compensated doping over a 300 nm thick layer without annealing, and over 150 nm after annealing.
TEM	No epi-wafer interface. 5 to 10 nm high islands.

Table 6 – Summary of results obtained from different characterization techniques performed on samples grown with the conditions CR60803B (See Table 5).

4.5.5. Growth on Si(111) substrates

From a technological point of view, achieving doped epitaxial growth on Si(111) substrates would pave the way to manufacturing epitaxial emitter on textured wafers. This would allow both manufacturing epitaxial emitters on the front side of a solar cell or on the rear side of a bifacial solar cell. However, the growth of epi-layers on Si(111) substrates by PECVD below 300°C has not been reported yet and the process leads to the deposition of amorphous silicon [33]. However the growth from $SiF_4/H_2/Ar$ chemistry shows interesting results. Note that all the samples studied in this part have been processed in the Cluster with the former shower head (nozzle density=0.1 cm^{-2}). Ellipsometry spectra of layers grown with $SiF_4/H_2/Ar$ chemistry for a substrate temperature varying from 200°C to 300°C are shown in Fig. 4.47. The growth time is constant and fixed at 1800 s. At 200°C the layer is fully amorphous. However from 250°C, the layer becomes crystalline with an important roughness. Modelling of the spectroscopic ellipsometry indicates a roughness of 12 nm. When the substrate temperature is further increased to 300°C, the layer is still crystalline and smoothens. Thus, the increase of temperature has a beneficial effect on the crystallinity of the layer grown on Si(111) substrates. From these ellipsometry results we can expect achieving epitaxial growth below 300°C. However no interferences are observed, so, as detailed previously for the doped layers processed at 3 Torr and an inter-electrode distance of 30 mm, the question arises to know if an actual epitaxial growth occurs or if it is just a roughening of the surface. Fig. 4.48 shows ellipsometry spectra for several conditions of pressure, RF power, H_2 flow rate and growth time. At 2.5 Torr, when the H_2 flow

rate is increased to 4 sccm the layers becomes amorphous. Interestingly the same behavior is observed on Si(100) substrates when the H_2 flow rate is increased.

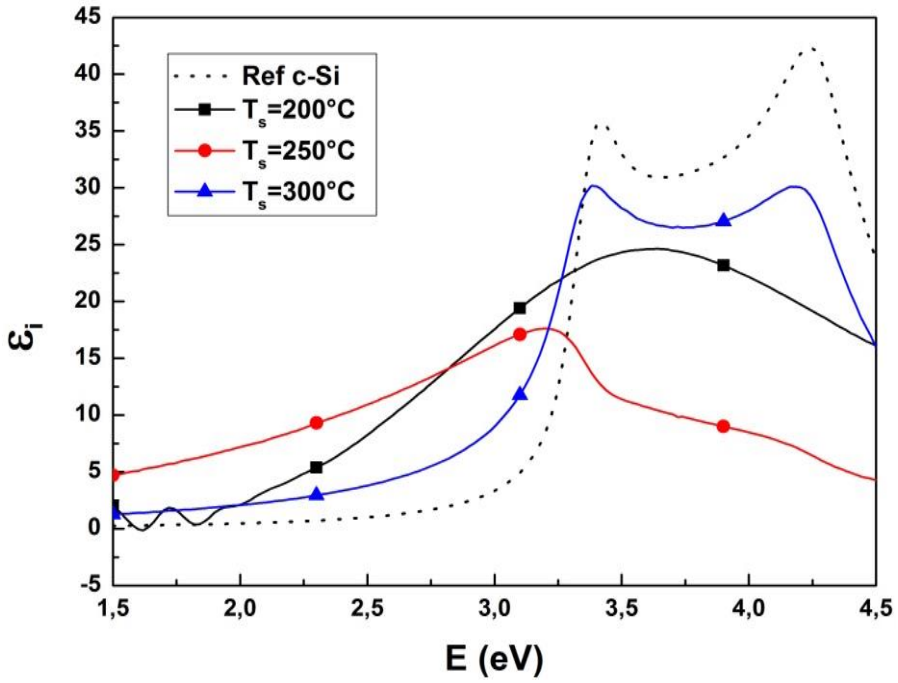

Fig. 4.47 – a) Layers grown in Cluster on Si(111) substrates for substrate temperatures varying from 200°C to 300°C. Process conditions are: P_{RF}= 40 W, p=2.5 Torr, d=20 mm, $SiF_4/H_2/Ar$=20/3/300 sccm, T_{RF}=200°C. The growth time is 1800s.

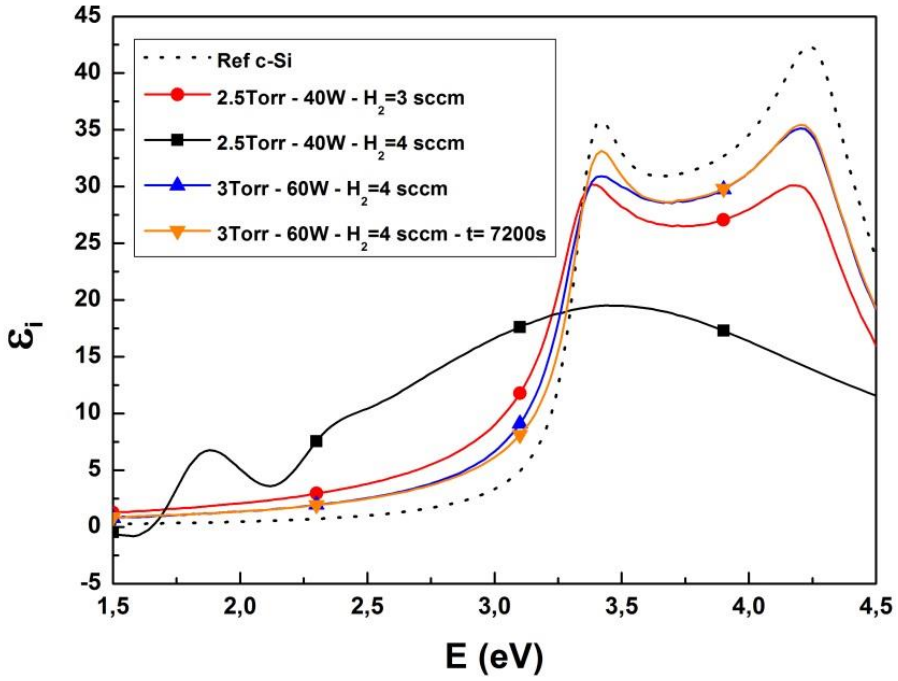

Fig. 4.48 – a) Layers grown in Cluster on Si(111) substrates for various H_2 flow rate, pressure, RF power and deposition time. The substrate temperature is fixed at 300°C. Process conditions: d=20 mm, $SiF_4/H_2/Ar$=20/x/300 sccm, T_{RF}=200°C. For black (squares), red (circles) and blue (up triangles) curves the growth time is 1800s, and 7200s for the orange one.

However by both increasing the RF power and the pressure to 60 W and 3 Torr respectively (in blue), it is possible to obtain a crystalline layer and even to improve the structural properties. These three samples have been processed with a growth time of 1800 s. An interesting result is that when the growth time is further increased to 7200 s, for process conditions at 60 W and 3 Torr, the structural properties improve. Thus, this is very likely that an epitaxial growth occurs, else in case of etching a longer growth time should lead to an increase of the roughness.

However, these ellipsometry spectra do not feature interferences neither, and a clear conclusion about the epitaxial growth is not possible. To tackle this issue, B_2H_6 has been added to the gas mixture. If a doped epitaxial growth occurs we should measure a sheet resistance. The spectrum of the layer after a growth time of 14400s (4 hours) is shown in Fig. 4.49. As one can see, the layer is still crystalline and the optical modelling indicates a roughness of 5 nm. For this layer a sheet resistance of 200 Ω has been measured while no R_{sheet} was measured on the intrinsic layers. Even though at the beginning we thought that a doped epi-layer was grown on the Si(111) substrate, we may face to the same specific case showed previously on Si(100) substrates in similar conditions (3 sccm of B_2H_6, p=3 Torr and d=30 mm). The R_{sheet} measured could be that of the wafer. Therefore, unfortunately, even though this is very likely that epitaxial growth occurs on Si(111) substrates, it is difficult to conclude with certainty.

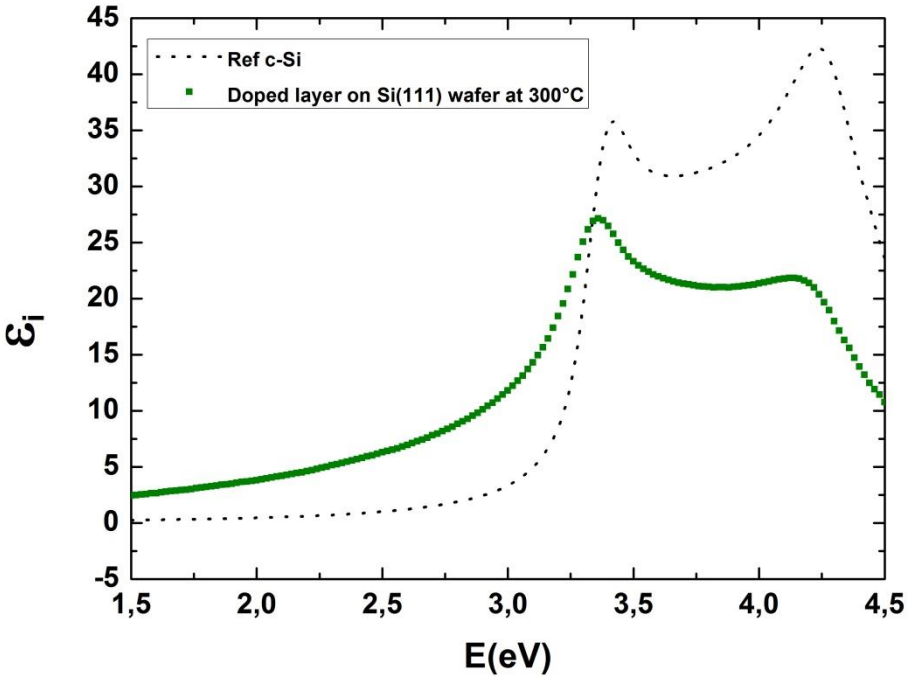

Fig. 4.49 – a) Layers grown in Cluster on Si(111) substrates at 300°C with 3 sccm of B_2H_6. Process conditions are: P_{RF}=60 W, p=3 Torr, d=20 mm, $SiF_4/H_2/Ar/B_2H_6$=50/0/500/3 sccm, T_{RF}=200°C. The growth time is 14400s.

4.6. Passivation

This part is dedicated to the analysis of the lifetime measurement for samples grown on Si(100) c-Si substrates and passivated with aluminum oxide (AlO_x). Preliminary investigations of epi-layers

passivated by a-Si:H showing very poor results with lifetimes lower than 10 µs, afterwards the study was turned towards passivation by AlO_x using atomic layer deposition (ALD). The samples were analyzed by quasi steady state photoconductance (QSS-PC) and by photoconductance calibrated photoluminescence (PC-calibrated PL) using a BT Imaging R2 tool.

In Fig. 4.50 are shown PC-calibrated PL images of samples composed of 200 nm thick intrinsic epi-layers grown at 2 and 3 Torr on double-side mirror polished (DSMP) intrinsic (5 kΩ.cm) 4" FZ wafer. The conditions at 3 Torr are the same as the conditions CR60803B except that the B_2H_6 has been replaced by H_2. Note that in the case of intrinsic deposition we have been able to measure a layer by ellipsometry. The samples have been passivated on both sides with 10 nm of AlO_x deposited at 200°C and annealed for 5 min at 350°C. This recipe of AlO_x leads to a lifetime of 24 ms on a bare intrinsic (5 kΩ.cm) FZ wafer. QSS-PC measurements are also performed on these samples. It provides an average lifetime values measured on a 3 cm diameter circular area. As one can see in Fig. 4.50, a strong difference of lifetime is observed between the region exposed and not exposed to the plasma. Indeed, the crown at the edge of the wafer corresponds to the region lying on the substrate holder, therefore not exposed to the plasma. In this region the lifetime reaches 500 µs at 2 Torr and 250 µs at 3 Torr. However in the region where epitaxy occurs the lifetime is significantly smaller. At 2 Torr the lifetime is homogenous and is around 100 µs.

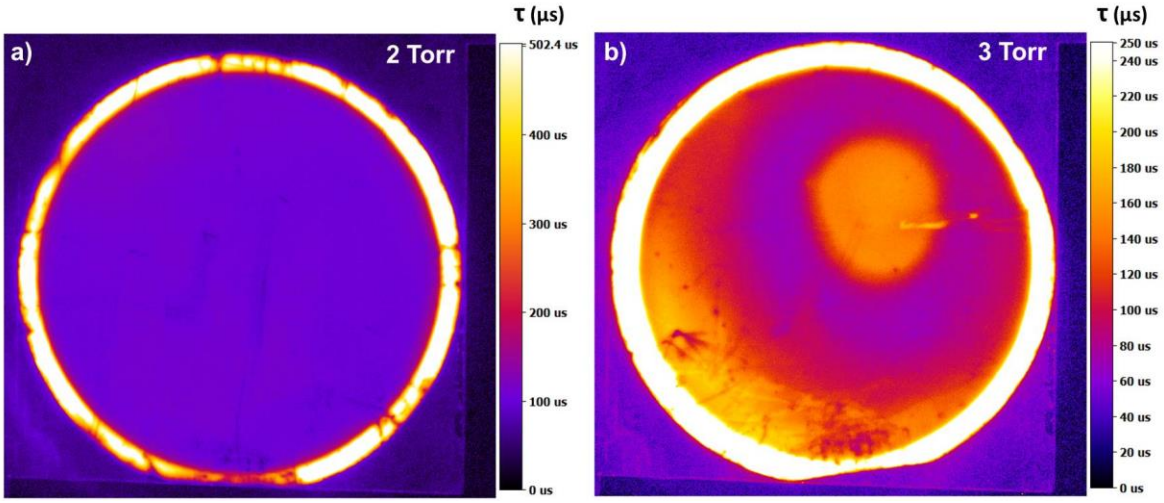

Fig. 4.50 – PC-calibrated PL imaging of an epi-layer grown at a) 2 Torr and b) 3 Torr. The process conditions are: $SiF_4/H_2/Ar$=50/4/500 sccm, d=30 mm, P_{RF}=50 W, T_s/T_{RF}=300/200°C. Substrates used are DSP intrinsic 4" FZ wafers. Layers are passivated with 10 nm of AlO_x deposited at 200°C by ALD and annealed at 350°C for 5 min in forming gas. The lifetime is measured at an injection level $D_n=1.10^{15}$ cm^{-3}.

Conversely, at 3 Torr, although the average lifetime at the center (3 cm diameter area) at an injection level of 1.10^{15} cm^{-3} is also around 100 µs (See Fig. 4.51), a strong inhomogeneity is observed. A few cm diameter spot corresponding to the region in front of the main gas entry (the same region as the high R_{sheet} region in conditions CR60803B) features a lifetime around 160 µs while the lifetime in the region around this spot drops to 60 µs. Finally in the region close to the edge of the wafer but still exposed to the plasma the lifetime reaches 180 µs. Thus in spite of a reduced uniformity of the films, the growth at 3 Torr allows to reach higher lifetimes than at 2 Torr.

Fig. 4.51 indicates that while at an injection level of 1.10^{15} cm^{-3} results are similar between layers grown at 2 and 3 Torr, a difference up to two orders of magnitude can be measured at 8.10^{13} cm^{-3}. A higher defect density in the layer grown at 2 Torr which would increase Shockley-Read-Hall

recombination may explain such a difference. Fig. 4.51 also shows that reaching injection level above 2.10^{15} cm^{-3} is not possible with our tool which can be explained by the high recombination rate in the layer due to defects.

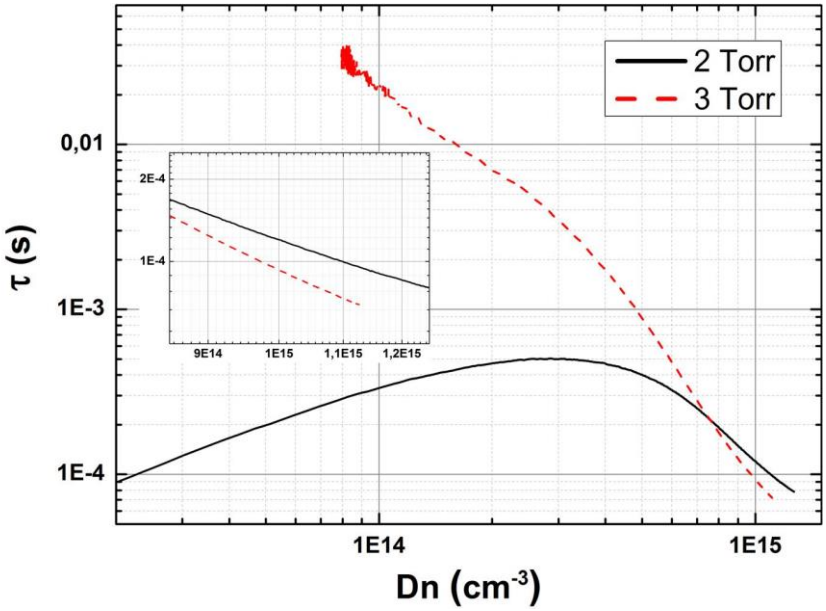

Fig. 4.51 – QSS-PC measurements performed at the center of intrinsic epi-layers grown at 2 and 3 Torr. The inset shows a zoom at Dn=10^{15} cm^{-3}. The lifetime is measured on a 3 cm diameter disk. These QSS-PC measurements are performed with the BT Imaging tool, as a result the QSS-PC measurement is performed at one single wavelength.

Despite the uncertainty concerning the epitaxial growth in the conditions CR60803B for a deposition time of 1800 s, the passivation of these layers has been studied. The investigation of the lifetime for such layers can provide insight on the electrical properties of the layer even though not fully understood. The samples have been passivated on both sides with 20 nm thick AlO_x layers deposited at 250°C. The photoconductance-calibrated photoluminescence imaging before and after annealing at 380°C during 20 min in forming gas is shown in Fig. 4.52. With these AlOx process conditions, the lifetime on a bare n-type FZ wafer (1-5 Ω.cm), used as reference sample, is 1.2 ms. Note that these AlO_x deposition conditions are different to those used above. These conditions have been processed at Air Liquid in a semi-industrial reactor suitable for 4" and 6" wafers. For the purpose of comparing passivation results of layers grown on 4" DSMP wafers and on 6" wafers after saw damage removal (SDR) and chemical polishing, we had to use the recipes developed by Air Liquide, which are quite different from ours.

As one can see, the pattern observed in R_{sheet} mappings is also observed in PL. Before annealing, in the low R_{sheet} region the lifetime is 90 µs and 40 µs in the high R_{sheet} region. After annealing, while the lifetime in the high R_{sheet} region is not significantly improved it rises to 160 µs in the low R_{sheet} region in the center part of the wafer. In the edge of the wafer a crescent-shaped region, the PC-calibrated PL image show a lifetime around 40 µs. This might be due to the AlO_x layer peeling-off. Except this low lifetime region, the annealing has a beneficial effect on the lifetime as confirmed in Fig. 4.53. The average lifetime is thus increasing from 70 µs to 115 µs. However, again, reaching injection levels above a few 10^{15} cm^{-3} with these samples remains impossible. From these measurements, the most likely explanation is that an epitaxial growth occurs in the high R_{sheet} region but not in the low R_{sheet} region.

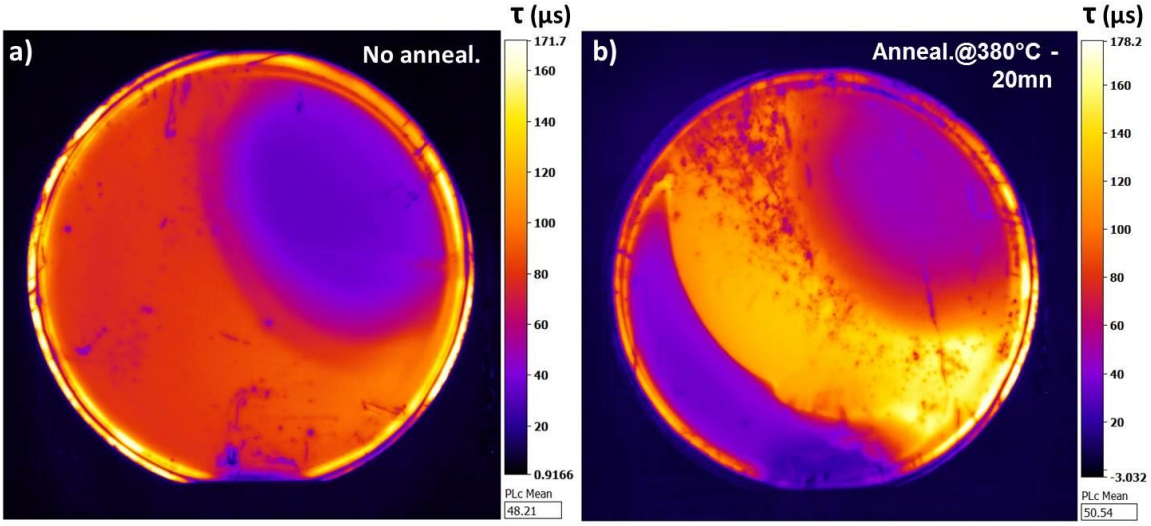

Fig. 4.52 – Photoconductance-calibrated photoluminescence imaging of a) as deposited and b) annealed samples grown on DSP polished 4" n-type wafer with conditions CR60803B and double-side passivated with 20 nm of AlO_x deposited at 250°C. The post-deposition annealing is carried out at 380°C during 20 min.

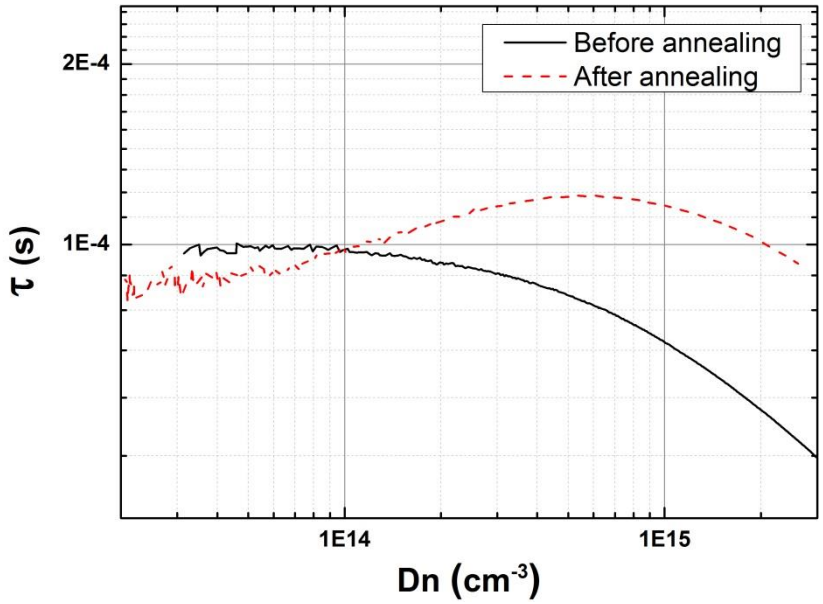

Fig. 4.53 – QSS-PC measurements obtained on layers grown with conditions CR60803B and double-side passivated with 20 nm AlO_x deposited at 250°C before and after an annealing at 380°C during 20 min.

The conditions CR60803B have also been processed on 6" wafers. This part has been carried out with the help of E. Drahi from Total, and Air Liquide.

Two type of substrates have been used, the first one are chemically polished etch pre-cells with an n^+ diffused layer at the back surface. On the front side, the layer processed in conditions CR60803B has been passivated by 6 nm of AlO_x deposited at 250°C followed by a post-deposition annealing (PDA) at 375°C during 20 min in forming gas. This AlO_x layer has been capped with a 70 nm thick silicon nitride (SiN_x) layer deposited at 400°C, on the rear side the n^+ diffused layer has also been passivated with a 70 nm thick SiN_x layer deposited at 400°C.

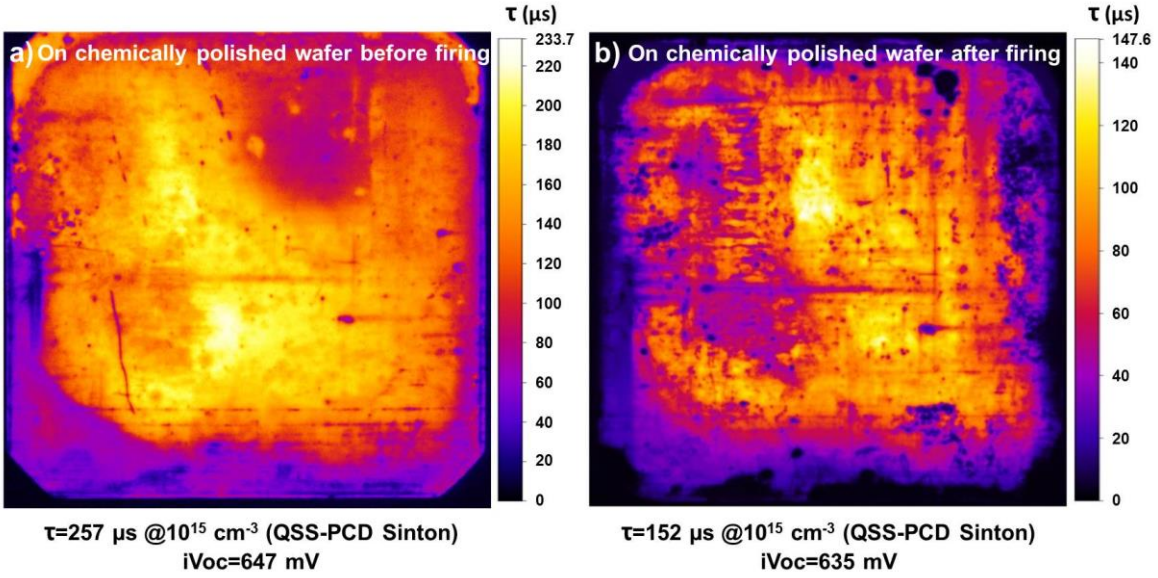

Fig. 4.54 – PC-calibrated PL images obtained on samples processed with conditions CR60803B on the front side of 6" chemically polished etch pre-cells with a n^+ diffused layer at the rear side. The front side is passivated with an AlO_x(6 nm)/SiN_x(70 nm) stack and the rear side with a 70 nm thick SiN_x layer. In a) the thermal budget applied to the sample is the AlO_x deposition at 250°C, the AlO_x PDA at 375°C for 20 min and the SiN_x deposition at 400°C. In b) in addition to this thermal budget, the thermal budget of the firing (2 min at 750°C) has been added. The values indicated below the PC-calibrated PL images have been measured by QSS-PC using a Sinton tool at the center of the wafers, the measurement area is 3 cm diameter.

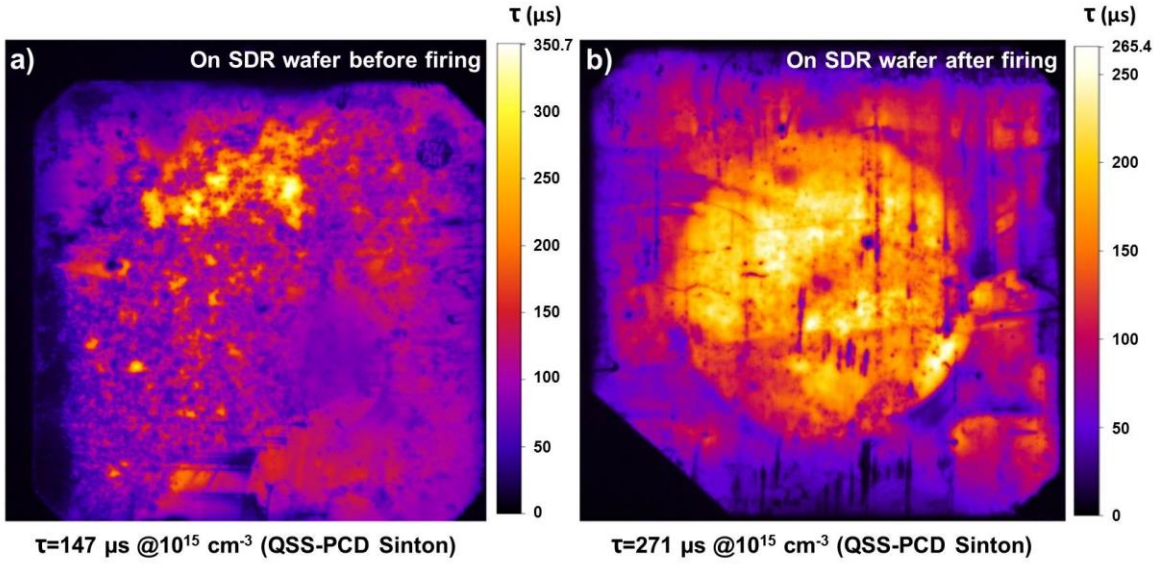

Fig. 4.55 – PC-calibrated PL images obtained on samples processed with conditions CR60803B on the front side of 6" wafers after saw damage removal (i.e. without chemical polishing). Both sides have been passivated with a 20 nm thick AlO_x layer annealed at 375°C for 20 min. In a) the thermal budget applied to the sample is the AlO_x deposition at 250°C and the AlO_x PDA at 375°C for 20 min. In b) in addition to this thermal budget, the thermal budget of the firing (2 min at 750°C) has been added. The values indicated below the PC-calibrated PL images have been measured by QSS-PC using a Sinton tool at the center of the wafers, the measurement area is 3 cm diameter.

Lifetime imaging by PC-calibrated PL and QSS-PC using a Sinton tool before and after application of the firing thermal budget, namely an annealing at 750°C during 2 min, are shown in Fig. 4.54.

Before firing, the average lifetime at the center measured by the Sinton tool is 257 µs on a chemically polished wafer. The pattern observed on the 4" FZ wafer corresponding to an inhomogeneous gas injection is still present but the low lifetime region seems smaller. In this region the lifetime is around 70 µs while it reaches between 140 µs and 180 µs on the major part of the wafer, as deduced from PC-calibrated images obtained using BT Imaging tool. After firing the average lifetime at the center measured by Sinton tool drops to 152 µs.

Surprisingly, the inverse behavior is observed on SDR wafers as shown in Fig 4.52. The passivation layers in this case are only composed of 20 nm thick AlO_x layers deposited on both sides. Before firing, the Sinton measurement indicates a lifetime of 147 µs, even though lifetimes up to 350 µs are measured by the BT Imaging tool in some small regions. After firing, the average lifetime increases to 271 µs. However, the probed area is not as large as the 6" wafer and this value corresponds to the lifetime in the region delimited by the circle which has a lifetime about twice higher than in the edge. We think that this pattern is induced by the 4" wafer used as stand for the PDA annealing after the AlO_x deposition, ensuring a better thermal coupling. Interestingly, this shape is only revealed after the firing and not after the PDA.

4.7. Conclusion

After a successful process conditions transfer for intrinsic epitaxy, the formation of phosphorus and boron-doped epitaxial layers has been investigated. Phosphorus doped epitaxial layers with R_{sheet} of 190 Ω have been achieved when the pressure is increased to 3 Torr. In spite of better structural properties, the increase of pressure induces a loss in the film uniformity and amorphous regions begin to appear. Boron-doped epi-layers with hole concentration between 2.10^{19} and 2.10^{20} cm^{-3} were also successively obtained, but a deposition rate of 0.07 Å/s and differences over two orders of magnitude of the hole concentration on a single quarter of wafer were not satisfactory.

Thus, fluid dynamics simulations were performed to model the gas injection in order to improve the homogeneity and the deposition rate. This allowed to determine that, in our process conditions, increasing the nozzle density from 0.1 to 0.65 cm^{-2} was beneficial on the gas injection homogeneity. As a result, intrinsic epi-layers with average crystalline fraction above 99% on a full 4" wafer with a standard deviation of 0.14% absolute were produced.

From this result we observed that B_2H_6 has a detrimental effect on the epi-layers homogeneity and their crystallinity. Nevertheless, boron-doped epi-layers with a hole concentration of 4.10^{19} cm^{-3} and with a doping efficiency up to 70% grown at a rate of 1.1 Å/s have been achieved. This is 15 times higher than the growth rate obtained with the initial shower head. We showed that at low pressure (2 Torr) the increase of RF power up to 90 W was dramatic on the crystalline quality, as observed from XRD scans, and as a result an increase of R_{sheet} values with the RF power was observed. While the increase of pressure was thought to be beneficial to grow doped epi-layers at high RF power with high crystallinity as shown by XRD and with a good doping uniformity as shown by R_{sheet} mapping, the different characterization techniques did not allow us to conclude about the question of actual growth in these conditions of high pressure (3 Torr). The growth of a doping compensated epi-layer or the

doping compensation of the top layers of the wafer induced by the plasma are the most likely explanations.

The investigation of epitaxial growth on Si(111) substrates has also been addressed. The fact that the crystallinity of the layer improves with the growth time indicates that a very likely epitaxial growth occurs on Si(111) substrates at 300°C. The study revealed that an increase of the temperature was beneficial on the crystallinity of the layer. Additionally, the increase of both RF power and pressure appears to be profitable to the quality of the layer.

As regards passivation of epi-layers, we have showed that for intrinsic epi-layers grown on Si(100) substrates, a low pressure (2 Torr) favors the homogeneity while a high pressure (3 Torr) enhanced the minority carrier lifetime to the detriment of a strong inhomogeneity. As a result, lifetimes up to 160 µs have been reached for an intrinsic epi-layer grown at 3 Torr on an intrinsic (5 kΩ.cm) FZ Si(100) wafer and passivated on both side by AlO_x.

References

[1] D. Shahrjerdi, B. Hekmatshoar, S. W. Bedell, M. Hopstaken, and D. K. Sadana, "Low-Temperature Epitaxy of Compressively Strained Silicon Directly on Silicon Substrates," *J. Electron. Mater.*, vol. 41, no. 3, pp. 494–497, Nov. 2011.

[2] J. Damon-Lacoste, M. Labrune, and S. Granata, "Crystalline silicon solar cellls with doped epitaxial silicon films obtained at low-T by PECVD," *IEEE PVSC Proc.*, 2010.

[3] K. Baert, J. Vanhellemont, W. Vandervorst, J. Nijs, and M. Konagai, "Heavily phosphorus-doped epitaxial Si deposited by low-temperature plasma-enhanced chemical vapor deposition," *Appl. Phys. Lett.*, vol. 59, no. 7, p. 797, Aug. 1991.

[4] B. S. Meyerson and M. L. Yu, "Phosphorus-Doped Polycrystalline Silicon via LPCVD - Process Characterization," *J. Electrochem. Soc.*, vol. 131, no. 10, p. 2366, 1984.

[5] B. S. Meyerson and M. L. Yu, "Phosphorus-Doped Polycrystalline Silicon via LPCVD - Surface Interactions of the Silane/Phosphine/Silicon System," *J. Electrochem. Soc.*, vol. 131, no. 10, p. 2361, 1984.

[6] Y. Tsukidate and M. Suemitsu, "Growth kinetics and doping mechanism in phosphorus-doped Si gas-source molecular beam epitaxy," *Appl. Surf. Sci.*, vol. 175–176, pp. 43–48, 2001.

[7] L. Kipp, R. D. Bringans, D. K. Biegelsen, J. E. Northrup, A. Garcia, and L. E. Swartz, "Phosphine adsorption and decomposition on Si(100) 2x1 studied by STM," *Phys. Rev. B*, vol. 52, no. 8, pp. 5843–5850, 1995.

[8] B. Cho *et al.*, "Phosphorus incorporation during Si(001):P gas-source molecular beam epitaxy: Effects on growth kinetics and surface morphology," *J. Appl. Phys.*, vol. 103, no. 12, pp. 1–10, 2008.

[9] R. J. Bennett and C. Parish, "Interpretation of the temperature dependence of partition and sticking coefficients for antimony, phosphorus and boron in silicon," *J. Phys. D. Appl. Phys.*, vol. 9, no. 18, pp. 2555–2564, Dec. 1976.

[10] E. Bardet *et al.*, "The grain size in microcrystalline silicon: correlation between atomic force microscopy, UV reflectometry, ellipsometry, and X-ray diffractometry," *J. Non. Cryst. Solids*, vol. 198–200, pp. 867–870, May 1996.

[11] L. Viña and M. Cardona, "Optical constants of pure and heavily doped silicon and germanium: Electronic interband transitions," *Phys. B+C*, vol. 117–118, pp. 356–358, Mar. 1983.

[12] A. Tempez, S. Legendre, and P. Chapon, "Depth profile analysis by plasma profiling time of flight mass spectrometry," *Nucl. Instruments Methods Phys. Res. Sect. B Beam Interact. with Mater. Atoms*, vol. 332, pp. 351–354, Aug. 2014.

[13] G. Masetti, M. Severi, and S. Solmi, "Modeling of carrier mobility against carrier concentration in arsenic-, phosphorus-, and boron-doped silicon," *IEEE Trans. Electron Devices Proc.*, vol. 30, no. 7, pp. 764–769, 1983.

[14] M. Moreno, G. Patriarche, and P. Roca i Cabarrocas, "Fine-tuning of the interface in high-quality epitaxial silicon films deposited by plasma-enhanced chemical vapor deposition at 200 °C," *J. Mater. Res.*, 2013.

[15] F. H. Horn, "Densitometric and Electrical Investigation of Boron in Silicon," *Phys. Rev.*, vol. 97, no. 6, pp. 1521–1525, Mar. 1955.

[16] G. Celotti, D. Nobili, and P. Ostoja, “Lattice parameter study of silicon uniformly doped with boron and phosphorus,” *J. Mater. Sci.*, vol. 9, no. 5, pp. 821–828, May 1974.

[17] J. Kucytowski and K. Wokulska, “Lattice parameter measurements of boron doped Si single crystals,” *Cryst. Res. Technol.*, vol. 40, no. 4–5, pp. 424–428, Apr. 2005.

[18] H.-J. Herzog, “X-Ray Investigation of Boron- and Germanium-Doped Silicon Epitaxial Layers,” *J. Electrochem. Soc.*, vol. 131, no. 12, p. 2969, 1984.

[19] J. -m Baribeau, S. J. Rolfe, and J.-M. Baribeau, “Characterization of boron-doped silicon epitaxial layers by x-ray diffraction,” *Cit. Appl. Phys. Lett*, vol. 58, 1991.

[20] G. Glass *et al.*, “Ultrahigh B doping (10^{22} cm^{-3}) during Si(001) gas-source molecular-beam epitaxy: B incorporation, electrical activation, and hole transport,” *Phys. Rev. B*, vol. 61, no. 11, pp. 7628–7644, Mar. 2000.

[21] T. Ulyanenkova, M. Myronov, and A. Ulyanenkov, “Boron doped cubic silicon probed by high resolution X-ray diffraction,” *Phys. status solidi*, vol. 12, no. 3, pp. 255–258, Mar. 2015.

[22] H. Li, “Mass transport analysis of a showerhead MOCVD reactor,” *J. Semicond.*, vol. 32, no. 3, p. 33006, Mar. 2011.

[23] M. Chang, D. N. K. Wang, J. M. White, and D. Maydan, “Inlet manifold and methods for increasing gas dissociation and for PECVD of dielectrics films,” US4854263, 1989.

[24] X. S. Guo, K. Koal, L. Chen, M. K. Bhan, and B. Zheng, “Pattern of apertures in a showerhead for chemical vapor deposition,” US6050506, 2000.

[25] L. Sansonnens, A. A. Howling, and C. Hollenstein, “A gas flow uniformity study in large-area showerhead reactors for RF plasma deposition,” *Plasma Sources Sci. Technol.*, vol. 9, no. 2, pp. 205–209, May 2000.

[26] A. Descoeudres, L. Sansonnens, and C. Hollenstein, “Attachment-induced ionization instability in electronegative capacitive RF discharges,” *Plasma Sources Sci. Technol.*, vol. 12, no. 2, pp. 152–157, May 2003.

[27] B. Bruneau *et al.*, “Ion Energy Threshold in Low-Temperature Silicon Epitaxy for Thin-Film Crystalline Photovoltaics,” *IEEE J. Photovoltaics*, vol. 4, no. 6, pp. 1361–1367, Nov. 2014.

[28] J.-M. Chauveau, Y. Androussi, A. Lefebvre, J. Di Persio, and Y. Cordier, “Indium content measurements in metamorphic high electron mobility transistor structures by combination of x-ray reciprocal space mapping and transmission electron microscopy,” *J. Appl. Phys.*, *J. Appl. Phys.*, vol. 93, no. 7, pp. 4219–4225, 2003.

[29] E. N. Shauly and S. Lachman-Shalem, “Activation improvement of ion implanted boron in silicon through fluorine co-implantation,” *J. Vac. Sci. Technol. B Microelectron. Nanom. Struct.*, vol. 22, no. 2, p. 592, 2004.

[30] K. Ohyu, T. Itoga, and N. Natsuaki, “Advantages of Fluorine Introduction in Boron Implanted Shallow p^+/n-Junction Formation,” *Jpn. J. Appl. Phys.*, vol. 29, no. Part 1, No. 3, pp. 457–462, Mar. 1990.

[31] N. M. Johnson, “Mechanism for hydrogen compensation of shallow-acceptor impurities in single-crystal silicon,” *Phys. Rev. B*, vol. 31, no. 8, pp. 5525–5528, Apr. 1985.

[32] P. Narchi, R. Cariou, M. Foldyna, P. Prodhomme, and P. Roca i Cabarrocas, “Nanoscale Investigation of Carrier Lifetime on the Cross Section of Epitaxial Silicon Solar Cells Using Kelvin Probe Force Microscopy,” *IEEE J. Photovoltaics*, vol. 6, no. 6, pp. 1576–1580, Nov.

2016.

[33] M. Labrune, “Silicon surface passivation and epitaxial growth on c-Si by low temperature plasma processes for high efficiency solar cells,” Ecole Polytechnique, 2011.

5. Conclusion and perspectives

n-PERT solar cells are gaining more in more interest as a possible next step for the PV industry. The current fabrication process of the doped layers in such technology relies on diffusion. An alternative approach consists in replacing the diffusion process by a high temperature epitaxy using APCVD. This leads to conversion efficiency up to 22.5%. In this PhD we focused on an innovative way to manufacture the doped layers by low temperature epitaxy (<300°C) using PECVD. In particular, this thesis focuses on the epitaxial growth from $SiF_4/H_2/Ar$ gas mixtures and carries on J.C. Dornstetter's work about µc-Si:H.

Achievements

Three main topics were addressed during this thesis: i) the definition of process conditions for intrinsic epitaxy and the causes of epitaxy breakdown, ii) the growth mechanisms behind such unexpected epitaxy process and iii) the development of boron and phosphorus doped epi-layers, their scale-up to 156×156 mm^2 wafers and their passivation.

The study of the influence of the plasma parameters on the structural properties of the layers characterized by spectroscopic ellipsometry, Raman spectroscopy, TEM and XRD, allowed to define process conditions for intrinsic epitaxial growth in Philix, a 4 inches research PECVD reactor. First, the full H_2 depletion, measured with a residual gas analyzer, has been identified as a necessary condition for the epitaxial growth. Under this condition, a $[H_2]/[SiF_4]$ gas ratio below 1/3 is required to grow monocrystalline layers free of H-platelets.

Thus, to increase the growth rate which is controlled by the H_2 flow rate, an increase of the H_2 flow rate requires an increase of the RF power to stay in the full H_2 depletion regime (or H_2-limited regime), which in turn requires an increase of the SiF_4 flow rate to keep the $[H_2]/[SiF_4]$ gas ratio below 1/3. For optimized process conditions, excellent structural properties have been obtained. Intrinsic epi-layers with a 100% crystalline fraction deduced from ellipsometry measurements have been achieved. Raman spectroscopy measurements of TO mode indicate that FWHM and peak positions of intrinsic epi-layers are identical to those of a c-Si wafer. Finally a variation of lattice parameter with respect to that of a c-Si wafer below 1.10^{-3} Å has been assessed by XRD. Furthermore, by correlating electron diffraction patterns and pole figures performed on samples after epitaxy breakdown, we also identified the formation of twins as the cause of epitaxy breakdown in epi-layers grown from $SiF_4/H_2/Ar$ gas mixtures.

The investigation of the growth mechanisms have been carried out by the correlation of *in situ* ellipsometry measurement and HR-TEM performed in the early stages of growth. The observation of a first phase of nucleation described by the roughening of the substrate through the presence of a few nm islands followed by the coalescence of these islands and the smoothening of the layer allowed to affirm that low temperature epitaxy by PECVD from $SiF_4/H_2/Ar$ chemistry relies on a Volmer-Weber growth mode.

Boron and phosphorus doped epi-layers have been developed after the successful transfer of the process conditions defined in Philix to Cluster, a 6 inches pre-pilot semi-industrial PECVD reactor.

Based on this, boron and phosphorus doped epitaxial layers with sheet resistances of 105 and 190 Ω, respectively, have been obtained. However these epi-layers were strongly inhomogeneous and the growth rate very low (0.07 Å/s for boron-doped layers). Therefore fluid dynamics simulations have been performed to optimize the shower head design in order to obtain a homogenous gas injection. As a result, intrinsic epi-layers with average crystalline fraction above 99% on a full 4" wafer with a standard deviation of 0.14% absolute were produced at a growth rate of 1.2 Å/s. This is 6 times faster than the layers grown with the initial shower head. From this result we observed that B_2H_6 has a detrimental effect on the epi-layers homogeneity and crystallinity. Nevertheless, boron doped epi-layers with an as-deposited hole concentration of 4.10^{19} cm^{-3} and a doping efficiency up to 70% have been achieved. The growth rate in these conditions reached 1.1 Å/s and is therefore 15 times faster than that obtained with the former shower head.

Finally a minority carriers lifetime of 160 µs was measured on a sample composed of a 200 nm thick intrinsic layer grown on a 4 inches wafer passivated on both sides with AlO_x. This lifetime is in the same order of magnitude to what was obtained with SiH_4/H_2 (150 µs) [1]. However, for doped epi-layers the lifetime dropped to 50 µs. We have shown that a low pressure (2 Torr) favors the homogeneity while a high pressure (3 Torr) enhanced the minority carrier lifetime to the detriment of the homogeneity. Although these lifetimes are not sufficient to achieve high performance devices, it is a significant improvement with respect to the 6 µs measured on the first intrinsic samples.

Concerning the potential applications and the pros and cons of this chemistry:

In light of the issues we encountered to achieve uniformly doped epi-layers, the transfer of process conditions to industry remains difficult. Moreover the process window for doped or undoped epitaxy is very tight. For epitaxial conditions at $SiF_4/H_2/Ar$=50/4/500 sccm, an increase of 1 sccm of H_2 in the gas mixture (from 4 to 5) leads to a fully amorphous layer. Thus, the margin of error is narrow, which is a serious drawback for industrial applications. In addition, the gas injection management is more difficult in $SiF_4/H_2/Ar$ than in SiH_4/H_2 chemistry. Finally, SiF_4 is not commonly used in the photovoltaics industry which represents a brake for a SiF_4-based process transfer. However if combined to other processes using SiF_4, such as the *in situ* silicon oxide removal and passivation layers (a-Si:H:F, fluorinated SiN_x), the transfer may be more attractive.

However to compare with SiH_4/H_2, the $SiF_4/H_2/Ar$ chemistry ensures a smaller variation of the lattice parameter with respect to that of the substrate (by one order of magnitude). Therefore, $SiF_4/H_2/Ar$ chemistry reduces risks of relaxation and consequent defective layer formation in the vicinity of the epi/wafer interface. This is attributed to the lower hydrogen incorporation in layers grown from $SiF_4/H_2/Ar$ gas mixtures. This could also explain the possibility to measure sheet resistances in as-deposited layers grown from $SiF_4/H_2/Ar/B_2H_6$ gas mixtures. Conversely, doped epi-layers grown by $SiH_4/H_2/B_2H_6$ or $SiH_4/H_2/B(CH_3)_3$ required a 270°C 30 min annealing before measuring a sheet resistance which may be attributed to the desorption of hydrogen and dissociation of B-H complexes.

Perspectives

Even though significant improvements have been achieved, especially in terms of homogeneity and deposition rate, the results are not fully satisfactory yet. A further development of boron doped epi-layers around 2.5 Torr to make a trade-off between higher lifetime and homogeneity could be the next step. The inter-electrode distance has to be varied in such a way that $p \times d$ remains between 5 to 8 Torr.cm to keep a high deposition rate. Besides, additional fluid dynamics simulations to design a fully

optimized shower head with a nozzle profile adapted to the gas used in the mixtures should be addressed. This would allow to use a wider range of pressure and inter-electrode distance, keeping good uniformity, to focus on the electrical properties.

In addition, the properties of the layers grown at a pressure 3 Torr and an inter-electrode distance of 3 cm have to be understood. The question of the doping compensation is very interesting from a scientific and technological point of view and could lead to innovative applications.

The increase of temperature is also an axis to investigate. We showed in this thesis, that the increase of the substrate temperature had a beneficial effect on the growth rate and the crystallinity of the layer grown on Si(100) substrates. We also showed that rising the substrate temperature enhanced the crystallinity of layers grown on Si(111) substrates but the growth rate was too low for practical applications. The increase of the substrate temperature to 400°C should provide interesting results.

Above all, the priority is to develop proper wafer cleaning sequences prior to epitaxy. This is paramount for two main reasons. First, the quality of the interface is very important for the electrical performances of an epitaxial emitter. All the more so since dopants diffuse over short distance (<100 nm) in the wafer due to the low temperature of the process, the defective interface is contained in the space charge region which is even more critical. Second, removing contaminations at the surface prior to epitaxy would allow a better understanding of the influence of the surface state on the early stages of growth and in particular on the formation of the initial defective layer. Moreover, additional insights on the growth mechanisms involved in LTE by PECVD would be provided. Thus, from a technological and scientific point of view the surface state is a major concern. Different cleaning processes can be suggested. Recamán Payo *et al.* [2], from IMEC reached up to 22% efficient IBC solar cells with epitaxial emitters grown after RCA cleaning. They also observed that a simplified cleaning such as piranha clean followed by HF/HCl dip or only piranha leads to similar results. Kuzma-Filipek *et al.* [3], also from IMEC, compared the performances of n-PERT solar cells with rear side epitaxial emitters grown after different cleaning processes. They showed that using simplified cleaning sequences such as sulfuric acid and ozone mixtures (SOM) or deionized water and ozone mixtures (IPV) lead to similar results at device levels as a more standard but more expensive cleaning using sulfuric acid and peroxide mixtures (SPM). Thus, SOM and IPV cleaning on textured surfaces lead to J_{0e} of 13.4 ± 0.7 and 11.7 ± 0.6 fA.cm^{-2} respectively, while the SPM, used a reference, leads to a J_{0e} of 14.0 ± 0.7 fA.cm^{-2}. The development of the efficient and sulfur-free IPV cleaning process could thus be an interesting perspective.

After this, the investigation of recombination in epi-layers is an important issue to address. We showed by ellipsometry, XRD and Raman spectroscopy that the structural properties of the layers achieved with $SiF_4/H_2/Ar$ gas mixtures are similar to those of c-Si wafers. However lifetimes measured on the epi-layers are too low to expect to reach high efficiency solar cells. The first investigation should focus on the identification of the highly recombinant regions. To tackle this, electron beam induced current carried out on the cross-section of epi-layers is a relevant approach. This would allow to map the diffusion length of minority carriers throughout the epi-layers and to identify if the full epi-layer is highly recombinant or if recombination mostly occurs in the interface region. This crucial information would indicate the priority issues to address. Moreover this study should be carried out for process conditions leading to different hydrogen incorporation. We have seen that hydrogen incorporation has a negative effect on the structural properties, the layer is more strained and has a variation of lattice parameter along its thickness. Inversely, hydrogen incorporation can favor the passivation of defects and improve the minority carriers lifetime. The second investigation to focus on is the identification of recombination mechanisms. High crystalline fractions and low

mosaicity are necessary conditions to obtain good electrical properties but the characterization of point defects is difficult to address with the techniques we used during this PhD, namely ellipsometry, Raman spectroscopy and XRD. Deep level transient spectroscopy (DLTS), positron annihilation spectroscopy (PAS) and electron paramagnetic resonance (EPR) are techniques allowing the characterization of point defects such as vacancies. Thus the identification of electrically active defects via these techniques would be of interest.

More long term studies can also be suggested. The use of quadrupole mass spectrometry (QMS) opens a new path of research for the identification of species in the plasma. This would provide additional insight on the growth mechanisms and could give guidelines for the enhancement of growth rate. In order to increase the growth rate the use of high frequencies (27.12, 40.68, 60 MHz) PECVD correlated with QMS studies are also promising options to investigate.

Finally, another promising perspective is the silicon epitaxial growth on III-V substrates. We observed that for epitaxial process conditions at the H_2 depletion transition performed on a GaAs substrate, a polycrystalline growth of silicon is possible as shown in Fig. 5.1. The fit of the ellipsometry spectrum indicates a polycrystalline fraction (large grains poly-Si from Jellison [4]) of 100% and an amorphous fraction of 0%. These results are encouraging for the formation of multi-junction solar cells by PECVD using $SiF_4/H_2/Ar$ chemistry.

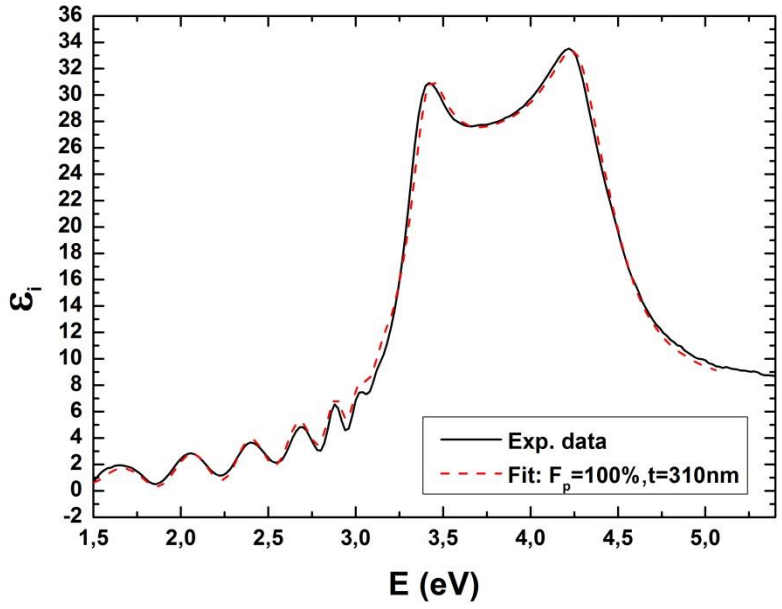

Fig. 5.1 – Ellipsometry spectrum of a polycrystalline silicon layer grown on a GaAs substrate at 200°C. This experiment has been carried out in Philix. The experimental data fit with a 100% poly-Si (large grains) and 310 nm thick layer. Process conditions: $SiF_4/H_2/Ar$=3.6/2/88, P_{RF}=10 W, d=200 mm, p=3 Torr. The deposition rate is 3.2 Å/s.

References

[1] R. Cariou, “Epitaxial growth of Si(Ge) materials on Si and GaAs by low temperature PECVD: towards tandem devices,” PhD thesis, Ecole Polytechnique, 2015.

[2] M. Recamán Payo, N. Posthuma, A. de Castro, M. Debucquoy, and J. Poortmans, “Boron-doped selective silicon epitaxy: high efficiency and process simplification in interdigitated back contact cells,” *Prog. Photovoltaics Res. Appl.*, vol. 22, no. 7, pp. 711–725, 2014.

[3] R. H. I. Kuzma-Filipek, M. Recamán, F. Duerinckx, TS. Ravi1, M. E. Cornagliotti, P. Choulat, A. Sharma, J. John, and J. S. & J. P. Aleman, L. Tous, R. Russell, A. Uruena, “22.5% n-PERT Solar Cells on Epitaxially Grown Silicon Wafers,” in *EUPVSEC Proceedings*, 2016.

[4] G. E. Jellison, M. F. Chisholm, and S. M. Gorbatkin, “Optical functions of chemical vapor deposited thin-film silicon determined by spectroscopic ellipsometry,” *Appl. Phys. Lett.*, vol. 62, no. 25, pp. 3348–3350, Jun. 1993.

List of publications

Peer reviewed publications

- R. Léal, F. Haddad, G. Poulain, J.-L. Maurice, P. Roca i Cabarrocas, "High quality boron-doped epitaxial layers grown at 200°C from $SiF_4/H_2/Ar$ gas mixtures for emitter formation in crystalline silicon solar cells", *AIP Advances*, vol. 7, no. 2, p. 25006, Feb. 2017.

- W. Chen, R. Cariou, G. Hamon, R. Léal, J.-L. Maurice, P. Roca i Cabarrocas, "Influence of deposition rate on the structural properties of plasma-enhanced CVD epitaxial silicon", *Scientific Reports*, vol. 7, p. 43968, Mar. 2017.

- W. Chen, G. Hamon, R. Léal, J.-L. Maurice, L. Largeau, and P. Roca i Cabarrocas, "Plasma-enhanced epitaxial growth of stable tetragonal Si," *To be published in Journal of Crystal Growth.*

Conference proceedings

- R. Léal, J.-C. Dornstetter, F. Haddad, G. Poulain, J.-L. Maurice, P. Roca i Cabarrocas, "Silicon epitaxy by low-temperature RF-PECVD using $SiF_4/H_2/Ar$ gas mixtures for emitter formation in crystalline solar cells", IEEE 42nd Photovoltaic Specialist Conference (PVSC), pp. 1-5, 2015.

- R. Léal, J.-C. Dornstetter, F. Haddad, B. Bruneau, R. Cariou, W. Chen, I. Cosme, G. Poulain, J.-L. Maurice, P. Roca i Cabarrocas, "Epitaxial growth of silicon thin films by low temperature RF-PECVD fom $SiF_4/H_2/Ar$", *30th EUPVSEC Proceedings*, 2014.

Intellectual property

- **Patent:** R. Léal, G. Poulain, J. Damon-Lacoste, *European Procedure*

- **Invention Disclosure Form**: R. Léal, E. Drahi, G. Poulain, P. Roca i Cabarrocas

Distinctions

- Finalist for the Best Visual Presentation, *42nd IEEE PVSC*, 2015

- Best Presentation Award, *Workshop on Energy Transition*, 2015

université PARIS-SACLAY

ÉCOLE DOCTORALE
INTERFACES
Approches Interdisciplinaires : Fondements, Applications et Innovation

Titre : Croissance épitaxiale à basse température pour la formation de l'émetteur dans les cellules en silicium cristallin par dépôt chimique en phase vapeur assisté par plasma à partir de $SiF_4/H_2/Ar$

Mots clés : épitaxie basse température, émetteur épitaxié, SiF_4, silicium cristallin, cellule solaire

Résumé : Cette thèse de doctorat évalue le potentiel de la croissance épitaxiale à basse température (200-300°C) par dépôt chimique en phase vapeur assisté par plasma à partir de $SiF_4/H_2/Ar$ pour la formation de l'émetteur dans des cellules solaires de type nPERT. La première partie concerne l'identification et l'optimisation des conditions de dépôt pour réaliser des couches épitaxiées faiblement contraintes avec une interface epi/wafer de bonne qualité. La perte d'épitaxie a également été étudiée et nous avons mis en évidence que la formation de macles au cours de la croissance était responsable de la dégradation de la cristallinité. Ensuite, l'étude des mécanismes de croissance a été menée et l'analyse des phases initiales de croissance a permis d'identifier un mode de croissance de type Volmer-Weber. Les conditions de dépôt ont ensuite été transférées à un réacteur PECVD semi-industriel de 6 pouces. Les problèmes d'homogénéité et de vitesse de croissance ont été abordés par le design d'une nouvelle « shower head » grâce aux simulations d'écoulement du gaz. Des couches épitaxiées dopées bore avec un dopage de type *p* de 4.10^{19} cm^{-3} et une efficacité de dopage jusqu'à 70% ont ainsi été fabriquées à seulement 300°C. La vitesse de croissance dans ces conditions atteint 1.1 Å/s, i.e. 15 fois plus rapide que les premiers résultats obtenus. Enfin, la passivation des couches épitaxiées a été étudiée et un temps de vie de 160 µs a été obtenu sur des couches intrinsèques de 200 nm d'épaisseur passivées avec 10 nm d'oxyde d'aluminium.

Title: Low-temperature formation of epitaxial emitter in crystalline silicon solar cells by plasma-enhanced chemical vapor deposition using $SiF_4/H_2/Ar$ gas mixtures

Keywords: low-temperature epitaxy, PECVD, epitaxial emitter, SiF_4, crystalline silicon, solar cell

Abstract: This doctoral work aimed to assess the potential of low-temperature (200-300°C) epitaxy by plasma-enhanced chemical vapor deposition (PECVD) using $SiF_4/H_2/Ar$ gas mixtures for the emitter formation in nPERT solar cells. The first part of this PhD thesis concerned the identification and the optimization of the process conditions to perform lowly strained intrinsic epi-layers with a smooth epi/wafer interface. We also investigated the causes of epitaxy breakdown and found out that a twinning-induced mechanism was responsible. Subsequently we focused on the growth mechanisms by studying the initial stages of growth and a Volmer-Weber growth mode has been highlighted. Finally, the process conditions for intrinsic epitaxy were transferred from a research PECVD reactor to a 6 inch semi-industrial one. Inhomogeneity and growth rate issues have been tackled by fluid dynamics simulations resulting in the design of a new shower head. Boron-doped epi-layers grown at 300°C with an as-deposited hole concentration of 4.10^{19} cm^{-3} and a doping efficiency up to 70 % have been achieved keeping a low mosaicity and a low variation of the lattice parameter. The growth rate in these conditions reached 1.1 Å/s, i.e 15 times higher than what obtained at the beginning of this PhD for boron-doped epi-layers. Finally, the passivation of epitaxial layers has been investigated and lifetimes up to 160 µs for a 200 nm thick intrinsic layer passivated with 10 nm of aluminum oxide have been reached.